Departamento de Química Física
y Termodinámica Aplicada
Universidad de Córdoba

ORGANIZACIÓN MOLECULAR EN PELÍCULAS DE LANGMUIR. ESTUDIOS POR SIMULACIÓN Y APLICACIÓN EN DISPOSITIVOS ORGÁNICOS ELECTROLUMINISCENTES.

MOLECULAR ORGANIZATION OF LANGMUIR FILMS. COMPUTER SIMULATION STUDIES AND APPLICATION TO ORGANIC LIGHT EMITTING DEVICES

Tesis Doctoral

Juan José Giner Casares

Córdoba, Abril 2009

TITULO: *Organización molecular en películas de langmuir. Estudios por simulación y aplicación en dispositivos orgánicos electroluminiscentes*

AUTOR: *JUAN JOSÉ GINER CASARES*

Campus de Rabanales
Ctra. Nacional IV, Km. 396
14071 Córdoba

www.uco.es/publicaciones
publicaciones@uco.es

ISBN-13: 978-84-7801-964-9
D.L.: CO-751/2009

ORGANIZACIÓN MOLECULAR EN PELÍCULAS DE LANGMUIR.
ESTUDIOS POR SIMULACIÓN Y APLICACIÓN
EN DISPOSITIVOS ORGÁNICOS ELECTROLUMINISCENTES.

LOS DIRECTORES

Fdo.: Luis Camacho Delgado
Catedrático del Departamento de Química Física y Termodinámica Aplicada.
Universidad de Córdoba.

Fdo.: María Teresa Martín Romero
Profesora Contratada Doctora del Departamento de Química Física y Termodinámica Aplicada. Universidad de Córdoba.

Fdo.: José Javier López Cascales
Profesor Titular del Departamento de Arquitectura y Tecnología de la Edificación.
Área de Química Física.
Universidad Politécnica de Cartagena.

Trabajo presentado para optar al grado de Doctor en Ciencias Químicas

Fdo.: Juan José Giner Casares
Licenciado en Ciencias Químicas

DEPARTAMENTO DE QUÍMICA FÍSICA
Y TERMODINÁMICA APLICADA
UNIVERSIDAD DE CÓRDOBA

D. Luis Camacho Delgado, Catedrático y Director del Departamento de Química Física y Termodinámica Aplicada de la Universidad de Córdoba,

INFORMA:

Que el trabajo presentado como Tesis Doctoral por D. Juan José Giner Casares, titulado "*Organización Molecular en Películas de Langmuir. Estudios por Simulación y Aplicación en Dispositivos Orgánicos Electroluminiscentes*" ha sido realizado en los laboratorios de este Departamento, así como en las instalaciones del Grupo de Bioinformática y Macromoléculas de la Universidad Politécnica de Cartagena (España), el Center for Photochemical Sciences de la Bowling Green State University (Estados Unidos de América) y en el Centre for Molecular and Nanoscale Electronics de la Universidad de Durham (Reino Unido), y reúne las condiciones exigidas según legislación vigente.

Y para que conste, firmo el presente en Córdoba a cinco de Marzo de dos mil nueve.

Fdo.: Luis Camacho Delgado

Mediante la defensa de esta memoria se pretende optar a la obtención de la **mención de "Doctorado Europeo"**, habida cuenta que el doctorando reúne los requisitos exigidos para tal mención:

1. Se cuenta con los informes favorables de dos doctores pertenecientes a instituciones de Enseñanza Superior, o instituto de investigación, de países europeos distintos al nuestro.
2. En el Tribunal, que ha de evaluar la Tesis, existe un miembro de un centro de Enseñanza Superior de un país europeo distinto al nuestro.
3. Parte de la redacción y defensa de la Memoria se realizará en la lengua oficial de un país europeo distinto al nuestro.
4. El doctorando ha realizado una parte del trabajo experimental en las instalaciones del Centre for Molecular and Nanoscale Electronics de la Universidad de Durham (Reino Unido). Esta estancia, de un trimestre de duración, se ha realizado gracias a la concesión de ayuda para estancias breves en el extranjero asociada a la beca de Formación de Profesorado Universitario del Ministerio de Ciencia e Innovación.

El trabajo que engloba la presente Memoria se ha realizado durante el periodo de disfrute de una Beca de Formación de Profesorado Universitario del Ministerio de Ciencia e Innovación, asociada a los proyectos financiados por la D. G. I. C. Y T. "*Preparación, caracterización y estudio del funcionamiento de películas ultrafinas en la escala del nanómetro como sensores ópticos y dispositivos electroluminiscentes*" (CTQ2004/03246/BQU) y "*Influencia de la organización molecular en fenómenos de transferencia eléctrica y de transferencia de energía. Aplicaciones al diseño de dispositivos nanoestructurados*" (CTQ2007/64474)

Índice General

Objetivos **5**

1. Introducción **9**

1.1. Películas de Langmuir y Langmuir−Blodgett (LB) 11

1.1.1. Formación y Caracterización de Monocapas en la Interfase Aire−Agua 12

1.1.2. Formación y Caracterización de Películas de Langmuir-Blodgett 22

Referencias 28

1.2. Dinámica Molecular 31

1.2.1. Fundamento Físico 32

1.2.2. Campo de Fuerzas. Aproximaciones en Dinámica Molecular 36

Referencias 42

1.3. Dispositivos Orgánicos Electroluminiscentes, OLEDs 43

Referencias 51

2. Experimental **53**

2.1. Técnicas de Caracterización de la Monocapa en la Interfase Aire−Agua 55
2.2. Técnicas de Caracterización de Películas en la Interfase Aire-Sólido 60
2.3. Dinámica Molecular. GROMACS 3.3. 61
2.4. Materiales, Reactivos y Tratamiento de Datos 62
Referencias 64

3. Organización Molecular de Películas Delgadas Mixtas en la Interfase Aire−Agua 65

3.1. Effect of the Molecular Methylene Blue Aggregation on the Mesoscopic Domain Morphology in Mixed Monolayers with DMPA 67
3.1.1. Introduction 68
3.1.2. Experimental 70
3.1.3. Results and Discussion 72
3.1.4. Conclusions 96
3.1.5. Supporting Information: Reflection of an Anisotropic Thin Film on Isotropic Substrate 97
References 105
3.2. Molecular Organization of a Water-Insoluble iridium (III) Complex in Mixed Monolayers 109
3.2.1. Introduction 110
3.2.2. Experimental 112
3.2.3. Results and Discussion 114

3.2.4. Conclusions 130
References 133
3.3. Segregation of Lipid in Ir-dye/DMPA Mixed Monolayers as Strategy to Fabricate 2D Supramolecular Nanostructures at the Air−Water Interface 137
3.3.1. Introduction 138
3.3.2. Experimental 140
3.3.3. Results 143
3.3.4. Discussion 153
3.3.5. Conclusions 160
References 163

4. Simulación de Monocapas de Langmuir mediante Dinámica Molecular 167

4.1. Effect of the Barometric Phase Transition of a DMPA Bilayer on the Lipid/Water Interface 169
4.1.1. Introduction 170
4.1.2. Method and Model 173
4.1.3. Results and Discussion 176
4.1.4. Conclusions 192
References 194
4.2. A DMPA Langmuir monolayer study: From gas to solid phase. An atomistic description by Molecular Dynamics Simulation . 197
4.2.1. Introduction 198
4.2.2. Method and Model 199

4.2.3. Results and Discussion 204
4.2.4. Concluding remarks 217
References 219
4.3. Effect of Na^+ and Ca^{2+} ions on a $DMPA^-$ lipid Langmuir monolayer 223
4.3.1. Introduction 224
4.3.2. Method and Model 225
4.3.3. Results and Discussion 227
4.3.4. Conclusions 237
References 240

5. Dispositivos Orgánicos Electroluminiscentes 243

5.1. Highly Pure and Stable White Light from an Externally Modified Organic Light-Emitting Device 245
5.1.1. Introduction 246
5.1.2. Experimental 248
5.1.3. Results and discussion 251
5.1.4. Conclusions 258
References 260

6. Conclusiones 261

7. Trabajo Pendiente de Publicación 267

Objetivos

La presente Memoria presentada como Tesis Doctoral se encuadra en la línea de investigación "*Organización Molecular en Películas Superficiales*"del grupo FQM-204 de la Junta de Andalucía. Los objetivos globales que se han marcado son:

1. Preparar películas ultrafinas de materiales orgánicos de interés (lípidos, colorantes y complejos organometálicos de metales de transición) en la interfase aire−agua y realizar su posterior transferencia a soportes sólidos mediante la técnica de Langmuir−Blodgett.

2. Planificar y diseñar diferentes vías de interacción y ensamblaje para la obtención de estructuras supramoleculares con una composición y arquitectura determinados.

3. Estudiar, mediante diferentes técnicas de tipo óptico, la organización molecular de las películas formadas tanto en la interfase aire−agua como en la interfase aire−sólido.

4. Complementar y ampliar, hasta donde sea posible, la descripción experimental de los sistemas estudiados mediante técnicas computacionales.

5. Desarrollar modelos y métodos teóricos generales capaces de explicar la organización molecular de los sistemas estudiados en esta Memoria.

A estos objetivos hay que añadir además, aquellos que en la búsqueda de nuevas formas de estudio y aplicación, han surgido durante el desarrollo del presente trabajo. Así, fruto de la colaboración con otros grupos de investigación, se encontró la oportunidad de analizar la funcionalidad práctica de un sistema concreto, marcándose un nuevo objetivo:

6. Preparar y caracterizar dispositivos orgánicos electroluminiscentes (OLEDs) emisores de luz blanca para su uso en iluminación.

The work described in this Report belongs to the research line "*Molecular Organization in Thin Films*", within the group FQM-204 (Junta de Andalucía classification). The main goals of this research were as follows:

1. To prepare thin films of several organic materials such as lipids, dyes and transition metals organometallic complexes, both at the air−water interface and on solid supports, by using the Langmuir−Blodgett technique.

2. To design different ways of assembling in order to produce well-defined supramolecular structures.

3. To study the molecular organization of the previously formed films by using different optical techniques.

4. To complement and expand the experimental description of the studied systems by means of computational methods.

5. To develop theoreticals methods and models in order to explain the molecular organization of the systems under study.

To the aims stated above, it should be added those that appeared when looking for new ways of study and application. In this way, as a result of the close collaboration with other research groups, the opportunity of examine the practical application of a specific system has been found. The following goal has been set:

6. To prepare and characterize white light organic light-emitting devices (OLEDs) for lightning purposes.

Capítulo 1

Introducción

1.1. Películas de Langmuir y Langmuir−Blodgett (LB)

Benjamin Franklin (1706-1790) realizó, desde una perspectiva científica moderna, los primeros estudios sobre monocapas en la interfase aire−agua. No obstante, la aportación más relevante en este campo de la ciencia llegó de Irving Langmuir (1881-1957), que destacó por su trabajo en Química de Superficies, valiéndole el Premio Nobel de Química en 1932. Su trabajo, junto con el de Lord Rayleigh (1842-1919), permitió confirmar que las capas de moléculas anfifílicas esparcidas sobre superficies acuosas tienen el espesor de una única capa molecular y, además, concluir que las moléculas anfifílicas están orientadas en la superficie del agua, con su grupo funcional polar inmerso en ella, y con la cadena alifática situada hacia el exterior, en ocasiones casi verticalmente a la superficie acuosa. Sus experimentos apoyaron la hipótesis de la existencia de interacciones de corto alcance, y dieron la base para predecir los tipos de moléculas que podían formar este tipo de películas, denominadas películas de Langmuir en su honor. Un esquema con algunas moléculas anfifílicas ampliamente usadas, así como otras recientemente utilizadas en la bibliografía reciente, se muestra en la Figura1.1.

Katherine Blodgett (1898-1979), colaboradora de Irving Langmuir, transfirió por primera vez monocapas de ácidos grasos desde la superficie acuosa a un soporte sólido, vidrio hidrofílico, consiguiendo así las denominadas películas de Langmuir−Blodgett (LB).

Desde entonces hasta nuestros días, el abanico de posibilidades que ofrece la técnica de Langmuir-Blodgett (LB) ha aumentado considerablemente.

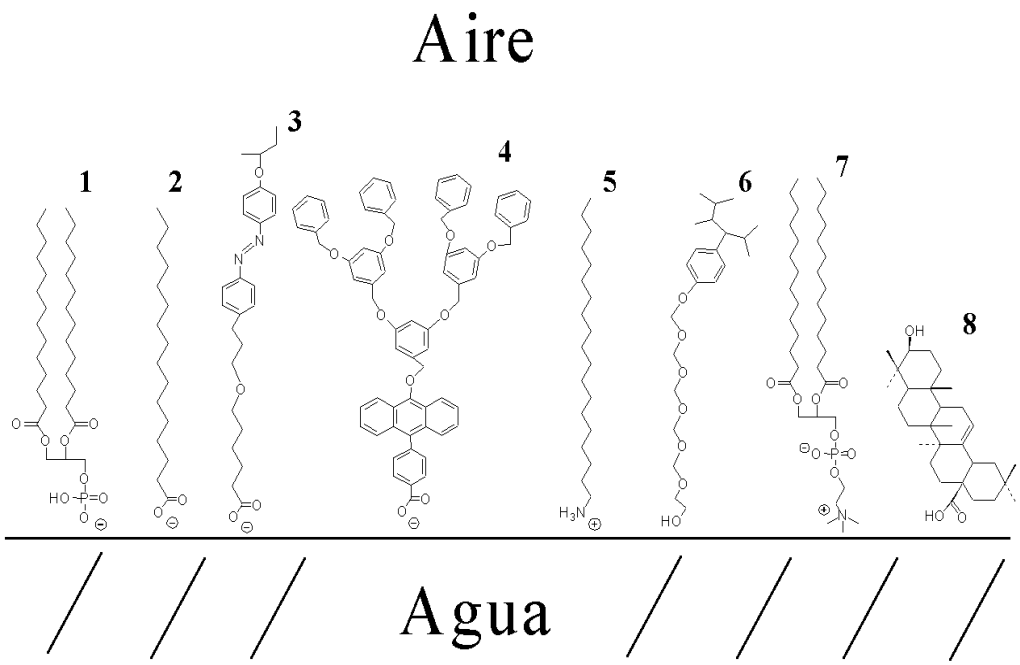

Figura 1.1: Algunos ejemplos de moléculas con caracter anfifílico. De izquierda a derecha: **1**, DMPA: Ácido dimiristoilfosfatídico. **2**, Ácido esteárico. **3**, Derivado quiral de azobenceno (Haro et al., Langmuir, 2008, 24, 10916-203). **4**, Dendrímero asimétrico *fan shaped* (Lee et al., Langmuir, 2008, 24, 12426-30). **5**, Eicosilamina. **6**, Etoxilato de alquilfenol. **7**, DPPC: dipalmitoilfosfatidilcolina. **8**, Ácido oleanólico (Brezesinski, G. y Vollhardt, D., ChemPhysChem, 2008, 9, 1670-72).

Actualmente, esta técnica constituye una herramienta elegante para la construcción de dispositivos supramoleculares con aplicaciones en diferentes áreas como óptica no lineal, sensores, electrónica molecular y fotocromismo.[1–3]

1.1.1. Formación y Caracterización de Monocapas en la Interfase Aire−Agua

La formación de monocapas de Langmuir en la interfase aire−agua se basa en la naturaleza anfifílica de las moléculas que la constituyen. Las molécu-

las anfifílicas poseen una parte apolar hidrofóbica con una o varias cadenas alifáticas, y otra polar hidrofílica, como por ejemplo, grupos funcionales tipo ácido, alcohol o amina.[4,5] La preparación de las monocapas en la interfase aire−agua consiste en añadir una cantidad determinada de moléculas anfifílicas, disueltas en un disolvente volátil e inmiscible en agua, sobre la superficie acuosa. Una vez evaporado el disolvente, las moléculas anfifílicas ocupan toda la superficie disponible (Figura 1.2)

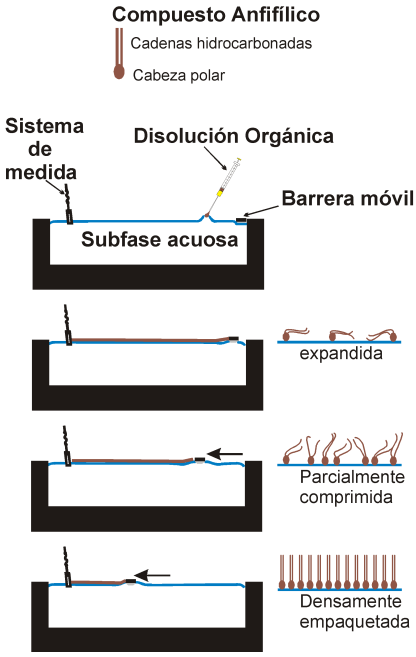

Figura 1.2: Esquema de la formación de una monocapa de Langmuir y su posterior compresión.

En este proceso, la elección del disolvente, o mezcla de disolventes, es fundamental, ya que debe favorecerse la máxima dispersión de las moléculas sobre el agua.[6] Evaporado el disolvente, cabe esperar que la disposición de las moléculas en la monocapa sea aquella en la que su situación energética resulte más favorable, esto es, con los grupos polares inmersos en la subfase

acuosa y las colas hidrófobas fuera de la misma.[4] En esta situación, la tensión superficial (γ) de la zona cubierta por la monocapa disminuye respecto a la tensión superficial de la superficie del agua limpia (γ_0). Este cambio se expresa en función de la presión superficial, π, que se define como:

$$\pi = \gamma_0 - \gamma \tag{1.1}$$

En principio, cualquier método para determinar la tensión superficial puede usarse para medir la presión superficial. En la mayoría de los casos descritos en la bibliografía, se utilizan dos tipos de sistemas, el tipo Wilhelmy y el tipo Langmuir.[7]

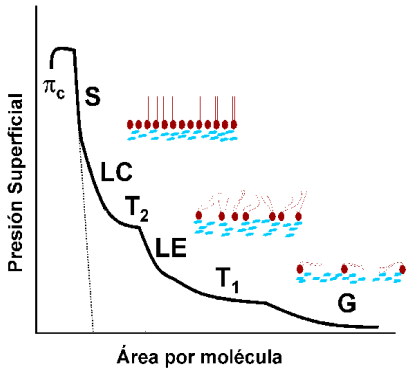

Figura 1.3: Isoterma $\pi - A$ idealizada donde se muestran las regiones mas comunes de forma esquemática para un fosfolípido.

Tras la evaporación del disolvente, la monocapa se comprime, de forma que el área superficial disponible se reduce,[4] la densidad superficial de las moléculas se incrementa. De esta forma, en la representación de la presión superficial, π, frente al área por molécula, A, π obtenida a temperatura constante, isoterma π - A aumenta cuando el área disminuye (ver Figura 1.3),

siendo la analogía bidimensional de una isoterma presión−volumen. Las isotermas π - A dan información acerca de la estabilidad de la monocapa en la interfase aire−agua, así como de la organización de las moléculas en la monocapa y de las interacciones entre ellas.

A partir de las isotermas $\pi - A$ se obtienen dos parámetros de especial relevancia. Por una parte, el valor del área limite, obtenido por extrapolación del tramo de mayor pendiente de la isoterma a presión superficial cero, que corresponde al área ocupada por una molécula en una situación de máximo empaquetamiento (líneas de puntos en la Figura 1.3). Por otra, el valor de presión superficial al cual la monocapa pierde su estabilidad, conocido con el nombre de presión de colapso (π_c en la Figura 1.3). Además, las isotermas presión superficial−área muestran distintas regiones que corresponden a los diferentes estados de organización o fases en los que se encuentra la monocapa, así como regiones en las que coexisten dos fases.[4] En la isoterma $\pi - A$ mostrada en la Figura 1.3 se indican de forma idealizada las distintas fases para una sustancia anfifílica simple. No obstante, debe resaltarse que el número y la complejidad de las fases observadas en una isoterma varían en función del sistema molecular estudiado, así como de las condiciones experimentales bajo las cuales se realizan dichas isotermas. En esta Figura destacan:

- Fase gaseosa, G: Las moléculas se encuentran bastante diluidas, y tienen un gran área disponible por molécula, constituyendo una fase denominada gas bidimensional.

- Líquido expandido, LE: Cuando la presión superficial aumenta se llega a una fase fluida muy compresible, en la que las moléculas experimentan

unas fuerzas atractivas lo suficientemente intensas como para que empiecen a adoptar una estructura compacta, formándose lo que se llama líquido expandido (LE). Entre las dos fases descritas, G y LE, ocurre un proceso parecido a la condensación de un gas, es decir, una zona de coexistencia de ambos estados, en la que tiene lugar una transición de fase, T_1.

- Líquido condensado, LC: Aumentos posteriores de presión dan lugar a un estado menos compresible y más ordenado, conocido como líquido condensado (LC). La organización de la monocapa es compacta y la parte hidrófoba de las moléculas se orienta casi perpendicularmente a la interfase. De nuevo, puede observarse una segunda transición de fase, T_2, entre la situación de líquido expandido y la de líquido condensado.

- Fase sólida, S: Al continuar comprimiendo la monocapa, y antes de que ésta llegue al colapso, se alcanza un estado sólido, S, donde la película es muy rígida y las cadenas hidrófobas forman un apilamiento compacto. La presión de colapso, a pesar de ser un parámetro característico de cada monocapa, y estar discutida ampliamente,[4] sigue siendo objeto de investigación reciente.[8] En un trabajo recogido en la presente Memoria, la presión de colapso se ha relacionado, para monocapas mixtas de un complejo organometálico de Iridio (III) y un fosfolípido, con la segregación total de dos fases distintas de la monocapa.

El método tradicional para la formación de películas de Langmuir requiere el empleo de moléculas anfifílicas. De esta forma, la gama de moléculas que pueden formar monocapas estables es, en principio, limitada. En las últimas

décadas, se han desarrollado estrategias para fabricar películas de Langmuir con componentes que por sí solos no pueden formar este tipo de películas. Estos métodos se basan en la construcción de monocapas complejas, cuyos componentes se organizan bajo control externo, ofreciendo la posibilidad de estudiar y/o utilizar las interacciones intermoleculares específicas de cada sistema.

Uno de los métodos propuestos consiste en añadir molécuñas solubles a la subfase acuosa, de forma que dichas moléculas puedan adsorberse, por ejemplo, mediante interacciones electrostáticas, sobre una determinada matriz lipídica, y así ser retenidas en la interfase. Más efectivo, sin embargo, se ha mostrado el método denominado de coesparcimiento, mediante el cual sobre la superficie acuosa[9–15] una mezcla de la molécula a estudiar y un anfifílico se coesparce en el mismo disolvente, de tal forma que ésta queda retenida en la interfase mediante interacciones, principalmente, electrostáticas. Con estos métodos, se amplía el rango de moléculas que pueden ser estudiadas mediante la técnica de formación de monocapas de Langmuir. En este sentido, cabe destacar el uso de una matriz fosfolipídica para el anclaje a la interfase aire−agua de moléculas solubles en agua, tales como porfirinas,[12,16] o colorantes como el azul de metileno.[17]

Caracterización de Películas de Langmuir

Junto a las medidas de presión superficial en la balanza de Langmuir, existe una gran variedad de técnicas disponibles que permiten caracterizar las monocapas en la interfase aire−agua. Además de las técnicas ya existentes,

Técnicas	Parámetro medido	Información
Presión superficial	π frente a A	Area por molécula, presión de colapso, estado de la monocapa
Potencial superficial	ΔV frente a A	Dipolos superficiales, orientación de los grupos
Reflexión UV-vis	ΔR	Densidad, orientación y agregación de la molécula cromóforo
Viscosidad superficial	η_S	Cambios de viscosidad
Elipsometría	Polarización de la radiación reflejada	Índice de refracción y espesor de la monocapa
Difracción de rayos X / neutrones	Reflectividad	Espaciado y estructura de capas empaquetadas
Generación de segundos armónicos	Polarización de la susceptibilidad del segundo armónico	Valor medio del ángulo entre el eje de la molécula y la normal a la interfase
Espectroscopía IR con transformadas de Fourier	Reflectividad	Orientación media de las cadenas alifáticas
PM-IRRAS	Diferencia en reflectividad de radiación polarizada	Orientación del dipolo de transición
Microscopía de fluorescencia	Fluorescencia de una molécula sonda	Estructura de la monocapa y orientación de las fases
Microscopía de ángulo Brewster (BAM)	Reflectividad	Morfología de la monocapa y orientación de las fases

Tabla 1.1: Técnicas de caracterización de monocapas en la interfase aire−agua.

que continuamente están siendo mejoradas por la industria y los investigadores, surgen nuevas técnicas de caracterización. En la tabla 1.1[18] se recogen algunas de las técnicas más importantes usadas en la caracterización de las monocapas en la interfase aire−agua, así como los parámetros medidos y la información obtenida a partir de ellas. De entre estas técnicas se detallan

a continuación la espectroscopía de reflexión UV-visible y la microscopía de ángulo Brewster (BAM), por ser las utilizadas para la realización del trabajo presentado en esta Memoria.

Espectroscopía de Reflexión UV-vis en la Interfase Aire−Agua

Esta técnica se basa en la diferencia de reflectividad existente entre una superficie acuosa cubierta con una monocapa y la superficie acuosa limpia. El método aplicado en esta Memoria, representado en la Figura 1.4, utiliza luz no polarizada, la cual se hace incidir de forma normal sobre la superficie del agua.

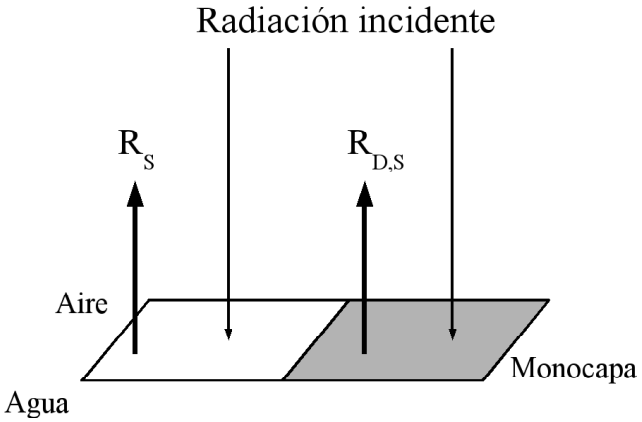

Figura 1.4: Diferencia de reflectividad entre la interfase aire−agua limpia y la interfase aire−agua cubierta por una monocapa.

Sean R_S y $R_{D,S}$ las cantidades de radiación reflejadas en ausencia y en presencia de monocapa, respectivamente. Cuando la reflexión y la absorción son pequeñas, se cumple aproximadamente que[19]

$$R_{D,S} = R_S + R_D + A\sqrt{R_S} \tag{1.2}$$

donde R_D y A son la reflexión y la absorción propias de la monocapa, respectivamente. El término $A\sqrt{R_S}$ representa la amplificación de la luz reflejada a consecuencia de la absorción. Asimismo, $R_D \approx A \cdot A_M/4$ donde A_M es la absorción máxima.

La medida experimental es directamente la diferencia entre $R_{D,S}$ y R_S:

$$\Delta R = R_{D,S} - R_S = A(\sqrt{R_S} + \frac{A_M}{4}) \approx A\sqrt{R_S} \tag{1.3}$$

En general, la absorción de una monocapa es lo suficientemente pequeña como para despreciar el término $(A_M/4)$. Asimismo, en este caso, absorción y absorbancia están relacionadas por un factor numérico 2.303, con lo que

$$\Delta R = 2{,}303 \times 10^3 f_0 \varepsilon \Gamma \sqrt{R_S} \tag{1.4}$$

donde ε representa la absortividad molar en sus unidades habituales (mol·L^{-1} ·cm), Γ es la concentración superficial en mol·cm^{-2}, el factor 10^3 da cuenta del cambio de unidades necesario para que ΔR sea adimensional, y, por último, f_0 es el factor de orientación, que compara las orientaciones promedio del dipolo de transición de las moléculas cromóforo en disolución y en la interfase aire−agua.

La ecuación 1.4 propone un método para detectar la presencia de cromóforos en la interfase aire−agua a partir de diferencias de reflexión de la monocapa con respecto a la interfase limpia, permitiendo además cuantificar la cantidad de moléculas existente en dicha interfase y obtener, como se describirá más adelante, información acerca de la orientación del cromóforo.

Microscopía de Ángulo Brewster (BAM)

La microscopía de ángulo Brewster tiene como objetivo la observación directa de la morfología de películas delgadas a nivel mesoscópico, es decir, a nivel de micrómetros. La información a este nivel puede ser de mucha importancia y despejar muchas incógnitas en la investigación de la estructura molecular de la monocapa. La técnica BAM es una herramienta excelente para el estudio de películas de Langmuir, ya que permite visualizar transiciones de fase, así como la forma y estructura interna de los dominios que se originan durante los procesos de compresión-descompresión de la monocapa.[20–24]

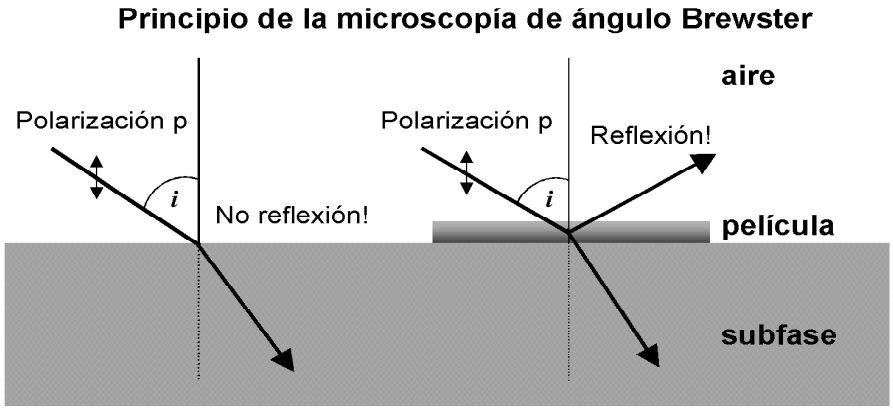

Figura 1.5: Principio físico para la microscopía de ángulo Brewster.

La microscopía de ángulo Brewster se basa en el siguiente principio, esquematizado en la Figura 1.5: cuando se hace incidir un haz de luz sobre la interfase aire−agua con un ángulo $i = 53.1°$, ángulo Brewster, y polarización paralela al plano de incidencia, polarización p, toda la radiación es transmitida, sin producirse reflexión. Si sobre la subfase acuosa se esparce una monocapa de moléculas se forma una nueva interfase, cuyo índice de re-

fracción varía ligeramente. Como consecuencia, el ángulo Brewster disminuye también ligeramente. En estas condiciones, manteniendo constante el ángulo de incidencia original, parte de la radiación se refleja debido a la presencia de la monocapa. Si, a continuación, esta radiación se recoge con una cámara, se puede observar directamente la morfología de la película durante su proceso de formación y/o compresión. Así pues, la reflectividad de una monocapa en BAM viene determinada por el índice de refracción y por el espesor de la capa. Fases de la monocapa con moléculas inclinadas muestran a menudo anisotropía óptica en el plano. Como ejemplos, moléculas con largas cadenas hidrocarbpnadas, cuya polarizabilidad es mayor a lo largo del eje de la cadena que perpendicular al mismo, presentan dominios con anisotropía óptica que puede observarse mediante BAM. También, en la región de coexistencia de dos fases, es habitual la formación de dominios, que cuando son lo sufinientemente grandes se hacen visibles en BAM. Estos dominios generalmente presentan distinto brillo debido a diferencias en la inclinación de las moléculas.[20,22,25] Esta técnica, frente a otras como la microscopía de fluorescencia, ofrece la ventaja de no requerir una sonda fluorescente.

1.1.2. Formación y Caracterización de Películas de Langmuir-Blodgett

Existe un gran interés sobre la construcción de sistemas formados por moléculas que interactúan entre sí como partes de una máquina. Son los denominados ensamblajes moleculares organizados, constituyentes básicos de la Nanotecnología. Una vía para construir estos sistemas consiste en la in-

corporación de moléculas activas dentro de monocapas de matrices lipídicas apropiadas, y en el ensamblaje de las mismas de una manera predeterminada. Cada monocapa se prepara en la interfase aire−agua mediante esparcimiento de las moléculas de una forma adecuada, para posteriormente transferirse sobre un soporte sólido formando estructuras supramoleculares con características definidas.

Con el objeto de construir, ensamblar y manipular películas simples, preparadas previamente en la interfase aire−agua, Irving Langmuir y Katherine Blodgett desarrollaron la técnica que lleva su nombre, Langmuir-Blodgett (LB). No obstante, no es hasta principios de los 60 debido, en gran parte, al trabajo realizado por Kuhn y col,[26] cuando la necesidad de construir sistemas organizados complejos mediante el ensamblaje de monocapas de manera controlada impulsa el desarrollo de la técnica LB. Este interesante campo de la ciencia ha experimentado un rápido crecimiento durante las últimas décadas.[2,26–28]

El método LB consiste, básicamente, en colocar un soporte sólido perpendicular a la interfase aire−agua cubierta por la monocapa que se va a transferir y, mediante inmersión y/o emersión de dicho soporte, las moléculas se van depositando sobre el sustrato sólido, tal como se muestra en la Figura 1.6. Durante la transferencia se hace avanzar la barrera móvil para compensar la pérdida de moléculas y un mecanismo feed-back mantiene constante la presión superficial.

Además de este método, en la bibliografía se encuentran descritos otros métodos de transferencia,[4] como la técnica de deposición horizontal introducida por Langmuir y Schaefer.[29] En esta técnica, el substrato sólido se hace

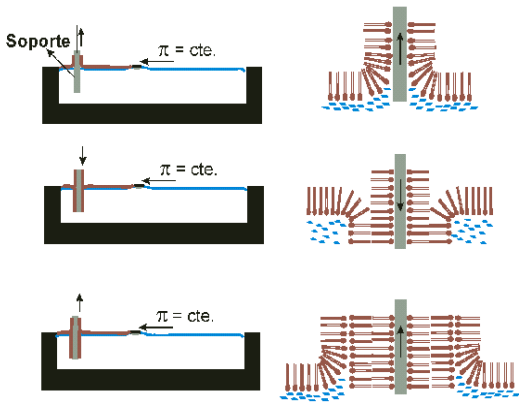

Figura 1.6: Técnica de Langmuir−Blodgett.

contactar con la superficie de la monocapa, paralelo a la interfase aire−agua, de forma que la monocapa se transfiere con la parte apolar sobre el soporte y la parte polar en contacto con el aire. Otro ejemplo es el método de contacto de Schulman,[30] en el cual se usan dos fases, una orgánica y la otra acuosa. En primer lugar, se deposita una capa de tensioactivo mediante quimisorción y, a continuación, una capa de un compuesto apolar como puede ser por ejemplo, el colesterol, mediante la denominada adsorción sensibilizada, basada en interacciones del compuesto apolar con las cadenas hidrocarbonadas del tensioactivo. Otro método de transferencia es el de Kossi y Leblanc,[31] en el cual el soporte sólido, en este caso puede ser una membrana porosa, se coloca inclinado con respecto a la interfase aire−agua un ángulo de unos 40 °y, entonces, se sumerge en el agua. Se transfiere la monocapa elevando el soporte de forma similar a como se hace en una deposición tipo Langmuir−Blodgett. A continuación, se transfiere otra monocapa al soporte mediante el método de Langmuir-Schaefer,obteniéndose como resultado una estructura de bicapa.

En la actualidad no se conocen con exactitud todos los mecanismos por

los que las monocapas en la interfase aire−agua se transfieren a los substratos sólidos.[1,27] Se ha descrito que las interacciones moleculares implicadas en la deposición de la primera capa pueden ser bastante diferentes de las responsables de la transferencia de las siguientes. Además, para algunos materiales, la deposición de la película parece estar asociada con un cambio de fase al cambiar de interfase. Sin embargo, no siempre pueden explicarse fenómenos como los diferentes modos de transferencia, y la adecuada velocidad a la que los materiales pueden depositarse. De hecho, la comprensión de los fenómenos fisicoquímicos que gobiernan la transferencia LB son, todavía, objeto de investigación.[32,33]

La fabricación de películas LB de alta calidad requiere de un alto grado de destreza, asícomo de un control cuidadoso de todas las variables experimentales, como son: estabilidad y homogeneidad de las moléculas que forman la monocapa, propiedades de la subfase (composición, fuerza iónica, pH y temperatura), naturaleza del substrato (estructura y carácter hidrofóbico o hidrofílico), velocidad de inmersión y emersión del soporte, ángulo de penetración del sustrato en la subfase, presión de compresión durante el proceso de deposición, y número de monocapas transferidas.

En la parte inferior de la Figura 1.6 se muestra la deposición de una monocapa sobre un soporte sólido mediante la técnica LB. En este caso, se supone un sustrato hidrofílico de forma que la primera monocapa se transfiere cuando el sustrato emerge de la subfase, lo que implica que dicho sustrato ha de colocarse dentro de la misma antes de esparcir la monocapa. En este modo de deposición denominado tipo Y,[1,27] el ordenamiento de la película es centrosimétrico, estableciéndose una configuración cabeza−cabeza y cola−cola en

sucesivas transferencias (Figura 1.7, izquierda).

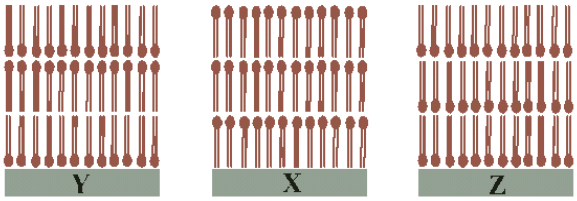

Figura 1.7: Distintos tipos de transferencia LB

En la bibliografía[1,27] se encuentran oelículas cuya deposición es tipo X, en las que la monocapa se transfiere únicamente durante la inmersión del soporte a través de la interfase, y películas tipo Z, en las que la deposición de la monocapa sólo tiene lugar al emerger el sustrato de la subfase. En ambos casos se obtienen películas centro-asimétricas (Figura 1.7, centro y derecha).

Tendría que indicarse que el ordenamiento molecular final en una capa LB no siempre es tan perfecto como aparece en la Figura 1.7, ya que en muchos casos se produce una reorganización de las moléculas en la película depositada.

Con objeto de cuantificar el grado de transferencia desde la interfase aire−agua a la interfase aire−sólido, se usa la denominada relación de transferencia, τ, dada por:

$$\tau = \frac{A_L}{A_S} \tag{1.5}$$

donde A_L es la disminución del área ocupada por la monocapa sobre la interfase aire−agua, a presión constante, y A_S es el área cubierta del substrato sólido. Así, valores de τ próximos a la unidad indican una transferencia

prácticamente completa de la monocapa desde la interfase aire−agua al soporte sólido.

Una vez formada la película LB, para controlar su arquitectura y organización, es necesario conocer los distintos factores que afectan a la estructura supramolecular de la misma. Con este objeto se pueden usar diversas técnicas de caracterización, muchas de las cuales han sido referidas previamente para el estudio para el estudio de monocapas en la interfase aire−agua (Tabla 1.1). Así, se encuentran técnicas espectroscópicas tales como: espectroscopía de absorción UV-vis, espectroscopía IR con transformada de Fourier y Raman (SERS), elipsometría, difracción de rayos X. Existen diversas microscopías, como la de ángulo Brewster (BAM), electrónica de barrido (SEM) y de transmisión (TEM), de efecto túnel (STM) y de fuerza atómica (AFM).[1,2,7,22,26,34,35] Estas técnicas constituyen un grupo de herramientas muy importante dentro de este campo, puesto que mediante ellas no sólo se obtiene información sobre la densidad de las moléculas soportadas, sino también acerca de la estructura (orden), morfología (topología) y composición, permitiendo determinar el tamaño, orientación e interacción entre los dominios formados, si los hubiese, así como datos sobre los defectos de la película. Toda esta información ayuda a construir los modelos de organización molecular en la película.

Referencias

1. Ulman, A. *An Introduction to Ultrathin Organic Films from Langmuir-Blodgett to Self Assembly;* Academic Press: San Diego, 1991.

2. Petty, M. C. *Langmuir-Blodgett Films: An Introduction;* Cambridge University Press: Cambridge, 1996.

3. Miyama, S.; Nalwa, H. S. *Organic Electroluminescent Materials and Devices;* Gordon and Breach: Amsterdam, 1997.

4. Gaines, G. L. *Insoluble Monolayers at Liquid-Gas Interfaces;* Wiley-Interscience: New York, 1966.

5. Adamson, A. W. *Physical Chemistry of Surfaces;* Wiley-Interscience: New York, 1982.

6. Ishii, T. *Thin Solid Films* **1989,** *178,* 47.

7. Kuhn, H.; Möbius, D.; Bucher, H. *Physical Methods of Chemistry;* 1972.

8. Lee, K. Y. C. *Annu. Rev. Phys. Chem.* **2008,** *59,* 771-91.

9. Hada, H.; Hanawa, R.; Haraguchi, A.; Jonezawa, Y. *J. Phys. Chem.* **1985,** *89,* 560-562.

10. Cordroch, W.; Möbius, D. *Thin Solid Films* **1992,** *210,* 135.

11. Ahuja, R. C.; Caruso, P.; Möbius, D.; Wildburg, G.; Ringsdorf, H.; Philp, D.; Preece, J. A.; Stoddart, J. F. *Langmuir* **1993,** *9,* 1534.

12. Martín, M. T.; Prieto, I.; Camacho, L.; Möbius, D. *Langmuir* **1996,** *12,* 6554-6560.

13. Brezesinski, G.; Vollhardt, D.; Iimura, K.; Cölfen, H. *J. Phys. Chem. C* **2008,** *112,* 15777-15783.

14. Philosof-Mazor, L.; Volinsky, R.; Comin, M. J.; Lewin, N. E.; Kedei, N.; Blumberg, P. M.; Márquez, V. E.; Jelinek, R. *Langmuir* **2008,** *24,* 11043-11052.

15. Qaqish, S. E.; Paige, M. F. *Langmuir* **2008,** *24,* 6146-6153.

16. Prieto, I.; Martín, M. T.; Camacho, L.; Möbius, D. *Langmuir* **1998,** *14,* 4175-4179.

17. Prieto, I.; Fernández, A.; Muñoz, E.; Martín, M. T.; Camacho, L. *Thin Solid Films* **1996,** *284-285,* 162-165.

18. Dynarowicz-Latka, P.; Dhanabalan, A.; Oliveira, Jr., O. N. *Adv. Coll. Int. Sci.* **2001,** *91,* 221-293.

19. Grüniger, H.; Möbius, D.; Meyer, H. *J. Chem. Phys.* **1983,** *79,* 3701-3710.

20. Hönig, D.; Möbius, D. *J. Phys. Chem.* **1991,** *95,* 4590.

21. Siegel, S.; Hönig, D.; Vollhardt, D.; Möbius, D. *J. Phys. Chem.* **1992,** *96,*.

22. Henon, S.; Meuinier, J. *Rev. Sci. Inst.* **1991,** *62,* 936-939.

23. Mann, E. K.; Henon, S.; Langevin, D.; Meunier, J. *Journal de Physique II* **1992,** *2,* 1683-1704.

24. Meunier, J. *Coll. and Surf. A* **2000,** *171,* 33-40.

25. Vollhardt, D. *Adv. Coll. Int. Sci.* **1996,** *64,* 143.

26. Kuhn, H.; Möbius, D. *Monolayer Assemblies*. In *Investigations of Surfaces and Interfaces*, Vol. IXB; Rossiter, B. W.; Baetzold, R. C., Eds.; John Wiley and Sons, Inc: New York, 1993.

27. Roberts, G. G. *Langmuir-Blodgett Films;* Plenum: New York, 1990.

28. Ulman, A. *In Fourier Transform Infrared Spectrometry in Colloid and Interface Science;* ACS Symposium Series 447: Washington, D.C., 1991.

29. Langmuir, I.; Schaefer, V. J. *J. Am. Chem. Soc.* **1938,** *60,* 1351.

30. Schulmann, J. H.; Waterhouse, R. B.; Spink, J. A. *Kolloid. Z.* **1956,** *146,* 77.

31. Kossi, C. N.; Leblanc, R. M. *J. Colloid Interface Sci.* **1981,** *80,* 426.

32. Kovalchuk, V. I.; Bondarenko, M. P.; Zholkovskiy, E. K.; Vollhardt, D. *J. Phys. Chem. B* **2008,** *112,* 11333-11340.

33. Bondarenko, M. P.; Kovalchuk, V. I.; Zholkovskiy, E. K.; Vollhardt, D. *J. Phys. Chem. B* **2007,** *111,* 1684-1692.

34. Hönig, D.; Overbeck, G. A.; Möbius, D. *Adv. Mater.* **1992,** *4,* 419.

35. Rivière, S.; Hénon, S.; Meunier, J.; Schwartz, D. K.; Tsao, M. W.; Knobler, C. M. *J. Chem. Phys.* **1994,** *101,* 10045.

1.2. Dinámica Molecular

Introducción a las Simulaciones en Ordenador. Modelos Matemáticos

Las simulaciones en ordenador son una parte de la Ciencia que trata de reproducir una realidad virtual mediante modelos matemáticos, más o menos complejos,[1,2] donde dichos modelos son evaluados para situaciones concretas de forma que nos validen dichos modelos.

En la actualidad, con el aumento del poder de cálculo de los ordenadores y la mejora de los algorítmos matemáticos de simulación, las simulaciones en ordenador están sufriendo un auge exponencial en diferentes áreas de la Ciencia, tales como la Química Macromolecular, Física de partículas o fluidos, Biofísica, etc. La ventaja fundamental de estas simulaciones consiste en que, una vez validados los modelos a emplear, se cuenta con la posibilidad de obtener información sobre el comportamiento de diferentes sistemas en condiciones difíciles de medir y/o reproducir con las técnicas experimentales disponibles. Un ejemplo sería el comportamiento de ciertas macromoléculas biológicas, tales como proteínas o ADN, donde su estudio mediante cristalografía o RMN supone una desnaturalización de dichas moléculas como paso previo al estudio experimental. Sin embargo, mediante técnicas de simulación apropiadas, puede reproducirse el comportamiento de dichos sistemas en condiciones que se aproximan a sus condiciones fisiológicas y, de ahí, estudiar ciertas propiedades de interés. La Figura 1.2 muestra un esquema de la relación entre las simulaciones por ordenador y la experimentación. Es

importante resaltar el valor fundamental del paso en el cual las predicciones obtenidas mediante técnicas computacionales es validad mediante datos experimentales. No obstante, la utilización de las técnicas de simulación en

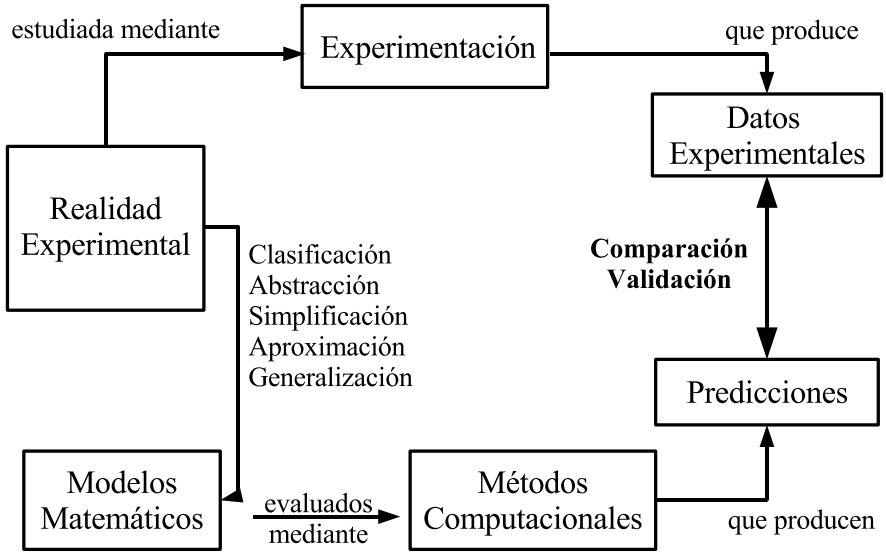

Figura 1.8: Esquema general del uso de simulaciones por ordenador.

ordenador no tiene como objetivo reemplazar a las técnicas experimentales, sino usar su capacidad para servir de **complemento** a los experimentos. En la Tabla 1.2, adaptada de la revisión de van Gunsteren y Berendsen,[3,4] se muestran cuatro casos generales en los cuales las simulaciones pueden aportar un complemento de mucha utilidad a las mediciones experimentales.

1.2.1. Fundamento Físico

La técnica de simulación utilizada en esta Memoria ha sido la Dinámica Molecular. La Dinámica Molecular consiste en el uso de la Mecánica Clásica

¿Cuando?	Por ejemplo...
El experimento es imposible	Choques de galaxias, predicción del tiempo
El experimento entraña peligro	Comportamiento de sustancias radioactivas, explosivos
El experimento es caro	Comportamiento a altas presiones
No se puede acceder mediante la experimentación a la magnitud deseada	Propiedades observables en escalas de tiempo y/o espacio muy pequeñas

Tabla 1.2: Cuatro situaciones generales en los cuales la simulación por ordenador puede resultar un complemento a la experimentación

para obtener información tanto de propiedades estacionarias como dinámicas del sistema estudiado. En Dinámica Molecular, se obtiene la evolución temporal de todas las partículas constituyentes del sistema, lo que se denomina *trayectoria* del sistema, a partir de:

$$m_i \frac{\partial^2 \mathbf{r}_i}{\partial t^2} = \mathbf{F}_i,\ i = 1, 2 \ldots N \tag{1.6}$$

$$\mathbf{F}_i = -\frac{\partial V(\mathbf{r}_i)}{\partial \mathbf{r}_i} \tag{1.7}$$

donde m_i, $\mathbf{r}_i$ son la masa y la posición de las partículas, respectivamente. $\mathbf{F}_i$ se refiere a la fuerza ejercida sobre cada partícula i de un sistema con N partículas, t el tiempo y $V(\mathbf{r}_i)$ la energía potencial del sistema. Esta energía potencial es función de las coordenadas de cada partícula, $\mathbf{r}_i$. La resolución de ambas ecuaciones se realiza mediante integración numérica para cada paso de simulación, Δt, que en la mayoría de las simulaciones de sistemas moleculares es de 1-4 fs.

Las propiedades estacionarias pueden calcularse como promedio de un muestreo estadístico a lo largo de la trayectoria, siempre que dicho muestreo sea lo suficientemente grande como para ser representativo del sistema. En el cálculo de propiedades dinámicas, se estudia la evolución de una determinada propiedad respecto al tiempo a lo largo de la trayectoria de simulación.

Limitaciones de la Dinámica Molecular

Las limitaciones más importantes de la Dinámica Molecular son cuatro:

- **Uso de la Mecánica Clásica para la interacción entre partículas.** El sistema molecular se describe como un sistema de masas puntuales moviéndose en un potencial efectivo, que se deriva de un campo conservativo dependiente únicamente de las coordenadas instantáneas de las masas puntuales. El movimiento de estas masas puntuales se puede describir, con una determinada precisión, por las leyes de la Mecánica Clásica. Sin embargo, existe una gran variedad de casos en los que la Mecánica Clásica no puede aplicarse, como pueden ser a aquellos sistemas que se encuentran a muy baja temperatura (0-10 K) o en sistemas en los que intervienen partículas/átomos muy ligeros (como el hidrógeno). Para el estudio de estos sistemas es necesaria la utilización de la Mecánica Cuántica.

- **Tamaño del sistema. Grados de libertad considerados.** La cantidad de partículas que pueden simularse en el ordenador viene limitada por la potencia de cálculo del propio ordenador. En general, el número de partículas que pueden incluirse va del orden de 10^3 a 10^5 átomos. Así,

la dimensiones de los sistemas estudiados son varios órdenes de magnitud más pequeños que los empleados en el laboratorio, que vienen a ser de aproximadamente 10^{23}, el número de Avogadro. De cualquier forma, el tamaño del sistema se genera tan grande como sea posible, con el fin de generar una muestra estadística que abarque suficientemente las distintas conformaciones del sistema.

- **Muestreo de distintas configuraciones. Escala de tiempo.** La simulación por ordenador genera una muestra estadística de las distintas configuraciones del sistema bajo estudio. Esta muestra depende del algorítmo de simulación utilizado. En el caso ideal, la muestra estadística es representativa de todos los estados del sistema, es decir, es posible superar todas las barreras de la superficie energética multidimensional, o *hipersuperficie*, del sistema. En simulación, la escala de tiempos que se alcanza está bastante limitada, sobre todo si se compara con los tiempos usados en el laboratorio. Las simulaciones ocupan escalas de tiempos del orden de $10 - 10^3$ ns. Existen multitud de procesos esenciales, plegamientos de proteinas, ciertos procesos de difusión, etc., que se encuentran fuera del alcance de estas escalas de tiempo tan cortas.

- **Precisión del modelo molecular.** Asumiendo un determinado modelo molecular para un sistema dado, se propone un potencial o campo de fuerzas, bajo el cual se realiza la simulación. Existen una gran variedad de campos de fuerzas, en los cuales diferentes propiedades físicas son modeladas. La elección de un campo de fuerzas depende del nivel de precisión requerido y de la potencia de cálculo disponible.

1.2.2. Campo de Fuerzas. Aproximaciones en Dinámica Molecular

Solución Numérica de las Ecuaciones de Newton mediante Algoritmo *Leap-Frog*

Los requisitos previos a la generación de la trayectoria de un sistema son la información relativa al tamaño de la caja de simulación y a las coordenadas espaciales y velocidades de cada uno de los átomos incluidos en la misma. Una vez fijados, se usa el algoritmo de Leap-Frog[5,6] para la integración de la ecuación de movimiento. Así, para un tiempo dado, $t - \frac{\Delta t}{2}$, el algoritmo de Leap-Frog tiene en cuenta que cada partícula tiene una determinada posición $\mathbf{r}$ y una velocidad $\mathbf{v}$. A continuación, tomando las fuerzas $\mathbf{F}(t)$, se actualizan los valores de posición y velocidad para cada partícula, según:

$$\mathbf{v}(t + \frac{\Delta t}{2}) = \mathbf{v}(t - \frac{\Delta t}{2}) + \frac{\mathbf{F}(t)}{m}\Delta t \tag{1.8}$$

$$\mathbf{r}(t + \Delta t) = \mathbf{r}(t) + \mathbf{v}(t + \frac{\Delta t}{2})\Delta t \tag{1.9}$$

Estas ecuaciones del movimiento se modifican para incluir las restricciones que se hayan programado, por ejemplo, en lo referente a acoplamientos de presión o temperatura.

Componentes del Potencial Aplicado

Un campo de fuerzas típico usado en Dinámica Molecular para un sistema de N partículas con masas m_i, $i = 1, 2, ..., N$ y posiciones cartesianas

denotadas por los vectores $\mathbf{r}_i$, tiene la siguiente forma:

$$\mathbf{V}(\mathbf{r}_1, \mathbf{r}_2, ..., \mathbf{r}_N) = \sum_{enlaces} \frac{1}{2} K_b [b - b_0]^2 + \sum_{angulos} \frac{1}{2} K_\theta [\theta - \theta_0]^2$$

$$+ \sum_{diedros\ impropios} \frac{1}{2} K_\xi [\xi - \xi_0]^2 + \sum_{diedros} K\varphi [1 + \cos(n\varphi - \delta)] \qquad (1.10)$$

$$+ \sum_{pares(i,j)} [C_{12}(i,j)/\mathbf{r}_{i,j}^{12} - C_6(i,j)/\mathbf{r}_{i,j}^{6} + q_i q_j/(4\pi\varepsilon_0\varepsilon_r \mathbf{r}_{i,j})]$$

Los cuatro primeros términos describen las interacciones de enlace, es decir, de corto alcance entre átomos vecinos. El último término da cuenta de las interacciones de no enlace; contiene un sumatorio extendido a todos los pares de átomos de la caja, e incluye las interacciones de tipo Lennard-Jones y las interacciones coulómbicas entre todos los pares i, j de átomos del sistema.

Periodicidad. Condiciones de contorno

Dada la naturaleza finita de los sistemas estudiados en simulación, las condiciones de contorno de los mismos son fundamentales. Las condiciones de contorno más básicas serán aquellas en las que se consider al sistema rodeado por vacío. Se trata de una consideración simple, con la que se pueden confinar las moléculas de disolvente mediante la aplicación de un potencial de contorno. No obstante, estas condiciones de contorno pueden originar artefactos en los límites del sistema.

Por ello, para la mayoría de simulaciones por ordenador se establecen las condiciones de contorno periódicas. Mediante la periodicidad se evitan

errores de cálculo en la frontera del sistema, haciendo posible un tratamiento consistente de las interacciones de largo alcance. Sin embargo, la periodicidad es una solución computacional y debe evaluarse el efecto de la misma sobre el cálculo de las propiedades de interés. El método más común para establecer condiciones periódicas implica colocar a los átomos del sistema en un cubo, o de forma más general, en una caja periódica. Esta caja periódica se considera que está rodeada por $3^3 - 1^3 = 26$ cajas idénticas a ella y sólo se tienen en cuenta las interacciones de las partículas con sus vecinos más próximos. En general, se asume que una partícula perteneciente a la caja central interactúa tan sólo con otra partícula de la misma caja central, o bien, con alguna de sus imágenes, siempre que la distancia que las separe sea inferior a la mitad del eje de la caja central, evitando de esta manera la cristalinidad en el estudio de sistemas amorfos o no cristalinos.

Algoritmo de Berendsen. Presión y Temperatura Constante

La temperatura de un sistema viene dada por la energía cinética de todas los partículas que lo constituyen. En las simulaciones por ordenador, existe una cierta imprecisión numérica asociada a los procesos de redondeo numérico, que tiene como resultado que la temperatura del sistema diverja del valor inicial a lo largo de la trayectoria. Además, la presión del sistema simulado depende de las posiciones de cada partícula, así como de las fuerzas aplicadas sobre el mismo, por lo que puede variar en el proceso de simulación. Es por ello que ambas magnitudes deben controlarse en el sistema a simular.

Para controlar la temperatura y presión del sistema a simular existen distintos algoritmos, entre los que destaca el acoplamiento débil mediante un baño termostático/isobárico de Berendsen,[7] usado en esta Memoria. Otros son el algoritmo de Andersen[9] o aquellos que incluyen métodos para restringir la temperatura o presión[8] al valor deseado.

El baño acoplado de Berendsen imita el acoplamiento débil a un baño termostatizado, de temperatura T_0, con una cinética de primer orden. El efecto sobre el sistema simulado es que cualquier desviación de la temperatura de éste con respecto a la temperatura inicial, T_0, se corrige lentamente mediante:

$$\frac{dT}{dt} = \frac{T_0 - T}{\tau} \tag{1.11}$$

De acuerdo con la ecuación anterior, cualquier desviación de la temperatura cae exponencialmente respecto a un valor de tiempo constante τ. Una de las ventajas de este método es la facilidad para cambiar la fuerza del acoplamiento de la temperatura. Así, para casos en los que se requiere alcanzar el equilibrio rápidamente, como por ejemplo cuando se realiza el equilibrado inicial del sistema, τ se escoge con un valor pequeño, de unos 0.01 ps. Sin embargo, para la producción de trayectorias y su posterior análisis, normalmente se eligen valores más altos, por ejemplo de 0.5 ps, con el objetivo de minimizar su influencia sobre el sistema.

El flujo de calor intercambiado por el sistema se lleva a cabo escalando el valor de velocidad de cada partícula en cada uno de los pasos de simulación mediante el factor λ, dependiente del tiempo, dado por:

$$\lambda = \left[1 + \frac{\Delta t}{\tau_T}\left\{\frac{T_0}{T(t - \frac{\Delta t}{2})} - 1\right\}\right]^{1/2} \tag{1.12}$$

donde el parámetro τ_T tiene un valor cercano, pero no igual, a la constante temporal τ, definida por:

$$\tau = 2C_V\tau_T/N_{df}k \tag{1.13}$$

siendo C_V la capacidad calorífica total del sistema, k la constante de Boltzmann y N_{df} el número total de grados de libertad.

Hay que hacer notar que el cambio de energía cinética causado al escalar las velocidades de las partículas se redistribuye entre la energía cinética y la energía potencial. De ahí que el cambio en la temperatura es menor que el de la energía de escalado y, por tanto, $\tau_T \neq \tau$. En la práctica, la relación τ_T/τ va desde 1 en un sistema gaseoso a 2 en un sólido armónico, hasta un 3 en agua. De hecho, cuando en esta Memoria se menciona la constante temporal de acoplamiento de temperatura, se hace referencia a τ_T, ya que es el parámetro que determina directamente λ, de ahí el flujo de calor y por tanto la velocidad con la que la temperatura del sistema es ajustada. En la mayoría de los casos, el factor de escalada λ se limita al rango $0.8 \leq \lambda \leq 1.25$, para evitar el escalado mediante valores altos, que podría colapsar el sistema. Normalmente, λ estará muy cercano a la unidad.

Formalmente, es necesario el valor de la temperatura T a un tiempo t dado para calcular el factor de escalado. Sin embargo, este algoritmo no puede proporcionar dicho valor, de forma que se usa el valor de temperatura del paso previo. Esta solución se considera totalmente aceptable, ya que la constante temporal de acoplamiento se extiende mucho más en el tiempo que un paso de simulación, por lo que el algoritmo es estable hasta que $\tau_T \sim \delta t$.

De forma análoga al control de la temperatura, es posible aplicar al sistema un baño de presión. En este caso, el algoritmo de Berendsen reescala las coordenadas y los vectores de la caja en cada paso de simulación con una matriz, $\boldsymbol{\mu}$, de forma que corrige la presión del sistema mediante una cinética de relajación de primer orden hacia una presión de referencia $\boldsymbol{P}_0$:

$$\frac{d\boldsymbol{P}}{dt} = \frac{\boldsymbol{P}_0 - \boldsymbol{P}}{\tau_P} \tag{1.14}$$

donde τ_P es la constante temporal de acoplamiento de presión, de forma equivalente a τ_T para el acoplamiento de temperatura.

Referencias

1. Smit, B.; Frenkel, D. *Understanding Molecular Simulation;* Academic Press: 2nd ed.; 2001.

2. Ramachandran, K. I.; Deepa, G.; Namboori, K. *Computational Chemistry and Molecular Modeling;* Springer-Verlag: Berlin, 2008.

3. van Gunsteren, W. F. *et al. Angew. Chem. Int. Ed.* **2006,** *45,* 4064.

4. van Gunsteren, W. F.; Berendsen, H. J. C. *Angew. Chem. Int. Ed.* **1990,** *29,* 992.

5. Berendsen, H. J. C.; van Gunsteren, W. F. Practical algorithms for dynamic simulations. In *Molecular Dynamics Simulation of Statistical Mechanical Systems*; Ciccotti, G.; Hoover, W., Eds.; Soc. Italiana di Fisica: 1986.

6. Hockney, R. W.; Goel, S. P.; Eastwood, J. *J. Comp. Phys.* **1974,** *14,* 148.

7. Berendsen, H. J. C.; Postma, J. P. M.; DiNola, A.; Haak, J. R. *J. Chem. Phys.* **1984,** *81,* 3684.

8. Woodcock, L. V. *Chem. Phys. Lett.* **1971,** *10,* 257.

9. Andersen, H. C. *J. Chem. Phys.* **1980,** *72,* 2384.

1.3. Dispositivos Orgánicos Electroluminiscentes, OLEDs

Desarrollo y Perspectivas

Desde la década de los años 60 se han desarrollado numerosos estudios sobre electroluminiscencia de compuestos orgánicos. Estas investigaciones han permitido identificar y comprender algunos de los procesos básicos por los que se produce este fenómeno. En 1987, Tang y Van Slyke[1] obtuvieron el primer OLED, Organic Light-Emitting Diode, basado en una película de tris-8-hidroxiquinolinato de aluminio, Alq_3, el cual emitía luz verde de forma intensa. En 1996, estos investigadores de la compañía Eastman Kodak consiguieron mejorar la estabilidad del dispositivo mediante la adicción de nuevas capas, llegando a obtener tiempos de vida media de hasta 4000 horas.[2] Paralelamente, Burroughes y col.[3] fabricaban el primer diodo emisor de luz basado en un polímero π-conjugado, poli(fenilvinil), PPV, cuyas ventajas principales eran que sustituía el proceso de la evaporación térmica a alto vacío y de coste elevado, por el de spin-coating más barato y, en principio, extrapolable a la producción industrial, y que permitía aumentar las dimensiones del dispositivo.

Otro paso cualitativo fue el uso de emisores fosforescentes en OLEDs,[4] que sube el límite máximo teórico de eficiencia interna desde un 25 % hasta un 100 %. En ese sentido, la incorporación de complejos organometálicos de transición como materiales activos ha abierto aún más el campo de posibles moléculas utilizables en OLEDs.[5] Posteriormente, esta estrategia dió lugar a

la idea de combinar un emisor azul fluorescente con emisores verdes y rojos fosforescentes, haciendo del OLED un emisor de luz blanca, de gran interés para su uso en iluminación.[6–10] De hecho, esta ha sido la estrategia usada en el último capítulo de esta Memoria, en el cual se usa un emisor fosforescente, formado por CaS:Eu, que modifica un OLED azul.

Lo que empezó siendo una curiosidad de laboratorio, hoy ha dado lugar a toda una rama de la Ciencia y la Tecnología, conocida como "Electrónica Orgánica', donde confluyen la Física, la Química y la Ingeniería. Tal como anticipa el Prof. Forrest:[11] *Los materiales orgánicos ya han hecho una entrada considerable en la investigación y, de hecho, en ciertos aspectos comerciales a gran escala de la tecnología.* Estos materiales orgánicos podrían suplir, y aventajar, a los materiales inorgánicos usados en la actualidad. Como ventajas principales, su bajo coste, su peso ligero y, para algunos usos, la posibilidad de fabricar dispositivos flexibles. En la actualidad, los OLEDs ya se usan para algunos dispositivos, como pantallas de teléfonos móviles, y el salto a la fabricación de OLEDs blancos para uso en iluminación, se espera cercano.[12]

A lo largo de estos años se ha trabajado de forma intensa en la mejora del funcionamiento y rendimiento de los OLEDs, gracias a los avances desarrollados tanto en los procesos de deposición de películas, como en la síntesis y purificación de moléculas activas. El uso de dopantes en los polímeros electroluminiscentes ha mejorado considerablemente las características finales de los OLEDs.[13] Hoy día existen para los investigadores muchos retos aún por superar, antes del uso masivo por parte de la sociedad de esta tecnología. No obstante, los avances logrados y las nuevas perspectivas quedan reflejadas en la bibliografía reciente, de la que, sin pretender abarcarla toda en esta

Memoria, puede destacarse la siguiente: Por una parte, trabajos en los que el **procesado de los polímeros** está siendo objeto de intensa investigación, dado que es un paso fundamental tanto en la eficacia final del dispositivo, como en el coste de la producción a gran escala de OLEDs. En ese sentido, los investigadores han usado distintas estrategias, como por ejemplo, el uso de polímeros que, una vez depositados, pueden ser tratados fotoquímicamente.[14] Otra estrategia, usada recientemente[15] con una repercusión importante, es la deposición de polímeros disueltos en disolventes *ortogonales*. Se trata de usar en la deposición de una determinada capa un disolvente capaz de disolver el polímero a depositar, pero inerte ante las capas previamente depositadas.[16,17] Por otra parte, existen trabajos en los que se aborda, de manera muy original, el problema de la **deposición de las capas orgánicas**. Así, el grupo del Pr. Kafafi[18] ha conseguido fabricar OLEDs a escala nanométrica, usando una superficie con un patrón de agujeros del orden del nanómetro. Investigadores japoneses han fabricado un OLED depositando las capas orgánicas mediante un spray.[19] Por último, una de las limitaciones más importantes en este momento de estos dispositivos es el **tiempo de vida**. Con ese objetivo, hay investigadores revisando la degradación de los OLEDs desde un punto de vista fundamental,[20] mientras que otros grupos están diseñando estrategias para alargar el tiempo de funcionamiento de los dispositivos. Este es el caso del grupo del Dr. Bolink,[21,22] que está realizando un enorme avance mediante el diseño y síntesis de nuevas moléculas, que dan lugar a tiempos de vida considerablemente mayores que los establecidos.

Fundamento Físico

La estructura básica de un OLED consiste en una o más películas orgánicas semiconductoras situadas entre dos electrodos. El cátodo está constituido por un metal o aleación de metales de baja función trabajo (Al, Ca, Li-Al, Mg-Ag...), depositado mediante evaporación térmica a vacío. Su función es la inyección de electrones en el dispositivo. El ánodo es un conductor de alta función trabajo y ópticamente transparente, de forma que puedan detectarse a través de su superficie los fotones generados. Suele emplearse una película de ITO, óxido de estaño e indio, depositada sobre soporte sólido de vidrio de o plástico, mediante sputtering o evaporación por bombardeo de electrones. Su función es la inyección de huecos.

Una primera clasificación de los OLEDs puede realizarse según la naturaleza de las películas orgánicas empleadas. De esta forma, se distinguen entre OLEDs compuestos por moléculas orgánicas de bajo peso molecular, small molecule devices, y aquellos que emplean polímeros orgánicos, organic polymer devices. La elección de la técnica de deposición de una película orgánica depende fundamentalmente de la naturaleza del material. Así, lo más habitual es utilizar spin-coating en el caso de polímeros, y evaporación térmica para moléculas pequeñas.

Supóngase un dispositivo en el que una sola película de naturaleza polimérica está colocada entre el ánodo y el cátodo. En esta situación, el material polimérico debe realizar varias funciones: transporte de los huecos, h^+, y electrones, e^-, inyectados desde los electrodos, recombinación de ambos y formación de excitones. Los niveles energéticos HOMO, orbital molecular

ocupado de más alta energía, y LUMO, orbital molecular vacío de más baja energía, de este material semiconductor equivalen a las bandas de valencia y de conducción, respectivamente, de un semiconductor inorgánico. Si ahora quitamos un electrón e^- a la película del nivel HOMO, la situación es similar a oxidar una unidad y formar, por tanto, el radical catión correspondiente. Este e^- puede ser sustituido por otro de la unidad monomérica vecina, y así sucesivamente, convirtiéndose en un conductor eléctrico. Esta función, extracción de e^- de la película, la realiza el ánodo. Se genera de este modo un flujo de electrones hacia el electrodo positivo, o lo que es igual, un flujo de cargas positivas o ausencia de cargas negativas hacia el cátodo. La falta de un e^- en la película es equivalente a la presencia de un hueco, h^+, cuya carga es +1. Por otro lado, la función del cátodo es introducir un e^- en el sistema que ocupe el nivel energético LUMO. Al igual que ocurre con el h^+, el e^- pasa de una unidad monomérica a otra vecina, produciéndose la reducción secuencial de éstas, y se establece una corriente de electrones desde el electrodo negativo al positivo. Este proceso se representa en la Figura 1.9, donde bajo la acción de un campo eléctrico externo, e^- y h^+ se mueven en direcciones opuestas. La tendencia de un e^- que se mueve en el nivel LUMO será siempre la de ocupar el nivel de menor energía posible, mientras que un h^+ situado en el HOMO tenderá a ocupar niveles vacíos más energéticos. Se puede afirmar que el ánodo es un electrodo inyector de h^+ y el cátodo, un inyector de e^-.

Cuando un e^- que se mueve en el LUMO y un h^+ que lo hace en el HOMO se encuentran próximos en el espacio, se produce una interacción de tipo coulómbica que da lugar a la formación de un par $h^+ - e^-$, el cual posee

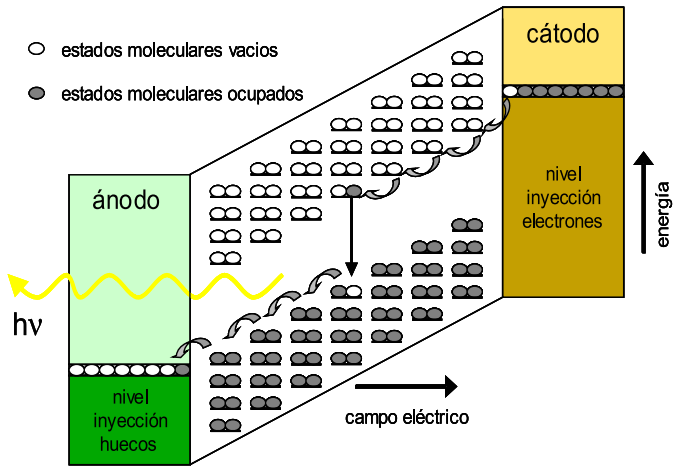

Figura 1.9: Inyección y migración de huecos y electrones.

una menor energía debido al aumento de la estabilidad. Este par $h^+ - e^-$ se denomina excitón, se comporta como una partícula eléctricamente neutra que puede ser creada y extinguida, y posee movilidad quele permite difundirse a través de la película. La creación de excitones dentro del dispositivo es el motor del funcionamiento de un LED, tanto inorgánico como orgánico. El excitón formado puede estar, en función del spin, en estado singlete o triplete, siendo las probabilidades de formación de ambos estados del 25 % y 75 %, respectivamente. De esta forma, la eficiencia máxima teórica de un dispositivo electroluminiscente fluorescente es del 25 %. Un material que emita desde el estado triplete puede, en teoría, proporcionar al dispositivo una eficiencia del 100 %. Es por ello que los OLEDs basados en compuestos fosforescentes son de gran interés.[4] Para estos dispositivos, los compuestos más usados son los complejos organometálicos de metales de transición, en especial, los complejos organometálicos de Ir (III).[23–27]

Finalmente, el excitón decae hasta el estado electrónico fundamental de

forma radiativa, emitiendo un fotón, o no radiativa. Como el ánodo es un electrodo ópticamente transparente, la emisión radiativa de fotones puede escapar y ser detectada a su través. La energía del fotón generado será responsable del color de la luz emitida y corresponde, aproximadamente, a la diferencia energética entre los niveles HOMO/LUMO del material emisor, también llamada bandgap. La Figura 1.10 muestra un esquema idealizado de todo el proceso.

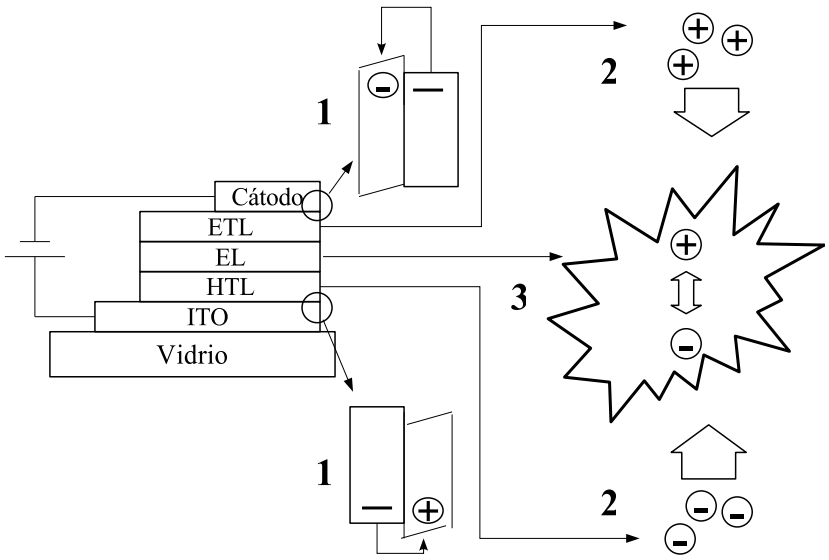

Figura 1.10: Esquema de un OLED en funcionamiento. **1**, inyección de huecos y electrones, respectivamente, desde el ánodo y el cátodo, a las capas HTL (capa transportadora de huecos) y ETL (capa transportadora de electrones). **2**, migración de huecos y electrones en sentidos opuestos. **3**, combinación de huecos y electrones en la capa EL (capa electroluminiscente) para producir excitones, con posterior emisión de luz.

La configuración electrónica del excitón no es el único factor que afecta a la eficiencia de un OLED. Se ha comprobado que las movilidades de h^+ y e^- en el seno del dispositivo influyen de forma crucial en el funcionamiento y la eficiencia de éste. Así, en el diseño del dispositivo, es preciso procurar

un equilibrio entre las movilidades de h^+ y e^- para que las recombinaciones sean efectivas y se produzcan en la zona deseada, esto es, en el material emisor. Este equilibrio se consigue mediante la modificación de la estructura del diodo, añadiendo nuevas películas, mezclando dos o más compuestos en una misma capa, etc., de forma que se incrementen o disminuyan dichas movilidades.

Referencias

1. Tang, C. W.; VanSlyke, S. A. *Appl. Phys. Lett.* **1987,** *51,* 913.

2. Van Slyke, S. A.; Chen, C. H.; Tang, C. W. *Appl. Phys. Lett.* **1996,** *69,* 2160.

3. Burroughes, J.; Bradley, D.; Brown, A.; Marks, R.; Mackay, K.; Friend, R.; Burns, P.; Holmes, A. *Nature* **1990,** *347,* 539.

4. Baldo, M. A.; O'Brien, D. F.; You, Y.; Shoustikov, A.; Sibley, S.; Thompson, M. E.; Forrest, S. R. *Nature* **1998,** *395,* 151.

5. Slinker, J.; Bernards, D.; Houston, P. L.; Abruña, H. D.; Bernhard, S.; Malliaras, G. G. *Chem. Comm.* **2003,** 2392.

6. Sun, Y.; Giebink, N. C.; Kanno, H.; Ma, B.; Thompson, M. E.; Forrest, S. R. *Nature* **2006,** *440,* 908.

7. D'Andrade, B. W.; Forrest, S. R. *Adv. Mater.* **2004,** *16,* 1585.

8. Ahn, J. H.; Bertoni, C.; Dunn, S.; Wang, C.; Talapin, D. V.; Gaponik, N.; Eychmüller, A.; Hua, Y.; Bryce, M. R.; Petty, M. C. *Nanotechnology* **2007,** *18,* 335202.

9. Duggal, A. R.; Shiang, J. J.; Heller, C. M.; Foust, D. F. *Appl. Phys. Lett.* **2002,** *80,* 3470.

10. Krummacher, B. C.; Choong, V. E.; Mathai, M. K.; Choulis, S. A.; So, F.; Jermann, F.; Fiedler, T.; Zachau, M. *Appl. Phys. Lett.* **2006,** *88,* 113506.

11. Forrest, S. R. *Nature* **2004,** *428,* 911.

12. Tullo, A. H. *Chem. and Eng. News* **2008,** *86,* 20.

13. Gross, M.; Müller, D. C.; Nothofer, H. G.; Scherf, U.; Neher, D.; Bräuchle, C.; Meerholz, K. *Nature* **2000,** *405,* 661.

14. Müller, C. D.; Falcou, A.; Reckefuss, N.; Rojahn, M.; Wlederhirn, V.; Rudati, P.; Frohne, H.; Nuyken, O.; Becker, H.; Meerholz, K. *Nature* **2003,** *421,* 829.

15. Lee, J. K.; Chatzichristidi, M.; Zakhidov, A. A.; Taylor, P. G.; DeFranco, J. A.; Hwang, H. S.; Fong, H. H.; Holmes, A. B. Malliaras, G. G.; Ober, C. K. *J. Am. Chem. Soc.* **2008,** *130,* 11564.

16. Meerholz, K. *Nature* **2005,** *437,* 327.

17. Gong, X.; Wang, S.; Moses, D.; Bazan, G. C.; Heeger, A. J. *Adv. Mater.* **2005,** *17,* 2053.

18. Yamamoto, H.; Wilkinson, J.; Long, J. P.; Bussman, K.; Christodoulides, J. A.; Kafafi, Z. H. *Nano Letters* **2005,** *5,* 2485.

19. Echigo, T.; Naka, S.; Okada, H.; Onnagawa, H. *Jpn. J. Appl. Phys.* **2005,** *44,* 626.

20. Luo, Y.; Aziz, H.; Xu, G.; Popovic, Z. D. *Chem. Mater.* **2007,** *19,* 2079.

21. Graber, S.; Doyle, K.; Neuburger, M.; Housecroft, C. E.; Constable, E. C.; Costa, R. D.; Ortí, E.; Repetto, D.; Bolink, H. J. *J. Am. Chem. Soc.* **2008,** *130,* 14944.

22. Bolink, H. J.; Coronado, E.; Costa, R. D.; Ortí, E.; Sessolo, M.; Graber, S.; Doyle, K.; Neuburger, M.; Housecroft, C. E.; Constable, E. C. *Adv. Mater.* **2008,** *20,* 3910.

23. Nazeerudin, M. K.; Humphry-Baker, R.; Berner, D.; Rivier, S.; Zuppiroli, L.; Graetzel, M. *J. Am. Chem. Soc.* **2003,** *125,* 8790.

24. Avilov, I.; Minoofar, P.; Cornil, J.; De Cola, L. *J. Am . Chem. Soc.* **2007,** *129,* 8247.

25. Rehmann, N.; Ulbricht, C.; Köhnen, A.; Zacharias, P.; Gather, M. C.; Hertel, D.; Holder, E.; Meerholz, K.; Schubert, U. S. *Adv. Mater.* **2008,** *20,* 129.

26. Slinker, J.; Bernards, D.; Houston, P. L.; Abruña, H.; Bernhard, S.; Malliaras, G. G. *Chem. Commun.* **2003,** *19,* 2392.

27. Lowry, M. S.; Bernhard, S. *Chem. Eur. J.* **2006,** *12,* 7970.

Capítulo 2

Experimental

2.1. Técnicas de Caracterización de la Monocapa en la Interfase Aire−Agua

Balanza de Langmuir

Los registros de isotermas presión superficial-área por moléculas ($\pi - A$) y las curvas de estabilidad de área frente al tiempo, a presión superficial constante, constituyen el primer paso en la caracterización de una monocapa de Langmuir. Para ello se emplea la balanza de Langmuir. Este instrumento consta básicamente de los siguientes elementos: una cuba de material plástico, teflón, donde se aloja el líquido que constituye la subfase, normalmente, agua ultrapura MilliQ o, en ocasiones, una disolución acuosa, y sobre el que se deposita la disolución que contiene el material que va a formar la película; una barrera móvil que separa la superficie de trabajo, donde se esparce la película, de la superficie limpia, y que es la encargada de comprimir la monocapa; y un sistema de medición de presión superficial.

El sistema de medida de presión superficial de las balanzas de Langmuir empleadas en esta Memoria fue del tipo Wilhemy. El dispositivo experimental de este sistema está constituido por una lámina metálica, o de papel, que se encuentra parcialmente sumergida en la subfase y conectada, por el otro extremo, a una microbalanza electrónica de alta sensibilidad. De los tres tipos de fuerza a los que se encuentra sometida la lámina, peso, empuje y tensión superficial, sólo esta última varía por la presencia de la monocapa sobre la subfase respecto de la subfase limpia. Por tanto, la diferencia entre la fuerza medida antes y después de esparcir la monocapa es debida únicamente a la

diferencia de tensión superficial, esto es, la presión superficial: $\pi = \gamma_0 - \gamma$.

En la Figura 2.1 se muestra un esquema de balanza de Langmuir. En esta Memoria se han utilizado dos balanzas comerciales NIMA de tipo rectangular, modelos 611D y 601BAM, con una o dos barreras móviles, respectivamente.

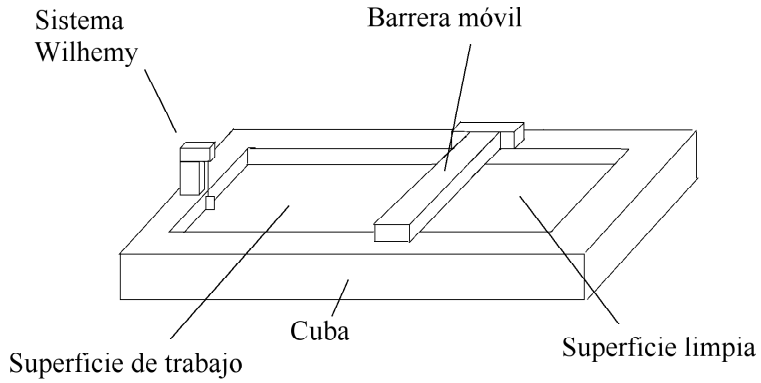

Figura 2.1: Esquema de una balanza de Langmuir.

Espectroscopía de Reflexión UV-Visible

Las medidas de reflexión en la interfase aire−agua se han realizado en un equipo diseñado por Nanofilm, RefSpec[2] cuya fotografía se muestra en la Figura 2.2.

Para su mejor descripción, en la Figura 2.3 se recoge un esquema de dicho espectrofotómetro.[1–3] La fuente de luz consiste en dos lámparas, una de deuterio y otra de tungsteno, ambas instaladas en un soporte de cerámica. La luz sale por una ventana de cristal de cuarzo, que la colima hacia la fibra óptica. Posteriormente esta radiación pasa por un monocromador instalado

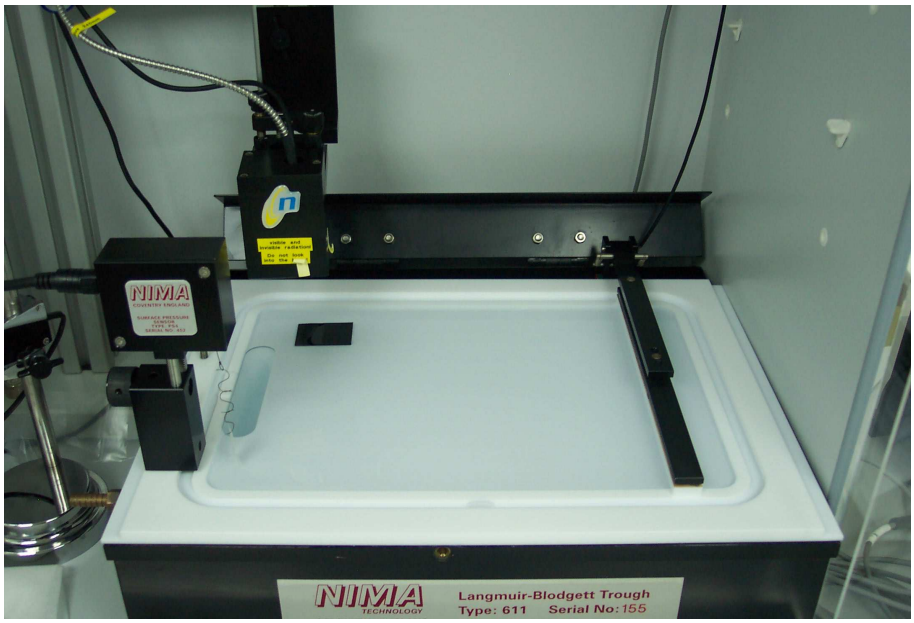

Figura 2.2: Fotografía del reflectómetro UV-visible.

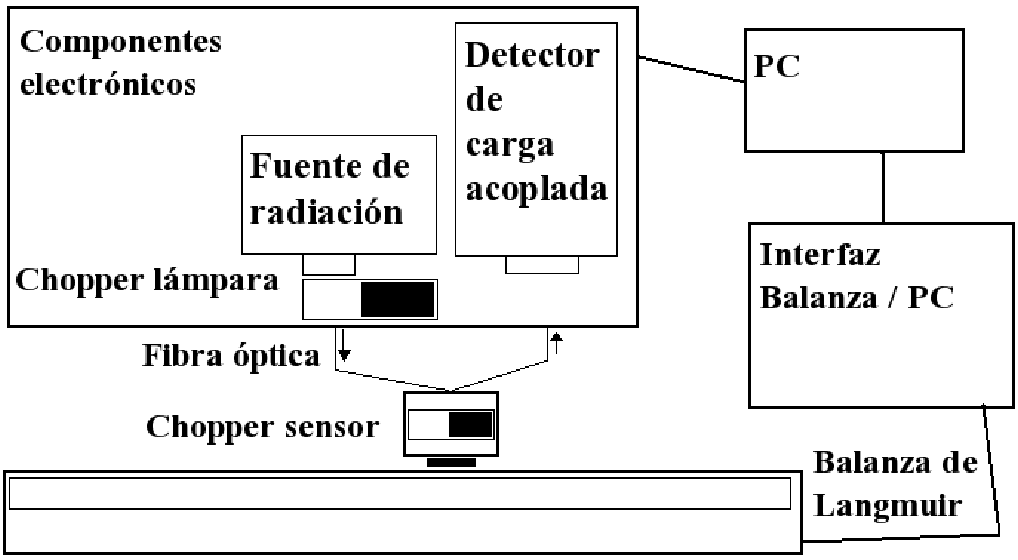

Figura 2.3: Esquema del reflectómetro modelo RefSpec[2].

en el sensor. De ahí sale e incide en la muestra, esparcida sobre la interfase aire−agua. Este mismo sensor enfoca la luz reflejada hacia una fibra óptica, para que llegue al detector. Existen dos choppers que permiten alternar entre la radiación emitida por la lámpara y la reflejada por la muestra, ambos controlados electrónicamente. El chopper del sensor tiene su parte trasera cubierta por un espejo de forma que, además, sirve como referencia estática para las oscilaciones de la lámpara. En el fondo de la balanza se colocan una placa negra que actúa como trampa de luz para absorber los rayos transmitidos. De esta manera, la radiación reflejada entra al detector CCD, detector de carga acoplada que envía la señal al ordenador donde se registra y procesa adecuadamente.

Microscopía de Ángulo Brewster (BAM)

Las imágenes de microscopía de ángulo Brewster han sido obtenidas en un sistema comercial I-Elli2000 de Nanofilm (Göttingen, Alemania). El montaje experimental[4,5] del microscopio BAM se halla acoplado a una balanza de Langmuir donde se extiende la monocapa objeto de estudio. La Figura 2.4 muestra una fotografía del equipo usado en esta Memoria.

El dispositivo se compone de un láser verde (Nd:YAG, 50 mW, 532 nm) que produce un rayo de luz de 1.3 mm de diámetro, el cual tras atravesar un polarizador adquiere polarización p, e incide posteriormente sobre la interfase con un ángulo de 53.1°, ángulo Brewster. En este sistema, la intensidad de luz refractada es absorbida por una trampa de luz colocada en el fondo de la balanza, mientras que la radiación reflejada pasa a través de un objetivo cuya

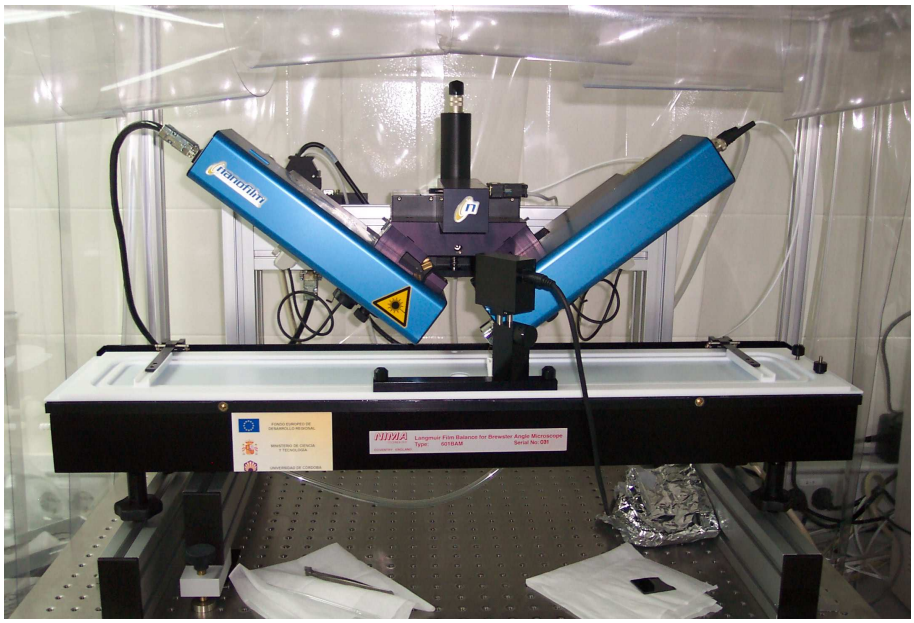

Figura 2.4: Fotografía del microscopio de ángulo Brewster usado en esta Memoria.

distancia focal es de 20 mm y llega a una cámara CCD de alta sensibilidad, donde se recoge la reflectividad debida a la presencia de la monocapa en la interfase. La cámara CCD es capaz de registrar de forma electrónica la intensidad y el punto de llegada de pequeñísimas cantidades de luz, que, a través de la aplicación informática que controla el equipo son convertidas a imágenes de mapa de bits (768 x 562 píxeles) para su representación y análisis. El procesamiento de la imagen incluye la corrección geométrica de ésta, así como el uso de filtros para reducir interferencias y ruido. Asimismo, el brillo de la imagen se reescala para mejorar el contraste.

La resolución lateral del sistema óptico en el plano de la superficie acuosa es de 2 μm. El microscopio está equipado con un analizador que permite observar la posible anisotropía óptica en el interior de los dominios en que se

organizan las moléculas que forman la película. De este modo, mediante la rotación del analizador respecto a la dirección de la luz incidente p-polarizada, se pueden observar diferencias en el contraste dentro de un mismo dominio, fenómeno indicativo de una diferente orientación molecular. Tanto el microscopio como la balanza están situados sobre una mesa antivibratoria Halcyonics MOD-2 S (Göttingen, Alemania), dentro de una cámara limpia.

2.2. Técnicas de Caracterización de Películas en la Interfase Aire-Sólido

La transferencia de monocapas a soportes sólidos desde la balanza de Langmuir, técnica de Langmuir-Blodgett, se llevó a cabo mediante el uso de un brazo mecánico acoplado a la balanza, que se mueve perpendicularmente a la interfase y que es controlado por ordenador. Los principales parámetros a tener en cuenta en la transferencia son la relación de transferencia, así como la velocidad a la cual ésta se lleva a cabo. La velocidad de transferencia osciló entre 5 y 10 $mm \cdot min^{-1}$. La fabricación de multicapas se realizó mediante la inmersión y/o emersión sucesiva del soporte en la monocapa mantenida en la interfase aire-agua a presión superficial constante. Por último, los soportes empleados fueron vidrio, CaF_2 o electrodos transparentes ITO.

Espectroscopía de Absorción UV-Visible

Los espectros de absorción UV-visible se obtuvieron en un espectrofotómetro Varian Cary 100 Bio. Los soportes de cuarzo, vidrio e ITO cubiertos con

la monocapa transferida se colocaron en el paso de luz, situando un soporte de cuarzo, vidrio o ITO limpio, respectivamente, como referencia. De igual manera, se han realizado los espectros de las disoluciones utilizadas en este trabajo, tanto acuosas como orgánicas, empleando cubetas de cuarzo Hellma de paso óptico 2 mm o 1 cm.

Espectroscopía de FTIR

Los espectros FTIR se obtuvieron con un espectrofotómetro IR-FT Mattson, Research Series, acoplado a un ordenador, utilizando un detector DTGS, sulfato de triglicina deuterado. Para registrar los espectros de transmisión de las películas LB, éstas se transfirieron sobre un soporte de CaF_2. Como referencia, se usó un soporte limpio del mismo material sobre el que se depositó la monocapa. La adquisición de los espectros se llevó a cabo con una resolución de 4 cm^{-1}, efectuando una acumulación de 1024 barridos para cada espectro. En todos los casos, con anterioridad al registro de los espectros, y a fin de evitar interferencias, se procedió a eliminar del sistema el vapor de agua y CO_2, mediante una purga de aire seco proporcionada por una columna purificadora de Peak Scientific.

2.3. Dinámica Molecular. GROMACS 3.3.

Como motor de Dinámica Molecular, se usó el paquete GROMACS 3.3[6] (www.gromacs.org), desarrollado en la Universidad de Gröningen (Holanda). Este motor toma como archivos de entrada, la información correspondiente a la topología de las moléculas, así como su densidad electrónica, y los archi-

vos que definen las condiciones y longitud de la trayectoria a generar. Para el caso de las moléculas estudiadas en esta Memoria, se construyó su topología usando la base de datos de GROMACS, así como métodos semiempíricos en HyperChem.[7] Una vez generada la trayectoria, el análisis de la misma se llevó a cabo mediante software desarrollado por el propio grupo de investigación. Para ello, se usó el lenguaje de programación Fortran 90/95.[8] Los *snapshots* o fotografías de las trayectorias se realizaron mediante el software gráfico PyMol.[9]

2.4. Materiales, Reactivos y Tratamiento de Datos

Salvo los complejos organometálicos de Iridio (III), sintetizados en el grupo del Dr. Bolink del Instituto de Ciencia y Tecnología Molecular de la Universidad de Valencia (www.icmol.es), los demás materiales y reactivos usados en las experiencias de la presente Memoria fueron adquiridos en las diferentes firmas comerciales que se citan en los Capítulos correspondientes. En todas las experiencias, el agua utilizada es ultrapura y procede de una unidad Millipore Mill-Q, pretratada en un sistema Millipore de ósmosis inversa (18 $M\Omega \cdot cm^{-1}$). Para la limpieza previa al uso de los soportes de vidrio, cuarzo, y electrodos ITO empleados en este trabajo, se siguió el siguiente protocolo: a) inmersión de los soportes sólidos en una disolución Extran:agua (1:1) durante 10-15 minutos aplicando ultrasonidos, b) enjuague con agua ultrapura y etanol, c) inmersión en isopropanol durante al menos 15 minutos

con ultrasonidos, d) inmersión en etanol durante 15 minutos en ultrasonidos, e) aclarado con acetona y f) secado bajo una corriente de aire comprimido.

Los soportes de CaF_2 utilizados en la medida de espectros IR de transmisión de las películas LB, se sometieron a un tratamiento de limpieza diferente: a) inmersión de los soportes sólidos en cloroformo durante 5 minutos, b) limpieza en Extrano durante 30 minutos, c) aclarado con agua y d) inmersión en cloroformo.

Los datos adquiridos en el laboratorio de forma digital se trataron con los programas SigmaPlot[10] y MathCad,[11] que a su vez se utilizaron en la realización de las figuras que se presentan en esta Memoria. Asimismo, se procedió al tratamiento de imágenes con el paquete Corel, que incluye entre otros Corel Photopaint o Corel Draw,[12] empleándose además este último en la preparación de los esquemas gráficos que aparecen en los distintos Capítulos.

Referencias

1. Kuhn, H.; Möbius, D.; Bücher, H. *Physical Methods of Chemistry;* John Wiley and Sons: 1972.

2. Grüniger, H.; Möbius, D.; Meyer, H. *J. Chem. Phys.* **1983,** *79,* 3701.

3. Vandevyver, M.; Barraud, A.; Ruaudel-Teixier, A.; Maillard, P.; Gianotti, C. J. *J. Colloid Interface Sci.* **1982,** *85,* 571.

4. Hönig, D.; Möbius, D. *J. Phys. Chem.* **1991,** *95,* 4590.

5. Hönig, D.; Overbeck, G. A.; Möbius, D. *Adv. Mater.* **1992,** *4,* 419.

6. Van Der Spoel, D.; Lindahl, E.; Hess, B.; Groenhof, G. Mark, A. E.; Berendsen, H. J. C. *J. Comp. Chem.* **2005,** *26,* 1701.

7. "HyperChem 8.5", 1999 Hypercube, Inc.

8. Chapman, S. J. a. *Fortran 90/95 for Scientists and Engineers;* McGraw-Hill Science: 2nd ed.; 2003.

9. DeLano, W. L. "The PyMOL Molecular Graphics System", 2002.

10. "SigmaPlot 7th Edition", 2001 Jandel Scientific.

11. "MathCad 14.0", 2008 Mathsoft, Inc.

12. "CorelDraw 9 ed.", 1995 Corel Corporation. Ottawa, Ontario, Canada.

Capítulo 3

Organización Molecular de Películas Delgadas Mixtas en la Interfase Aire–Agua

3.1. Effect of the Molecular Methylene Blue Aggregation on the Mesoscopic Domain Morphology in Mixed Monolayers with DMPA

The molecular organization and the domain morphology of an anionic matrix dimyristoylphosphatidic acid (DMPA) as influenced by the presence of a cationic water-soluble methylene blue (MB) have been studied by using Brewster angle microscopy and reflection spectroscopy at the air−water interface. Mixed monolayers of DMPA:MB, molar ratios 5:1 and 1:1, were formed by the cospreading method. BAM images show particular domain morphologies as a function of the MB density in the mixed film: circular domains for DMPA:MB = 5:1, and domains with hexagonal shape for DMPA:MB = 1:1. The reflection measurements during the compression process of the mixed films reveal a blue shift of the visible band with respect to that of the MB monomer. This blue shift is larger for the DMPA:MB = 5:1 in comparison with that for the 1:1 monolayer, despite lower MB density. By using the extended dipole model, we demonstrate that such blue shift is due to the formation of a 2D hexagonal network of MB molecules underneath of the DMPA monolayer in the mixed 1:1 film, while it is due to an infinite lineal aggregates in the 5:1 monolayer. BAM domain textures have been simulated by using the Fresnel equations for biaxial anisotropic materials. The results fit correctly the predictions of the extended dipole model.

Paper accepted in *J. Phys. Chem. C*, D.O.I. 10.1021/jp810935x

3.1.1. Introduction

The development of organic thin films with well-ordered structures has been the subject of numerous investigations.[1,2] The formation of self-assembled molecular and nanoscopic systems with specific physical properties is determined by the relations between chemical composition, structure, and organization of such materials.[3] When the molecules forming these systems tend to aggregate, the molecular characteristics are also affected. In fact, the most important features of molecular aggregation in organic dyes are the significant changes in the chemical, but mainly the optical properties of the interacting chromophore units.[4,5]

Molecular aggregates, with significantly altered optical properties, are formed only under certain conditions.[5,6] This makes necessary an intense research effort not only to control the type of molecular assembly on the surface, but also it is greatly interesting to characterize in situ the interfacial ordering and aggregation degree of the molecules.

In this sense, the air−water interface is an ideal model for these purposes, as it is easy to prepare in a pure state and also because the surface coverage can be smoothly adjusted by using the Langmuir trough technique.[7] Thus, the control of the association and orientation of molecules is feasible, in appropriate systems, at the molecular level in a reproducible way. In a suitable manner, the evaluation of aggregates formation and molecular orientation in monolayers at the air−water interface during the compression is easily achieved by means of UV-Vis spectroscopy,[8–11] and light microscopic techniques such as Brewster angle microscopy (BAM). This technique

has provided new insigths into the relation between molecular packing and the morphology of monolayers, phase transitions, and the shape and inner structure of domains.[12–17] Moreover, BAM studies have revealed an exciting large variety of morphological textures, also designated as condensed phase domains. These domains can exhibit a striking inner anisotropy and form subdomains of different brightness, which have been attributed to regions of different molecular orientation.[16–21]

In the present work, the molecular organization of mixed films containing an anionic matrix, dimyristoyl-phosphatidic acid (DMPA), and a cationic dye, methylene blue (MB), has been investigated at the air−water interface. The behavior of these compounds in the mixed monolayers has been studied by using reflection spectroscopy as well as Brewster angle microscopy. The influence on the domain morphology of the MB surface concentration, which can be varied either by the surface pressure during the compression process or by the molar proportion of the dye in the mixture, has been analyzed.

The results obtained demonstrate the significant control of the molecular arrangement on the optical properties of the monolayers. The compression process of the monolayers leads to a blue shift of the MB visible reflection band with respect to the maximun wavelength of pure MB monomer, which has been assigned to H-aggregates formation.[22–28] However, the blue shift increases for such mixtures where the molar ratio of MB is smaller. In addition, BAM images reveal the formation of domains with eye-catching inner textures and different morphology, as a function of the molar ratio. Thus, the DMPA:MB = 1:1 mixed monolayer show domains with outstanding hexagonal shapes, while circular domains are observed for the DMPA:MB = 5:1

mixed film. In this work, the relation between the aggregation detected by the reflection spectroscopy and the mesoscopic domain morphology observed by BAM is proved. The quantification of the blue shift of the maximum absorption band by the extended dipole model, together with the explanation of the domain textures by means of a theoretical simulation, is described in detail.

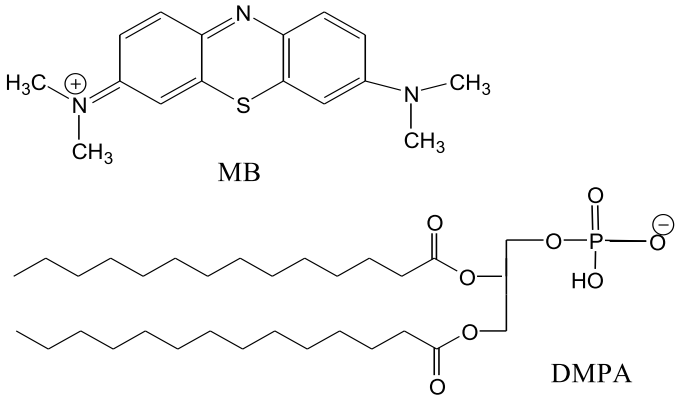

Figure 3.1: Molecular structures of methylene blue (MB) and dimyristoyl phosphatidic acid (DMPA).

3.1.2. Experimental

Materials

Methylene blue (MB) and Dimyristoyl-phosphatidic acid (DMPA) were purchased from Sigma Chemical Co. and used as received. Their molecular structures are depicted in Figure 3.1. A mixture of chloroform:methanol, ratio 3:1 (v/v), was used as spreading solvent for solving both components. The pure solvents were obtained without purification from Aldrich (Germany).

Ultrapure water, produced by a Millipore Milli-Q unit, pre-treated by a Millipore reverse osmosis system (resistivity = 18.2 $M\Omega \cdot cm^{-1}$), was used as a subphase. The subphase temperature was 21°C with pH 5.7.

Methods

Two different models of Nima troughs (Nima Technology, Coventry, England) were used in this work, both provided with a Wilhelmy type dynamometric system using a strip of filter paper: a NIMA 611D with one moving barrier for the measurement of the reflection spectra, and a NIMA 601, equipped with two symmetrical barriers to record BAM images.

UV−visible reflection spectra at normal incidence as the difference in reflectivity (ΔR) of the dye film-covered water surface and the bare surface[29] were obtained with a Nanofilm Surface Analysis Spectrometer (RefSpec^2, supplied by Nanofilm Technologies, Göttingen, Germany).

Images of the film morphology were obtained by Brewster angle microscopy (BAM) with a I-Elli2000 (Nanofilm Technologies) using a Nd:YAG diode laser with wavelength 532 nm and 50mW, which can be recorded with a lateral resolution of 2 μm. The image processing procedure included a geometrical correction of the image, as well as a filtering operation to reduce interference fringes and noise. The microscope and the film balance were located on a table with vibration isolation (antivibration system MOD-2 S, Halcyonics, Göttingen, Germany) in a large class 100 clean room.

3.1.3. Results and Discussion

Brewster Angle Microscopy (BAM)

Monolayers of DMPA:MB, in molar ratios 5:1 and 1:1, have been formed at the air−water interface by the cospreading method. In a previous work,[30] details on the surface pressure−area ($\pi - A$) isotherms of variable DMPA:MB mole ratios (2:1, 1:1 and 1:0) are given. The discussion of such results demonstrates that (1) there is no appreciable loss of MB molecules into the aqueous subphase; (2) MB molecules are retained in the DMPA monolayer by formation of an electrostatic complex between the two molecules; (3) the MB molecule does not penetrate into the lipid monolayer, but rather is located underneath the head groups of the densely packed DMPA monolayer at high π values.[30] Figure 3.2 shows the $\pi - A$ isotherms of mixed DMPA:MB and pure DMPA monolayers, and an enlargement of the phase transition region (inset).

Simultaneous to the isotherm recording, the morphology of the mixed monolayer at the air−water interface is directly observed by BAM. Figures 3.3 and 3.4 show the BAM images recorded under compression of the DMPA:MB = 5:1 and 1:1 monolayers, respectively.

At low surface pressure, before the phase transition, only the gas phase is observed, and any domain formation is appreciated. For both mixed monolayers, just when the surface pressure increases to the phase transition, the formation of small bright domains is recorded. Such domains grow under compression and define particular morphology as a function of the MB density in the mixed film, monitoring well-define circular and hexagonal domains

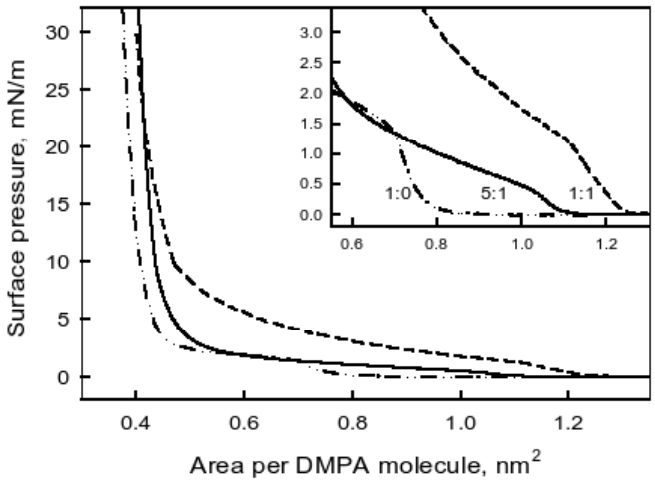

Figure 3.2: Surface pressure−area ($\pi - A$) isotherms of the cospread DMPA:MB monolayers, molar ratios 5:1 (solid line), 1:1 (dashed line) and pure DMPA (dot-dashed line). Inside, an enlargement of the phase transition is also shown. All curves are plotted versus area per DMPA molecule.

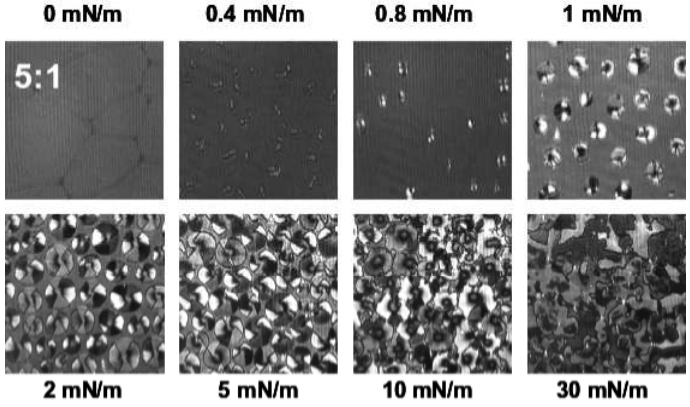

Figure 3.3: Brewster angle microscope (BAM) images of the mixed DMPA:MB = 5:1 monolayer under different surface pressure at the air−water interface. Image size: 210 μm width.

for DMPA:MB = 5:1 (Figure 3.3) and DMPA:MB = 1:1 (Figure 3.4), respectively. Furthermore, all domains have inner textures with different brightness.

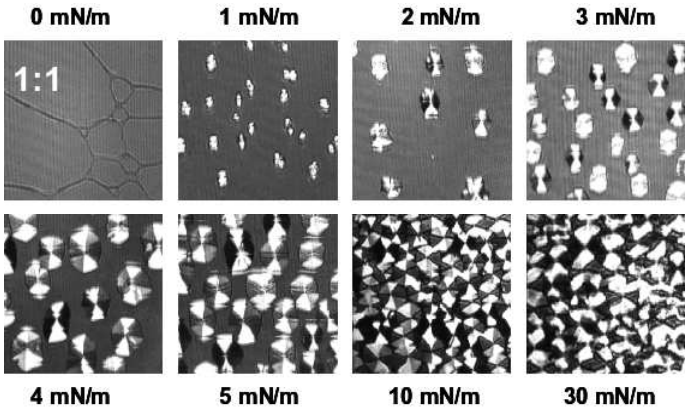

Figure 3.4: BAM images recorded simultaneously to the compression of mixed DMPA:MB = 1:1 monolayer. Image size: 210 μm width.

It should be noted that the pure DMPA monolayer does not show this type of morphological behaviour, that is, circular or hexagonal domains with inner textures.[31,32]

Upon further compression, the morphology of the domains of both mixed films is conserved, and their density increases , filling the whole area focused. Those domains do not coalesce. In addition, in the particular case of the DMPA:MB = 5:1 film, the domains distort and their inner textures vanish at very high surface pressures (Figure 3.3).

Reflection Spectroscopy

Direct evidence for the presence of MB in the mixed monolayer with DMPA is obtained by measuring the reflection spectrum of the monolayer. This method detects only those molecules that are at the interface and contribute to enhanced reflection from the air−water interface.[29] This technique gives us valuable information on the organization, density, and orientation of the

chomophore molecules located at the air−water interface.[7,11,33,34]

Figure 3.5 shows the reflection spectra of mixed monolayers DMPA:MB in molar ratios 5:1 (solid line) and 1:1 (dashed line) for two different surface areas: before the phase transition, 1.0 nm^2 per DMPA molecule (Figure 3.5A), and in condensed phase, 0.43 nm^2/DMPA molecule (Figure 3.5B). The reflection spectra obtained indicated, undoubtedly, the presence of MB at the air−water interface.

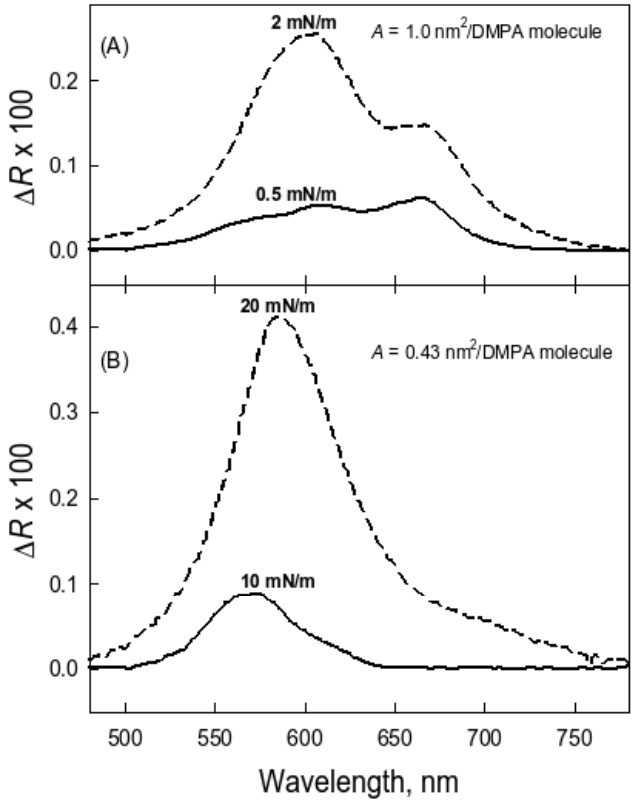

Figure 3.5: Reflection spectra ΔR of the mixed DMPA:MB monolayers, molar ratios 5:1 (solid lines) and 1:1 (dashed lines), at two different surface areas: A) A = 1.0 nm^2/DMPA molecule; B) A = 0.43 nm^2/DMPA molecule.

As can be observed, ΔR increases when the MB molar ratio increases and

the surface area decreases, that is, increasing the surface concentration of MB at the interface. Moreover, the shape and position of the bands changes as a function of the surface area and the MB molar ratio in the mixed monolayer. A more detailed discussion of this phenomenon will take place below.

Also, reflection spectra at different surface pressures were measured during several compression and expansion cycles (data not shown). In any mixed films, the reflection spectra are identical during the compression and expansion processes, and during several cycles. The coincidence of those spectra confirms that there is no appreciable loss of MB molecules into the aqueous subphase, at least after the cospreading process.

Figures 3.6 and 3.7 show the normalized reflection spectra, ΔR_{norm}, obtained at different surface pressures for DMPA:MB, in molar ratios 5:1 and 1:1, respectively. $\Delta R_{norm} = \Delta R \cdot A_{MB}$, where A_{MB} (nm^2/MB molecule) is the surface area of methylene blue according to the stoichiometry in each mixture, i.e., $A_{MB} = 5 \cdot A_{DMPA}$ and $A_{MB} = A_{DMPA}$ for the DMPA:MB = 5:1 and 1:1 films, respectively, where A_{DMPA} (nm^2 per DMPA molecule) is taken from the isotherm (Figure 3.2). Provided that all molecules of MB remain at the interface during the compression process, the reflection spectra normalized to the same surface density of MB, ΔR_{norm}, show more clearly possible changes of the orientation and/or association of the dye.

At low surface pressure ($\pi \sim 0$mN/m), the reflection spectra for both mixed films show two bands at 663 ($n - \pi^*$) and 614 nm,[35] at the same wavelengths as in aqueous solution (gray short-dashed lines in Figures 3.6 and 3.7). The 663 nm peak belongs to the known monomer absorption band, while that of 614 nm is associated with the 0-1 vibration and/or the dimer

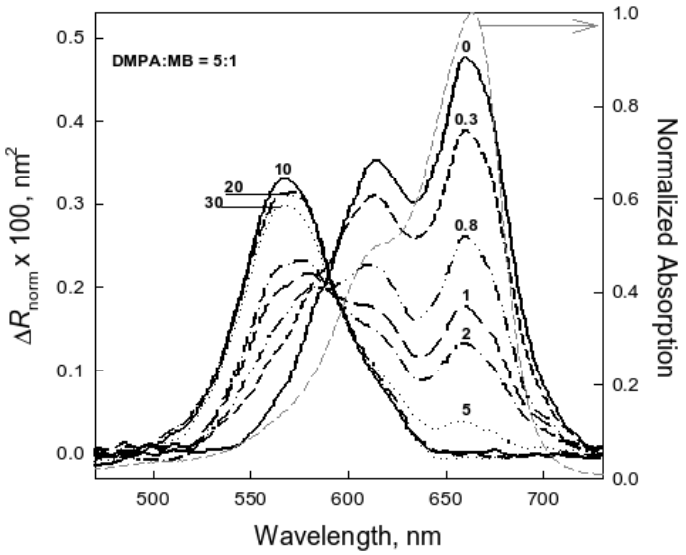

Figure 3.6: Reflection spectra normalized of MB, $\Delta R_{norm} = \Delta R \cdot A_{MB}$, for a monolayer of DMPA:MB = 5:1 under compression. The numbers indicate the surface pressure values (mN/m). As reference, the solution spectrum of MB is also shown (grey-dashed line).

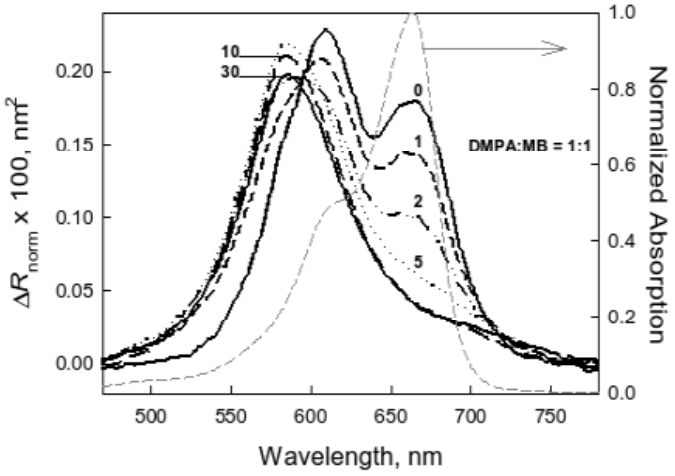

Figure 3.7: ΔR_{norm} *versus* λ for a monolayer of DMPA:MB = 1:1 at different surface pressures. The numbers indicate the surface pressure values (mN/m). As reference, the solution spectrum of MB is also shown (grey-dashed line).

absorption band.[22,23] In the case of the DMPA:MB = 5:1 mixture under compression (Figure 3.6), the intensity of the 663 and the 614 nm peaks decreases, while a new peak emerges at $\sim$ 568 nm. Once $\pi \sim$ 5mN/m is reached, only the 568 nm peak is detected, and its shape and position remain unchanged under further compression.

For the DMPA:MB 1:1 film (Figure 3.7) at $\pi \sim$0 mN/m, and contrary to that observed in the 5:1 mixture, the height of the peak at 664 nm is always smaller than that of 610 nm. Under compression, the 664 and 610 nm peaks disappear and a new peak at 586 nm emerges, the shape and position of which is conserved at $\pi \geq$10 mN/m.

The disappearance of the 664 and 610 nm bands together with the gradual appearance of the 568 or 586 nm bands as the surface pressure increases must be assigned to the H-aggregate formation of MB molecules.[22–28] However, it should be noted that the shift of the visible band with respect to the monomer (664 nm) of the DMPA:MB = 5:1 monolayer (at 568 nm) is larger than that of the mixed 1:1 (at 586 nm), despite the smaller MB density in the 5:1 film. In molecular aggregates, the shift of a band is a function of the aggregation number and of the tilt between chromophores.[11] In the next section, the extended dipole model[11,36,37] will be applied to explain this behaviour.

Analysis of Molecular Organization of the Methylene Blue in the Mixed DMPA:MB Monolayers

As the surface pressure increases, two phenomena take place in the reflection band: First, ΔR_{norm} decreases, which should be related to a decreasing

of the polar tilt angle of the chromophores and/or the decreasing of its oscillator strength; second, the blue shift of the maximum wavelength is attributed to the formation of H aggregates of the MB chromophores,[22–28] its magnitude being a function of the aggregation number and of the relative tilt between chromophores. To analyze these phenomena, the following parameters are defined: polar angle, θ, as the angle between the MB transition moment, μ, and the normal to the air−water interface; and azimuthal angle, ϕ, as the angle between the projection of μ on the x-y plane and the x axis (see Figure 3.8A). These coordinates are internal, which would be different for each domain.

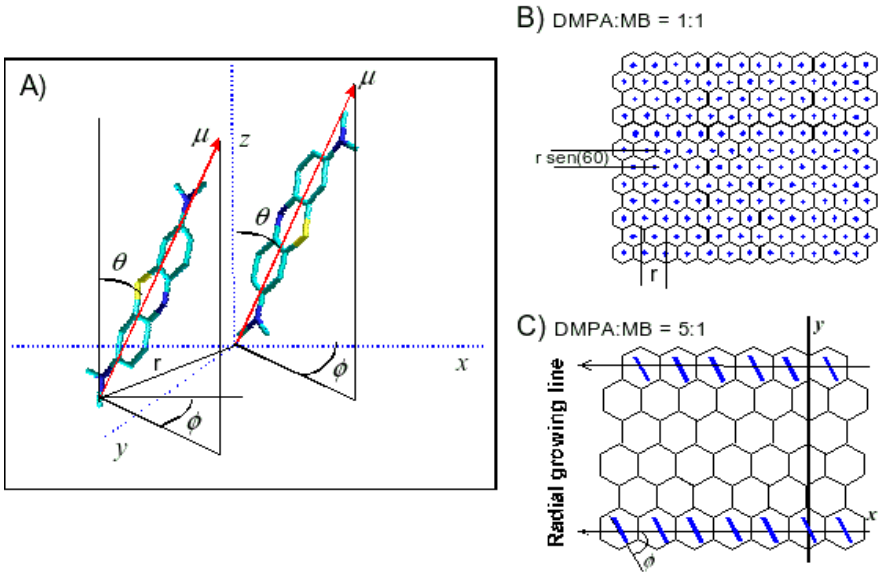

Figure 3.8: A) Graphic definition of the moment transition dipolar, μ, the polar tilt angle, θ, and the azimuthal angle, ϕ, of the MB molecules under the DMPA matrix at the air−water interface (the interface plane coincides with x-y plane); B) Organization model of the 2D hexagonal network of the mixed DMPA:MB = 1:1 film (hexagon: DMPA molecules; dots inside: MB molecules); C) Model of the MB infinite linear aggregates under the DMPA matrix for the DMPA:MB = 5:1 mixture (hexagon: DMPA organization; lines inside: MB transition dipoles).

Determination of MB Polar Angle in the Mixed DMPA:MB Monolayers

For low values of absorption, the reflection ΔR has been shown to be proportional to the surface concentration of the dye and is given in a reasonable approximation by[29]

$$\Delta R = 2{,}303 \cdot 10^3 \, \Gamma \, f_{orient} \, \varepsilon \, \sqrt{R_i} \tag{3.1}$$

where Γ is the surface concentration in mol cm^{-2}, $R_i = 0.02^8$ the reflectivity of the air−water interface at normal incidence, ε the extinction coefficient given as $L \; mol^{-1} \; cm^{-1}$, and f_{orient} is a numerical factor that takes into account the different average orientation of the square transition moment of the dye in solution as compared to the monolayer at the air−water interface.

For the hexagonal and circular domains observed in BAM images, the features of inner bright and dark regions indicate anisotropy. However, for a large region of the interface that includes numerous domains with a random distribution, an isotropic film in the plane is considered, and therefore there is not preferential azimuthal angle, ϕ. This just happens during the reflection measurements. In this case, f_{orient} is[11]

$$f_{orient} = \frac{3}{2}\langle \sin(\theta)^2 \rangle \tag{3.2}$$

where brackets indicate average values. The oscillator strength is defined as[38]

$$f = \frac{4 \cdot \varepsilon_0 \cdot 2{,}303 \cdot m_e \cdot c_0}{N_A \cdot e^2} \int_{Band} \varepsilon d\nu = 1{,}44 \cdot 10^{-19} \int_{Band} \varepsilon d\nu \qquad (3.3)$$

where ε_0 is the permittivity of vacuum, m_e the electron mass, e the elementary charge, c_0 the speed of ligth in a vacuum and N_A is the Avogadro constant. In eq 3.1.3, the numerical factor $1{,}44 \cdot 10^{-19}$ is expressed in $mol \cdot L^{-1} \cdot cm \cdot s$. The oscillator strength in solution was obtained by means of the integration between 480 and 750 nm, without considering whether the 614 nm peak is due to the dimer formation. In any case, we have used very low concentration of MB (10^{-6} M) to minimize such a possibility. In such a way, the oscillator strength obtained was $f = 0.545$, which is close to that given in the bibliography for the monomer (ranged between 0.5 and 0.6).[22,39]

From equations 3.1.3 and 3.1.3 is possible to define an apparent oscillator strength determined from the measured reflection spectra as[11]

$$f_{app} = f \cdot f_{orient} = 2{,}6 \cdot 10^{-12} \int_{Band} \Delta R_{norm} d\nu \qquad (3.4)$$

where the numeric factor $2{,}6 \cdot 10^{-12}$ is expressed in $nm^{-2} \cdot s$. Thus, f_{app} is obtained by the integration of the normalized reflection band in the range between 480 and 750 nm.

The values of f_{app} evaluated from reflection spectra of the different mixed DMPA:MB monolayers are plotted against the MB area, A_{MB}, in Figure 3.9. According to the Davidov model for exciton states of weak molecular interactions, the oscillator strength is conserved, that is, $f = \sum f_{aggreg}$, where f is teh free molecular oscillator strength, and $\sum f_{aggreg}$ is the corresponding to the different aggregates.[38,40,41] This fact has been tested for MB, obtaining that the sum of the oscillator strength of the MB dimer and polymer

aggregate is approximately equal to f (see table 4 of ref[22]). Therefore, if it is supposed that the oscillator strength is conserved for any aggregation degree, the observed variation of the f_{app} must be exclusively related to the MB tilt changes. Moreover, the ratio between the apparent oscillator transition and the oscillator strength from the solution ($f = 0{,}545$) gives the orientation factor, $f_{orient} = f_{app}/f$. Therefore, the average polar tilt angle θ is evaluated by using eq 3.1.3. The values thus obtained are plotting at the right axis in Figure 3.9.

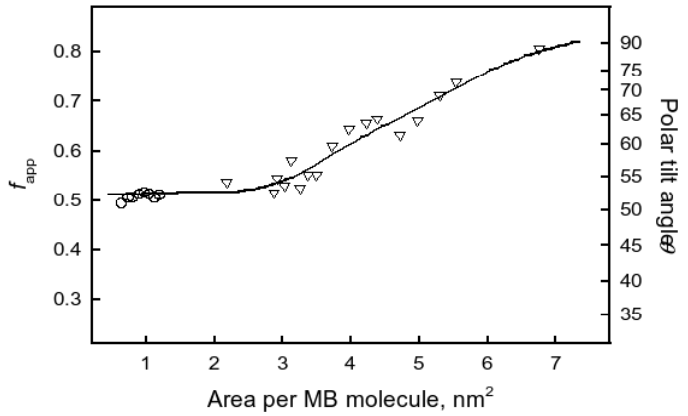

Figure 3.9: Plot of the apparent oscillator strength, f_{app}, and polar tilt angle, θ, against MB molecular area of the cospread DMPA:MB monolayers, molar ratios 5:1 (squares) and 1:1 (circles).

As can be seen in Figure 3.9 and for very large surface areas (only possible for the DMPA:MB = 5:1, inverted triangles in figure), $f_{app} \sim 0{,}8$,$f_{orient} \sim 1{,}5$ and $\theta \sim 90$ °. This f_{orient} value is possible only if the transition moment of all MB molecules is parallel to the interface and if all MB molecules initially spread at the air−water interface are retained by the DMPA matrix, otherwise lower f_{app} should be obtained. This fact together with the coincidence of

the reflection spectra during the compression and decompression processes is the definitive evidence of that all MB molecules are retained at the air−water interface. Moreover, the isotherms of the mixed films converge at high surface pressure with the DMPA isotherm (see Figure 3.2), which indicates that MB molecules do not occupy space at the interface and must be located underneath the polar lipid head groups. This behaviour is in agreement with those proposed for ionic water-soluble porphyrin,[34,42] or a cyclic bypiridinium tetracation,[33] attached electrostatically to lipid monolayers. Consequently, we confirm that the MB molecules are retained underneath the head group region of the DMPA monolayer by electrostatic interactions.[30]

As the A_{MB} decreases under compression, f_{app} also decreases, which is related to a change of the MB polar tilt angle (see Figure 3.9). For instance, for $A_{MB} < 3nm^2$ and any mixed monolayer, $f_{app} \sim 0{,}51 \pm 0{,}03$ and $\theta \sim 52° \pm 3°$. This value is just the polar tilt angle of MB in the hexagonal and circular domains observed by BAM.

Molecular Aggregation of the Methylene Blue in the Mixed DMPA:MB Monolayer

The blue shift of the visible MB absorption band can be estimated in a quantitative way according to the extended dipole model.[11,43,44] By this approximation, the molecules are replaced by their transition dipoles, $\mu = l$ x q, with fixed dipole length (l) and charge (q).

In the case of DMPA:MB = 1:1 monolayer with hexagonal domains, it is supposed the formation of a condensed 2D hexagonal network where each DMPA molecule holds about 0.43 nm^2 (see Figure 3.8B and 3.2) with MB

molecules retained underneath this 2D hexagonal network by means electrostatic interactions (stoichiometry 1:1). Thus, the gap between the geometrical centres of two consecutive DMPA hexagons is $r = (0{,}43)^{1/2} \sim 0.66\ nm$.

In our model sketched in Figure 3.8B, the MB molecules (points in Figure 3.8B) form an infinite 2D hexagonal network, where two consecutives molecules are spaced a distance r = 0.66 nm. Moreover, considering the inner domain, or segment domain with the same reflectivity in BAM, the tilt is the same for such MB molecules, that is, the same θ and ϕ angle values (see Figure 3.8A).

Given a MB reference molecule in the 2D hexagonal network, its excitation energy of this molecule due to the aggregation with N neighbour MB molecules can be expressed as[11,37]

$$\Delta E_N = \Delta E_{mon} + 2\sum_{i}^{N} J_i \tag{3.5}$$

where ΔE_{mon} is the excitation energy of the MB monomer, and J_i is the interaction energy between the dipoles corresponding to the reference molecule and each i molecules of the 2D network, which can be expressed in an approximately way by

$$J_i = \frac{q^2}{D} \cdot \left[\frac{1}{a_i} + \frac{1}{b_i} - \frac{1}{c_i} - \frac{1}{d_i}\right] \tag{3.6}$$

$D \sim 2{,}5$the dielectric constant, and a_i, b_i, c_i and d_i are the distances between ends of the dipoles positive-positive, negative-negative, positive-negative and negative-positive, respectively. Thus, the maximum wavelength of the aggregate λ_N, is:

$$\lambda_N = \lambda_{mon}\left[1 - \left(1 + \frac{h \cdot c \cdot 10^7}{2 \cdot \lambda_{mon} \cdot \sum_i^N J_i}\right)^{-1}\right] \tag{3.7}$$

with $\lambda_{mon} = 664$ nm being the maximum wavelength of monomer, that is, in the absence of aggregation. The application of this model requires the knowledge of l, q, and μ. The value $\mu = lxq = 11.04$ debye for the transition dipole has been obtained by integrating the absorption band in solution ($f = 0{,}545$). However, considering that l and q cannot be determined experimentally, eq 3.1.3 can not be applied. Nevertheless, those magnitudes may be obtained from the experimental wavelength shift of an aggregate with a well-known structure. Thus, for the dimer, $\lambda_{dimer} = 605$ nm,[22] and assuming $r = 0{,}66$ nm and a coplanar stacked MB dimer formation, values of $l = 0{,}25$ nm and $q = 0{,}915e$ can be obtained. These values are very close to those calculated previously.[22] Now, by using $l = 0{,}25$ nm and $q = 0{,}915e$, λ_N may be determined.

We have used a 2D hexagonal network formed by $N = 40$ x 40 molecules around the reference molecule, which is located at the coordinate origin (longer network do not change the obtained λ_N values). All calculus were done by MathCad 14.[45] λ_N was calculated for different θ and ϕ angles. Figure 3.10 top shows the variation of λ_N with θ angle for $\phi = 0°$(solid line), $\phi = 45°$(long-dashed line) and $\phi = 90°$(short-dashed line). As can be seen, the λ_N values show a strong dependence with θ angle, although they are almost independent of the ϕ angle. For the DMPA:MB = 1:1 monolayer and when the hexagonal domain is formed the MB absorption band appears at 586 nm (dotted line in Figure 3.10 top). In Figure 3.10 top, $\lambda_N = 586$nm is obtained with $\phi = 0°$(solid line) and $\theta \sim 52°$, while with $\phi = 90°$(dashed

line) and $\theta \sim 50°$. These polar angles approximately coincide with that obtained previously from the orientation factor (see Figure 3.9). This coincidence confirms the model proposed in the previous section, where is assumed that the oscillator strength is conserved. However, the model does not permit to evaluate the azimuthal angle, ϕ.

This model can not be applied to the circular domains observed for the DMPA:MB = 5:1 monolayer, because there is only one MB molecule for each five DMPA molecules. However, it is noteworthy that the MB absorption band appears at 568 nm, that is, 18 nm blue shifted with respect to the previous case, despite the molecular density of MB is lower. In any case, it is clear that the formation of the circular domains for the DMPA:MB = 5:1 film is induced by the MB aggregation (see Figures 3.3 and 3.6). Those circular domains grow in the radial direction, as detected by BAM (Figure 3.3). This radial growing may correspond to the formation of the MB lineal aggregates, and therefore a model based in MB infinite lineal aggregates is proposed (see Figure 3.8C). At high surface pressure, the DMPA package is identical to the previous case (see isotherms, Figure 3.2), and thus the spacing between MB dipoles is r = 0,66 nm (in eq 3.1.3). The model for the DMPA:MB = 5:1 organization is depicted in Figure 3.8C, where the MB transition dipoles are represented for lines inside of the hexagon (which represents the DMPA position), in such a way that only one of each five hexagon rows is occupied for MB molecules. In Figure 3.8C the azimuthal angle, ϕ, is also represented, and the x axis represents the aggregation line for the MB molecules.

For the calculus of λ_N, a lineal aggregate of $N = 80$ molecules around the reference molecule has been used. Figure 3.10, middle shows the plot of

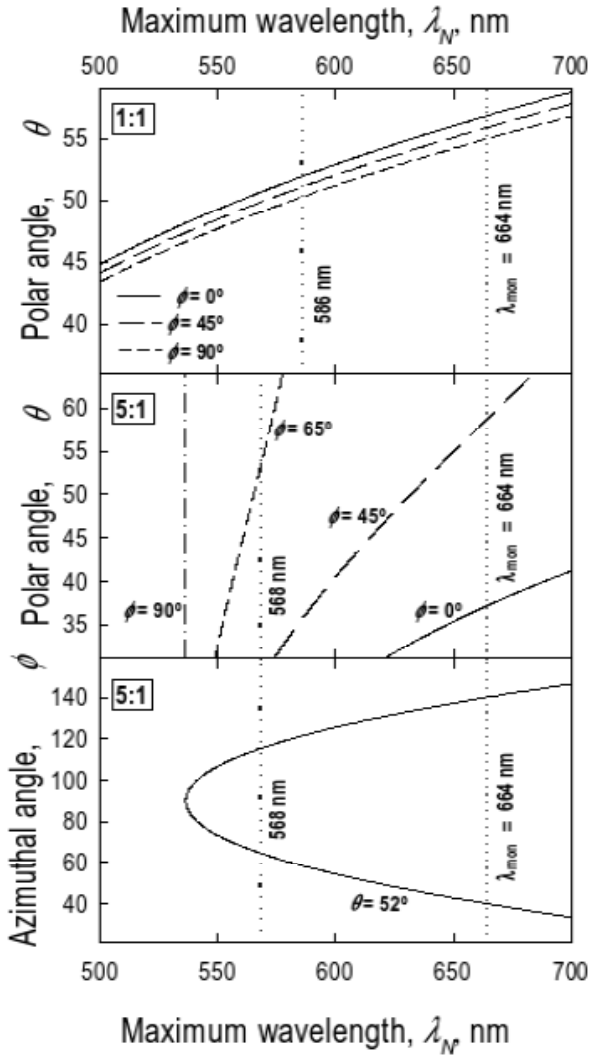

Figure 3.10: Plot of the calculated maximum wavelength, λ_N, against the polar tilt angle, θ, for different values of the azimuthal angle: Top, for the 2D hexagonal network of the mixed DMPA:MB = 1:1 monolayer, $\phi = 0°$(solid line), $\phi = 45°$(long-dashed line) and $\phi = 90°$(short-dashed line); Middle, for the lineal aggregate of the mixed DMPA:MB = 5:1 monolayer, $\phi = 90°$(dash-dotted line), $\phi = 65°$(short-dashed line), $\phi = 45°$(long-dashed line) and $\phi = 0°$(solid line). Bottom: Variation of the azimuthal angle, ϕ, with respect to the calculated maximum wavelength with $\theta = 52°$. The vertical dotted lines represent the λ_{max} for the monomer (λ_{mon} = 664nm), and the compressed monolayers DMPA:MB = 1:1 (586 nm) and 5:1 (568 nm).

λ_N against θ for $\phi = 0°$(solid line), $\phi = 45°$(long-dashed line), $\phi = 65°$(short-dashed line) and $\phi = 90°$(dash-dotted line). For the DMPA:MB = 5:1 monolayer and when the circular domains are formed the MB absorption band appears at 568 nm (dotted line in Figure 3.10, middle). For a fixed value of $\theta = 52°$(from the orientation factor), $\lambda_N = 568$ nm is obtained when $\phi = 65°$. However, this is not the unique possible solution. Figure 3.10, botttom (solid line) shows the plot of λ_N against ϕ with $\theta = 52°$. $\lambda_N = 568$ nm is found for $\phi = 65°$and $\phi = 115°$. Thus, the formation of MB lineal aggregate in such mixed film with $\theta = 52°$and $\phi = 65°$(or 115 °) causes the experimental blue shift of its absorption band ($\lambda_N = 568$ nm), and also evidences that its blue shift is larger than that for the DMPA:MB = 1:1 monolayer, despite the molecular density of the MB.

Simulation of domain textures

In a BAM experiment, p-polarized light reach the air−water interface with an angle $\alpha = 53{,}15°$, Brewster angle. Usually, the different BAM textures are observed due to changes of the refractive index resulting from differences in thickness, density and/or molecular orientation between the different regions of film. However, for our system, the MB aggregates absorb at 532 nm laser beam, whereas the monomer form does not absorb at such wavelength (see Figures 3.6 and 3.7). As previously suggested, the domain formation is induced by the MB aggregation whose absorption originates the strong changes in the film refractivity. Therefore, this phenomenon would be mainly responsible of the appearance in a first approximation of domain textures. In such a case, the Fresnel equations for biaxial anisotropic materials

on isotropic substrate should be used to calculate the reflection of the film.[46]

The DMPA:MB mixed film is assumed to be a biaxial material with complex refractive indices of $N_x = n_x - ik_x$, $N_y = n_y - ik_y$, and $N_z = n_z - ik_z$ (See Supporting Information).

To obtain the BAM images the analyzer was fixed at 0°, and therefore only the p component of the reflection is detected. Thus, the N_y component does not affect to the final result. Moreover, the absorption coefficients can be expressed as follows: $k_x = k_0 \cdot \sin(\theta) \cdot \cos(\phi)$, and $k_z = k_0 \cdot \cos(\theta)$. For such expression, ϕ must be redefined to a new coordinates (absolute laboratory coordinates, instead of the arbitrary coordinates represented in Figure 3.8A). From now on, the x axis (laboratory coordinates) is defined as the projection of the laser incidence axis on the interface (see Figure 3.11).

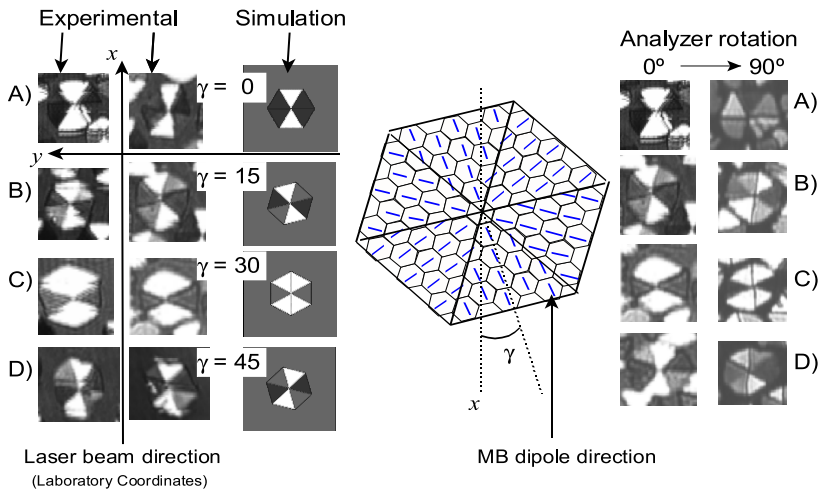

Figure 3.11: Center: Definition of the axis x of laboratory coordinates, and γ angle; Left side: Comparison of the simulated with the experimental domains (BAM images) of the mixed DMPA:MB = 1:1 monolayer ; Right side: BAM pictures for an analyzer position of 0°and rotated 90°.

Assuming values for the different constants ($k_0, n_x, n_z, \phi, \theta$ and the thickness of the film, d), the absolute reflectivity of the film can be determined. Following, this absolute reflection must be transformed to a relative grey level scale (from 255 to 0) for the simulation of the domain texture. Details of the simulation procedure are given in the Supporting Information. To simplify the simulation, it is assumed for all cases: $n_x = n_z$, $\theta = 52°$(determined previously), and $d \sim 3$ nm (thickness of the film, included DMPA and MB molecules). In such a way, the reflectivity depends exclusively on n_x, k_0 and ϕ. This simulation model is only approximate since the anisotropy of the DMPA alkyl chains is not considered.

The hexagonal domains observed in the DMPA:MB = 1:1 monolayer are subdivided into six identical equilateral triangles (Figure 3.4). The reflectivity inside of each triangle is constant, indicating a constant azimuthal orientation of the MB molecules, and probably of the DMPA aliphatic chains.[18–20] The hexagonal domains can be classified into four classes as a function of their inner texture (see Figure 3.11 A-D). Obviously, there are domains with intermediate reflectivity, but those four domain types are representatives of all observed textures. Domains B and D are specular images. In the BAM images shown in Figure 3.4 and Figure 3.11, the vertical direction is coincident with the laser incidence, and therefore with the x axis (laboratory coordinates). For all hexagonal domains, the triangles placed up and down of the hexagon are always more bright than those located at the lateral position. This fact indicates a preferential parallel orientation of the MB transition dipoles along to the bisector of the corresponding triangle. Therefore, for the simulation of the hexagonal domain texture, it is supposed that all MB dipoles inside of

each triangle have the same direction, being parallel to the bisector of each triangle (see Figure 3.11, center). In this way, if we denote by γ the angle between the x axis (laboratory coordinates), and the bisector of each triangle, which coincide with the θ angle, the refractivity of each triangle can be simulated. The different domain textures are obtained in base to the variation of γ values for each triangle, due to the hexagon rotation with respect to the x axis (laboratory coordinates). Taking these remarks into account and using $n_x = n_z = 1{,}5$, and $k_0 = 0{,}42$ (see Additional Material), the simulated images of domain textures with four different hexagon rotation angles, $\gamma = 0°$, 15°, 30°and 45°(corresponding to the γ value for the down triangle of the hexagon), are shown in Figure 3.11,left, together with the experimental images.

The comparison between the simulated and experimental images reveals a very good agreement; that is, the different textures of the experimental domains have been qualitatively reproduced by means of our simplified model.

Figure 3.11, right, shows the changes of the domain textures when the analyzer is rotated from 0°to 90°. The brightness of the inner domain regions changes by rotating the analyzer in the reflected beam path, which is indicative of optical anisotropy.

In the case of the circular domains observed for the DMPA:MB = 5:1 monolayer (Figure 3.3), six wedge-shaped segments with almost the same size and constant reflectivity, that is, constant azimuthal orientation of the molecules inside,[18–20] are observed. Like for the hexagonal domains, the circular domains observed can be classified into four classes as a function of their inner texture (see Figure 3.12, A-D). Contrary to the hexagonal do-

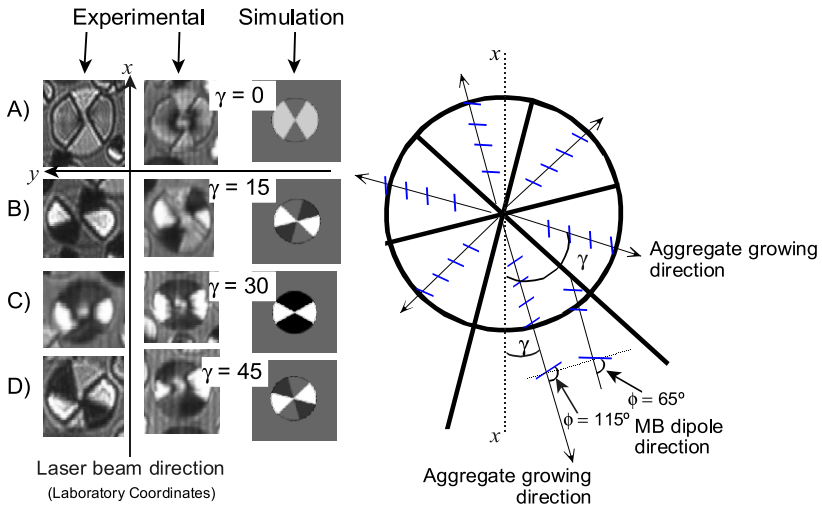

Figure 3.12: Left side: Calculated and experimental domains (BAM pictures) of the DMPA:MB = 5:1 thin film; Right side: Description of the of the characteristics of the circular domain.

main, in the circular domains B, C, and D (see Figure 3.12), the segments placed at the lateral position of the circle are brighter than those located up and down (see Figure 3.12). It is indicative of a strong tilt of the MB dipole with respect to the bisector of the each circular segment (see Figure 3.12, right). Also, domains B and D are specular images. Otherwise, the texture of the domains A is different (see 3.12), showing similar brightness in all segments. In any case, the description of the circular domains is incomplete, because their textures show bright circular central region and, often the anisotropic defect lines, which divided the different wedge-shaped segments, are not straight lines and thus the segments are not of identical size (see Figure 3.3 and 3.12). An additional notorious observation is that the defect lines are marked in the BAM images as black thick lines.

The simulation of all the characteristic of a circular domain is very complex. In a simplified way, the domain textures in Figure 3.12 are simulated by considering that each domain is formed by six identical wedge-shaped segments, their refractivity is only due to the MB absorption, and the MB molecules form lineal aggregates that grow parallel to the bisector direction of each segment. The MB transition dipole moments are rotated an angle ϕ with respect to this direction (see Figure 3.12 right). In the previous section, two possible ϕ values were obtained, $\phi = 65°$and $115°$, for the DMPA:MB = 5:1 monolayer. However, this ϕ angle was not determined with respect to the actual x axis (laboratory coordinates), but assigned to the axis of the linear aggregate, which is coincident with the bisector of each circular segment turned an angle γ with respect to this x axis. Therefore, the angle between the MB transition dipole and the x axis must be $\gamma + \phi$(see Figure 3.12). Since two possible θ values were obtained, the average value $\theta = (65°+ 115°)/2 = 90°$is now used for the simulation of the circular domains.

Simulation of the four domain types is shown in Figure 3.12, where the indicated values are the γ angle of the down circular segment. For the simulation $n_x = n_z = 1{,}43$, and $k_0 = 0{,}3$ (see Supporting Information), were used.

By comparing the calculated images with the experimental domain textures, they both are coincident. We can consider that our simplified model described correctly the preferential orientation of the MB dipoles, at least qualitatively. Moreover, this discussion fits correctly with the previous predictions by the extended dipole model. Domain texture and spectroscopic results confirm the aggregation model proposed here.

Relationship between the domain morphology and the MB aggregation in the mixed DMPA:MB monolayers

During the compression process, a monolayer of pure DMPA forms compact domains without inner texture and/or regular shape,[31,32] indicating that the line tension is quite small. However, at the solid condensed phase, a hexagonal highly-ordered arrangement,[47] is expected as confirmed by means FTIR of DMPA LB films.[48] In such a case, the domain shape is controlled by the competition between the dipolar energy of the domain and the line tension energy.[49] Thus, the repulsive dipolar interaction of the DMPA molecules within a domain favors a large boundary-to-area ratio, by which the electrostatic energy is reduced.[50] In this case, the domain morphology does not entirely correspond to the molecular lattice structure.

Why then do the domains have hexagonal shapes for the DMPA:MB = 1:1 monolayer, while they are circular for the DMPA:MB = 5:1 monolayer? In the DMPA:MB = 1:1 film, a 2D hexagonal network of MB molecules is formed underneath of the DMPA monolayer attached electrostatically to the lipid matrix.[33,34,51,52] This 2D hexagonal network is originated by the DMPA organization and stabilized because of the MB aggregation energy. It has been shown how other macrocations can be electrostatically attached to a DMPA matrix, but neither circular nor hexagonal domains were observed, probably due to the absence of the lateral aggregation between those chromophores. We can argue that the MB aggregation is the main factor which leading the domain structure. The MB aggregation energy increases considerably the domain line tension and it gives rise to the formation of regular

hexagonal domains, in which the domain morphology corresponds perfectly to the hexagonal lattice structure of the DMPA molecules.

In the case of the mixed DMPA:MB = 5:1 monolayer, linear MB aggregates are formed along the radial domain direction because of the small density of MB. With respect to the previous case, the main difference is the absence of a 2D network of MB molecules and therefore the decrease of the domain line tension. The growth of the lineal MB aggregate drives the domain morphology and under these circumstances, the domains adopt a circular line tension to minimize energy.

Another important issue is the origin of the different textures of the inner domain regions. For monolayer of pure amphiphilic, this phenomenon has been related with the different alkyl chain arrangement.[53] However, in our case, the texture of a particular region must be related to areas where all MB molecules have the same orientation, forming 2D hexagonal or linear aggregates. The internal lines of separation between regions with different textures are defect lines in the domain, where the orientation of MB changes discontinuously.[50] However, MB molecules are retained by means of electrostatic interactions to the DMPA lipid matrix, and therefore the defect lines must also respond to specific orientation of the head polar group and alkyl chain of the DMPA.

The central defect and the defect lines of the domains should be present in the central nucleus that starts the growth of the domain. In such a central nucleus, the MB molecules do not probably have a concrete organization, although the growth of the nucleus forming the domain, should be driven by the MB aggregation. This process increases the domain line tension, but the

structure of the domains responds to the arrangement of the molecular net of DMPA, so that it can be said that a 2D monocrystal has been formed.

3.1.4. Conclusions

The study of the cospread DMPA:MB mixed monolayer at the air−water interface, where the MB molecules are retained underneath of the lipid matrix by electrostatic interactions, shows different domain morphology as a function of the MB surface density, being a noticeable effect with respect to those domains formed by the pure DMPA monolayer. Thus, well-defined circular domains are observed for DMPA:MB = 5:1, while hexagonal shape is recorded for those of DMPA:MB = 1:1, and for both cases, all those domains have inner textures with different brightness. These facts are related with the aggregation of the MB molecules upon compression as indicated by the shift of the reflection spectra to shorter wavelengths, such a blue shift being larger for the DMPA:MB = 5:1 monolayer in comparison with that of the mixed 1:1, despite its MB density being smaller. In molecular aggregates the band shift is a function of the aggregation number and the tilt between chromophores. By using the extended dipole model, it is demonstrated that the different blue shift found for the two mixed monolayers corresponds to the formation of a 2D hexagonal network of MB molecules underneath the DMPA monolayer in the mixed DMPA:MB = 1:1 film, while to a infinite lineal aggregates for the 5:1 monolayer. The experimental domains textures have been simulated in the basis of the Fresnel equations for biaxial anisotropic materials on isotropic substrate, which permits us to calculate the refractivity of the

film. The results obtained fit in an approximately way with the predictions of the extended dipole model, that is, hexagonal domains of the DMPA:MB = 1:1 are the result of the formation of the 2D hexagonal network, while the circular domains of the cospread 5:1 mixed monolayer are produced by the infinite lineal aggregation, during the compression process at the air−water interface.

3.1.5. Supporting Information: Reflection of an Anisotropic Thin Film on Isotropic Substrate

The anisotropic thin film is assumed to be a biaxial material with complex refractive indices (N_{1x}, N_{1y}, N_{1z}). The reflection incidence angle, α_0, and transmission angle, α_2, of multiply reflected waves (Figure 3.13) are constants and related by $n_0 \sin(\alpha_0) = n_2 \sin(\alpha_2)$, where $n_0 = 1$ (air) and $n_2 = 1{,}333$ (water) show the real refractive indices of the ambient and substrate, respectively.

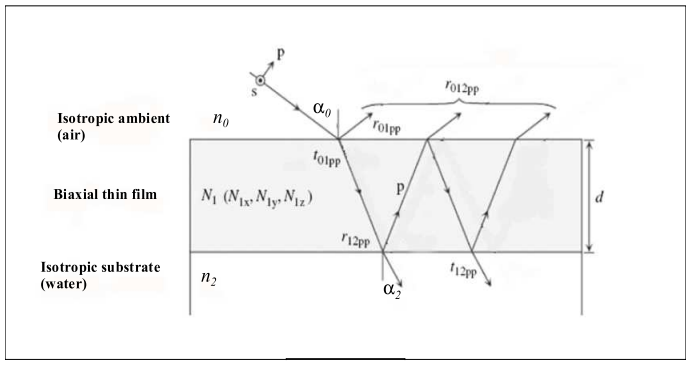

Figure 3.13: Reflection of an Anisotropic Thin Film on Isotropic Substrate

In BAM microscopy the incident light is p-polarized and when the analyzer is set to 0°, only the p component of the reflection is observed. In this case, the light reflection at the ambient/film interface can be expressed as follows (Fujiwara, H. *Spectroscopic Ellipsometry. Principles and Applications*; John Wiley and Sons: Chichester, England, 2007; pp. 224-)

$$r_{01PP} = \frac{N_x N_z \cos(\alpha_0) - n_0(N_Z^2 - n_0^2 \sin(\alpha_0^2))^{1/2}}{N_x N_z \cos(\alpha_0) - n_0(N_Z^2 + n_0^2 \sin(\alpha_0^2))^{1/2}} \tag{3.8}$$

$$r_{12PP} = \frac{n_2(N_x^2 - n_2^2 \sin(\alpha_2)^2)^{1/2} - N_x N_z \cos(\alpha_2)}{n_2(N_x^2 - n_2^2 \sin(\alpha_2)^2)^{1/2} + N_x N_z \cos(\alpha_2)} \tag{3.9}$$

The total reflection coefficient for p-polarization

$$r_{012PP} = \frac{r_{01PP} + r_{12PP} \cdot \exp(-i2\beta_P)}{1 + r_{01PP} \cdot r_{12PP} \cdot \exp(-i2\beta_P)} \tag{3.10}$$

where

$$\beta_P = \frac{2\pi d}{\lambda} \frac{N_x}{N_z} (N_x^2 - n_0^2 \cdot \sin(\alpha_0)_2)^{1/2} \tag{3.11}$$

being $\lambda = 532$ nm the wavelength of the laser beam and d the thickness of the biaxial thin film. The reflectances for p-polarized waves are obtained by

$$R_P = |r_{012PP}|^2 \tag{3.12}$$

The complex refractive indices of anisotropic materials along the x, y, and z axes, and are given by $N_x = n_x - ik_x$, $N_y = n_y - ik_y$, and $N_z = n_z - ik_z$, respectively, where n_i and k_i are the real and imaginary parts of the refractive index. As only the p-component of the reflection is analyzed, the N_y component does not affect to the final result. On the other hand, the absorption coefficients can be expressed by means of

$$k_x = k_0 \cdot \sin(\theta)^2 \cos(\phi)^2 \tag{3.13}$$

$$k_z = k_0 \cdot \cos(\theta)^2 \tag{3.14}$$

where the angles θ (52°) and ϕ are those defined in Figure 3.8 and α_0 = 53,15 °(Brewster angle). To simulate the reflectivity, several set of values for the other unknown parameters can be used. For example, the reflectivity of the hexagonal domains can be almost totally reproduced by the next set of parameters: $n_x = n_z$ = 1,5, d = 3 nm (thickness of the film including DMPA and MB), and k_0 = 0,42. In such a way, the reflectivity can be exclusively obtained as a function of ϕ. Figure 3.14 (red line) plots R_P versus ϕ with $n_x = n_z$ = 1,5, d = 3 nm and k_0 = 0,42.

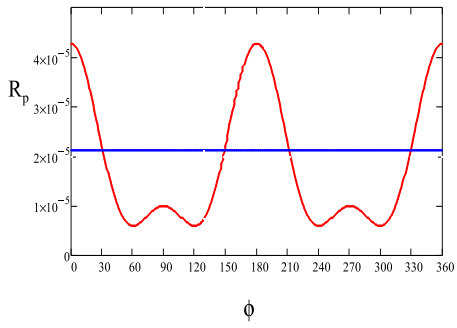

Figure 3.14: R_P versus ϕ

Figure 3.14 shows how the changes of reflectivity for ϕ values ranged between 45°-135°and 225°-315°are small in comparison with the overall variation in the reflectivity. For increase the contrast and visibility of the image, the BAM instrument has as an option the auto set gray level. The intensity of

an image in gray levels is measured in a scale from 255 (white) to 0 (black). When the auto set option is clicked, the gray level is rescaled by increasing the exposure time to the light in such a way that only the reflectivity under the threshold value can be discerned, being the maximum possible value (255) that reflectivity over the threshold value. The threshold value of reflectivity must be simulated as an additional unknown parameter. For the simulation of the hexagonal domains described in the manuscript $R_P(\text{threshold}) = 2{,}13 \cdot 10^{-5}$ (blue line in Figure 3.14) has been used. The relative reflection (R_{Rel}) of each domain´s segment is determined by means of:

$$R_{Rel} = \frac{R_P}{2{,}13}\frac{255}{10^{-5}} \; \{for R_P < 2{,}13 \cdot 10^{-5}\} \tag{3.15}$$

$$R_{Rel} = 255 \; \{for R_P \geq 2{,}13 \cdot 10^{-5}\} \tag{3.16}$$

In Figure 3.15 R_{Rel} is plotted versus ϕ

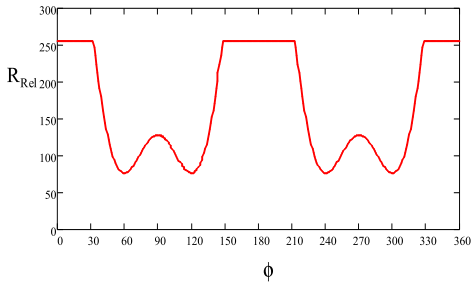

Figure 3.15: R_{Re1} versus ϕ

In the hexagonal domain $\gamma = \phi$ (see above). For the simulation of the domain textures, and known the γ angle of each segment of the hexagon,

the R_{Re1} value is obtained directly from the Figure 3.15. In Figure 3.16, some examples where the gray level is assigned to some domain segment as a function of its rotation angle γ, are shown.

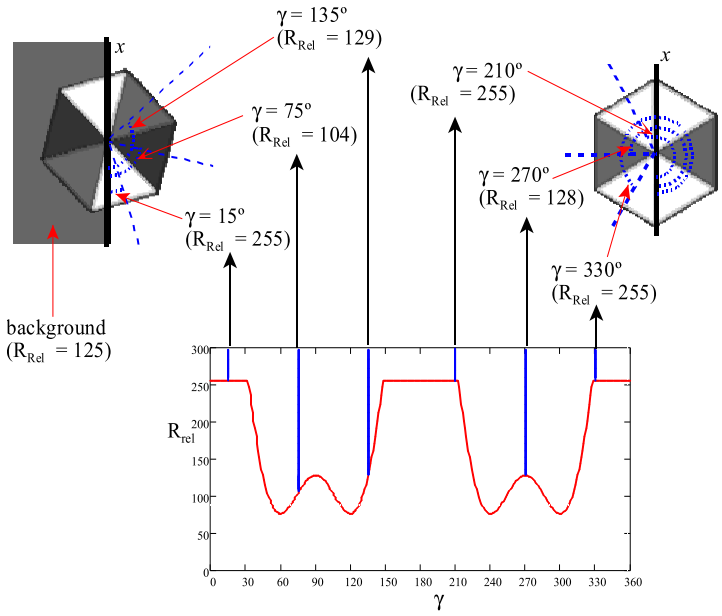

Figure 3.16: Gray level and γ angle

Different set of parameters must be used for the simulation of the circular domains. Thus, a set of parameters that well reproduces the reflectivity of the domains, is: $n_x = n_z = 1{,}43$, d = 3 nm, and $k_0 = 0{,}3$, being the remaining parameters as for the previous case. The Figure 3.17 shows the plot of R_P vs. ϕ, for the previous parameters.

As commented before, the threshold values of reflectivity must be fit to improve the contrast and visibility of the BAM images. For the simulation of the circular domains, $R_p(\text{threshold}) = 1{,}13 \cdot 10^{-5}$ (blue line in Figure 3.17). Thus, the relative reflection (R_{Rel}) of each domain´s segment is determined

by

$$R_{Rel} = \frac{R_P}{1{,}13\,10^{-5}} \frac{255}{} \{for R_P < 1{,}13 \cdot 10^{-5}\} \tag{3.17}$$

$$R_{Rel} = 255\,\{for R_P \geq 1{,}13 \cdot 10^{-5}\} \tag{3.18}$$

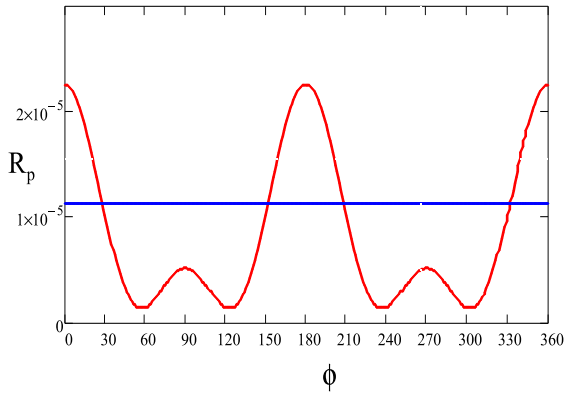

Figure 3.17: R_P vs. ϕ

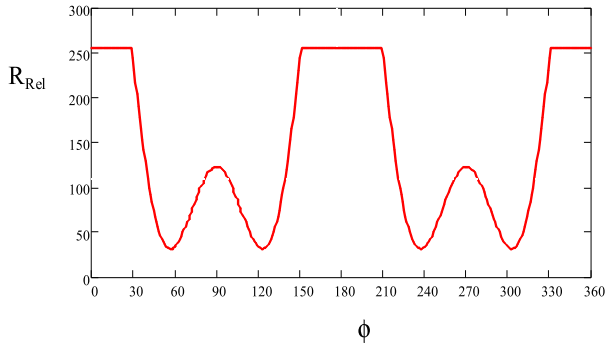

Figure 3.18: $R_{Rel} vs \phi$

Otherwise, for the hexagonal domains the angle between the x axis and the bisector of each one of the six segments of the domain, γ, coincides with

the ϕ angle (see Fig. 3.11). However, for the circular domains these angles do not coincide. In this last case, the linear aggregate grows parallel to the bisector of each circular segment. Thus, γ coincides with the angle between the x axis (laboratory coordinates) and the axis of the linear aggregate (see Fig. 3.12 above).

Furthermore, the extended dipole model predicts angles of 65°or 115°with respect to the axis of the linear aggregate for the MB dipole moment. Therefore, the angle between the MB dipole moment and the x axis must be $(\gamma + 65°)$ or $(\gamma + 115°)$. Both possibilities are equivalent, so an average value, i.e., $(\gamma + 90°)$, has been used to simulate the domain textures. Figure 3.19 shows the relative reflectivity (R_{Rel}) for $(\gamma + 90°)$ vs the tilt angle of each circular segment, γ. As can be seen, the lowest reflectivities are for $\gamma = 33°$,

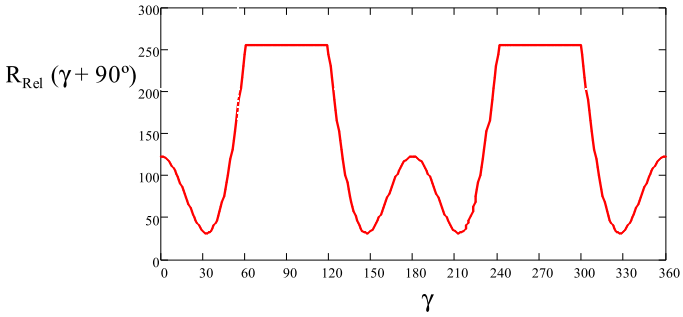

Figure 3.19: (R_{Rel}) for $(\gamma + 90°)$ versus γ

147°, 213°and 327°. Following, as before, the reflectivity obtained in Figure 3.19, scaled between 0-255, is used to simulate the gray level of the different segments of the circular domains as a function of its rotation angle γ.

Acknowledgments

We thank the Spanish CICYT for financial support of this research in the framework of Project CTQ2007-64474/BQU (FEDER A), and also thank the Junta de Andalucía (Consejería de Innovación, Ciencia y Empresa) for special financial support P06-FQM-01698 and P08-FQM-4011. M. Pérez-Morales thanks the Junta de Andalucía for a postdoctoral contract and J. J. Giner-Casares thanks the Ministerio de Ciencia e Innovación for a pre-doctoral contract (Formación de Profesorado Universitario, FPU).

References

1. Roberts, G. G. *Langmuir-Blogett Films;* Plenum Publ. Co.: New York, 1990.

2. Ulman, A. *An Introduction to Ultrathin Organic Films from Lagmuir-Blodgett to Self-Assembly;* Academic Press: San Diego, 1991.

3. Kaganer, V. M.; Möhwald, H.; Dutta, P. *Rev. Mod. Phys.* **1999,** *71,* 779.

4. Sasai, R.; Iyi, N.; Fujita, T.; López Arbeloa, F.; Martínez Martínez, V.; Takagi, K.; Itoh, H. *Langmuir* **2004,** *20,* 4715.

5. Bujdak, J.; Iyi, N. *J. Phys. Chem. B* **2006,** *110,* 2180-2186.

6. Ghanadzadeh, A.; Zanjanchi, M. *Spectrochim. Acta, Part A* **2001,** *57,* 1865.

7. Pérez-Morales, M.; Pedrosa, J. M.; Martín-Romero, M. T.; Möbius, D.; Camacho, L. *J. Phys. Chem. B* **2004,** *108,* 4457-4465.

8. Orrit, M.; Möbius, D.; Lehmann, U.; Meyer, H. *J. Chem. Phys.* **1986,** *85,* 4966.

9. Kawai, T.; Umemura, J.; Takenaka, T. *Langmuir* **1989,** *5,* 1378.

10. Ahuja, R. C.; Möbius, D. *Langmuir* **1992,** *8,* 1136.

11. Pedrosa, J. M.; Martín-Romero, M. T.; Camacho, L.; Möbius, D. *J. Phys. Chem. B* **2002,** *106,* 2583-2591.

12. Hönig, D.; Möbius, D. *J. Phys. Chem.* **1991,** *95,* 4590.

13. Hönig, D.; Overbeck, G.; Möbius, D. *Adv. Mater.* **1992,** *4,* 419.

14. Johann, R.; Vollhardt, D. *Mat. Sci. Eng. C* **1999,** *8-9,* 35-42.

15. Krasteva,Ñ.; Vollhardt, D. *Colloids Surf. A: Physicochem. Eng. Aspects* **2000,** *171,* 49-57.

16. Weidemann, G.; Gehlert, U.; Vollhardt, D. *Langmuir* **1995,** *11,* 864.

17. Vollhardt, D.; Melzer, V. *J. Phys. Chem.* **1997,** *101,* 3370.

18. Overbeck, G. A.; Hönig, D.; Möbius, D. *Thin Solid Films* **1994,** *242,* 213-219.

19. Weidemann, G.; Vollhardt, D. *Langmuir* **1996,** *12,* 5114-5119.

20. Weidemann, G.; Brezesinski, G.; Vollhardt, D.; Möhwald, H. *J. Phys. Chem. B* **1998,** *102,* 1224-1228.

21. Ignés-Mullol, J.; Claret, J.; Reigada, R.; Sagués, F. *Phys. Report* **2007,** *448,* 163.

22. Bergmann, K.; O'Konski, C. T. *J. Phys. Chem.* **1963,** *67,* 2169.

23. Heger, D.; Jirkovsky, J.; Klan, P. *J. Phys. Chem. A* **2005,** *109,* 6702-6709.

24. Jacobs, K. Y.; Schoonheydt, R. A. *J. Coll. Int. Sci.* **1999,** *220,* 103-111.

25. Fujita, K.; Taniguchi, K.; Ohno, H. *Talanta* **2005,** *65,* 1066-1070.

26. Ohline, S. M.; Lee, S.; Williams, S.; Chang, C. *Chem. Phys. Lett.* **2001,** *346,* 9-15.

27. Kobayashi, H.; Takahashi, M.; Kotani, M. *Chem. Phys. Lett.* **2001,** *349,* 376-382.

28. Li, F.; Zare, R. N. *J. Phys. Chem. B* **2005,** *109,* 3330-3333.

29. Grüniger, H.; Möbius, D.; Meyer, H. *J. Chem. Phys.* **1983,** *79,* 3701.

30. Prieto, I.; Fernández, A. J.; Muñoz, E.; Martín, M. T.; Camacho, L. *Thin Solid Films* **1996,** *284-285,* 162-165.

31. Lösche, M.; Duwe, H. P.; Möhwald, H. *J. Coll. Int. Sci.* **1988,** *126,* 432.

32. Pérez-Morales, M.; Pedrosa, J. M.; Muñoz, E.; Martín-Romero, M. T.; Möbius, D.; Camacho, L. *Thin Solid Films* **2005,** *488,* 247.

33. Ahuja, R. C.; Caruso, P. L.; Möbius, D.; Wildburg, G.; Ringsdorf, H.; Philp, D.; Preece, J. A.; Stoddart, J. F. *Langmuir* **1993,** *9,* 1534.

34. Martín, M. T.; Prieto, I.; Camacho, L.; Möbius, D. *Langmuir* **1996,** *12,* 6554.

35. Parkanyi, C.; Boniface, C.; Aaron, J. J.; Maafi, M. *Spectrochim. Acta, Part A* **1993,** *49,* 1715.

36. Pedrosa, J. M.; Dooling, C. M.; Richardson, T. H.; Hyde, R. H.; Hunter, C. A.; Martín-Romero, M. T.; Camacho, L. *Langmuir* **2002,** *18,* 7594.

37. de Miguel, G.; Martín-Romero, M. T.; Pedrosa, J. M.; Muñoz, E.; Pérez-Morales, M.; Richardson, T. H.; Camacho, L. *Phys. Chem. Chem. Phys.* **2008,** *10,* 1569-1576.

38. Kuhn, H.; Försterling, H. D. *Principles of Physical Chemistry;* John Wiley and Sons, New York, 2000.

39. Antonov, L.; Gergov, V.; Petrov, V.; Kubista, M.; Nygren, J. *Talanta* **1999,** *49,* 99.

40. *Electronic Processes in Organic Crystals and Polymers;* Oxford Science Publications, New York: 1999.

41. Hobayashi, T. *J-Aggregates;* World Scientific: Singapore: 1996.

42. Martín, M. T.; Möbius, D. *Thin Solid Film* **1996,** *284/285,* 663.

43. Czikkely, V.; Försterling, H. D.; Kuhn, H. *Chem. Phys. Lett.* **1970,** *6,* 11.

44. Czikkely, V.; Försterling, H. D.; Kuhn, H. *Chem. Phys. Lett.* **1970,** *6,* 207.

45. Mathcad., Mathsoft Inc.: 2003.

46. Fujiwara, H. *Spectroscopic Ellipsometry. Principles and Applications;* John Wiley and Sons: Chichester, England, 2007.

47. Möhwald, H. Phospholipid Monolayers. In *Handbook of Biological Physics*; Lipkowsky, R.; Sackmann, E., Eds.; Elsevier Science: Amsterdam, 1995.

48. Fernández, A. J.; Ruiz, J. J.; Camacho, L.; Martín, M. T.; Muñoz, E. *J. Phys. Chem. B* **2000,** *104,* 5573.

49. Thirumoorthy, K.; Nandi,Ñ.; Vollhardt, D. *J. Phys. Chem. B* **2005,** *109,* 10820.

50. Johann, R.; Vollhardt, D.; Möhwald, H. *Coll. Polym. Sci.* **2000,** *278,* 104.

51. Giner-Casares, J. J.; Pérez-Morales, M.; Bolink, H.; Muñoz, E.; de Miguel, G.; Martín-Romero, M. T.; Camacho, L. *J. Coll. Int. Sci.* **2007,** *315,* 278.

52. Prieto, I.; Martín-Romero, M. T.; Camacho, L.; Möbius, D. *Langmuir* **1998,** *14,* 4175.

53. Johann, R.; Brezesinski, G.; Vollhardt, D.; Möhwald, H. *J. Phys. Chem. B* **2001,** *105,* 2957.

3.2. Molecular Organization of a Water-Insoluble iridium (III) Complex in Mixed Monolayers

In this work, organized mixed monolayers containing a cationic water-insoluble iridium (III) complex, Ir-dye, $[Ir(ppy)_2(tmphen)]PF_6$, (tmphen = 3,4,7,8-tetramethyl-1,10-phenanthroline, and ppy = 2-phenylpyridine), and an anionic lipid matrix, DMPA, dimyristoyl-phosphatidic acid, with different molar proportions, were formed by the co-spreading method at the air−water interface. The presence of the dye at the interface, as well as the molecular organization of the mixed films, is deduced from surface techniques such as $\pi - A$ isotherms, Brewster angle microscopy (BAM) and reflection spectroscopy. The results obtained remark the formation of an equimolar mixed film, Ir-dye/DMPA = 1:1. BAM images reveal a whole homogeneous monolayer, with gradually increasing reflectivity along the compression process up to reaching the collapse of this equimolecular monolayer at $\pi \sim$37 mN/m. Increasing the molar ratio of DMPA in the mixture, the excess of lipid molecules organizes themselves forming dark flower-like domains of pure DMPA at high surface pressures, coexisting with the mixed Ir-dye/DMPA = 1:1 monolayer. On the other hand, unstable mixed monolayers are obtained by using an initial dye surface concentration higher than the equimolecular one. These mixed Langmuir monolayers have been successfully transferred onto solid substrates by the LB (Langmuir-Blodgett) technique.

Paper published in *J. Coll. Int. Sci.*, 2007, 315, 278-286

3.2.1. Introduction

Transition organometallic compounds are under active research due to their large potential for new photophysical and photochemical applications.[1,2] Specifically, organometallic triplet emitters, such as Ir(III) and Pt(II) complexes, are of particular interest because of their promising use as photosensitizers in catalytic photoinduced hydrogen production,[3] oxygen-sensing materials,[4] and in electroluminescent devices, OLEDs[5–8] and LECs,[9–12] as well. In these last devices, when using phosphorescent dyes, the triplet exciton contributes to light emission and the efficiency is greatly improved compared with that of conventional fluorescent devices, which use the emission from only the single exciton. Therefore, it is highly desirable to control the spectroscopic properties of these compounds, as a function of their molecular organization in the typical thin film configuration in which they are used.

Furthermore, since the deposition of this kind of complexes on semiconductor surfaces is needed, it is also fundamental the deposition technique. Among the different available deposition methods, e.g. spin-coating, drop-casting or thermal deposition, the Langmuir−Blodgett technique offers the possibility of arranging molecules and preparing highly-ordered ultrathin multilayers, which are expected to have enhanced their energy and transport transfer properties.

The modification of solid electrodes with metal complexes has been carried out by several methods.[13–15] For example, Goldenberg, by using the LB method, demonstrated the influence of the film thickness and the molecular organization of the electroactive substance on its electrochemical proper-

ties.[15] In this way, Santos et al. demonstrated the electrocatalytic behavior of an electrode, modified with a mixed ruthenium complex/lipid multilayer, in the presence of benzyl alcohol.[16] In this research field, our group has recently demonstrated the mediator and catalytic properties of electrodes modified with electrodeposited Ni-complexes on the redox behavior of certain LB films,[17] and the reversible storage of molecular dyoxigen in a Co-complex modified electrode.[18]

Different strategies to form monolayers containing transition organometallic dyes have been explored. A few reports concerning LB films from pure complexes can be found in the literature, mainly related to amphiphilic Ru(II) derivatives.[19,20] Special attention has to be paid to the work of Yam et al.,[21] who proved the fabrication of an operative OLED, which was built by LB multilayers containing an amphiphilic rhenium complex. In the case of water-soluble metal complexes, the most usual way to retain these molecules at the interface is by electrostatic interactions with a charged lipid matrix, either by the co-spreading[22,23] or adsorption[24] methods. Furthermore, the preparation of mixed films by co-spreading has been used to control the aggregation of certain Ru(II)[16,25,26] and Ir(III)[27] complexes that are able to form monolayer in absence of lipids.

Because of the hydrophobic character of the Ir(III)-dye investigated in this work, it does not form monolayers by itself at the air−water interface. The objective of this research was to achieve homogeneous Ir-dye films at the air−water interface (Langmuir monolayers), capable of being transferred by the LB method onto semiconductor surfaces for further applications in electroluminescent devices, modified electrodes, etc. For such purpose, the

phospholipid DMPA was chosen as a lipid matrix to organize the metallic complex at the air−water interface, by electrostatic interactions between both charged compounds.

3.2.2. Experimental

Materials

The Ir-dye complex used in this work, namely, $[Ir(ppy)_2(tmphen)]PF_6$, (tmphen = 3,4,7,8-tetramethyl-1,10-phenanthroline, and ppy = 2-phenylpyridine), was synthesized and kindly given by the research group of Dr. H. Bolink (Molecular Science Institute, University of Valencia). Dimyristoyl-phosphatidic acid (DMPA) was purchased from Sigma Chemical Co. and used as received. The molecular structures of Ir-dye and DMPA are shown in Figure 3.20. A mixture of chloroform and methanol (3:1 v/v) was used as cospreading solvent. All pure solvents were obtained from Aldrich (Germany), except methanol from Panreac (Spain). $IrCl_3 \cdot nH_2O$ was obtained from Pressure Chemical. Ultrapure water, produced by a Millipore Milli-Q unit, pre-treated by a Millipore reverse osmosis system (resistivity = 18.2 $M\Omega \cdot cm$) was used as a subphase. The subphase temperature was 21 °C and pH = 5.7.

Methods

Two different models of Nima troughs (Nima Technology, Coventry, England) were used in this work, both provided with a Wilhelmy type dynamometric system using a strip of filter paper: a NIMA 611D with one moving barrier (total area $\sim$ 505 cm^2) for transfer processes and reflection spectra,

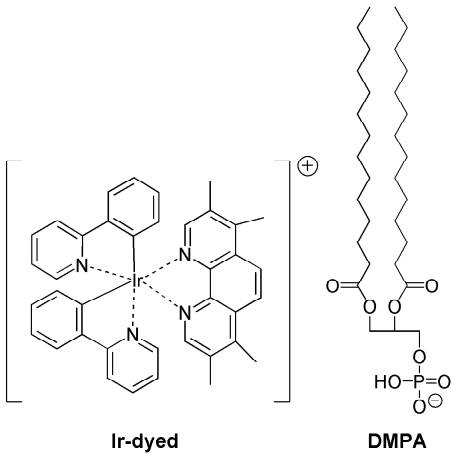

Figure 3.20: Molecular structures of the Ir-dye metal complex and DMPA.

and a NIMA 601, equipped with two symmetrical barriers placed on an antivibration table (total area $\sim$ 600 cm^2) to record BAM images.

Images via Brewster angle microscopy (BAM) were obtained with a I-Elli2000 apparatus (supplied by Nanofilm Technologies, Göttingen, Germany) using a Nd:YAG diode laser, which can be recorded with a lateral resolution of 2 μm. The image processing procedure included a geometrical correction of the image, as well as a filtering operation to reduce interference fringes and noise. Furthermore, the brightness of each image was scaled to improve contrast. The microscope and the film balance were located on a table with vibration isolation (antivibration system MOD-2 S, Halcyonics, Göttingen, Germany) in a large class 100 clean room.

UV-visible reflection spectra at normal incidence as the difference in reflectivity (ΔR) of the dye film-covered water surface and the bare surface were obtained with a Nanofilm Surface Analysis spectrometer (RefSPEC^2, supplied by Nanofilm).

UV-visible electronic absorption spectra of the transferred LB films were recorded locating the support directly in the light path on a Cary 100 Bio UV-visible spectrophotometer.

FTIR measurements were performed on a Mattson Research Series instrument equipped with a DTGS detector. The background spectrum was taken for a bare support of the same material. For the reflection spectra, ITO electrodes were used as substrates. The measurements $\Delta R/R_0 = (R - R_0)/R_0$ (where R_0 is the reflection of the bare electrode), were carried out at an external reflection configuration, p polarized within the incident plane at a grazing angle of 70° degrees. Drop-cast films were prepared by spreading Ir-dye or Ir-dye/DMPA chloroform-methanol (3:1 v/v) solutions onto the solid substrate. In all cases, the spectra were the accumulation of 1024 scans, and recorded with a 4 cm^{-1} resolution.

3.2.3. Results and Discussion

Surface Pressure-Area Isotherms

Mixed monolayers of Ir-dye/DMPA, from a chloroform-methanol (3:1 v/v) solution in different molar ratios (1:0.75, 1:1, 1:2, 1:3, and 1:5), were prepared at the air−water interface by the co-spreading method.[29] Previously, the same monolayers were prepared by using pure chloroform as co-spreading solvent, which led to poor reproducible isotherms in all cases.

The presence of the dye at the interface is evident, since the $\pi - A$ isotherms of the mixed films differ considerably from that of pure DMPA (Fig. 3.21, all isotherms are expressed per DMPA molecule), in which a noticeable

expansion can be observed. Thus, the expansion increases as the dye fraction in the film is raised.

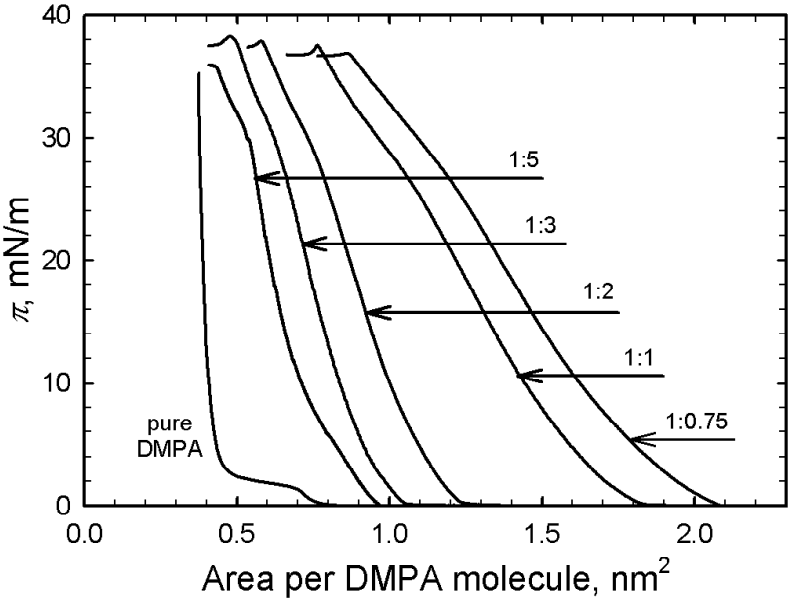

Figure 3.21: $\pi - A$ isotherms of mixtures of Ir-dye/DMPA with different molar ratios on pure water. The isotherm of pure DMPA is also plotted for comparison.

For these mixed films, two phenomena can be described. First, a new slope at high surface pressures is detected, which takes place at slightly different π depending on the mixture ratio, and ranges from ca. $\sim$ 26 mN/m to $\sim$ 30 mN/m for the mixed 1:0.75 and 1:5 monolayers, respectively. Second, a spontaneous decrease of the surface area is observed at around 37 mN/m, remaining the pressure constant, which indicates the collapse of the monolayer. For the Ir-dye/DMPA = 1:5 film, this phenomenon occurs at a lightly lower surface pressure. As previously commented, the pure Ir-dye does not form monolayer by itself, and yellow dye-islands are observed, to the naked eye, floating on the water surface when an Ir-dye organic solution is spread.

Thus, the DMPA matrix seems to organize the dye molecules at the interface and, considering their respective charges, it can be assumed that the DMPA polar heads bind electrostatically the Ir(III) complex.

To investigate the stability of the mixed monolayers formed at the air−water interface, successive compression-expansion cycles of the mixed films were carried out. In all cases, provided the collapse of the film is avoided, small hysteresis during the cycles is found, which decreases when the fraction of DMPA in the film increases, being almost negligible for the Ir-dye/DMPA = 1:5 system (data not shown). For instance, at π = 20 mN/m, a loss of area $\sim$ 2.4 % and 7 % has been calculated for Ir-dye/DMPA = 1:5 and 1:0.75 films, respectively. The isotherms of the different mixtures studied are very reproducible, except for the Ir-dye/DMPA = 1:0.75 film, which also shows poor stability. Moreover, co-spread Ir-dye/DMPA mixtures containing lower fractions of DMPA did not form monolayers at the air−water interface.

Brewster Angle Microscopy

The morphology of the mixed Ir-dye/DMPA films was directly visualized by BAM, simultaneously to the $\pi - A$ isotherm registering. Fig. 3.22 shows the images obtained at several increasing values of π, and recorded under continuous compression of the Ir-dye/DMPA = 1:1 (Fig. 3.22, up row) and 1:2 (Fig. 3.22, bottom row) monolayers at the air−water interface.

In the case of the 1:1 mixed monolayer, the film is homogeneous over the whole range of surface pressures, i.e., from 0 mN/m up to the collapse ($\sim$ 38mN/m), and the reflectivity of the interface increases gradually as the

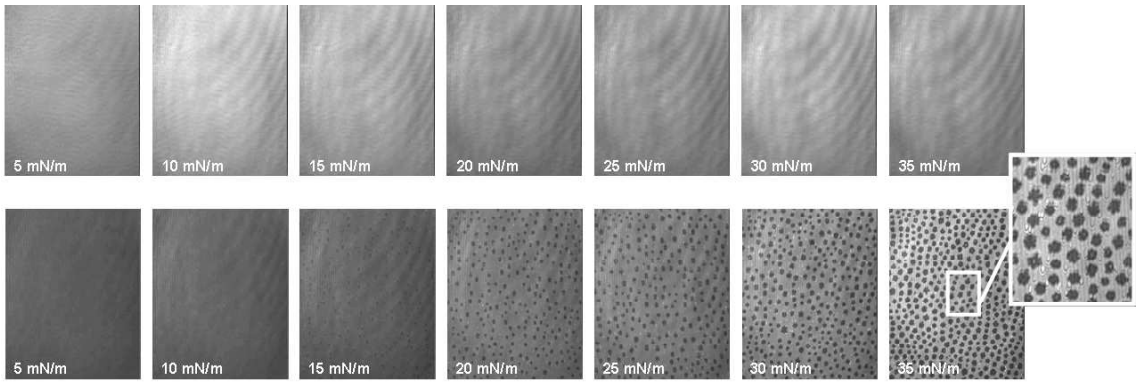

Figure 3.22: BAM images recorded simultaneously to the compression of the mixed monolayers: Ir-dye/DMPA = 1:1 (up row) and Ir-dye/DMPA = 1:2 (bottom row). Image size: 430 μm width.

monolayer is compressed.

In contrast, the films containing a lower fraction of Ir-dye (molar ratios 1:2, 1:3 and 1:5) behave differently. Thus, for the Ir-dye/DMPA = 1:2 mixed monolayer, a homogeneous film is observed until a surface pressure of 15 mN/m is achieved. Then, spontaneous small domains with lower brightness than the surrounding area are formed along the whole surface. Upon further compression, both the density and slightly the size of these dark domains become higher, up to the collapse of the film (see images from 15 mN/m to 35 mN/m). Comparing these different mixed films, bigger dark domains are detected as the fraction of DMPA increases, and also more defined flower-like domains are observed (images not shown). In fact, the low reflectivity of the dark domains could be indicative of the absence of the iridium complex in them. Consequently, the coexistence of these two phases (dark domains and bright surrounding area), may be related to pure DMPA and Ir-dye/DMPA regions, respectively. In this system, DMPA molecules are homogeneously

distributed over the whole surface up to reaching a certain surface pressure ($\sim$ 15 mN/m), from which dark domains appear. From this critical surface pressure, DMPA molecules organize in two different phases, in similarity to the pure DMPA monolayer,[30] that coexist in equilibrium (liquid-expanded and liquid-condensed phases), although in this mixed system, the more condensed phase corresponds to dark domains, while the more expanded phase corresponds to the bright area.

Reflection Spectroscopy at the Air−Water Interface

The presence of the Ir-dye in the mixed monolayers (molar ratios 1:0.75 ... 1:5) is evidenced by the measurement of the reflection spectra at the air−water interface. The different electronic transitions of the Ir-dye in the mixed Langmuir monolayers can be assigned by comparison with the organic solution spectrum (Fig. 3.23b). Two main bands in the UV region at $\lambda \sim$ 255 and 273 nm are observed, with extinction coefficients ε_{255} = 6,36 x 10^4 and ε_{273} = 7 x 10^4 L·mol^{-1}·cm^{-1}, respectively. The band at 255 nm has been assigned to the ligand centered $\pi - \pi^*$ transition of the ppy groups, while the peak at around 273 nm appears as a result of $\pi - \pi^*$ transitions of both ppy and tmphen ligands.[31,32] Also, two weak shoulders can be detected at around 350 and 420 nm. The first one has been assigned to the metal-to-ligand charge transfer ^{1}MLCT transition,[33] while the weak shoulder located in the visible region of the spectrum to the optical absorption band of the ^{3}MLCT.[34] Although this latter transition is essentially spin-forbidden, strong spin-orbit coupling on Ir(III) gives weak absorption.

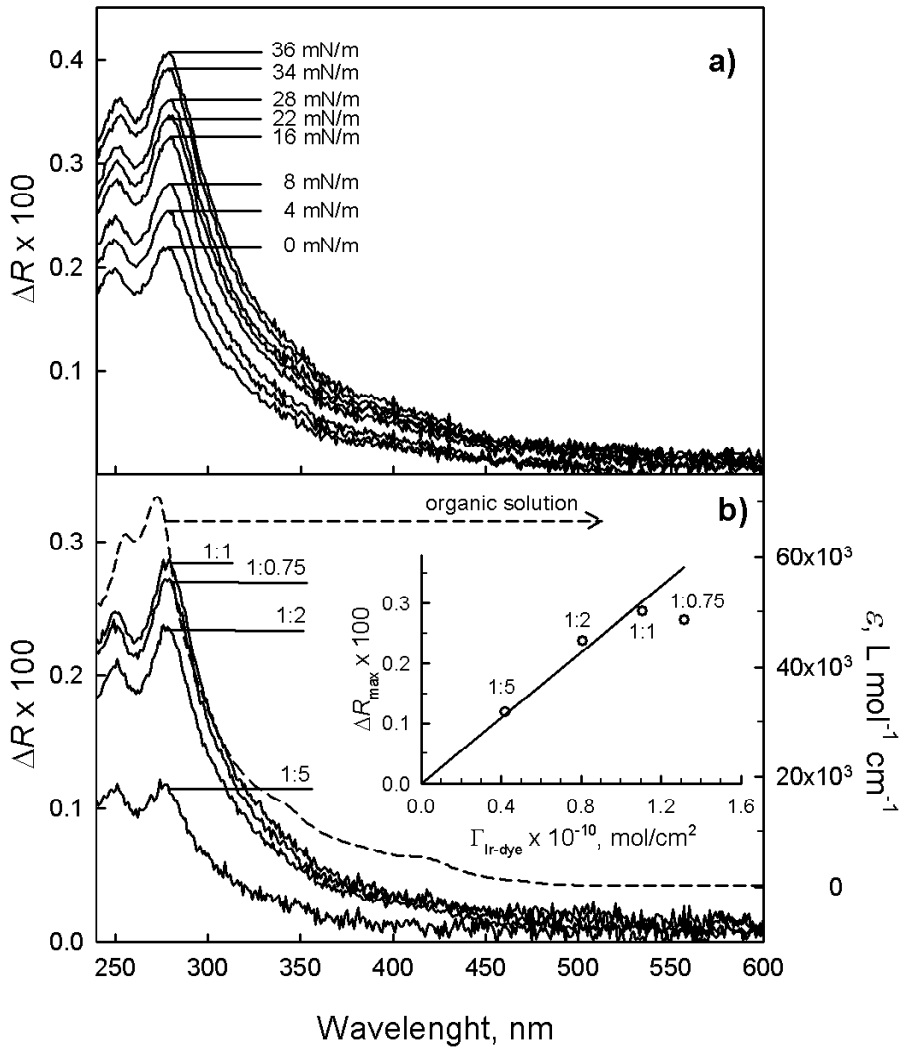

Figure 3.23: a) Reflection spectra of an Ir-dye/DMPA = 1:1 monolayer at different surface pressures; b) Absorption spectrum of the Ir-dye organic solution (chloroform-methanol 3:1, v/v) and reflection spectra of Ir-dye/DMPA = 1:5, 1:2, 1:1 and 1:0.75 monolayers at the air−water interface, measured at π = 8 mN/m. Inset: ΔR vs Ir-dye surface concentration (circles) and its corresponding linear regression (solid line).

A series of reflection spectra at different surface pressures were measured during the compression, for each co-spread mixture. In all cases, higher values of ΔR are detected as the film is compressed, which is indicative of the increasing surface density of the dye at the water surface. As an example, Fig. 3.23a shows a complete series of reflection spectra recorded during the compression of a mixed Ir-dye/DMPA = 1:1 monolayer.

In Fig. 3.23b, the reflection spectra obtained for different mixed Ir-dye/DMPA monolayers, measured at a constant surface pressure (π = 8 mN/m), are compared. As expected, higher the fraction of dye in the co-spread mixture, higher the reflection spectrum, except for the mixed 1:0.75 film. For all the mixtures studied, slight red shifts ($\Delta\lambda$ ~3 nm) of both absorption bands are observed when the film is compressed until high surface pressures (~ 30 mN/m). In the case of the 1:5 molar ratio film, red broader bands, instead of shifted ones, are detected in the condensed phase.

For low values of absorption, the reflection ΔR has been shown to be proportional to the surface concentration of the dye, and is given in a reasonable approximation by[35]

$$\Delta R = 2{,}303 \cdot 10^3 \, \Gamma_{Ir-dye} \, f_{orient} \, \varepsilon \, \sqrt{R_S} \tag{3.19}$$

where Γ_{Ir-dye} is the surface concentration of Ir-dye in mol cm^{-2}, R_S = 0.02 the reflectivity of the air−water interface at normal incidence,[36] ε the extinction coefficient given as L mol^{-1} cm^{-1}, and f_{orient} is a numerical factor that takes into account the particular orientation of the transition moment of the dye in solution, as compared to the monolayer at the air−water interface.[37]

The transition moment of the MLCT in the Ir(III) unit is spatially symmetrically distributed and, therefore, the orientation factor is equal to unity for all orientations of the complex.[22,23] Nevertheless, the visible ^{3}MLCT band at 420 nm is almost negligible in the reflection spectra at the air−water interface for the whole range of molar ratios studied, and only ligand centered $\pi - \pi^*$ bands are clearly detected. Thus, in the case of preferred orientation of the complex with respect to the water surface, the transition dipole of the ligand is also oriented and $f_{orient} \neq 1$. Unfortunately, for the Ir-dye complex investigated in this work, it is not possible to carry out an exhaustive analysis of the orientation of the ligands through their UV peaks, since the absorption of both ppy and tmphen ligands contributes to the band at $\sim$ 273 nm, and the band at $\sim$ 255 nm is due to the absorption of two differently oriented ppy ligands. Consequently, owing to the complex nature of the absorption bands, it would not be possible to explain the physical meaning of forient obtained from Eq. 3.2.3.

Inset in Fig. 3.23b plots the maximum value of reflection (at $\lambda = 278$ nm) vs the theoretical Ir-dye surface concentration (Γ_{Ir-dye}) at 8 mN/m (circles), assuming no loss of dye molecules. These values are obtained from the surface concentration of DMPA (from the $\pi - A$ isotherms) and the ratio of Ir-dye in each mixture. Thus, $\Gamma_{Ir-dye} = 4.2 \cdot 10^{-11}$, $8 \cdot 10^{-11}$, $1.1 \cdot 10^{-10}$ and $1.3 \cdot 10^{-10}$ mol·cm^{-2} are calculated for the 1:5, 1:2, 1:1 and 1:0.75 Ir-dye/DMPA mixtures, respectively. The experimental ΔR data corresponding to the different mixtures approx. fit a linear regression, except that for the mixed 1:0.75 film, which clearly deviates negatively from this relation. According to Eq. 3.2.3, a value $f_{orient} = 1.2$ is calculated from this linear regression for the

Ir-dye/DMPA = 1:5, 1:2 and 1:1 mixed films. Thus, one can conclude that, for the Ir-dye/DMPA = 1:x monolayers (being $x \geq 1$), the initially co-spread Ir-dye molecules remain at the interface, at $\pi = 8$ mN/m.

Due to the symmetry of the iridium complex investigated, the deviation of the experimental value for the 1:0.75 mixture from the theoretical relation cannot be due to a different orientation of the iridium complex at the interface. Moreover, different aggregation of the dye in this film can be discarded, since the spectra of these monolayers match in both shape and peak positions. Consequently, it should be related to a loss of a certain fraction of dye molecules from the mixed monolayer.

Molecular Organization at the Air−Water Interface

The theoretical calculation of the molecular area of Ir-dye complex has been done by using semiempirical ZINDO methods in Hyperchem,[38] and it has been estimated to range from ca. 1.12 nm^2, one of the ppy ligands lying parallel to the water surface, to 1.32 nm^2, the tmphen ligand lying parallel to the interface. However, the area per molecule at high surface pressure in the analyzed mixed films, obtained from extrapolation of the $\pi - A$ isotherms, is lightly different (see Fig. 3.21). Previous to the collapse of the pure DMPA monolayer, at 35 mN/m, each DMPA molecule occupies ~ 0.4 nm^2 in the condensed phase. In the case of the 1:1 mixed film, $A_{DMPA} = A_{Ir-dye} \sim 0.82$ nm^2 at 35 mN/m, value smaller than that expected for a theoretical Ir-dye monolayer (i.e., 1.12-1.32 nm^2).

Considering that Ir-dye and DMPA molecules are, respectively, monoca-

tionic and monoanionic species, the optimal binding would require an equimolecular ratio. However, the theoretical molecular area of the complex (1.12 - 1.32 nm^2) is much bigger than the area per DMPA in the condensed phase (0.38 nm^2). Consequently, one may expect that each Ir-dye molecule could accommodate, theoretically, a limited number of DMPA (2-3 molecules) in the film.

An understanding of the molecular organization of these mixed films can be provided by a detailed analysis of the BAM images.[39] Thus, the molecular area per DMPA in the isotherm of a mixture Ir-dye/DMPA = 1:x can be calculated by

$$A = A_d \cdot x_d + A_b \cdot (1 - x_d) = A_b - x_d \cdot (A_b - A_d) \tag{3.20}$$

where $x_d = x/(1+x)$, and x_d and A_d are the molar fraction and molecular area of DMPA in the dark domains, and A_b represents the molecular area per DMPA in the bright regions. Also, the molar fraction of DMPA in the dark regions can be expressed as a function of the fraction of dark surface area measured in the BAM images (f_d), by

$$x_d = \frac{f_d/A_d}{f_d/A_d + (1 - f_d)/A_b} \tag{3.21}$$

where f_d/A_d is proportional to the number of mols of DMPA in the dark regions, while $(1 - f_d)/A_b$ is to those of DMPA situated in bright areas. From Eqs. 3.2.3 and 3.2.3, one can obtain the following expression

$$\frac{1}{A} = \frac{1}{A_b} + f_d \cdot (\frac{1}{A_d} - \frac{1}{A_b}) \tag{3.22}$$

The graphical plot of the inverse of A (area of DMPA obtained from the isotherm) vs f_d (fraction of dark surface area, from BAM images) must keep a linear relationship, from which the A_b and A_d values can be obtained.

Figure 3.24 shows this representation for the Ir-dye/DMPA = 1:2 mixed monolayer, by using the values of f_d from the BAM images of Fig. 3.22. Thus, the values $A_b = 1.04$ nm^2 and $A_d = 0.37$ nm^2 are calculated from the linear regression of such plot.

The value $A_d = 0.37$ nm^2 coincides with that obtained from the isotherm of pure DMPA, which provides clear evidence of the absence of Ir-dye in the dark domains, as also deduced from the low reflectivity of this region. Therefore, it can be affirmed that the dark domains are exclusively formed by the excess of DMPA with respect to the equimolecular ratio. Such excess would be expelled from the regions where both compounds coexist (bright regions). On the other hand, the critical area $A_b = 1.04$ nm^2 should correspond to the area occupied by one DMPA molecule over the Ir-dye molecule. However, in the case of the 1:1 molar ratio, the area per DMPA at high surface pressure (previous to the collapse) is ~ 0.82 nm^2 (see Fig. 3.21). In fact, the area A_b can decrease lightly at high surface pressures. For the mixed Ir-dye/DMPA = 1:x films investigated (with $x > 1$), when this critical area per DMPA is reached ($A_b = 1.04$ nm^2), the segregation of a new phase takes place, containing the excess of lipid molecules. For a mixed 1:x monolayer, the area per lipid molecule at which the excess of DMPA is totally expelled from the bright regions can be calculated by Eq. 3.2.3. Thus, for instance, these two phases are totally separated for 0.7 nm^2 in the case of the mixed 1:2 monolayer.

Both the mixed 1:1 and 1:2 monolayers can be further compressed af-

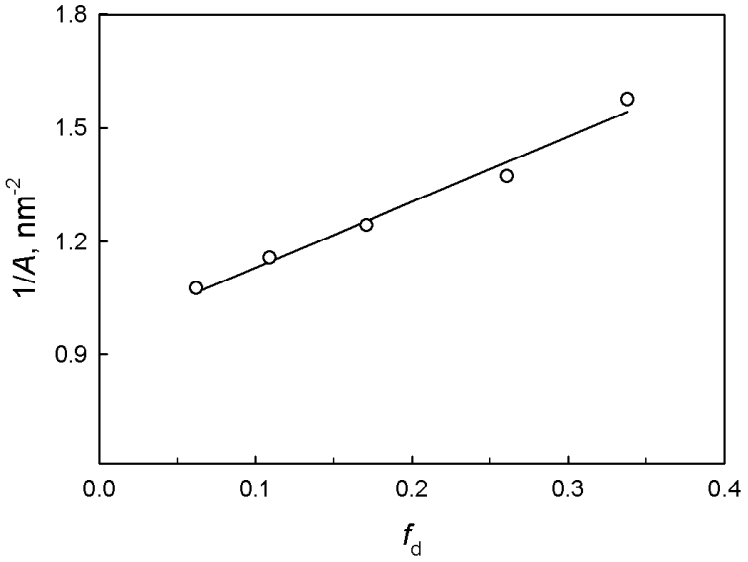

Figure 3.24: Plot of the inverse of the molecular area per DMPA (obtained from the isotherm, Fig. 3.21) vs fraction of dark surface area (obtained from BAM images, Fig. 3.22), for the Ir-dye/DMPA = 1:2 monolayers at the air−water interface (circles), and its corresponding linear regression (solid line).

ter reaching their critical area, 1.04 nm^2 and 0.7 nm^2, respectively, as can be observed in the isotherms of Fig. 3.21. As previously commented, a new slope around 28 and 30 mN/m can be observed for the 1:1 and 1:2 isotherms, respectively (see Fig. 3.21). Surprisingly, this phenomenon occurs at approximately the same area that the critical value. Actually, the DMPA molecules in the bright area are in liquid-expanded phase, and can allow further compression. A feasible explanation can be found in the reflection spectra measured at the air−water interface. In fact, for all the mixed films studied, both UV absorption bands shift to red ($\Delta\lambda \sim 3nm$) when the monolayer is compressed until high surface pressures. This red shift can probably be assigned to some type of J-aggregates, which are originated as a result of the

interaction between the planes of ligands belonging to neighboring iridium complex units. This leads to a reduction of the meaning molecular area per Ir-dye in the condensed phase, as detected in the $\pi - A$ isotherms.

UV-Visible Absorption Spectroscopy of LB Multilayers

Mixed Ir-dye/DMPA = 1:2 and 1:1 monolayers on the water surface were successfully transferred onto quartz or ITO-coated substrates, using the vertical dipping procedure (LB method), under constant pressure of 28 mN/m, and a lifting rate of 5 mm/min. In this way, the Ir-dye complex in the film is directly bound to the hydrophilic surface. For the first transferred monolayer, the transfer ratio varies with the molar ratio of the mixture, being in all cases close to unity (0.8-1). The absorption spectra of these mixed LB films were recorded (data not shown), and two phenomena can be appreciated: no shifts of the UV bands as the complex concentration was changed and similar shape for the corresponding normalized spectra. Therefore, a unique organization of the iridium complex in the transferred films can be supposed.

Among these organized mixed films, only multilayers of that containing the lowest fraction of DMPA were built. Thus, Ir-dye/DMPA = 1:1 multilayers were assembled by sequential monolayer transfer (withdrawal and immersion), and since a transfer ratio close to unity is obtained during the upstroke and 0.2 during the downstroke, almost Z-type multilayers are considered. The dry time for every deposited layer was about 5 min.

Different number of Ir-dye/DMPA = 1:1 layers were deposited and studied by UV-visible absorption spectroscopy. Fig. 3.25 shows the absorption of

1-, 11-, 27- and 33-layers on quartz substrates. The plot of the integration of each spectrum vs number of withdrawal transfers reveals a lineal relationship with slope equal to 1 and a zero intercept, as shown in the inset of Fig. 3.25. Consequently, this fact indicates that the Ir-dye molecules are homogeneously attached to the DMPA matrix, and can be successfully deposited layer by layer.

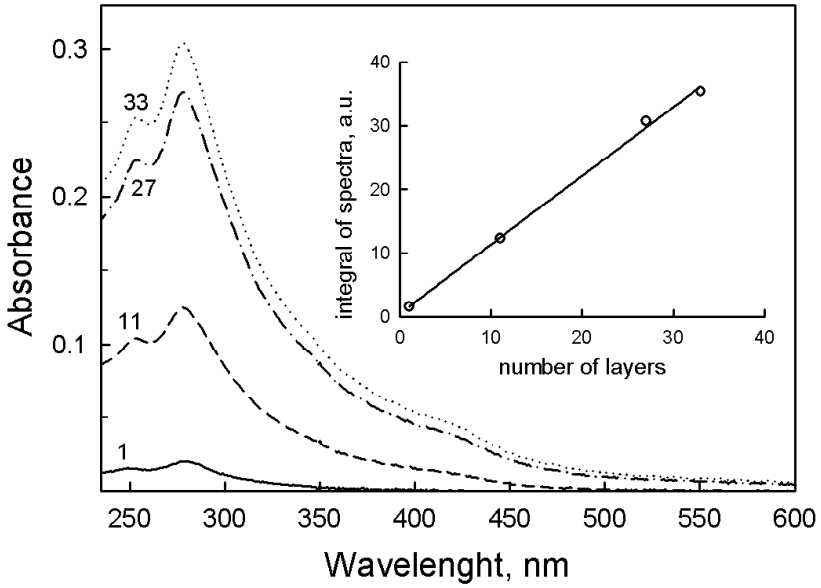

Figure 3.25: Absorption spectra of Ir-dye/DMPA = 1:1 multilayers: 1 monolayer (solid line), 11-layers (dashed line), 27-layers (dash-dotted line) and 33-layers (dotted line). Insert, integral of the UV absorption spectra vs number of layers (withdrawal processes).

The relation between reflection and absorption is given by the model of Grüniger et al.,[35] being expected a ratio $\Delta T/\Delta R = 8{,}5$. The value of this ratio (of the absorption and reflection) at the maximum of the lower energetic UV peak ($\lambda = 278$ nm), for the Ir-dye/DMPA = 1:1 monolayer at 28 mN/m, is calculated to be $\Delta T/\Delta R \sim 7{,}6$. This value slightly deviates from the

expected value 8.5 for a complete dye transfer.

FTIR Reflection Spectroscopy of LB Multilayers

Fig. 3.26c shows the reflection spectrum ($\Delta R/R_0$), under 70°incidence and p-polarized light, of 55-layers of Ir-dye/DMPA = 1:1, transferred onto ITO substrate at 28 mN/m by the LB technique. The figure also shows, as reference, FTIR reflection spectra of drop-cast films containing pure Ir-dye (a) and the Ir-dye/DMPA mixture in molar ratio 1:1 (b), both spread from chloroform-methanol (3:1, v/v) solutions onto ITO substrates. The main band positions and assignments are provided in Table 3.1.

The Ir-dye studied here is identified by its FTIR spectrum shown in (a), in which the bands corresponding to the aromatic rings and the counterion PF^{6-} are detected.[40] In the FTIR spectrum of the cast mixed film (b), both the Ir-dye and the DMPA vibration modes can be identified.

As can be deduced from spectrum (c), both species coexist in the LB film. However, it is noticeable the difference found in the relative peak heights between the Ir-dye/DMPA (1:1) cast film and Ir-dye/DMPA = 1:1 LB multilayers spectra. These intensity variations may be related to the different organization of the molecules in such films: dye and DMPA are randomly organized in the cast film (b), while in the LB film they present a more ordered structure (c). The bands corresponding to the stretching vibrations of the counterion PF^{6-} are not detected in the Ir-dye/DMPA LB film spectrum, which is indicative of electrostatic interactions between these molecules. Thus, the polar head group of the DMPA displaces the PF^{6-} counterion

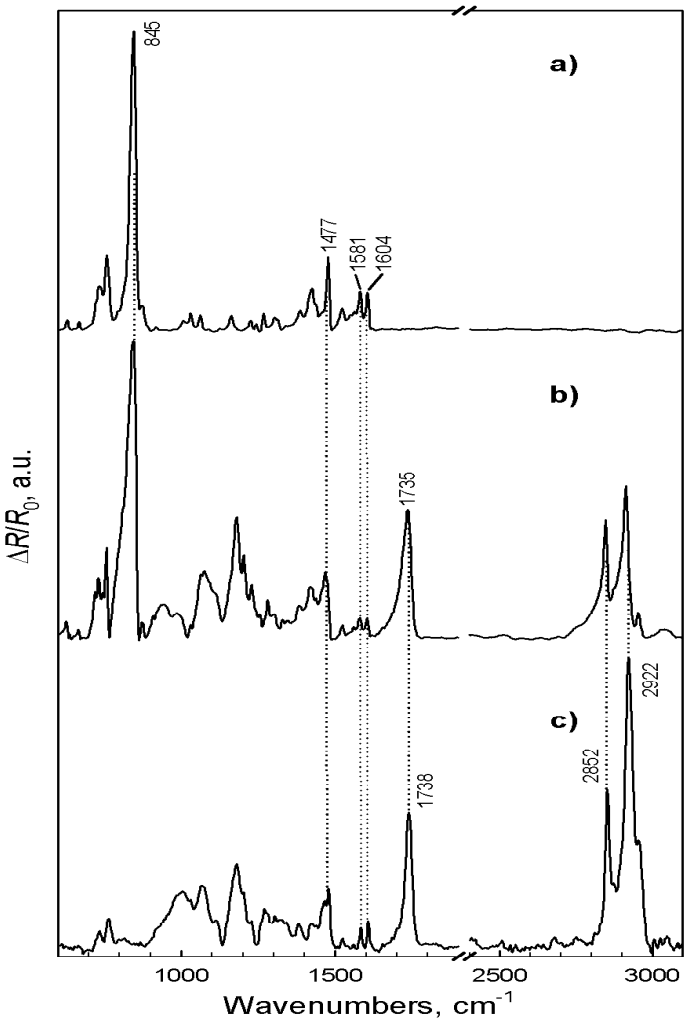

Figure 3.26: FTIR reflection spectra of drop-cast films prepared from chloroform-methanol (3:1) solutions of a) Ir-dye and b) Ir-dye/DMPA (1:1), and c) reflection spectrum of 55-monolayers of Ir-dye/DMPA = 1:1 LB film.

in the mixed LB film, compensating the positive charge of the iridium (III) complex, which confirms the electrostatic character of the Ir-dye/DMPA pair.

The positions of the $\nu_{as}(CH_2)$ and $\nu_s(CH_2)$ modes are sensitive indicators for the lateral interactions between alkyl chains.[41,42] Thus, the band position for the $\nu_{as}(CH_2)$ mode of a crystalline polymethylene chain (2920

cm^{-1}) is 8 cm^{-1} lower than that for the liquid state (2928 cm^{-1}), whereas the band position for the $\nu_s(CH_2)$ mode is 6 cm^{-1} lower in the crystalline sample (2850 cm^{-1}) than in the liquid state (2856 cm^{-1}).[43,44] The transmission and reflection FTIR spectra of DMPA LB film have been deeply described elsewhere.[45,46] The comparison of the wavenumbers for DMPA (ν_{as} = 2920 cm^{-1} and ν_s = 2951 cm^{-1})[45,46] and Ir-dye/DMPA (ν_{as} = 2922 cm^{-1} and ν_s = 2852 cm^{-1}) LB film spectra reveals the existence of a certain disorder in the alkyl chains in the mixed film, intermediate between a crystalline and a liquid state (*gauche* conformation).

Ir-dye cast film	Ir-dye/DMPA cast film	Ir-dye/DMPA LB multilayers	Assignments
848	846	-	$\nu(PF_6^-)$
-	1180	1180	ν_{as}(C-O-C)
1477	1477, 1467 (shoulder)	1478, 1467 (shoulder)	ν(C-C)$_{arom}$, $\delta(CH_2)$
1581	1579	1583	ν(C-C)$_{arom}$
1604	1602	1606	ν(C-C)$_{arom}$
-	1735	1738	ν_s(C=O)
-	2846	2852	$\nu_s(CH_2)$
-	2913	2922	$\nu_{as}(CH_2)$

Abbreviations: ν, stretching; δ, bending/deformation; arom, aromatic; subscripts as and s denote antisymmetric and symmetric modes, respectively.

Table 3.1: Band positions (cm^{-1}) and assignments for the main peaks of the films shown in Fig. 3.26.

3.2.4. Conclusions

In this work, the ability of a monocationic water-insoluble Ir-dye to form monolayers at the air−water interface, in presence of an anionic lipid matrix, has been investigated by using surface techniques as $\pi - A$ isotherms,

Brewster angle microscopy and reflection spectroscopy. In the case of the equimolecular Ir-dye/DMPA = 1:1 mixed film, a homogeneous monolayer is observed along the whole range of surface pressures applied, until the collapse of the monolayer at $\sim$ 38 mN/m. At high surface pressures, a dense-packed Ir-dye monolayer underneath a lipid matrix of DMPA is formed.

When the initial co-spread mixture contains high proportions of DMPA (Ir-dye/DMPA = 1:x, being $x > 1$), also homogeneous films are observed until a certain surface pressure. Then, as the monolayer is compressed, the segregation of a fraction of lipid molecules takes place, which organize forming dark flower-like domains of pure DMPA. This phase has been proved to be formed by the excess of DMPA from the equimolecular ratio. Thus, at high surface pressures, two different structures coexist at the water surface, dark domains of pure DMPA in the bulk of a highly reflective Ir-dye/DMPA = 1:1 mixed monolayer.

On the other hand, to minimize the presence of lipid in the film, Ir-dye/DMPA = 1:x mixtures, being $x < 1$, have been tested to form Langmuir monolayers. In this case, both $\pi - A$ isotherms and reflection measurements reveal the formation of an unstable and poorly reproducible film at the air-water interface, and a loss of iridium complex molecules from the mixed films cannot even be discarded.

Ir-dye/DMPA Langmuir monolayers with different molar ratios are successfully transferred onto solid substrates by the LB technique, as confirmed by UV-visible absorption and FTIR reflection spectroscopies. Furthermore, Ir-dye/DMPA = 1:1 multilayers can be assembled by successive upstroke/downstroke cycles, predominantly in a Z-type organization. Due to the

large area available per DMPA molecule at high surface pressure ($\sim$ 0.9 nm^2), the alkyl chains are in gauche conformation, i.e., intermediate between a crystalline and a liquid state.

Acknowledgments

The authors thank the Spanish CICYT for financial support of this research in the framework of Projects No. CTQ2004-03246/BQU and MAT2004-03849. Also, we thank the Ministerio de Educación y Ciencia for the contract (Ramón y Cajal Program) and the research fellowship (Formación de Profesorado Universitario) of two of the authors (H. J. B. and J. J. G. C., respectively).

References

1. Kalyanasundaram, K.; Grätzel, M. *Coord. Chem. Rev.* **1998,** *77,* 347.

2. Holder, E.; Langeveld, B.; Schubert, U. *Adv. Mater.* **2005,** *17,* 1109.

3. Goldsmith, J.; Hudson, W.; Lowry, M.; Anderson, T.; Bernhard, S. *J. Am. Chem. Soc.* **2005,** *127,* 7502.

4. DeRosa, M.; Hodgson, D.; Enright, G.; Dawson, B.; Evans, C.; Crutchley, R. *J. Am. Chem. Soc.* **2004,** *126,* 7619.

5. Baldo, M.; O'Brien, D.; You, Y.; Shoustikov, A.; Silvey, S.; Thompson, M.; Forrest, S. *Nature* **1998,** *395,* 151.

6. Baldo, M. A.; Lamansky, S.; Burrows, P. E.; Thompson, M. E.; Forrest, S. R. *Appl. Phys. Lett.* **1999,** *75,* 4.

7. Yersin, H. *Top Curr Chem* **2004,** *241,* 1.

8. Holder, E.; Marin, V.; Alexeev, A.; Schubert, U. *Polym. Chem.* **2005,** *43,* 2765.

9. Chen, F.; Yang, Y.; Pei, Q. *Appl. Phys. Lett.* **2002,** *81,* 4278.

10. Slinker, J.; Gorodetsky, A.; Lowry, M.; Wang, J.; Parker, S.; Rohl, R.; Bernhard, S.; Malliaras, G. *J. Am. Chem. Soc.* **2004,** *126,* 2763.

11. Bolink, H.; Cappelli, L.; Coronado, E.; Grätzel, M.; Ortí, E.; Costa, R.; Viruela, P.; Nazeeruddin, M. *J. Am. Chem. Soc.* **2006,** *128,* 14786.

12. Bolink, H.; Cappelli, L.; Coronado, E.; Parham, A.; Stössel, P. *Chem. Mater.* **2006,** *18,* 2778.

13. *Molecular design of electrode surfaces;* volume 22 of *Techniques of Chemistry* John Wiley and Sons, Inc.: New York, 1992.

14. Bedioui, F.; Devynck, J.; C.Bied-Charreton, *Acc. Chem. Res.* **1995,** *28,* 30.

15. Goldenberg, L. *J. of Electroanal. Chem.* **1994,** *379,* 3.

16. Santos, J. P.; Zaniquelli, M. E. D.; Batalini, C.; De Giovani, W. F. *J. Phys. Chem. B* **2001,** *105,* 1780.

17. Pérez-Morales, M.; Martín-Romero, M. T; Muñoz, E.; Camacho, L. *Electrochimica Acta* **2006,** *51,* 3714.

18. Pérez-Morales, M.; Muñoz, E.; Martín-Romero, M. T; Camacho, L. *Electrochem. Comm.* **2006,** *8,* 638.

19. Tamura, K.; Sato, H.; Yamashita, S.; Yamagishi, A.; Yamada, H. *J. Phys. Chem. B* **2004,** *108,* 8287.

20. Wohnrath, K.; Constantino, C.; Antunes, P.; Dos Santos, P.; Batista, A.; Aroca, R.; Oliveira, O. *J. Phys. Chem. B* **2005,** *109,* 4959.

21. Yam, V.; Li, B.; Yang, Y.; Chu, B.; Wong, K.; Cheung, K. *Eur. J. Inorg. Chem.* **2003,** 4035.

22. Huesmann, H.; Bignozzi, C.; Indelli, M.; Pavanin, L.; Rampi, M.; Möbius, D. *Thin Solid Films* **1996,** *284-285,* 62.

23. Huesmann, H.; Spohn, D.; Indelli, M.; Rampi, M.; Möbius, D. *Langmuir* **1997,** *13,* 4877.

24. Lu, W.; Guo, W.; Zhou, H.; He, P. *Langmuir* **2000,** *16,* 5137.

25. Pereira Santos, J.; Zaniquelli, M.; Batalini, C.; Ferraresi De Giovani, W. *Thin Solid Films* **1999,** *349,* 238.

26. Lu, W.; Zhou, H.; He, P.; Guo, W. *Thin Solid Films* **2000,** *365,* 67.

27. Samha, H.; Martinez, T.; Dearmond, M.; Garces, F.; Watts, R. *Inorg. Chem.* **1993,** *32,* 2583.

28. Sprouse, S.; King, K. A.; Spellane, P. J.; Watts, R. J. *J. Am. Chem. Soc.* **1984,** *106,* 6647.

29. Hada, H.; Hanawa, R.; Haraguchi, A.; Jonezawa, Y. *J. Phys. Chem.* **1985,** *89,* 560.

30. Möhwald, H. *Ann. Rev. Phys. Chem.* **1990,** *41,* 441.

31. Colombo, M.; Hauser, A.; Gädel, H. U. *Inorg. Chem.* **1993,** *32,* 3088.

32. Matsumura-Inoue, T.; Yamamoto, Y.; Yoshikawa, N.; Terashima, M.; Yoshida, Y.; Fujii, A.; Yoshino, K. *Opt. Mater.* **2004,** *27,* 187.

33. Adachi, C.; Baldo, M. A.; Forrest, S.; Thompson, M. E. *Appl. Phys. Lett.* **2000,** *77,* 904.

34. Xie, H. Z.; Liu, M. W.; Wang, O. Y.; Zhang, X. H.; Lee, C. S.; Hung, L. S.; Lee, S. T.; Teng, P. F.; Kwong, H. L.; Zheng, H.; Che, C. M. *Adv. Mater.* **2001,** *13,* 1245.

35. Grüniger, H.; Möbius, D.; Meyer, H. *J. Chem. Phys.* **1983,** *79,* 3701.

36. Grüniger, H.; Möbius, D.; Lehmann, U.; Meyer, H. *J. Chem. Phys.* **1986,** *85,* 4966.

37. Pedrosa, J. M.; Martín-Romero, M. T.; Camacho, L.; Möbius, D. *J. Phys. Chem. B* **2002,** *106,* 2583.

38. "HyperChem 8.5", 1999 Hypercube, Inc.

39. Pérez, M.; Pedrosa, J. M.; Martín-Romero, M. T.; Möbius, D.; Camacho, L. *J. Phys. Chem. B* **2004,** *108,* 4457.

40. Nakamoto, K. *Infrared and Raman spectra of inorganic and coordination compounds;* John Wiley and Sons, Inc.: 1986.

41. Katayama, N.; Enomoto, S.; Sato, T.; Ozaki, Y.; Kuramoto, N. *J. Phys. Chem.* **1993,** *97,* 6880.

42. Byrd, H.; Whipps, S.; Pike, J.; Ma, J.; Nagler, S.; Talham, D. *J. Am. Chem. Soc.* **1994,** *116,* 295.

43. Snyder, R. G.; Strauss, H. L.; Elliger, C. A. *J. Phys. Chem.* **1982,** *86,* 5145.

44. Snyder, R. G.; Maroncelli, M.; Strauss, H. L.; Hallmark, V. M. *J. Phys. Chem.* **1986,** *90,* 5623.

45. Fernández, A. J.; Ruiz, J. J.; Camacho, L.; Martín, M. T.; Muñoz, E. *J. Phys. Chem. B* **2000,** *104,* 5573.

46. Lozano, P.; Fernández, A. J.; Ruiz, J. J.; Camacho, L.; Martín, M. T.; Muñoz, E. *J. Phys. Chem. B* **2002,** *106,* 6507.

3.3. Segregation of Lipid in Ir-dye/DMPA Mixed Monolayers as Strategy to Fabricate 2D Supramolecular Nanostructures at the Air−Water Interface

A novel pseudospherical fluorinated iridium (III) derivative, Ir-dye/PF_6, [Ir(F_2-ppy)$_2$(bpy)]PF_6, (F_2-ppy = 2-(2,4-difluoro) phenylpyridine, bpy = 2,2'-bypyridine), has been organized by using a lipid matrix, DMPA (dimyristoyl-phosphatidic acid), in several molar ratios at the air−water interface. The molecular organization of both components and the degree of miscibility in the different mixed films have been inferred by surface techniques as $\pi - A$, ellipsometry, reflection spectroscopy, BAM, and IR spectroscopy for the LB films, additionally the results have been discussed according to the additivity rule. The equimolecular Ir-dye/DMPA mixture leads to a totally miscible, stable and homogeneous monolayer. Any surplus of DMPA with respect to the 1:1 ratio segregates under compression while forming domains. By varying the surface concentration of DMPA in the mixture we demonstrate that the Ir-dye can be confined to certain regions of the 2D patterned structure formed at the air−water interface. The fraction of surface containing the photofunctional complex can be controlled by both the fraction of lipid in the initial cospread mixture and the surface pressure applied to the film. Finally, the additivity rule has been applied, for the first time in our knowledge, to simulate the ellipsotherms of mixed monolayers.

Paper published in *J. Mater. Chem.*, 2008, 18, 1681-1688

3.3.1. Introduction

The fabrication of nanostructured organic materials has potential for applications in optics and electronics, e.g. chemical sensors, electroluminescent devices, molecular switches, non linear optics, etc. The organization of nanostructures materials in thin films is needed in many of these applications. Therefore, the formation of ordered molecular architectures, such as monolayers,[1,2] one-dimensional rods and tubules,[3,4] and two-dimensional aggregates on the surface[5] is an active research topic. Moreover, the heterogeneous functionalization of solid surfaces has been carried out by several techniques such as light-directed synthesis,[6] patterns of self-assembled monolayers by microcontact printing,[7] transfer of structural films by the LB technique,[1] or production of nanosized patterns by lithographic methods,[8,9] among others.

As widely described in the literature, the fabrication of thin films by the LB technique is a sophisticated and accurate method to control the molecular orientation and packing in a two-dimensional way.[2,10] Although most research on Langmuir monolayers has been focused on the fabrication of homogeneous films, this technique is also a very powerful tool for the preparation of patterned surfaces. Making use of the air-water interface and by varying both the contained materials and the transfer conditions the formation of composite nano-structured films can be achieved. Traditionally, the main problem with mixed systems is the phase separation of the components in the films, which generally leads to heterogeneous structures with domains of either one of the pure components, depending on their degree of miscibility.[10] Several studies have shown that macroscopic domains are formed in various mixed systems,

and only true molecular level mixing is attained for molecules having similar structure. However, many investigations demonstrate the formation of homogeneous mixed films, prepared by adsorption or cospreading[11] methods, containing molecules of different nature, which arrange in interlocked structures,[12] or in stratified films. One particular interesting class of molecules is organometallic complexes, which due to their special photophysical properties are used in wide variety of opto-electronic applications. These molecules, however, are difficult to fixate in homogenous solid matrices.[13,14] Nevertheless, in a previous work our group has reported a homogeneous mixed film containing an iridium derivative, organized underneath a lipid matrix obtained using the LB technique.[15]

In this paper we report on the formation of nanoscale patterned mixed monolayers at the air-water interface, containing an archetype monocationic and phosphorescent fluorinated Ir(III) derivative (Ir-dye) and an anionic lipid (DMPA). The Ir-dye molecule used in this work belongs to the family of the organometallic triplet emitters, which are of great interest because of their application in sensors and electroluminescent devices.[16–20] The literature concerning mixed films containing organometallic complexes is not extensive, and has been focused in the retention of water-soluble complexes by lipid matrices,[21,22] and the control of aggregation of Ru(II) and Ir(III) derivatives that are able to form monolayers by themselves.[13,14,23,24] However, the Ir-dye used here does not form monolayers in the absence of lipid, and has been successfully organized by using an anionic matrix. The formation of 2D patterned structures has been monitored by Brewster angle microscopy (BAM). The nature of these microstructures has been investigated by

the combination of surface techniques as $\pi - A$ isotherms, ellipsometry and reflection spectroscopy, and they are found to occur as a consequence of a particular phenomenon: the micro-segregation of lipid molecules from the Ir-dye/DMPA mixed film to form a new phase of pure lipid. The fact that the dye and the lipid can be distributed in two different structures coexisting in the composite film with controllable relative areas ratio, can lead to films with very interesting optical and electrical properties.

3.3.2. Experimental

Materials

The Ir-dye/PF_6 used in this work, namely, [Ir(F_2-ppy)$_2$(bpy)]PF_6, (F_2-ppy = 2-(2,4-difluoro) phenylpyridine, and bpy = 2,2'-bypyridyl), was synthesized and kindly given by the research group of Dr. H. J. Bolink (Molecular Science Institute, University of Valencia). Dimyristoyl-phosphatidic acid (DMPA) was purchased from Sigma Chemical Co. and used as received. The molecular structures of Ir-dye/PF_6 and DMPA are shown in Figure 3.27. A mixture of dichloromethane and methanol (4:1, v/v) was used as co-spreading solvent. All pure solvents were obtained from Aldrich (Germany), except methanol from Panreac (Spain). $IrCl_3 \cdot nH_2O$ was obtained from Pressure Chemical. Ultrapure water, produced by a Millipore Milli-Q unit, pretreated by a Millipore reverse osmosis system (resistivity = 18.2 MΩ·cm) was used as a subphase. The subphase temperature was 21 ^{o}C, with a pH 5.7.

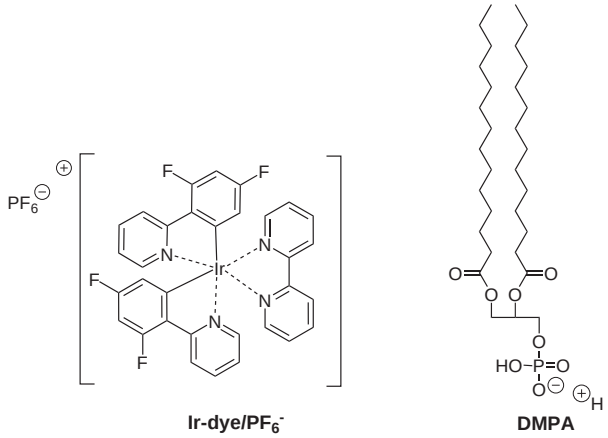

Figure 3.27: Molecular structures of the Ir-dye/PF_6 derivative and the lipid DMPA.

Methods

Two different models of Nima troughs (Nima Technology, Coventry, England) were used in this work, both provided with a Wilhelmy type dynamometric system using a strip of filter paper: a NIMA 611D with one moving barrier (total area $\sim$ 505 cm^2) for the measurement of the reflection spectra, and a NIMA 601, equipped with two symmetrical barriers (total area $\sim$ 600 cm^2) to record BAM images and to measure the ellipsometric angles.

Ellipsometric measurements were performed with a PCSA null imaging ellipsometer (I-Elli2000 supplied by NFT, Nanofilm Technologie, Göttingen, Germany) using a solid-state laser (wavelength 532 nm, 50 mW). The accuracy of the device is 0.02°in Δ and Ψ. For measurements of the films at the air−water interface we used an angle of incidence of 50°, and an angle set P = C = 20 and A = 14. The ellipsometric angles, Δ and Ψ, were measured on the whole surface illuminated by the laser beam. The I-Elli2000 is also equipped with an imaging device by which images of the film at the

Brewster angle can be recorded with a lateral resolution of 2 μm. The image processing procedure included a geometrical correction of the image, as well as a filtering operation to reduce interference fringes and noise. Furthermore, the reflection intensity of the images was scaled to improve contrast. The microscope and the film balance were located on a table with vibration isolation (anti-vibration system MOD-2 S, Halcyonics, Göttingen, Germany) in a large class 100 clean room.

UV-visible reflection spectra at normal incidence as the difference in reflectivity (ΔR) of the dye film-covered water surface and the bare surface[25] were obtained with a Nanofilm Surface Analysis spectrometer (RefSPEC^2, supplied by Nanofilm).

FTIR measurements were performed on a Mattson Research Series instrument equipped with a DTGS detector. The background spectrum was taken for a bare support of the same material. For the reflection spectra, ITO electrodes were used as substrates. The measurements $\Delta R/R_0 = (R - R_0)/R_0$ (where R_0 is the reflection of the bare electrode), were carried out at an external reflection configuration, p polarized within the incident plane at a grazing angle of 70° degrees. Drop-cast films were prepared by spreading an Ir-dye/PF_6 dichloromethane-methanol (4:1 v/v) solution onto the solid substrate. In all cases, the spectra were the accumulation of 1024 scans, and recorded with a 4 cm^{-1} resolution.

3.3.3. Results

$\pi - A$ and $\Delta - A$ isotherms

The fluorinated Ir-dye/PF_6 used here is water-insoluble and does not form Langmuir monolayers on pure water. Thus, mixed monolayers from dichloromethane-methanol (4:1 v/v) solutions containing Ir-dye/PF_6 and DMPA in different molar ratio (1:1, 1:2, and 1:5), were prepared by the co-spreading method[11] at the air−water interface. Previously, several chloroform-methanol mixtures were examined as spreading solvent, but this resulted in the aggregation of Ir(III) prior to the compression of the monolayer as visualized by BAM and the poor reproducible isotherms.

Figure 3.28 shows the surface pressure (π)-area (A) isotherms corresponding to the mixed Ir - Ir-dye/PF_6:DMPA = 1:1, 1:2 and 1:5 films (solid lines). The isotherm of pure DMPA has been also added for comparison. The presence of the iridium molecules at the interface is evident, as revealed by the pronounced expansion observed in the isotherms with respect to the pure lipid. Thus, the isotherm behavior as a function of spreading ratio shifts to larger effective molecular areas as the metal complex concentration is increased. In all cases, the collapse of the mixed films occurs at around 38 mNm^{-1}.

The isotherms of the different mixed films are highly reproducible. The stability of the mixed monolayers was analyzed by area-time diagrams and compression-expansion cycles (data not shown). The different mixed films are stable up to the collapse pressure. Besides, small hysteresis during the compression-expansion cycles is found in all cases, provided that the collapse

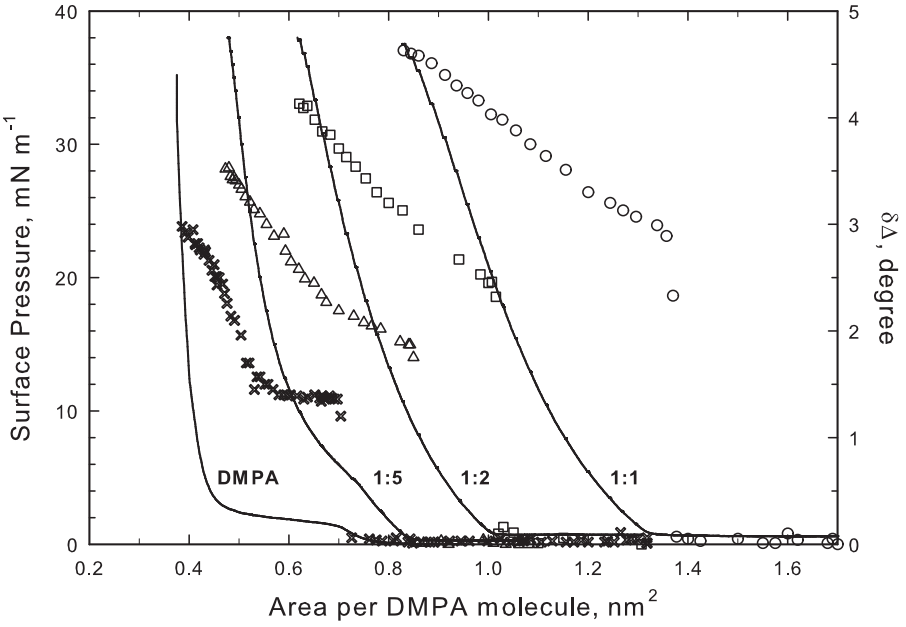

Figure 3.28: $\pi - A$ isotherms (solid lines) and ellipsotherms (symbols) of pure DMPA and mixtures of Ir-dye:DMPA = 1:x with different molar ratios on pure water: 1:1 (circles), 1:2 (squares), 1:5 (triangles) and DMPA (crosses). The molecular area is expressed per DMPA molecule in all cases.

of the film is avoided. However, when the fraction of Ir-dye in the mixture is higher than that of DMPA (Ir-dye/PF_6:DMPA = 1:x, being x < 1), the isotherms are not stable and reproducible, and reflective islands are visualized by BAM.

Figure 3.28 also shows the change of the ellipsometric angle $\delta\Delta$, ($\delta\Delta = \Delta - \Delta_0$, where Δ is measured in presence of the film and Δ_0 on the clean surface, i.e., water surface) *versus* molecular area during the compression of the different mixed films, obtaining the corresponding $\delta\Delta - A$ isotherms, so-called ellipsotherms. In this work, $\delta\Delta$ values correspond to the average on a large region of the film (430 μm x 530 μm, image size). Extremely

small changes in Ψ were detected during the compression process, remaining almost constant, as a consequence of the negligible absorption of the iridium chromophore at the laser wavelength (532 nm). Thus, Ψ angle will not be considered.[26]

All the ellipsotherms show a sudden change in Δ at low surface pressure (0.2 mN m^{-1}), increasing with increasing fraction of Ir-dye in the mixture. This variation in Δ suggests the transition from gas to liquid-expanded phases. Afterwards, Δ angle increases gradually as the films are compressed.

Evidence of the counterion exchange of the Ir-dye in the mixed films

To demonstrate the electrostatic interaction between the monocationic Ir-dye and the monoanionic dissociated DMPA molecules in the mixed films, implying the exchange of the PF_6- counterion of the Ir-dye by the lipid molecule, the Ir-dye/PF_6^-:DMPA = 1:1 mixed film was transferred onto an ITO substrate. Figure 3.29 shows the FTIR reflection spectrum corresponding to 10 mixed monolayers (dashed line), transferred by the Langmuir-Blodgett method at 28 mN m^{-1}. The figure also shows, as reference, the FTIR reflection spectrum of a drop-cast film containing pure Ir-dye/PF_6 (solid line), spread from a dichloromethane-methanol (4:1 v/v) solution. The band positions and assignments for the main peaks of the films are shown in Table 3.2.

In the FTIR spectrum of the Ir-dye/PF_6 cast film (Figure 3.29, solid line), the bands corresponding to the vibration modes of the Ir-dye, the aromatic

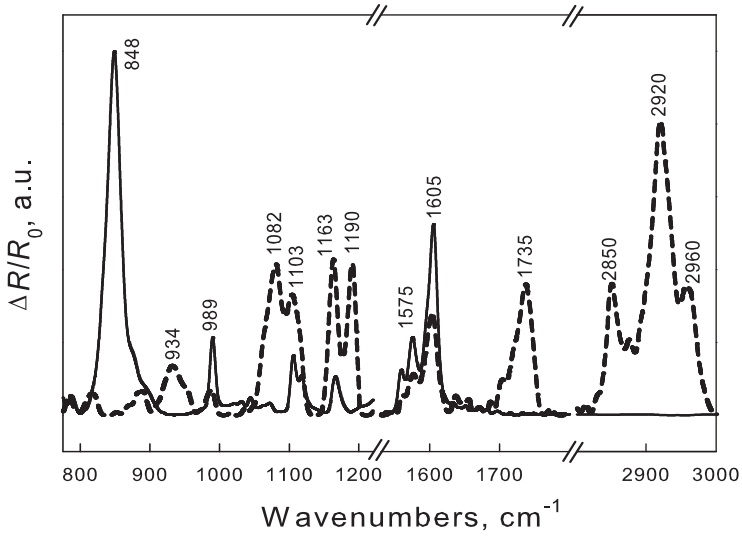

Figure 3.29: FTIR reflection spectra of a drop-cast film prepared from a dichloromethane-methanol (4:1 v/v) solution of Ir-dye/PF_6 (solid line), and reflection spectrum of 10 monolayers of Ir-dye/DMPA = 1:1 LB film (dashed line).

rings (1575 and 1605 cm^{-1}) and C-F (1166 cm^{-1}), and the counterion PF_6^- (848 cm^{-1}) are assigned in Table 3.2.[27,28] In the case of the spectrum of the Ir-dye/PF_6:DMPA = 1:1 mixed film (dashed line), the bands of the DMPA are clearly observed (see Table 3.2), as well as the corresponding to the Ir-dye, while the stretching vibrations of the counterion PF_6^- are not detected. This fact is indicative of the absence of this specie in the LB film and confirms that the polar head group of the DMPA displaces the PF_6^- counterion in the mixed film at the air−water interface, compensating the positive charge of the iridium (III) derivative, and consequently originating the formation of the Ir-dye/DMPA pair. From this point, once the counterion exchange of the Ir-dye in the monolayer has been demonstrated, we refer to the mixed film as Ir-dye/DMPA = 1:x.

Ir-dye/PF_6 cast film	Ir-dye/DMPA LB multilayers	Assignments
848	-	νPF_6^-
-	934	ν_{as}(P-O-C)asym stretch
989	995	Ring breathing mode
-	1082	ν_s(O-P-O) sym phosphate stretch + ν_s(C-O-C) sym stretch
1104[a]	1103[a,b]	[a]ν(C-H) arom in-plane bend [b]ν_s(P=O) sym phosphate stretch
1166[c]	1163[c,d]	[c]ν(C-F) aryl fluoride [d]ν_{as}(C-O-C) asym stretch
-	1190	ν_{as}(C-O-C) asym stretch
1575	1577	ν(C-C)$_{arom}$, ν(C-N)$_{arom}$
1605	1604	ν(C-C)arom, ν(C-N)$_{arom}$
-	1735	ν_s(C=O) sym stretch
-	2850	ν_s(CH_2) sym stretch
-	2920	ν_{as}(CH_2) asym stretch
-	2960	ν_{as}(CH_3) asym stretch

Abbreviations: ν, stretching; δ, bending/deformation; arom, aromatic; subscripts as and s denote antisymmetric and symmetric modes, respectively. Superscripts a-d denote particular assignments for the two different films.

Table 3.2: Band positions (cm^{-1}) and assignments for the main peaks of the films shown in Fig. 3.32.

Reflection measurements

Reflection spectroscopy permits the direct detection of the presence of chromophores situated at the air−water interface.[25] In this work, reflection spectra were recorded at different surface pressures (π) for the Ir-dye/DMPA = 1:x (x = 1, 2, 5) mixed films. As an example, Figure 3.30a shows a series corresponding to the equimolecular mixed monolayer. For comparison, the Ir-dye solution spectrum in CH_2Cl_2:CH_3OH (4:1 v/v) has been also included

(dash line). These reflection measurements clearly show that the Ir-dye is incorporated in the monolayer.

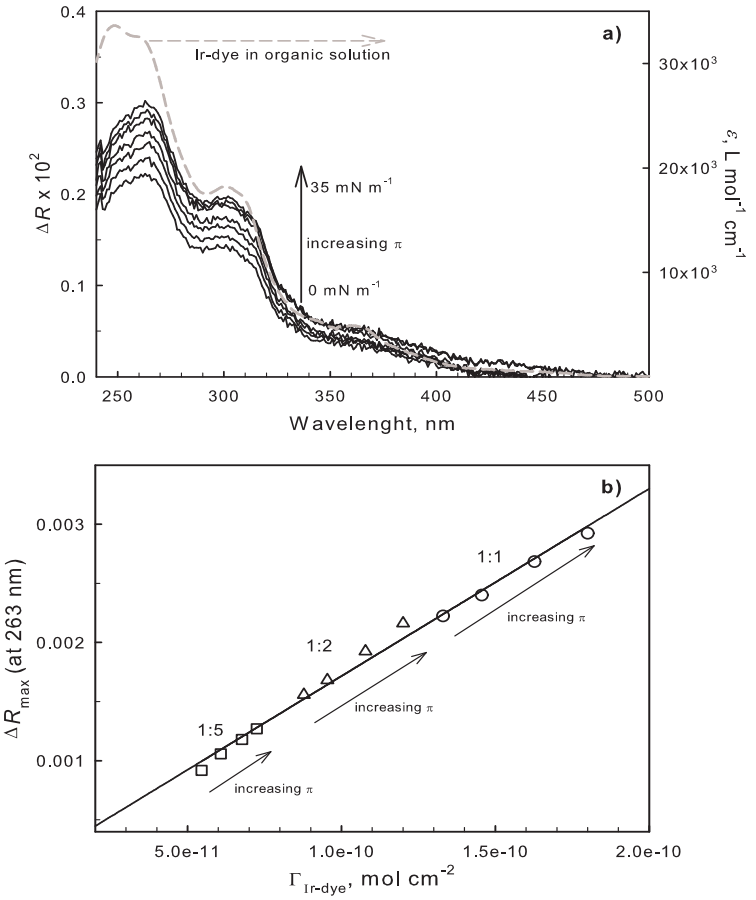

Figure 3.30: a) Reflection spectra of an Ir-dye/DMPA = 1:1 monolayer at different surface pressures (solid lines, spectra recorded each 5 mNm^{-1}), and absorption spectrum of the Ir-dye organic solution (dichloromethane-methanol 4:1 v/v); b) ΔR_{max} at 263 nm *versus* Γ_{Ir-dye} of Ir-dye/DMPA = 1:1 (circles), 1:2 (triangles), and 1:5 (squares) monolayers measured at π = 5, 10, 20 and 30 mN m^{-1}, and the corresponding linear regression (solid line).

The electronic transitions of the chromophore in the mixed films can be assigned by comparison with the solution spectrum. The intense absorption

band located in the UV region seems to arise from the contribution of at least two bands with maxima at 250 and 260 nm (see the solution spectrum). These bands are due to ligand-centered $\pi - \pi^*$ transitions of both bpy and F_2-ppy ligands.[29] In the reflection spectra these main UV bands are shifted toward the longer wavelength region. One peak is located at 263 nm, and the red shift of the band at 250 nm must be even higher, since both peaks appear together as a non-defined main band.

The reflection intensity increases with the surface pressure applied (Figure 3.30a), indicating that the surface density of the chromophore increases under compression of the film. Every mixture investigated shows a similar behavior and several phenomena can be detected in these spectra. First, the reflection spectra of every mixture investigated fit perfectly in shape. Second, all the reflection spectra of the different mixed films, measured at different π, are also coincident in the maximum band positions, i.e., no band shifts are observed during the compression process.

For low values of absorption, the reflection ΔR is given in a reasonable approximation by[25]

$$\Delta R = 2{,}303 \cdot 10^3 \, \Gamma_{Ir-dye} \, f_{orient} \, \varepsilon \, \sqrt{R_S} \tag{3.23}$$

where Γ_{Ir-dye} is the surface concentration of Ir-dye in mol cm^{-2}, $R_S = 0.02$ the reflectivity of the air−water interface at normal incidence,[30] ε the extinction coefficient given as L mol^{-1} cm^{-1}, and f_{orient} is a numerical factor that takes into account the particular orientation of the transition moment of the dye in solution, as compared to the monolayer at the air−water interface.[31,32]

Figure 3.30b plots the maximum value of reflection (at λ = 263 nm) *vs* the theoretical Ir-dye surface concentration at 5, 10, 20 and 30 mN m^{-1} for the Ir-dye/DMPA = 1:1 (circles), 1:2 (triangles) and 1:5 (squares) mixed monolayers. The Γ_{Ir-dye} values have been obtained from Γ_{DMPA} (from the isotherms) and the ratio of the Ir-dye in each mixture, and assuming no loss of dye molecules. As observed, the experimental values of ΔR_{max} at 263 nm of the different mixtures approximately fit a linear regression (solid line), i.e., of $\Delta R \times A \sim$ constant. Considering as an approximation $f_{orient} = 1$ (pseudospherical molecule),[21] the molar absorption coefficient of the Ir-dye in the mixed monolayers can be calculated from the slope of the regression shown in Figure 3.30b, obtaining ε_{263} = 4.9 x 10^4 L mol^{-1} cm^{-1}. This value is higher than that obtained in solution (ε_{260} = 3.2 x 10^4 L mol^{-1} cm^{-1}, see Figure 3.30a). The disagreement between these values can be related to the fact that both UV bands in the reflection spectra are located closer than in the solution spectrum, but can also be due to an almost flat orientation of the ligand (or ligands) responsible for the band with maximum at 263 nm, which would imply $f_{orient} > 1$.[32] In fact, the fluorinated ppy ligands are highly hydrophobic, and must be oriented toward the gas phase, while the bpy ligand is expected to be oriented towards the water subphase.

From the above arguments a constant value of $\Delta R_{max} \times A$ is obtained, and this result infers that, in all monolayers, the initially co-spread Ir-dye molecules remain at the interface during the compression process. Also, the organization of Ir-dye molecules at the air−water interface appears to be independent of the mixing ratio of the monolayer, and the formation of new dye aggregates or structures during the compression can be discarded, since

for all the reflection bands $\Delta\lambda \sim 0$ nm is found. Thus, these mixed films behave differently than a similar system recently investigated,[15] containing a non-fluorinated iridium derivative, in which J-aggregates of the iridium complex are detected by reflection spectroscopy at high π, which is consistent with a change in the slope of the $\pi - A$ isotherms, a phenomenon that has not been observed in the mixed systems investigated in this work (see isotherms in Figure 3.28).

Brewster angle microscopy (BAM)

Simultaneously to the $\pi - A$ isotherm recording, the mixed Langmuir films were directly visualized by BAM. Figure 3.31 shows images taken at different increasing surface pressures, that correspond to the Ir-dye/DMPA = 1:1 (up row, left), 1:2 (up row, right) and 1:5 (bottom row) mixed films. In the case of the equimolecular mixed film, a homogeneous monolayer is observed during the compression process, although a gradually increasing reflectivity of the surface up to reaching the collapse pressure (~ 38 mN m^{-1}) is detected. The brightness of the images had to be rescaled to improve their quality.

Compared to the equimolecular film, increasing fractions of lipid in the initially cospread mixture, 1:2 and 1:5, lead to monolayers with different morphologies, as observed in the images series shown in Figure 3.31. Up to a certain surface pressure, these mixed films seem to be homogeneous. Then, spontaneous small domains are detected along the whole visualized area, with lower brightness than the bulk phase in the case of the 1:2 mixed film, but brighter than the surrounding area for the 1:5 monolayer. The surface

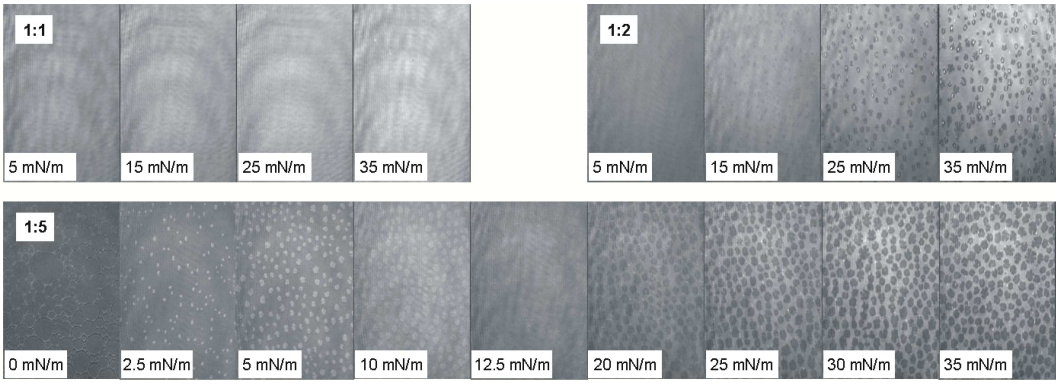

Figure 3.31: BAM images recorded simultaneously to the compression of the mixed monolayers Ir-dye/DMPA = 1:1 and 1:2 (up row, left and right, respectively), and 1:5 (bottom row). Image size: 430 μm width.

pressure at which such domains appear depends on the spreading ratio of the two components, and takes place at around 10 mN m^{-1} and 1.8 mN m^{-1} for Ir-dye/DMPA = 1:2 and 1:5, respectively. The amount and size of these domains become larger upon further compression, as well as the reflectivity of the bulk phase.

The behaviour of the Ir-dye/DMPA = 1:5 mixed monolayer in comparison with the other mixtures should be mentioned. In this case an inversion of the reflectivity of domains/bulk phase seems to happen at 12.5 mN m^{-1}. In fact, the reflectivity of the domains at low and high surface pressure is the same, although the reflectivity of the surrounding area increases gradually during the compression process. The contrast in the BAM images arises from a different film thickness and/or refractive index of the phases. Considering that the reflectivity of both phases is quite similar, the reflection intensity of the images had to be rescaled to improve the contrast, which caused this visual effect.

Although the imaging ellipsometry technique employed here allows the measurement of the ellipsometric angles Δ and Ψ over the different regions or domains visualized at the surface (i.e. regions of interest, ROI), it was unfeasible to carry out those measurements, since the domains were continuously moving, possibly as a consequence of being immersed in a liquid bulk phase. Fortunately, the measurement of the reflection intensity in different ROIs could be successfully carried out for the Ir-dye/DMPA systems, by using the recorded BAM images. In this way, a similar value of reflection intensity was obtained for the domains measured both at low and high surface pressures. Furthermore, these values were also coincident with those obtained in the domains formed in a pure DMPA monolayer.

3.3.4. Discussion

Simulation of isotherms and ellipsotherms by the additivity rule

As previously mentioned, the isotherms of Ir-dye/DMPA = 1:x mixed monolayers are expanded with respect to that for the pure lipid (Figure 3.28). This is indicative of the presence of the dye at the interface and, considering that the pure Ir-dye does not form a monolayer on the water surface, one can conclude that the DMPA matrix organizes the dye molecules at the interface.

The nature of the interaction between both molecules, as well as the molecular arrangement in the mixed system, can be examined by the miscibility of the two components. However, since the pure Ir-dye isotherm is unknown, miscibility studies between DMPA and Ir-dye can not be carried out. The pro-

perties of a mixed monolayer in which two components are immiscible reflect the properties of the separating individual component. Monolayer collapse behaviour at different compositions is a good indication of miscibility of the components of the system. When the components in the mixed system are immiscible, the formed monolayer collapses at a π corresponding to the component that collapses at the lower π, which forms the comparatively less stable monolayer.[10] This provides therefore a useful tool for detecting miscibility in multicomponent monolayers. It should be noted, however, that this criterion determines miscibility at the collapse surface pressure; it is possible for films at low pressure to be miscible, with phase separation occurring on compression, but before collapse. For pure DMPA, the collapse π is above 45 mN m^{-1}.[33] On the other hand, the mixed films investigated collapse at a similar pressure, 38 mN m^{-1}, regardless of the initial spread proportion. Thus, two immiscible monolayers, pure DMPA and a less stable Ir-dye/DMPA = 1:x film (x = 1 or 2 or 5), are expected to coexist at the air−water interface.

The stability of the mixed film is attributed to the ion pair interaction among DMPA polar heads and Ir-dye molecules. Because they are monoanionic and monocationic species, electrostatically binding in a 1:1 ratio seems to be the most preferred option. Moreover, the Ir-dye/DMPA = 1:1 monolayer is homogeneous along the whole compression process up to the collapse of the film, as revealed by BAM. Therefore, for $x > 1$, the coexistence of two immiscible monolayers, pure DMPA and the equimolecular mixture, are considered for the following discussion.

The molecular area at a given π for the Ir-dye/DMPA = 1:2 and 1:5 monolayers could be calculated by a simple additivity rule between the areas

of the isotherms of pure DMPA and the equimolecular 1:1 mixed film, as follows:

$$A_{1:2}^{cal} = \frac{A_{DMPA} + A_{1:1}}{2} \qquad A_{1:5}^{cal} = \frac{4 \times A_{DMPA} + A_{1:1}}{5} \tag{3.24}$$

where $A_{1:x}^{cal}$ represents the molecular area per DMPA calculated by the additivity rule for the 1:x mixed monolayer, A_{DMPA} the molecular area per DMPA in the pure DMPA isotherm, and $A_{1:1}$ means the molecular area per DMPA in the isotherm of the equimolecular mixed film, all of them at a given π.

The simulated $\pi - A_{1:x}^{cal}$ isotherms are shown in Figure 3.32 by closed and open circles for Ir-dye/DMPA = 1:2 and 1:5, respectively. Additionally, the experimental isotherms are included for comparison (solid and long-dash lines). A clear convergence among calculated and experimental isotherms is observed at high surface pressures, but there is a clear deviation at low and intermediate surface pressures. Coincident isotherms would correspond to a situation in which a pure DMPA monolayer coexists with the equimolecular mixed film at the air−water interface. Obviously, this deviation in the isotherms suggest that the molecules are differently arranged along the low and intermediate pressures range, but this hypothetical situation of two coexisting immiscible monolayers seems to exist only at high π, prior to the collapse of the films.

Considering the ellipsometric data, a similar treatment has been carried out by applying the additivity rule. The calculated ellipsotherms of the 1:2 and 1:5 mixed monolayers have been obtained by the simple substitution of A by Δ values in Eq. 3.3.4. However, although the simulated ellipsotherms

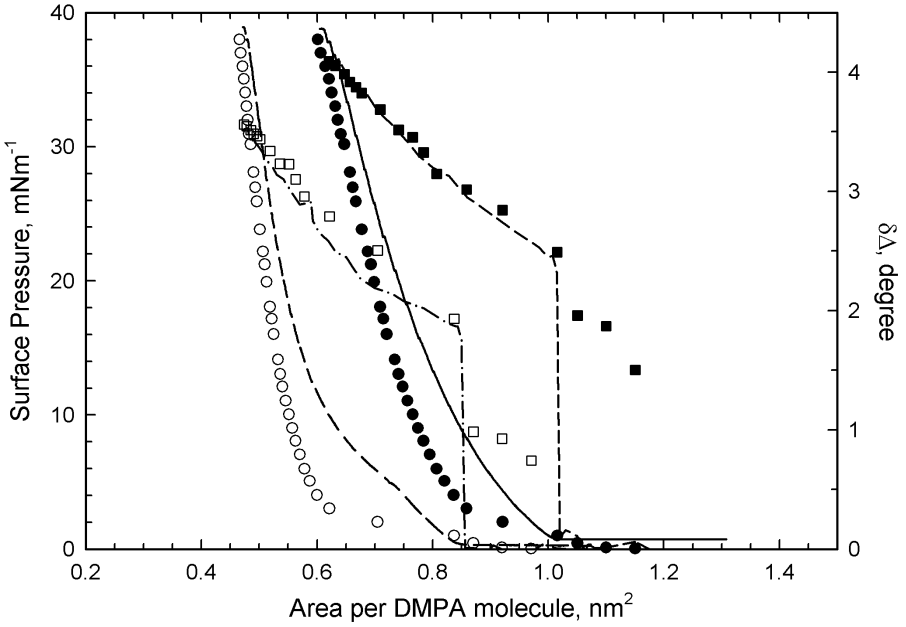

Figure 3.32: Comparison between the experimental isotherms of the Ir-dye/DMPA = 1:2 and 1:5 monolayers (solid and long-dash lines) and the calculated by the additivity rule (closed and open circles, respectively). Measured ellipsotherms of the Ir-dye/DMPA = 1:2 and 1:5 films (short-dash and dash-dot lines, respectively), and simulated ellipsotherms corrected by the molecular area fraction (closed and open squares). See text for details.

are close to the experimental data (data not shown), calculated Δ angles deviate at intermediate and high surface pressures. Indeed, the simulation of the ellipsotherms can be improved by modifying the additivity rule with a correction factor that accounts the fraction of the molecular area of DMPA at each π. This fraction is obtained from the isotherms of pure DMPA and the equimolecular mixed film.

$$\begin{aligned} \Delta_{1:2}^{cal} &= \Delta_{DMPA} \times \frac{A_{DMPA}}{A_{DMPA} + A_{1:1}} + \Delta_{1:1} \times \frac{A_{1:1}}{A_{DMPA} + A_{1:1}} \\ &\textit{and} \\ \Delta_{1:5}^{cal} &= \Delta_{DMPA} \times \frac{4 \times A_{DMPA}}{4 \times A_{DMPA} + A_{1:1}} + \Delta_{1:1} \times \frac{4 \times A_{1:1}}{A_{DMPA} + A_{1:1}} \end{aligned} \tag{3.25}$$

where $\Delta_{1:x}^{cal}$ is the angle calculated by the corrected additivity rule for the 1:x mixed monolayer. The $\Delta_{1:x}^{cal} - \Delta_{1:x}^{cal}$ isotherms are also included in Figure 3.32, by closed and open squares for $x = 2$ and 5, respectively. As clearly observed in the different curves, high concordance is now achieved between the experimental (short-dash and dot-dash lines, for $x = 2$ and 5) and the simulated ellipsotherms.

Analysis of BAM images

Further information on the molecular organization of the Ir-dye/DMPA = 1:x monolayers can be extracted from a detailed analysis of the BAM images shown in Figure 3.31. The molecular area per DMPA in the isotherm of a mixture Ir-dye/DMPA = 1:x (A) can be calculated using $A = A_d x_d + A_b x_b$, where $x_d = x/(1+x)$, A_d and A_b are the molecular area of DMPA in domains and bulk phase, and x_d and x_b represent the molar fraction of DMPA in domains and bulk phase. Also, the molar fraction of DMPA in domains can be expressed as a function of the fraction such domains surface area measured in the BAM images (f_d), calculated by using the SigmaScan image processing program,[34]

$$x_d = \frac{f_d/A_d}{f_d/A_d + (1 - f_d)/A_b} \tag{3.26}$$

where f_d/A_d is proportional to the number of moles of DMPA in the domains, while $(1 - f_d)/A_b$ is to those of DMPA situated in surrounding areas. From these equations, A can be expressed as

$$\frac{1}{A} = \frac{1}{A_b} + f_d(\frac{1}{A_d} - \frac{1}{A_b}) \tag{3.27}$$

The graphical plot of the inverse of A (values obtained from the isotherm) *versus* f_d must keep a linear relationship, from which the values A_b and A_d can be obtained. Figure 3.33 shows these plots for the Ir-dye/DMPA = 1:2 (closed circles) and 1:5 (open circles) films, as well as their corresponding linear regression (solid line). The areas occupied by each DMPA molecule in domains and surrounding area are calculated from this linear regression, giving $A_d = 0.38$ nm^2 and $A_b = 0.88$ nm^2 for the 1:2 and 1:5 monolayers. In fact, the value A_d calculated agrees with that obtained for a dense-packed DMPA monolayer, which is a clear evidence of the absence of the iridium derivative in the domains. On the other hand, the critical area A_b represents the surface area occupied by one lipid molecule localized on the top of an iridium derivative, i.e., the area occupied by each Ir-dye, which controls the molecular organization of the mixed film. As observed, A_b approximately agrees with the area per DMPA reached at high surface pressure in the equimolecular mixed film ($\sim$0.85 nm^2, see isotherm in Figure 3.28).

The lower reflectivity in the domains is related to the absence of metal chromophore in this region. Once the formation of small domains starts, DMPA molecules are being distributed in two different phases that coexist in equilibrium, similar as in the pure DMPA monolayer.[33] However, in these systems, the more expanded phase corresponds to the surrounding area

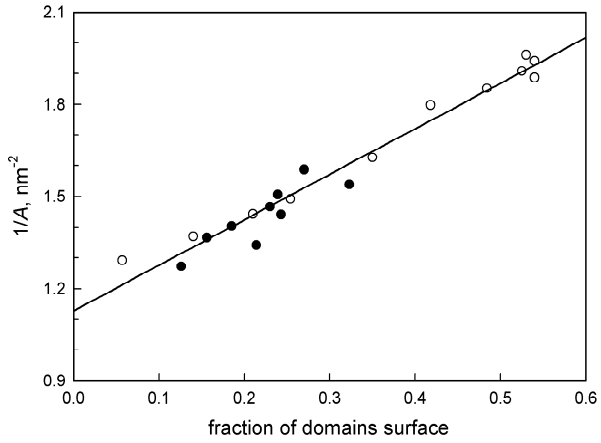

Figure 3.33: Plot of the inverse of the molecular area per DMPA (obtained from the isotherms, Figure 3.28) *vs* fraction of domains surface area (obtained from BAM images, Figure 3.30), for the Ir-dye/DMPA = 1:2 and 1:5 monolayers at the air−water interface (closed and open circles, respectively), and the corresponding linear regression (solid line).

or bulk phase (Ir-dye/DMPA mixture), while the more condensed phase to domains (pure DMPA).

In the Ir-dye/DMPA = 1:5 mixed film an inversion of reflectivity is observed. The first domains are visualized at low surface pressure ($\sim$ 1.8 mN m^{-1}), when the bulk phase contains low Ir-dye surface density, and therefore also shows low reflectivity. However, as the film is compressed, the migration of lipid molecules from the bulk phase to form bigger domains occurs and the Ir-dye surface density increases in the surrounding areas, and consequently the reflectivity in the bulk phase increases. From π = 12.5 mN m^{-1}, the mixed 1:5 and 1:2 monolayers behave similarly, i.e., dark domains coexisting with a bright bulk phase. In Figure 3.33, the values of f_d corresponding to the bright domains observed by BAM, for the Ir-dye/DMPA = 1:5 at $\pi <$ 12.5 mN m^{-1}, have been also included in the adjustment to calculate A_d

and A_b. This provides clear evidence that the composition of bright and dark domains has to be the same, *i.e.*, dense DMPA.

According to the value of A_d calculated from Figure 3.33, the domains are exclusively formed by the lipid migrated from the bulk phase. The segregation of the excess of DMPA with respect to the equimolecular ratio begins when an area A $\sim$ 0.88 nm^2 is reached ($A = A_b$), independently of the value of x in the mixture, i.e., at π = 7.5 and 0.2 mN m^{-1} for the Ir-dye/DMPA = 1:2 and 1:5 monolayers, respectively. As expected, although the molecular segregation of DMPA molecules to form domains occurs from the latter surface pressures, these domains are too small to be detected by BAM, and only from approximately π = 10 (for 1:2) and 1.8 (for 1:5) mN m^{-1}, the new phase can be observed (Figure 3.31).

The molecular area at which the surplus of lipid is totally expelled from the bulk phase can be calculated using $A = A_d x_d + A_b x_b$. The molecular segregation of DMPA, which is produced by the excess of lipid from the 1:1 molar ratio, should be completed at 0.88, 0.63 and 0.48 nm^2/DMPA for the Ir-dye/DMPA = 1:1, 1:2 and 1:5 monolayers, respectively. Surprisingly, these areas practically coincide with those reached at high π, previous to the collapse of the different films: 0.85, 0.62 and 0.48 nm^2/DMPA for x = 1, 2 and 5 (see isotherms in Figure 3.28).

3.3.5. Conclusions

A novel hydrophobic fluorinated iridium (III) derivative has been successfully organized in mixed Langmuir films, by using a charged lipid matrix of

DMPA. Several mixed Ir-dye/DMPA = 1:x monolayers (x = 1, 2 or 5) have been investigated by means of surface techniques as $\pi - A$ isotherms, imaging ellipsometry, BAM and reflection spectroscopy.

Collapse pressure and the application of the additivity rule are indicators of the degree of miscibility of the two components of the mixture system. The experimental data (BAM, ΔR and $\delta\Delta$) reveal that the mixture with an Ir-dye/DMPA ratio of 1:1 is totally miscible and leads to the formation of a homogeneous and stable mixed monolayer at the air−water interface. Due to the hydrophobic character of the fluorinated ligands of the Ir-dye, the chromophores in the mixed films are preferred oriented at the air−water interface, with the F_2-ppy ligands situated towards the gas phase, and the bpy to the water subphase. In the case of Ir-dye/DMPA = 1:x mixtures, with $x > 1$, the films are totally miscible at low surface pressures. However, any surplus of DMPA in the spreading mixture with respect to the equimolecular monolayer is segregated from the bulk phase to form domains upon compression of the film, from $A = 0.88$ nm^2, independently of the value of x in the Ir-dye/DMPA = 1:x mixture (*i.e.*, x = 2, 3, 4, etc). The segregation of DMPA continues until high surface pressure, up to the collapse of these films. At this point, two immiscible phases coexist in equilibrium: the Ir-dye/DMPA = 1:1 monolayer (bright bulk phase), and the excess pure DMPA (dark domains).

The additivity rule has been applied for the first time, as far as we know, for the analysis and treatment of the ellipsometric data to predict the ellipsotherms in mixed monolayers. However, it has to be remarked that this new method has to be handled with care and used only under specific situations as those described in this work: absence of absorption of the sample at the

laser wavelength, and a similar reflectivity of both coexisting phases, domains and bulk phase. Furthermore, in this work, the additivity rule has not been applied between two pure compounds. Instead, the simulation of isotherms and ellipsotherms of the 1:2 and 1:5 mixed films has been successfully realized by the additivity between the corresponding curves of pure DMPA and the 1:1 mixed films.

Finally, by using the DMPA lipid matrix, the pseudospherical fluorinated Ir-dye is not only organized at the air−water interface, but also undesired aggregation phenomena are avoided. Furthermore, what is more interesting, the presence of the photofunctional iridium derivative can be confined to certain regions of the monolayer. The fraction of surface containing the dye can be controlled by varying both the fraction of lipid in the spreading mixture and the surface pressure applied to the monolayer. These two regions containing different compositions also present different optical properties such as refraction index and absorptivity, which can lead to films with very interesting optical and electronic properties.

Acknowledgments

The authors thank the Spanish CICYT for financial support of this research in the framework of Projects No. CTQ2004-03246/BQU, CTQ2007-64474/BQU and MAT2004-03849. Also, we thank the Ministerio de Educación y Ciencia and Junta de Andalucía for the contracts (Ramón y Cajal Program and Proyecto de Excelencia) and the research fellowship (Formación de Profesorado Universitario) of three of the authors.

References

1. Roberts, G. G. *Langmuir-Blodgett Films;* Plenum: New York, 1990.

2. Ulman, A. *An Introduction to Ultrathin Organic Films from Langmuir-Blodgett to Self Assembly;* Academic Press: San Diego, 1991.

3. Wiegand, G.; Jaworek, T.; Wegner, G.; Sackmann, E. *Langmuir* **1997,** *13,* 3563.

4. Chen, P.; Gao, P.; Zhan, C.; Liu, M. *ChemPhysChem* **2005,** *6,* 1108.

5. Pérez-Morales, M.; Pedrosa, J. M.; Martín-Romero, M. T.; Möbius, D.; Camacho, L. *J. Phys. Chem. B* **2004,** *108,* 4457.

6. Vossmeyer, T.; DeIonno, E.; Heath, J. R. *Angew. Chem. Int. Ed.* **1997,** *36,* 1080.

7. Smith, R. K.; Lewis, P. A.; Weiss, P. S. *Progress in Surface Science* **2004,** *75,* 1.

8. Mamin, H. J.; Rugar, D. *Appl. Phys. Lett.* **1992,** *61,* 1004.

9. Xie, X. N.; Chung, H. J.; Sow, C. H.; Wee, A. T. S. *Mat. Sci. Eng. R* **2006,** *54,* 1.

10. Gaines, G. L.*Insoluble Monolayers at Liquid-Gas Interfaces;* Wiley-Interscience: New York, 1966.

11. Hada, H.; Hanawa, R.; Haraguchi, A.; Jonezawa, Y. *J. Phys. Chem.* **1985,** *89,* 560.

12. Kuhn, H. *Thin Solid Films* **1989,** *178,* 1-16.

13. Santos, J. P.; Zaniquelli, M. E. D.; Batalini, C.; Ferraresi De Giovani, W. *Thin Solid Films* **1999,** *349,* 238.

14. Lu, W. X.; Guo, W. H.; Zhou, H. L.; He, P. S. *Langmuir* **2000,** *16,* 5137.

15. Giner-Casares, J. J.; Pérez-Morales, M.; Bolink, H. J.; Muñoz, E.; de Miguel, G.; Martin-Romero, M. T.; Camacho, L. *J. Coll. Int. Sci.* **2007,** *315,* 278.

16. Goldsmith, J. I.; Hudson, W. R.; Lowry, M. S.; Anderson, T. H.; Bernhard, S. *J. Am. Chem. Soc.* **2005,** *127,* 7502.

17. DeRosa, M. C.; Hodgson, D. J.; Enright, G. D.; Dawson, B.; Evans, C. E. B.; Crutchley, R. J.*J. Am. Chem. Soc.* **2004,** *126,* 7619.

18. Baldo, M. A.; O'Brien, D. F.; You, Y.; Shoustikov, A.; Silvey, S.; Thompson, M. E.; Forrest, S. R. *Nature* **1998,** *395,* 151.

19. Holder, E.; Langeveld, B. M. W.; Schubert, U. S. *Adv. Mater.* **2005,** *17,* 1109.

20. Bolink, H. J.; Cappelli, L.; Coronado, E.; Gratzel, M.; Orti, E.; Costa, R.; Viruela, P.; Nazeeruddin, M. K. *J. Am. Chem. Soc.* **2006,** *128,* 14786.

21. Huesmann, H.; Bignozzi, C. A.; Indelli, M. T.; Pavanin, L. A.; Rampi, M. A.; Möbius, D. *Thin Solid Films* **1996,** *284-285,* 62.

22. Lu, W. X.; Zhou, H. L.; He, P. S.; Guo, W. H. *Thin Solid Films* **2000,** *365,* 67.

23. Santos, J. P.; Zaniquelli, M. E. D.; Batalini, C.; De Giovani, W. F. *J. Phys. Chem. B* **2001,** *105,* 1780.

24. Samha, H. A.; Martinez, T. J.; Dearmond, M. K.; Garces, F. O.; Watts, R. J. *Inorg. Chem.* **1993,** *32,* 2583.

25. Grüniger, H.; Möbius, D.; Meyer, H. *J. Chem. Phys.* **1983,** *79,* 3701.

26. Azzam, R. M. A.; Bashara, N. M. *Ellipsometry and Polarized Light;* Elsevier Science B. V.: Amsterdam, The Netherlands, 1999.

27. Shurvell, H. F. *Sample Characterization and Spectral Data Processing;* volume 3 of *Handbook of Vibrational Spectroscopy* John Wiley and Sons Ltd: 2001.

28. Nakamoto, K. *Infrared and Raman spectra of inorganic and coordination compounds;* John Wiley and Sons Inc., New York.: 1986.

29. Colombo, M. G.; Hauser, A.; Gadel, H. U. *Inorg. Chem.* **1993,** *32,* 3088.

30. Grüniger, H.; Möbius, D.; Lehmann, U.; Meyer, H. *J. Chem. Phys.* **1986,** *85,* 4966.

31. Martín, M. T.; Prieto, I.; Camacho, L.; Möbius, D. *Langmuir* **1996,** *12,* 6554.

32. Pedrosa, J. M.; Martín-Romero, M. T.; Camacho, L.; Möbius, D. *J. Phys. Chem. B* **2002,** *106,* 2583.

33. Möhwald, H. *Ann. Rev. Phys. Chem.* **1990,** *41,* 441.

34. "Sigma Scan Pro", SPSS inc, Chicago, 1999.

Capítulo 4

Simulación de Monocapas de Langmuir mediante Dinámica Molecular

4.1. Effect of the Barometric Phase Transition of a DMPA Bilayer on the Lipid/Water Interface

Understanding the structure and dynamics of phospholipid bilayers is of fundamental relevance in biophysics, biochemistry and chemical physics. Lipid Langmuir monolayers are used as a model of lipid bilayers because they are much more easily studied experimentally, although some authors question the validity of this model. With the aim of throwing light on this debate, we used Molecular Dynamics simulations to obtain an atomistic description of a membrane of $DMPA^-$ (Dimyristoylphosphatidic acid) under different surface pressures. Our results show that, at low surface pressure, the interdigitation between opposite lipids (that is, back-to-back interactions) controls the system structure. In this setting and due to the absence of this effect in the Langmuir monolayers, the behavior between these two systems differs considerably. However, when the surface pressure increases the lipid interdigitation diminishes and so, monolayer and bilayer behavior converges. In this work, four computer simulations were carried out, subjecting the phospholipids to lateral pressures ranging from 0.17 to 40 mN/m. The phospholipids were studied in their charged state since this approach is closer to the experimental situation. Special attention was paid to validating our simulation results by comparison with available experimental data, therebeing in general, excellent agreement between experimental and simulation data. In addition, the properties of the lipid/solution interface associated with the lipid barometric phase transition were studied.

Paper published in *J. Phys. Chem. B*, 2007, 111, 13726-13733

4.1.1. Introduction

This work was focused on the venerable and still prominent topic of Lipid Bilayer structure, which plays a crucial role controlling the diffusion of nutrients, ions and water between the inner and outer cell together, while providing a suitable environment to other molecules embedded in the membrane, such as membrane proteins or cholesterol, among others.[1,2] Understanding the atomic interactions that control the behavior of this complicated system is of unquestionable importance. One of the aspects that has attracted increasing interest during recent decades is the polymorphic phase transition of lipid bilayers associated with temperature, due to the importance of this process from a biological viewpoint. In this respect, a temperature denoted Transition Temperature (T_m) defines the temperature at which lipids change from a gel (P'_β) to a liquid crystaline state (L_α) at a constant external pressure.[3,4]

However, polymorphic phase transition may also be associated with different states induced by an external pressures or barometric transition.[5,6] To understand the atomic interactions that govern these phase transitions induced by an external pressure, Langmuir air-water lipid monolayers have been widely studied,[7] mainly because they enable the surface pressure on the lipids that form the monolayer to be studied, and also because a monolayer is basically half of a symmetric lipid bilayer. For this purpose, different experimental techniques have been used, such as scattering techniques, X-ray and Neutron Reflectivity Measurements, Infrared Reflection-Absorption Spectrometry (IRRAS), NMR studies and the Ellipsometric technique.[7–13] In

the case of monolayers, different barometric phases have been denoted, such as G (gaseous); LE (liquid expanded); LC (liquid condensed) and SC (solid condensed).[7]

Improvements made in simulation algorithm and the increases in the computing power attained during recent years have led to Molecular Dynamics Simulation[14] emerging as a powerful and precise technique that provides atomic detail insight into the dynamic and steady properties related with lipid bilayers and monolayers.[15–19] Keeping this in mind, with the aim of obtaining an atomic insight into the interactions that control the phase transition of a lipid bilayer, a computer simulation of a lipid bilayer of $DMPA^-$ was carried out. The main reasons why we chosen this type of lipid instead of DPPC or DPPE were: First, because charged lipids at physiological conditions play a crucial role in the structure and functions of cellular membranes introducing an asymmetry between the inner and outer side of the membrane, which can constitute up to 20 % of the total lipids and second, because $DMPA^-$ is a lipid widely used in the study of lipid monolayers.[9,11–13,20,21] In this setting, considering that electrostatic interactions control the lipid-lipid interactions in charged lipids,[16] it is expected that different lipid packing associated to their barometric phase transitions, can modify noticeably the lipid/water interface.

Thus, the main goal of this work was, in a first instance, to validate the force field of $DMPA^-$, since, as far as we know, this is the first time that this type of lipid has been simulated. To this end, the properties of the bilayer were studied and compared with available experimental data. After checking and validating the force field for their liquid crystaline state (L_α), the system

was subjected to high surface pressures, bringing the bilayer close to Liquid Condensed state (LC), with the goal of describing its barometric behavior. Thus, changes in the lipid structure associated with pressure are described and how these variations affect the lipid/solvent interface properties is discussed.

Assuming that lipid bilayers and monolayers are, in fact, different physical systems, our hypothesis is that these systems behave differently and we propose an explanation in terms of lipid−lipid interactions. We present here is a systematic and detailed study that supports our hypothesis. The obtained results suggest that the simulated system behaves like a bilayer in its liquid crystaline state at low surface pressure, but behaves more like a monolayer in its Liquid Condensed state, when subjected to high pressure.

For low surface pressures, the most important lipid interaction is related with lipid tail interdigitation (back−to−back interactions). However, since this kind of interaction is impossible to achieve in a lipid monolayer, monolayers do not reproduce bilayer behavior. However, at higher values of surface pressure, the interdigitation associated with lipid tails vanishes, and the most important effects are related with lateral interaction between neighboring lipids. Thus, at sufficiently high pressures, lipid bilayers and monolayers show the same behavior. In this way, as has been seen for DPPC bilayers,[19] lipid bilayers at high surface pressures reproduce Langmuir monolayer behaviour. Finally, a detailed study of the lipid/water interface was carried out for different lipid packing of the membrane.

4.1.2. Method and Model

Periodical boundary conditions were considered along the three dimensional space, X, Y and Z. The computer simulation box was generated by placing two leaflets of 144 $DMPA^-$ (i.e. 288 lipids in total), pointing the lipid heads toward the two water layers placed on both sides of the computing box. Figure 4.1 depicts two snapshots of the system at two different surface pressures. To maintain the electroneutrality of the system, 288 water molecules were substituted by 288 sodium ions (Na^+), so that the whole system was constituted by 288 $DMPA^-$, 288 Na^+ and 9780 SPCE water molecules,[22] which amounted 41436 atoms in total.

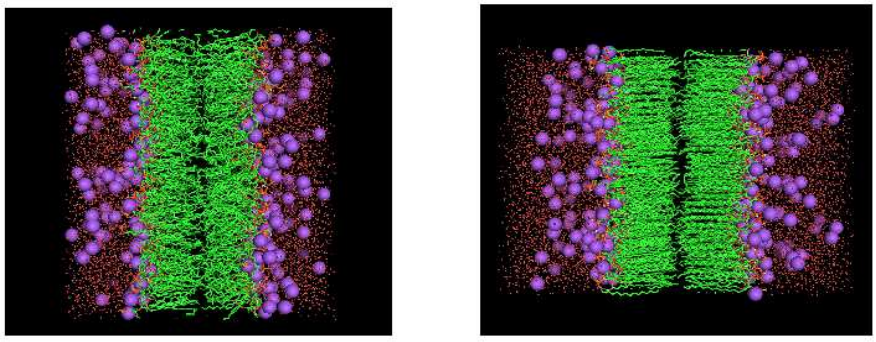

Figure 4.1: Snapshots of the $DMPA^-$ bilayer at two different surface pressures: (a) 0.17mN/m and (b) 40mN/m.

GROMACS 3.3. package[23,24] was used to run the Molecular Dynamics (MD) simulations, and the generated trajectories were analyzed with a software code developed by ourselves. A $DPPS^-$ (DipalmitoylPhosPhatidylSerine) modified force field[16] was used to carry out these simulations. The charge

distribution of a lipid $DMPA^-$ molecule was determined by CNDO semiempirical method implemented in HyperChem.[25] Thus the charge borne by each atom of the system is depicted in Table 4.1, corresponding to the atomic numeration shown in Figure 4.2. Long range interactions were modeled by the Lennard-Jones potential, with a cut-off of 0.8 nm, and the electrostatic interactions by the Ewald algorithm.[26,27] All the bonds of the system were constrained by SHAKE.[28] The time step used in all the simulations was 2 fs (femtoseconds).

Molecule	Atom number	Atom type	Charge (e)
$DMPA^-$	1	H	0.054
	2	O	-0.460
	3	P	0.680
	4	O	-0.394
	5	O	-0.394
	6	O	-0.434
	7	CH_2	-0.050
	8	CH	-0.036
	9	O	-0.196
	10	C	0.432
	11	O	-0.164
	12	CH_2	-0.036
	13-23	CH_2	0.000
	24	CH_3	0.000
	25	CH_2	0.124
	26	O	-0.202
	27	C	0.384
	28	O	-0.292
	29	CH_2	-0.014
	30-40	CH_2	0.000
	41	CH_3	0.000
Ion		Na^+	1.000
SPCE water		HW	-0.8476
		OW	0.4238

Table 4.1: Charge density for each atom of lipid $DMPA^-$ molecule, Na^+ ions and SPCE water molecules, as obtained by CNDO method.

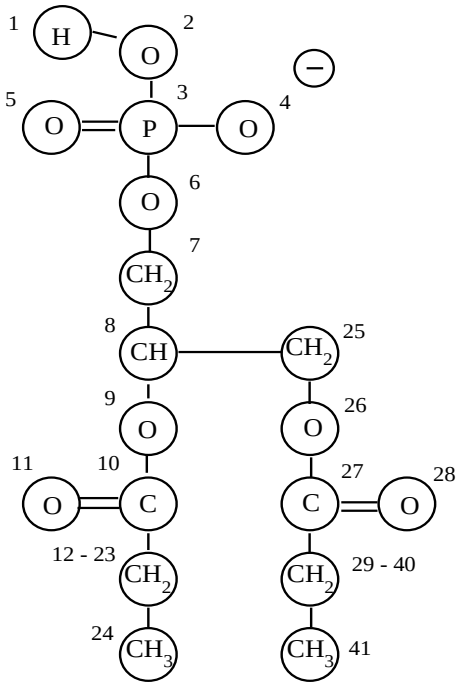

Figure 4.2: Atom numeration used in this work for a molecule of Dimyristoylphosphatidic acid, $DMPA^-$.

Simulations were carried out on a HPC160 parallel computer using 16 processors, with a performance of 1.5 ns of trajectory length per hour.

In this regard, after setting up the system, the whole system was subjected to a steepest descent energy minimization process to remove undesired overlaps between neighboring atoms.

Once the system reached a certain energy minimum, four simulations were carried out at the same normal pressure of 1 atm (Z axis) and each one to different surface pressures (in the X-Y plane of the membrane) at 1, 6, 60 and 225 atm, which corresponds to 0.17, 1, 10 and 40 mN/m, respectively. Because a thermodynamic NTP (that is, constant moles number, temperature and pressure) state has been simulated, the system was coupled to an ex-

ternal temperature and pressure bath, with temperature coupling constants of τ_T of 0.1 ps and pressure coupling constant τ_P of 1 ps. In both cases, the Berendsen's algorithm was used.[29]

To avoid undesired simulation artifacts associated to the starting conformation of the system, the first simulation at 0.17 mN/m was carried out at 500 K during 500 ps. The end conformation of this simulation was the starting point at 0.17 mN/m. Next, the system was cooled down to 350 K, and the above mentioned 4 simulations were carried out for 20 ns, where the end conformation of each trajectory was the starting point of the next simulation at higher surface pressures. In the four cases, the temperature of 350 K is above the $DMPA^-$ phase transition temperature, $T_m = 328$ K, in a range of pH from 4 to 9.[30] The first 2 ns of trajectory lenth were discarded for analysis purposes since this was the time required to reach the equilibrium in the four cases.

4.1.3. Results and Discussion

Lipid Area

Figure 4.3 depicts the area evolution of lipids as a function of time for several surface pressures. From these curves, we observe how for a trajectory length above 2 ns, the system reaches a steady state in the four cases. Thus, the dimension of the equilibrated computing boxes were: (8.82, 8.68, 7.92), (8.76, 8.72, 8.04), (8.38, 8.26, 8.75) and (7.61, 7.41, 10.27), for the x, y and z axis of the computing box in nm, at 0.17, 1, 10 and 40 mN/m surface pressure, respectively.

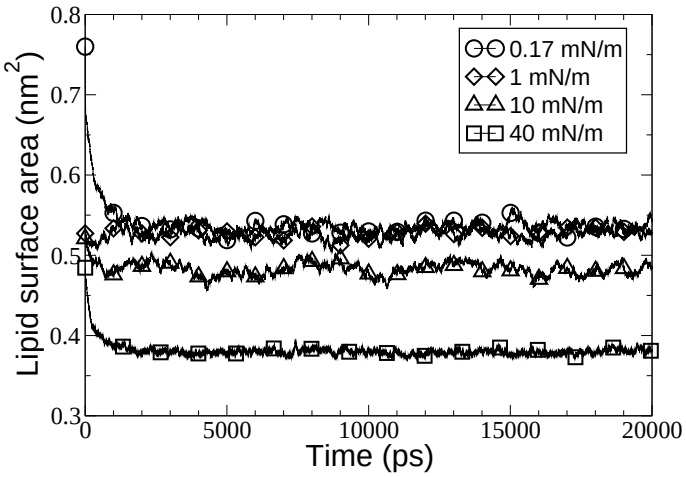

Figure 4.3: Lipid running area as a function of time for different surface pressures.

The area per $DMPA^-$ molecule obtained from our simulation was compared with experimental data. Note that at low surface pressure, 0.17 mN/m (or 1 atm), the simulated area was 0.54 ± 0.07 nm^2, which agrees well with the experimental data obtained by Ziegler et al.,[31] 0.58 nm^2 for its liquid crystaline state, L_α. At the same surface pressure, for $DMPA^-$ monolayers at the air−water interface, a surface area of 0.8 nm^2 was measured from the isotherm surface pressure-lipid area (π-A isotherm) by Lozano et al.[32] When surface pressure is increased to 40 mN/m, the surface area per $DMPA^-$ molecule obtained by our simulations was 0.40 ± 0.07 nm^2, which agrees perfectly with the area of 0.4 nm^2 obtained for monolayer π-A isotherm in its Liquid Condensed State (LC).[32] These results are depicted in Figure 4.4. The effect of the interdigitation between opposite lipid leaflets can be observed from the density of methylene groups of lipid tails of the two lipid leaflets, as shown in Figure 4.5. Thus, we observe how an increasing in the surface pressure produces a diminishing of the methylene overlap of opposite leaflets i.e. a

diminishing in the lipid-lipid interdigitation.

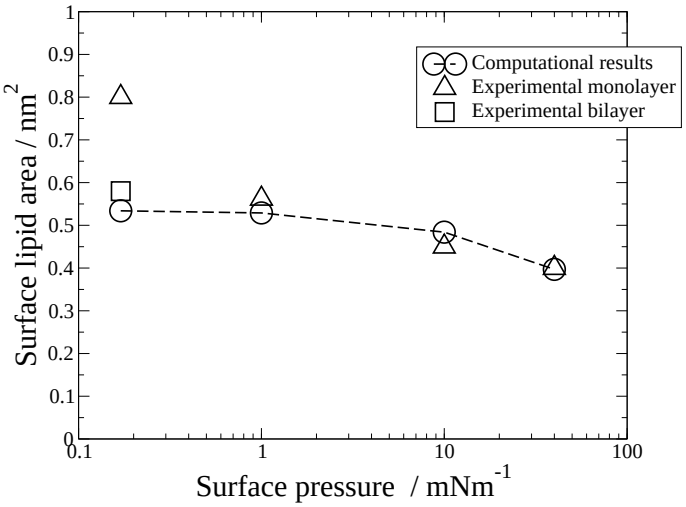

Figure 4.4: DMPA$^-$ surface area for different surface pressures: circles represent the simulated data, squares the experimental data for a DMPA$^-$ bilayers, and triangles the experimental data for DMPA$^-$ monolayers.

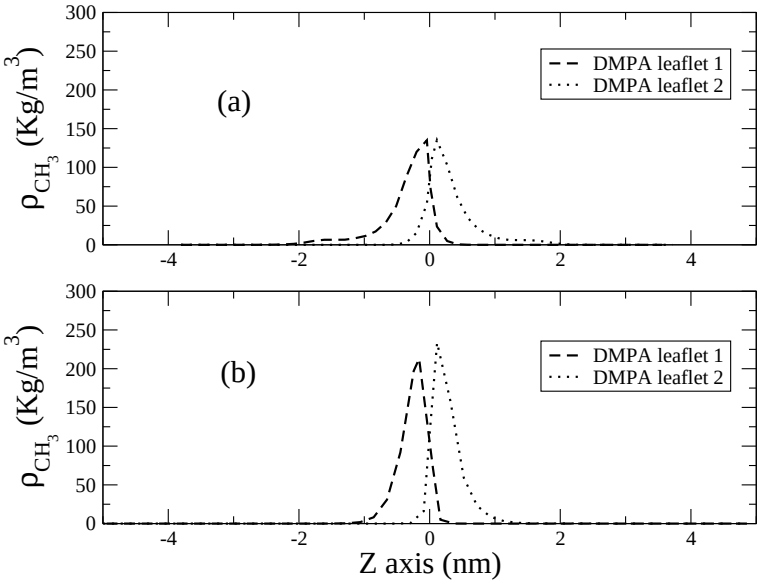

Figure 4.5: Lipid tail ethylene density ρ in kg/m^3 along the Z axis, for surface pressures of 0.17 mN/m (a) and 40 mN/m (b). The origin of the Z-axis was placed in the center of the box.

Lipid-Lipid Lateral Interactions and Lipid Hydration

The radial distribution function $g(r)$ provides valuable atomic information concerning neighboring molecules. Thus, the radial distribution function $g(r)$ is defined as:

$$g(r) = \frac{N(r)}{4\pi r^2 \rho \delta r} \tag{4.1}$$

where $N(r)$, is the number of atoms in a spherical shell at distance r and thickness δr from a reference atom, and ρ is the number density in the computing box.

Hence, the radial distribution function of the atoms numbers 4, 11 and 28 (two carbonyl and a phosphate oxygens) around the phosphorus of a neighboring lipid $DMPA^-$ was calculated. By integrating the first maximum of the radial distribution function $g(r)$, the coordination numbers of the above mentioned atoms (4, 11 and 28) over a phosphorus atom as a function of the surfaces pressures were calculated, such as depicted in Table 4.2.

Note that an increase in the surface pressure applied produces an increase in the coordination numbers $N(r)$ between lipids, which clearly reflects the importance of lateral interactions at high values of surface pressures. Indeed, the coordination number for atom 4 (phosphate oxygen) around a phosphorus atom undergoes a dramatic increase of 73 % from 0.17 to 40 mN/m. Less pronounced is the increase in coordination of the carbonyl oxygens around

Atom number	Surface pressure (mN/m)	Coordination number
4	0.17	0.26
	1	0.27
	10	0.32
	40	0.45
11	0.17	0.23
	1	0.22
	10	0.25
	40	0.28
28	0.17	0.22
	1	0.23
	10	0.25
	40	0.27

Table 4.2: Different values of coordination number around the phosphorus atoms (atom 3) by oxygen atoms (atoms 4, 11 and 28) from neighboring lipids at different value of surface pressure.

the phosphorus atom, which is only around 25 % under analogous conditions.

Coordination numbers of water oxygens around atoms 4 and 28 of the lipid molecule (oxygen of phosphate and carbonyl group, respectively) are depicted with their standard error in Figure 4.6. From this figure, we observe how there is no significant variation in the coordination number for pressures ranging from 0.1 mN/m to 10 mN/m. For higher pressures (40 mN/m or higher) a dehydration of the polar lipid heads becomes clear. To quantify this effect, the hydration number of the lipid head was calculated from the radial distribution function of water around the heads of the lipid molecules. It was found that 4.20, 4.19, 4.16 and 4.05 water molecules formed the first hydration shell around phosphate oxygen for 0.17, 1, 10 and 40 mN/m, respectively . As regards to the carbonyl oxygen tail, values of 1.12 (for 0.17 mN/m), 1.11 (for 1 mN/m), 1.09 (for 10 mN/m) and 0.85 (for 40 mN/m) were calculated. With

these data, lipid hydration, estimated as the sum of the hydration number of the phosphate group, was calculated, reaching a value of 6.44 (for 0.1 mN/m), 6.41 (for 0.17 mN/m), 6.34 (for 10 mN/m) and 5.75 (for 40 mN/m) water molecules. These values are in good agreement with experimental data provided by Schalke et al.[9] for $DMPA^-$ Langmuir monolayers, where the number of water molecules that coordinates the lipid head ranges from 6.2 to 4.8 for a surface pressure ranging from 2 to 45 mN/m, respectively.

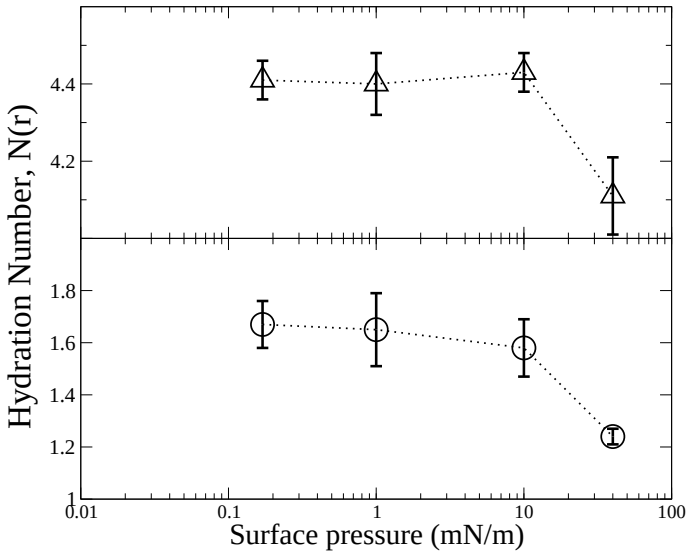

Figure 4.6: Coordination number for water molecules: Circles, carbonyl oxygens (atom 28), and triangles, phosphate oxygen (atom 4), attending atom numeration of Figure 4.2.

Hydrocarbon Tail Structure.

The structure of the hydrocarbon tail can be studied in NMR experiments by measuring the deuterium order parameters along the lipid ethylene tails. The order parameter tensor is defined as

$$S_{ab} = \frac{\langle 3\cos(\theta_a)\cos(\theta_b) - \delta_{ab}\rangle}{2} \qquad a, b = x, y, z \tag{4.2}$$

where x and y and z are the local coordinates of the system, θ_a is the angle made by the molecular axis with the bilayer normal, and δ_{ab} is the Kronecker delta. From simulation, the order parameter, $-S_{CD}$, can be determined using the relation proposed by Egberts and Berendsen[33]

$$-S_{CD} = \frac{2S_{xx}}{3} + \frac{S_{yy}}{3} \tag{4.3}$$

where S_{xx} and S_{yy} are the terms of the order parameter tensor of equation 4.2.

Using equation 4.2, we can calculate the order parameters of a $DMPA^-$ molecule for different surface pressures. In Figure 4.7 these results can be compared with experimental data of the $DMPA^-$ bilayer in its liquid crystaline state.[20] From a comparison simulation with experimental data, we observe the good agreement between both results at low pressures. Moreover, from the simulation, we observe how the hydrocarbon structure of the lipid tails is not perturbed at surface pressures up to 1 mN/m. Above this, increasing the surface pressures increases the order of the lipid tails. This increase is more noticeable for pressures above 40 mN/m, corresponding to the pressure at which the barometric transition state of the lipids takes place from its liquid crystaline state (L_α) to gel state (L'_β), which is comparable

with the liquid condensed state (LC) in lipid monolayers.

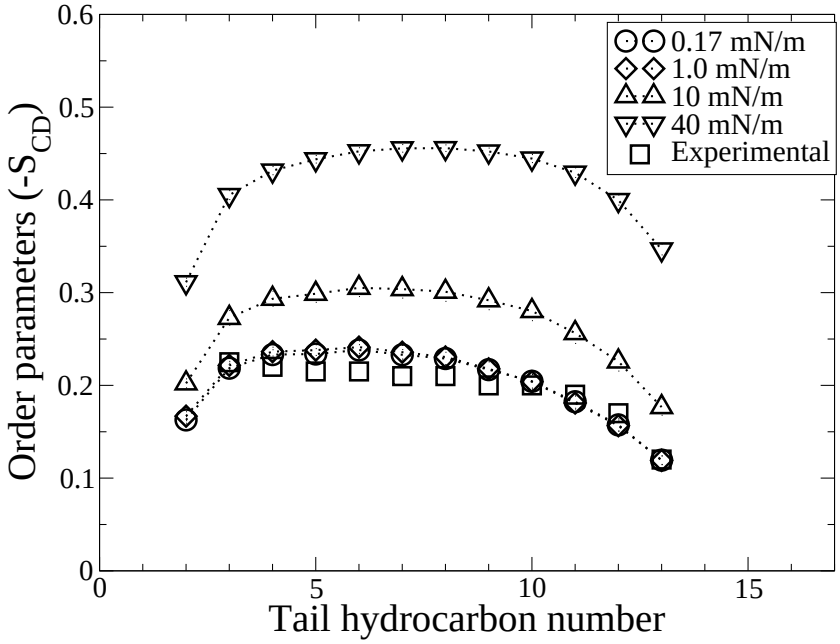

Figure 4.7: Order parameters ($-S_{CD}$) along hydrocarbon tails for 0.17, 1, 10 and 40 mN/m. The experimental results[20] are represented by squares.

Furthermore, an angle θ was defined as the angle between the vector along the lipid chains and the perpendicular direction to the lipid/water interface. The values of the angle θ obtained were of θ = 29.5, 29.7, 22.1, and 9.2. degrees for 0.17, 1, 10 and 40 mN/m, respectively. In this regard, Schale et al.,[9] measured an angle θ of 9 degrees at 40 mN/m by X-ray, which is in good agreement with our simulation results, for pressures at which bilayer and monolayer behaviors converge. In this sense, these data confirm the increasingly packed arrangement found in both monolayer and bilayer as preassure increases and is in good agreement with the surface area per lipid reported above.

Considering the lipid packaging, $DMPA^-$ monolayers are arranged in hexagonal structure at high surface pressures. In Figure 4.8, the center of mass of the ethylene lipid tails is plotted in the $X - Y$ plane (lipid plane). The hexagonal structure associated with the gel structure L'_β (in bilayers) and liquid condensed state LC (in monolayers) can be clearly seen for a pressure of 40 r

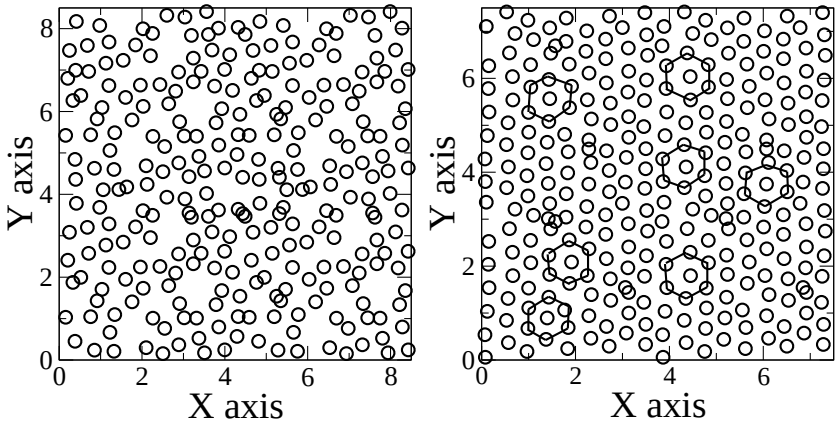

Figure 4.8: Lipid packing for one of the two $DMPA^-$ leaflets. Center of mass of each lipid tail is represented by a circle. Left: Surface pressure of 0.17 mN/m. Right: Surface pressure of 40 mN/m. Lines remarks the hexagonal packing of this arrangement.

In addition, the lipid head orientation with respect to the normal to the lipid plane was studied, obtaining values of 49.7, 48.8, 42.3 and 44.7 degrees at 0.17, 1, 10 and 40 mN/m respectively. These values show how the $DMPA^-$ heads in their liquid crystaline state are much more oriented toward the water layer than DPPC, where an orientation almost parallel to the surface of the lipid layer has been reported.[10,19] This increase in head orientation can be explained by the greater degree of head hydration and lipid packaging of them than the DPPC ones. In this regard, Schalke et al[9] reported that the

head orientation of $DMPA^-$ in its liquid condensed state LC for a pressure of 40 mN/m was 47 degrees, which agrees with our simulation result of 44.7 degrees. Unfortunately, no experimental data of $DMPA^-$ head orientation in bilayers has been reported to compare with its liquid crystaline state L_α.

By means of FTIR, Lozano et al.[32] observed that, in the monolayers of pure $DMPA^-$ at high surface pressures, the transition dipole moment of carbonyl group aligned with the interface. The angular distribution function of the bonding vector for this C=O group was calculated for each surface pressure studied. Thus, from Figure 4.9 can be observed how for high pressures, e.g. 40 mN/m, the distribution takes a sharper form, with two maximum peaks at 90 and 97 degrees, reflecting the above mentioned change in orientation of the carbonyl moiety. This dense packing of a $DMPA^-$ monolayer at high surface pressure is in a perfect accordance with experimental data.

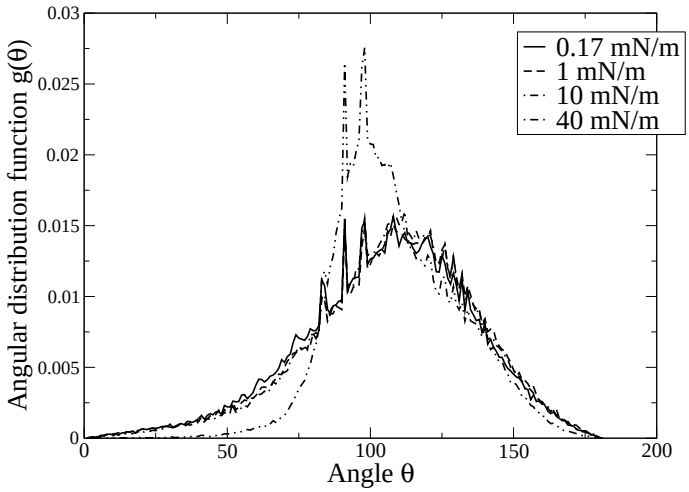

Figure 4.9: Angular distribution function for the vector bonding of the C=O moiety (atoms 27 and 28, condidering the atom numeration of Figure 2) with respect to the perpendicular axis to the lipid/water interface and different surface pressures.

Electrostatic Potential.

The electrostatic potential ψ across the lipids layers was computed from the double integral of the charge density:[34]

$$\psi(z) - \psi(0) = -\frac{1}{\varepsilon_0} \int_0^z dz' \int_0^{z'} \rho(z'')dz'' \tag{4.4}$$

where the origin z of the electrostatic potential $\psi(0)$ is taken at the middle of the lipid bilayer. The electrostatic potential computed in this way agrees with the computed charge density using Poisson's equation, without using a cut-off radius.[35] Hence, Figure 4.10 depicts the electrostatic potential averaged on both symmetric lipid leaflets.

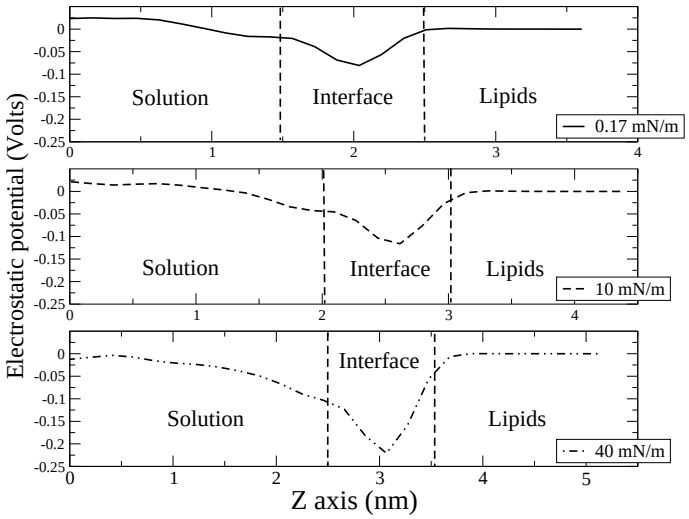

Figure 4.10: Electrostatic potential across the Z axis for each surface pressure. For clarity, each region is delimited with dotted lines. The zero Volts is placed in the middle of the water layer.

Of note is the dramatic effect of surface pressure on the potential difference at the interface, which ranges from -0.08 V at 0.17 mN/m to -0.22 V at 40 mN/m, an effect which is of great relevance in the electrochemistry for developing modified electrodes using Langmuir-Blodgett's method.[36]

Solution Properties

Having established the lipid structure associated to barometric transitions, the way in which the solution properties are perturbed by the barometric isomorphic lipid transition was studied. For that purpose, the computation box was sliced to 19 slabs parallel to the $x-y$ plane (lipid leaflet), so that slab number 10 matched the midle of lipid bilayer.

Water and Sodium (Na^+) Translational Diffusion Coefficient, D_t

First of all, the diffusion coefficients of water and Na^+ ions were calculated using the treatment described by Cascales et al.[16] which permitted us to estimate their diffusion coefficient in each zone of the computing box. The results for water are shown in Figure 4.11. As can be seen, the regions on both sides of the box are composed of bulk water, reaching a steady value for the $D_{t,xy}$. Note that the diffusion coefficient of bulk water for SPC at 349 K is 7.5 x 10^{-5} cm^2 s^{-1},[37] very close to our value of 6.5 x 10^{-5} cm^2 s^{-1}. Also of interest is that there is no significative variation in the water diffusion coefficient with respect to pressure, indicating that our conclusions are not affected by any simulation artifact. From the results depicted in Figure 4.11, it can be observed how, there is almost no correlation between the diffusion

coefficient and surface pressure at the lipid/water interface, where a minimum value of around 2.5 x 10^{-5} cm^2 s^{-1} was measured in the four cases in the vicinity of the lipid interface, regardless of the isomorphic state of the lipids.

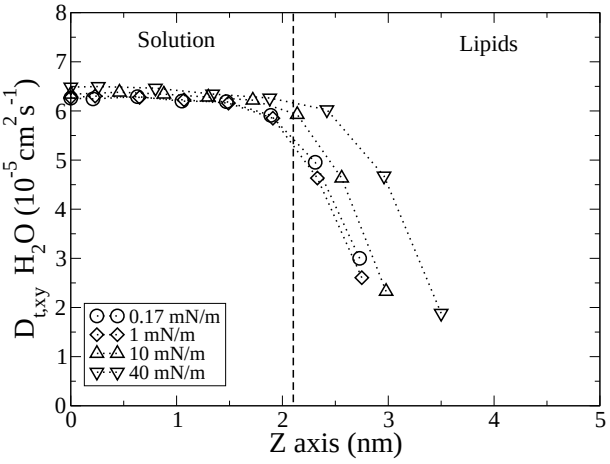

Figure 4.11: Translational diffusion coefficient $D_{t,xy}$ of water for different positions in the computing box along the axis perpendicular to the lipid/water interface, and different surface pressures.

A similar trend was observed for Na^+ ions, where the values of 4.5, 4.3, 4.2, 4.4 x 10^{-5} cm^2 s^{-1} were measured for the bulk water and 1.2, 1.1, 1.2, 1.2 x 10^{-5} cm^2 s^{-1} in the vicinity of the lipid surface, respectively. These results are in good agreement with experimental data for sodium ion in bulk water[38] and in the vicinity $DPPS^-$ layers,[39] where values of 3.8 x 10^{-5} cm^2 s^{-1} have been reported for bulk water at 298 K, and a value of $2{,}1 \pm 1{,}1$ x 10^{-5} cm^2 s^{-1} in the vicinity of a $DPPS^-$ bilayer at 350 K.

The first conclusion from the values reported above is that the barometric phase transition of lipids does not perturb the profile of sodium diffusion from the bulk water to the vicinity of the lipid interface.

Water Rotational Relaxation Time, τ

Using the same regions as described above, we estimated the rotational diffusion coefficient of water molecules.[16] The reorientation of water molecules is described by the correlation function

$$\langle P_1(t) \rangle = \sum_{i=1}^{3} a_i \; exp(-t/\tau_i) \tag{4.5}$$

from which an *apparent mean relaxation time* τ_{app} can be obtained:

$$\tau_{app} = \frac{\sum_{i=1}^{3} a_i \tau_i}{\sum_{i=1}^{3} a_i} \tag{4.6}$$

Within this procedure, we calculated τ_{app} from the beginning of the lipid/water interface to bulk water, at each surface pressure (Table 4.3). As an example, the fit of the calculated data to eq. 4.1.3 for 0.17 and 40 mN/m in the central region and near the lipid/water interface is depicted in Figure 4.12.

The assumption of bulk water in the midle of the aqueous region and the absence of any simulation artifact due to surface pressure is again confirmed by this study. The 2.11 ps of our simulated value is in good agreement with

	τ_{app} / ps			
slab number	π (mN/m)			
	0.17	**1**	**10**	**40**
4	11.85	9.82	10.98	12.64
5	7.77	9.21	7.75	6.79
6	3.81	4.73	5.06	3.56
7	2.32	2.56	2.28	2.07
8	2.09	2.30	2.12	2.07
9	2.04	2.05	2.04	2.03
10	2.11	2.09	2.07	2.04

Table 4.3: Reorientational relaxation time (τ_{app}) of water for different regions of the computing box and surface pressures

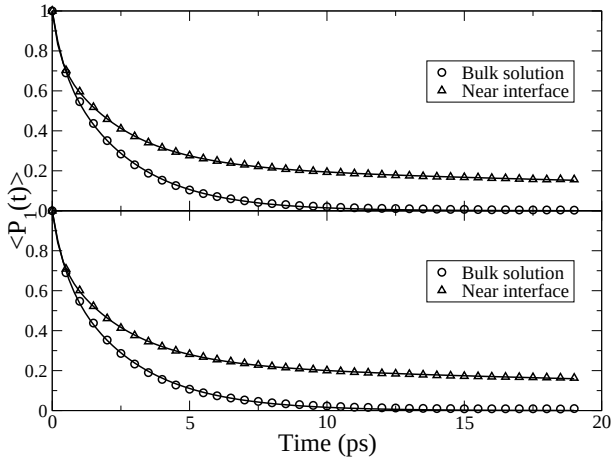

Figure 4.12: Reorientational correlation function of water dipole at 0.17 mN/m (top) and 40 mN/m (down) surface pressures. Symbols: simulation results. Line: Fitted curve.

the 1.7 ps[37] reported for bulk water at 349 K. The slight difference between the results can be attained to the fact that in our simulations some water molecules that were hydrating sodium ions were considered rather than the pure water in Postma's work.[37] As regards the rotational relaxation time in the vicinity of the lipid surface, it increased up to 11,3$\pm$1,1 ps, independently of the surface pressure. In other words, we can assert that lipid barometric

phase transition did not perturb the dynamic properties of water from bulk to water/lipid interface in the range of pressures studied.

Sodium Ion Hydration

Using the radial distribution function of Equation 4.1.3, we are able to calculate the hydration number of sodium ions in solution. As it is shown in Figure 4.13, a value of 5.0 water molecules was estimated in bulk water and 1.0 water molecule near the lipid/water interface. The results for bulk water are in good agreement with experimental[40] and simulation[41] data in aqueous solution, where values of 4.6 and 3.8 have been reported at 298 K. At the lipid/water interface, Cascales et al. reported[39] a value of 1.2 in the vicinity of a $DPPS^-$ bilayer which agrees with the value of 1.1 obtained here for all the simulated surface pressures.

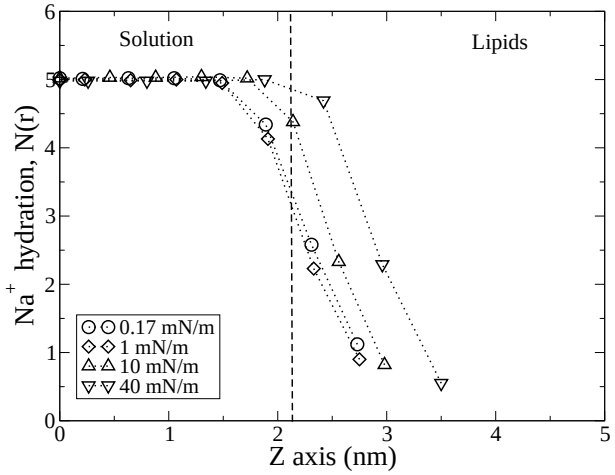

Figure 4.13: Values of coordination number for water molecules surrounding the Na^+ ions for different surface pressures and regions of the computing box.

4.1.4. Conclusions

Four $DMPA^-$ bilayers were subjected to different lateral pressures in a range from 0.17 to 40 mN/m. The results demonstrated that the lipid bilayer and monolayer follow the same behavior only when surface pressure is sufficiently high. On the other hand, their behavior differed low pressures.

Validation of the $DMPA^-$ force field was made by comparison with experimental data, for both bilayer and monolayer. The experimental data corresponding to hydrocarbon order parameters and surface area per lipid molecule showed excellent agreement with our simulation results at low surface pressures, which reproduced the $DMPA^-$ bilayer behavior. At high surface pressures, the area per lipid molecule, orientation of the carbonyl moiety, tail orientation, head orientation and hexagonal arrangement of the lipid tails reflected monolayer behavior in the Liquid Condensed (LC) phase.

In addition, we focused our interest on how this barometric polymorphic phase transition affects the lipid/solution interface. Thus, the water reorientational time, the water and sodium translational diffusion coefficient and sodium hydration were studied. From the simulation results, we can assert that barometric polymorphic lipid transition does not perturb the lipid/water interface properties, in the range of the pressures studied.

Acknowledgments

JJLC wishes to thank the Spanish Government (Ministerio de Educación y Ciencia, MEC) and Fundación Seneca for his financial support through projects BQU-2001-04777 and 00483/PI/04, respectively. LC, MTMR and

JJGC thank the Spanish CICYT for financial support of this research in the framework of Projects No. CTQ2004-03246/BQU and MAT2004-03849. Also, JJGC thanks the Ministerio de Educación y Ciencia for a Formación Profesorado Universitario (FPU) predoctoral fellowship.

References

1. Cullis, P.; Hope, M.; de Kruijff, B.; Verkleij, A.; Tilcock, C. Structural properties and functional roles of phospholipids in biological membranes. In *Phospholipids and cellular regulation.*; Kuo, J., Ed.; CRC-Press: 1985.

2. Yeagle, P. *The FASEB Journal* **1989,** *3,* 1833.

3. Nagle, J.; Tristram-Nagle, S. *Biochimica et Biophysica Acta* **2000,** *1469,* 159.

4. Yeagle, P. L. The mesomorphic phase behavior of lipid bilayers. In *The structure of biological membranes*; Yeagle, P., Ed.; CRC Press: 1992.

5. Ichimori, H.; Hata, T.; Matsuki, H.; Kaneshina, S. *Biochimica et Biophysica Acta* **1998,** *1414,* 165.

6. R.Winter, *Curr. Op. Coll. Int. Sci.* **2001,** *6,* 303.

7. Möhwald, H. Phospholipid Monolayers. In *Handbook of biological physics*; Lipowsky, R.; Sackmann, E., Eds.; Elsevier Science B.V.: 1995.

8. Hunt, R.; Mitchell, M.; Dluhy, R. *J. Mol. Struct.* **1989,** 93.

9. Schalke, M.; Krüger, P.; Weygand, M.; Lösche, M. *Biochimica et Biophysica Acta* **2000,** 113.

10. Dluhy, R. *Appl. Spectr. Rev.* **2000,** *35,* 315.

11. Schalke, M.; Lösche, M. *Adv. Coll. Int. Sci.* **2000,** *88,* 243.

12. Mendelsohn, R.; Flach, C. *Curr. Top. Membranes* **2002,** *52,* 57.

13. Pedrosa, J. M.; Pérez, M.; Prieto, I.; Martín-Romero, M. T.; Möbius, D.; Camacho, L. *Phys. Chem. Chem. Phys.* **2002,** *4,* 2329.

14. van Gunsteren, W. F.; Berendsen, H. J. C. *Angew. Chem Int. Ed.* **1990,** *29,* 992.

15. Alper, H. E.; Bassolino-Klimas, D.; Stouch, T. R. *J. Chem. Phys.* **1993,** *99,* 5554.

16. Cascales, J.; Berendsen, H.; García de la Torre, J. *J. Phys. Chem* **1996,** *100,* 8621.

17. Tieleman, D.; Marrink, S.; Berendsen, H. *Biochimica et Biophysica Acta* **1997,** *1331,* 235.

18. Kaznessis, Y.; Kim, S.; Larson, R. *Biophys. J.* **2002,** *82,* 1731.

19. Cascales, J. L.; Otero, T.; Romero, A. F.; Camacho, L. *Langmuir* **2006,** *22,* 5818.

20. Pott, T.; Maillet, J.; Dufourc, E. *Biophys. J.* **1995,** *69,* 1897.

21. Wu, F.; Gericke, A.; Flach, C.; Mealy, T.; Seaton, B.; Mendelsohn, R. *Biophys. J.* **1998,** *74,* 3273.

22. Berendsen, H.; Grigera, J.; Straatsma, T. *J. Phys. Chem.* **1987,** *91,* 6269.

23. Lindahl, E.; Hess, B.; van der Spoel, D. *J. Mol. Mod.* **2001,** *7,* 306.

24. Berendsen, H.; van der Spoel, D.; van Drunen, R. *Comp. Phys. Comm.* **1995,** *91,* 43.

25. "HyperChem 8.5", 1999 Hypercube, Inc.

26. Darden, T.; York, D.; Pedersen, L. *J. Chem. Phys.* **1993,** *98,* 10089.

27. Essmann, U.; Perea, L.; berkowitz, M.; Darden, T.; Lee, H.; Pedersen, L. *J. Chem. Phys.* **1995,** *103,* 8577.

28. van Gunsteren, W.; Berendsen, H. *Mol. Phys.* **1977,** *34,* 1311.

29. Berendsen, H. J. C.; Postma, J. P. M.; van Gunsteren, W. F.; DiNola, A.; Haak, J. R. *J. Chem. Phys.* **1984,** *8,* 3684.

30. Blume, A.; Eibl, H. *Biochim. Biophys. Acta* **1979,** *558,* 476.

31. Ziegler, W.; Blume, A. *Spectrochimica Acta Part A* **1995,** *51,* 1763.

32. Lozano, P.; Fernández, A. J.; Ruiz, J. J.; Camacho, L.; Martín, M.; Muñoz, E. *J. Phys. Chem. B* **2002,** *106,* 6507.

33. Egberts, E.; Berendsen, H. *J. Chem. Phys.* **1988,** *89,* 3718.

34. van Buuren, A.; Berendsen, H. *Langmuir* **1994,** *10,* 1703.

35. Pandit, S.; Bostick, D.; Berkowitz, M. *Biophys. J.* **2003,** *84,* 3743.

36. Goldenberg, L. *J. Electroanal. Chem.* **1994,** *379,* 3.

37. Postma, J. *A molecular dynamics study of water,* Thesis, Rijkuniverseit Groningen, The Netherlands, 1985.

38. Lide, D., Ed.; *Handbook of Chemistry and Physics;* CRC Press: 2002.

39. Cascales, J. L.; de la Torre, J. G. *Biochimica et Biophysica Acta* **1997,** *1330,* 145.

40. Bockris, J.; Reddy, A. *Modern Electrochemistry;* Plenum Press: 1998.

41. Impey, R.; Madden, P.; McDonald, I. *J. Phys. Chem.* **1983,** *87,* 5071.

4.2. A DMPA Langmuir monolayer study: From gas to solid phase. An atomistic description by Molecular Dynamics Simulation

In this work, a DMPA Langmuir monolayer at the air/water interface was studied by molecular dynamics simulations. Thus, an atomistic picture of a Langmuir monolayer was drawn from its expanded gas phase to its final solid condensed one. In this sense, some properties of monolayers that were traditionally poorly or even not reproduced in computer simulations, such as lipid domain formation or pressure−area per lipid isotherm, were properly reproduced in this work.

Thus, the physical laws that control the lipid domain formation in gas phase and the structure of lipid monolayers from gas to solid condensed phase were studied. Thanks to the atomistic information provided by the molecular dynamics simulations, we were able to add valuable information to the experimental description of these processes and to access experimental data related to the lipid monolayers in their expanded phase, which is difficult or inaccessible to study by experimental techniques. In this sense, properties such as lipids head hydration or lipid structure were studied.

Paper published in *Langmuir*, 2007, 24, 1823-1828

4.2.1. Introduction

In spite of the pile of publications related with molecular dynamics simulation of lipid bilayers,[1–5] much less attention has been paid to the study of lipid monolayers at the air/water interface since the pioneering work.[6,7] From our viewpoint, this may be due, in part, to some fundamental barriers, such as inaccuracy in the results when attempts were made to reproduce the π (surface pressure)−lipid area isotherm and the collapse or instability of some models of lipid monolayers that were simulated. In this sense, most of the published papers dealing with Langmuir monolayers simulations either did not calculate the $\pi-$ area per lipid isotherm,[8–10] or overestimated it.[11,12] Also, some of these studies were carried out under unrealistic temperatures compared to experimental conditions.[13]

In this context and despite the power and accuracy of some experimental techniques such as X-ray and neutron reflectivity measurements, infrared attenuated total reflectance ATR-IR and IRRAS studies,[14–18] which provided a detailed description of the Langmuir monolayers in their solid (S) and liquid (LC or LE) state, they were not able to provide an atomistic description of the monolayer. In this regard, and because of the limited sensitivity of the above-mentioned experimental techniques, they are not able to provide detailed information about the expanded gas (G) phase.

In this work, insight with atomic detail of a Langmuir monolayer formation process is provided. In this sense, amazing agreement between simulation and experimental data is obtained for lipid monolayers in their gas and solid phase. Moreover, a full description of the gas phase is given, which remains

unreachable by experimental techniques. In this setting, lipid domain formation was observed during our simulated trajectories, which reproduces this phenomena for lipid monolayers.[19] Thus, we are able to relate the first step in the domain formation at the gas phase with experimental data that is not accessible by BAM or fluorescence microscopy. Indeed, as far as we know, this is the first simulation in which such lipid domain formation has been simulated with atomic detail.

The Langmuir monolayer was studied using the acid $DMPA^-$ (dimyristoylphosphatidicacid) as lipid monolayer formation. This lipid has been widely studied in Langmuir monolayers,[20–23] beacuse of, among other factors, its capacity to bear charge, depending of the pH of the solution. Thus, $DMPA^-$ was modeled in its monoanionic form by adjusting the solution pH to a value of 7.[21]

With the aim of understanding the lipid-lipid and lipid-solvent interactions that control the properties of the lipid monolayers, other relevant properties such as lipid head hydration, lipid-lipid atomic charge bridges, and the tilt of the lipid tails and heads with respect to the direction perpendicular to the lipid surface were studied.

4.2.2. Method and Model

Periodical conditions were considered in 3D space. The absence of interactions between both lipid leaflets along the z axis was achieved by introducing an empty gap of 2 nm above and below of each lipid leaflet, Figure 4.14. The final dimensions of the computing box were 8.75, 8.67 and 12.05 nm, for the

x, y and z axes, respectively. The system was set up by placing the water layer confined between two $DMPA^-$ leaflets forming a sandwich structure, where lipid heads were pointing toward the water layer. Figures 4.15a,b depicts two snapshot of the system at different surface areas per lipid. Thus, the system was originally built considering 288 lipids and 144 lipids/leaflet, which corresponds to a lipid surface area of 0.4 nm^2/lipid. With the goal of maintaining the electroneutrality of the system, 288 water molecules were substituted by 288 sodium ions (Na^+). Hence, the whole system was constituted by 288 $DMPA^-$, 288 Na^+ and 9780 SPCE water molecules,[24] which amounted a total of 41 436 atoms.

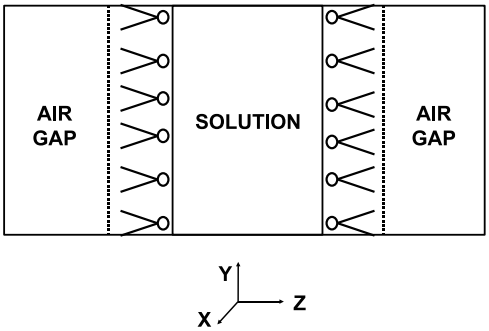

Figure 4.14: Scheme of the computational arrangment used in this work.

Gromacs 3.3. package[25,26] was used to run the MD simulations, and the analisis of the generated trajectories was performed with software code developed by us. Table 4.4 depicts the charge distribution on each lipid, assuming the atomic lipid numeration of Figure 4.16. Long range interactions were modeled by the Lennard-Jones potential, with a cut-off of 0.8 nm, and the electrostatic interactions were modeled by the Ewald algorithm.[27,28] All

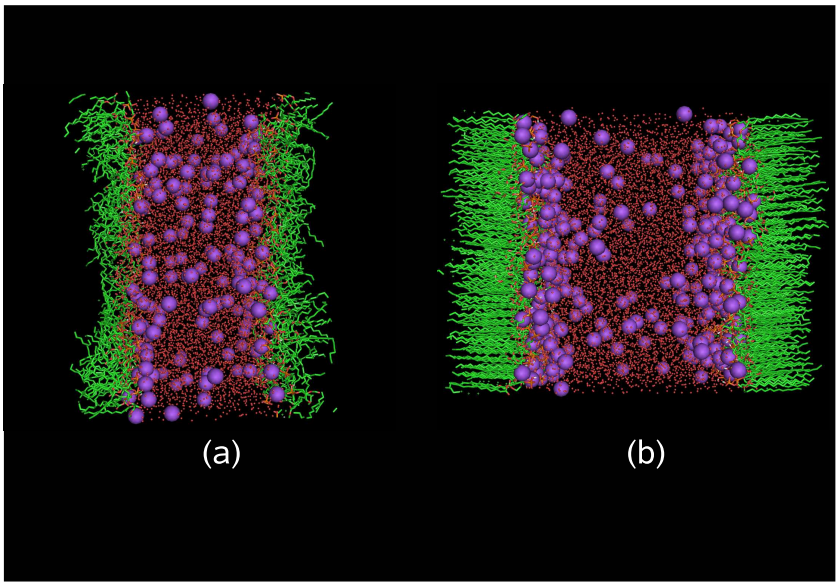

Figure 4.15: Snapshot of the $DMPA^-$ monolayers with an area per lipid molecule of 1.00 nm2 (a) and 0.40 nm^2 (b).

of the bonds of the system were constrained by SHAKE.[29] The time step used in all the simulations was 2 fs (femtoseconds).

The simulations were carried out on an HP160 parallel computer using 16 processors, with a performance of 1.5 ns of trajectory length/h.

In this regard, after the system was set up, the whole system was subjected to a steepest descent energy-minimization process to remove undesired overlaps between neighboring atoms. Once the system reached a relative energy minimum, five simulations were carried out for different values of the lipid surface area. Thus, the desired value of surface area per lipid was fitted by removing a certain number of lipids in both leaflets until the right value was achieved. Details concerning the simulations that were carried out in this work can be found in Table 4.5. Because our system was simulated under NVT thermodynamic conditions (i.e., the number of particles of the system

Molecule	Atom number	Atom type	Charge (e)
DMPA$^-$	1	H	0.054
	2	O	-0.460
	3	P	0.680
	4	O^-	-0.394
	5	O	-0.394
	6	O	-0.434
	7	CH_2	-0.050
	8	CH	-0.036
	9	O	-0.196
	10	C	0.432
	11	O	-0.164
	12	CH_2	-0.036
	13-23	CH_2	0.000
	24	CH_3	0.000
	25	CH_2	0.124
	26	O	-0.202
	27	C	0.384
	28	O	-0.292
	29	CH_2	-0.014
	30-40	CH_2	0.000
	41	CH_3	0.000
Ion		Na^+	1.000
SPCE water		HW	-0.8476
		OW	0.4238

Table 4.4: Charge density for each atom of lipid DMPA$^-$ molecule, Na^+ ions and SPCE water molecules, as obtained by CNDO method.

N, box volume V and temperature T remained constant), the system was coupled to an external temperature bath using the Berensend algorithm[30] with a coupling temperature constants τ_T of 0.1 ps. All the simulations were carried out for 15 ns. The simulations were carried out at 293 K, which is the usual temperature at laboratory conditions. In all cases, the first 5 ns of trajectory length were discarded for analysis because this was the time required to reach the equilibrium.

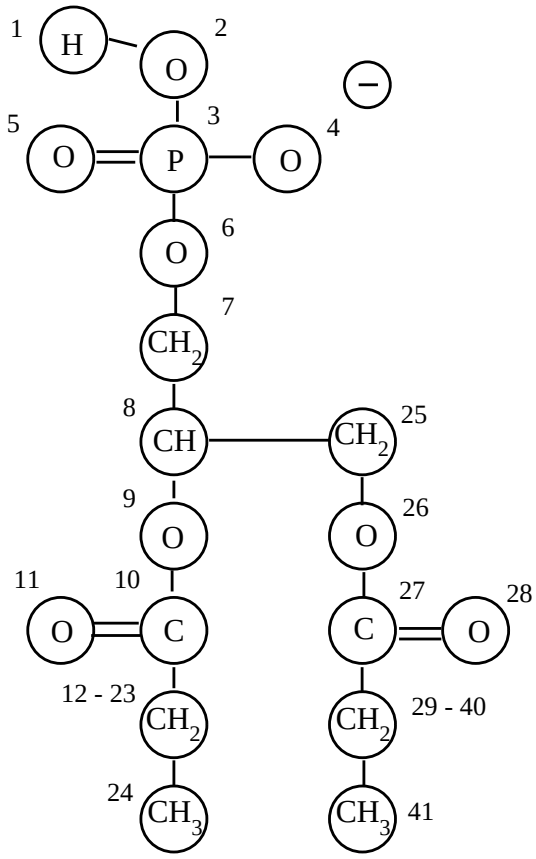

Figure 4.16: Lipid atom numbering used in this work.

Area per lipid molecule(nm^2)	Lipid number	Total number of atoms
0.40	2 x 144	41436
0.53	2 x 128	40092
0.70	2 x 108	38412
0.79	2 x 96	37404
0.91	2 x 84	36396
1.00	2 x 76	35613

Table 4.5: Computational details of the differents simulations.

Furthermore, with the goal of exploring the role played by the electrostatic interactions between neighboring lipids in the formation of lipid domains,[31–33]

two additional simulations were carried out under analogous simulation conditions to those described above, at 0.4 and 1 nm surface area/lipid molecule, using modified DMPA molecules called DDMPA (dummy-DMPA) in which the charge of each DMPA molecule was divided by 2, and, accordingly, the number of sodium ions was also reduced to half to maintain the electroneutrality of the system.

4.2.3. Results and Discussion

Surface Pressure−Area Isotherm

Because the surface pressure(π)−area per lipid isotherm is, in most of the cases, the first target in the experimental studies in Langmuir monolayer, it is crucial to try to reproduce it as a validation method of our simulations. Thus, the surface tension (γ) can be computed from the simulated trajectories as:[13]

$$\gamma = -\frac{1}{2}(\frac{p_x + p_y}{2} - p_z)L_z \tag{4.7}$$

where p_x, p_y and p_z are the diagonal components of the pressure tensor averaged along the simulated trajectory and L_z is the length of the computing box along the Z axis, perpendicular to the lipid/water interface. The surface tensor γ was computed for each of the simulated systems, and then the surface pressure π was calculated as follows:

$$\pi = \gamma_0 - \gamma \tag{4.8}$$

where γ_0 represents surface tension of a clean air/water interface, with a value of 72.75 mN/m at 293K[34] and γ represents the surface tension of an air/water interface covered by a monolayer.

Figure 4.17 depicts the surface pressure−lipid area isotherm compared with experimental data[35] at the same temperature, 293K. Although a slight overestimation of the surface pressure is attained from simulation, these data reproduce the same profile as the experimental curve, from the gas phase to the solid condensed structure. This slight overestimation of our simulation results can be attributed to a systematic error, given that the calculated isotherm is ca. 5 mN/m over the experimental one. This error could be ascribed to a wrong value of γ_0, because of the presence of Na^+ ions, or to a constant error in the model used.

Lipid Domain Formation at Gas Phase

From BAM and other surface experimental techniques, 2D lipid domains could be observed on several anphiphilic monolayers at the air/water interface[19] in the liquid and solid states. However, as mentioned previously, pure lipid monolayers at gas (G) phase are difficult to study experimentally, and lipid domain formation at gas phase could not be observed. Figure 4.18 depicts the center of mass of hydrophilic heads on the XY plane (parallel to the interface), with a mean surface area of 1 nm^2 per lipid molecule on average. From this Figure, we see how, during the simulation time, aggregations emerged due to charge bridges between neighboring lipids. Thus, from the movie[36] produced with atomic detail from the simulated trajectories, we watch the

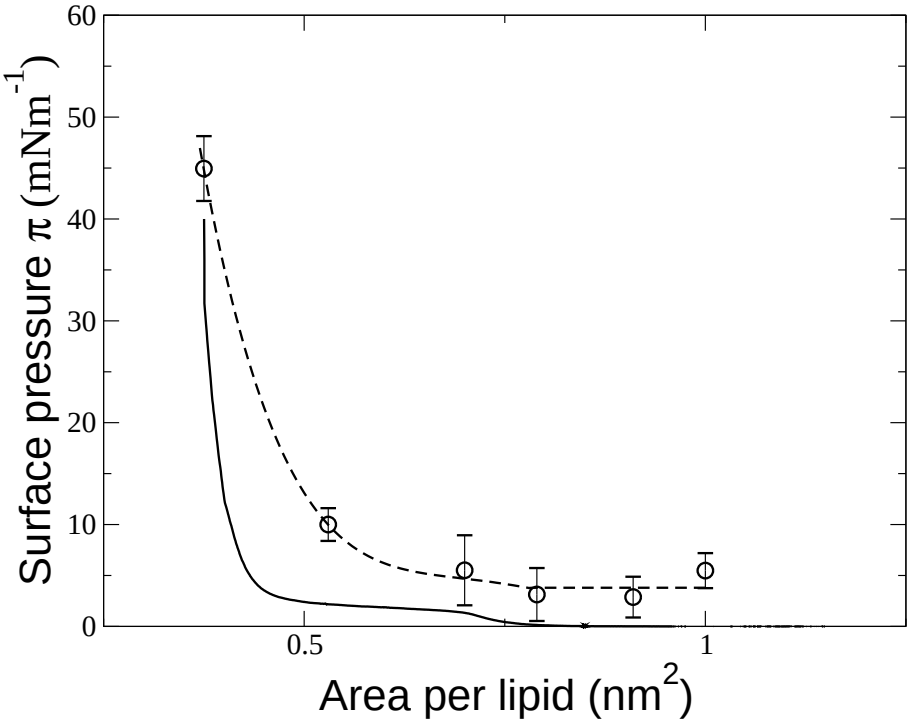

Figure 4.17: Experimental DMPA surface pressure−area isotherm (line) and calculated from our simulation (circles) with its error bars.

formation of domains in the lipid leaflet, starting from a homogeneous lipid distribution. As already been pointed out by Vollhardt et al.,[37] the physical origin of these mesoscopic domains is related with the atomic interactions between neighboring lipids. Thus, with the aim of better understanding this matter better, a detailed study was carried out in this work.

With the aim of attaining insight related to the intriguing process in Langmuir monolayer formation via head interactions, the nature of hydrophilic head-to-head interactions and their evolution with the area per lipid along the isotherm curve were investigated at atomic level.

For that purpose, we used information provided by the radial distribution

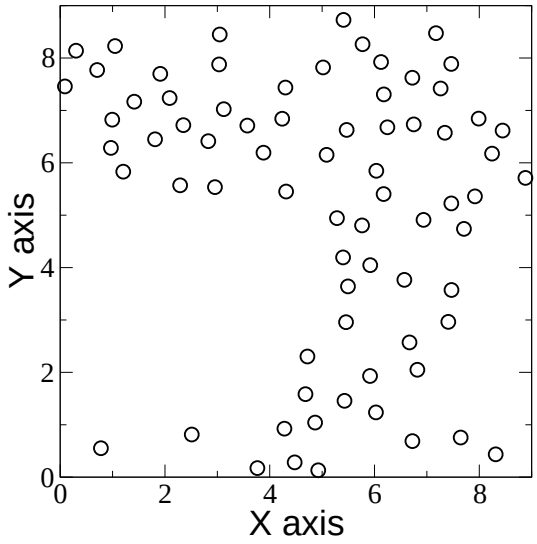

Figure 4.18: Center of mass of the lipid heads plotted on the lipid plane (xy), in its gas phase (1 nm^2 per lipid molecule).

function $g(r)$, which was defined as:

$$g(r) = \frac{N(r)}{4\pi r^2 \rho \delta r} \tag{4.9}$$

where $N(r)$ is the number of atoms in a spherical shell at distance r and thickness δr from a reference atom and ρ is the number density in the computing box.

The radial distribution function $g(r)$ of atoms numbers 11, 28 and 4 (corresponding to the two tail carbonyl oxygens and one phosphate oxygen, respectively, see Fig. 4.16) around the phosphorus atom of a neighboring lipid DMPA$^-$ was calculated. In Figure 4.19, $g(r)$ of a phosphate oxygen (atom 4) and the carbonyl oxygen (atom 28) around the phosphorous atom of a neighboring lipid is depicted. The larger the radial distribution function, the more coordination that exists for the given oxygen around the P atom of a

neighboring lipid. From that Figure, it can be seen that the $g(r)$ for atom 4 (phosphate oxygen) above a neighboring lipid P atom increases with the reduction of the area per lipid. However, an inverse evolution is obtained for the $g(r)$ of atom 28 (carbonyl oxygen) above a neighboring lipid P atom, showing a decrease with the reduction of the area per lipid.

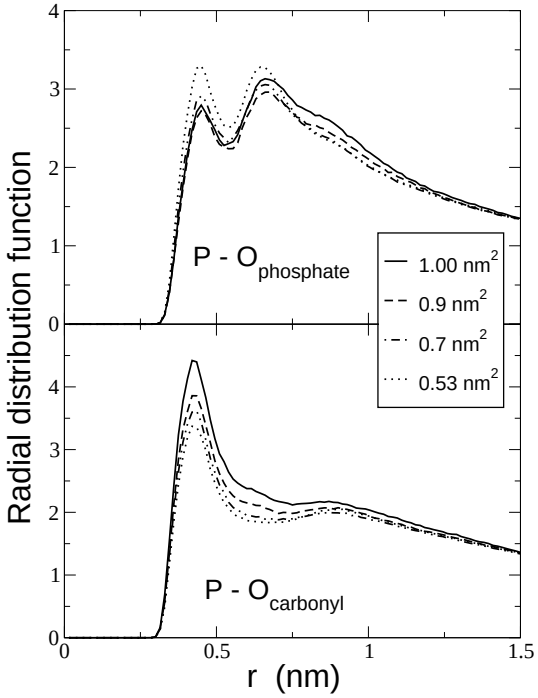

Figure 4.19: Radial distribution function for phosphate oxygens (up) and carbonyl oxygen (down), around a P atom of neighbouring lipids for different values of lipid area.

Initially, we could mark this result as surprising, given that an increasing in both types of coordination (carbonyl and phosphate oxygen to P atom of a neighboring lipid) should be expected because lipids get closer with compression. Our explanation was that, for larger areas available per lipid, the main dipole of the hydrophilic head, P−O, is compensated for by the dipoles

of tail carbonyl groups. With compression, the available area is reduced and the lipids are forced to arrange closely. Upon compression, phosphate oxygen displaces the carbonyl oxygen because of the crystallographic arrangement of the lipids in their solid state, and then its radial distribution function diminishes. However, coordination between phosphate oxygen of neighboring lipids increases as a result of crystallographic arrangements [*]. It is worthwhile to note that the distance r of the maximum first peak of both radial distribution functions (for carbonyl and phosphate oxygens) does not vary with compression. It is usually assumed that, at high available areas per lipid, lipid molecules are separated. Our results point out that, even at the expanded gas phase, lipid molecules remains in contact at a certain distance, leaving a fraction of surface water uncovered.

The following goal was to gain more information about the nature of lipid-to-lipid interactions for the most expanded situation. Because the phosphate oxygen (atom 4) has a negative charge density and the carbonyl carbon atom (atom 27, see Fig. 4.16) has a positive charge as a result of the strong dipole moment $C^{\delta+} \rightarrow O^{\delta-}$, an interaction between these two atoms with an electrostatic origin is expected. Figure 4.20 shows the radial distribution function of the carbon (C) atom of carbonyl moiety around the phosphate oxygen (O). A surprisingly large peak, which corresponds to strong coordination, is found for an area per lipid molecule of 1 nm^2. This coordination is being reduced with compression. To get a better view of both two limit situations of the

[*]This explanation is illustrated in the video movie[36] produced from the simulated trajectories, where we observe how for high pressures, almost no interactions between neighboring lipids are observed due to the arrangements that they must adopt in their solid phase.

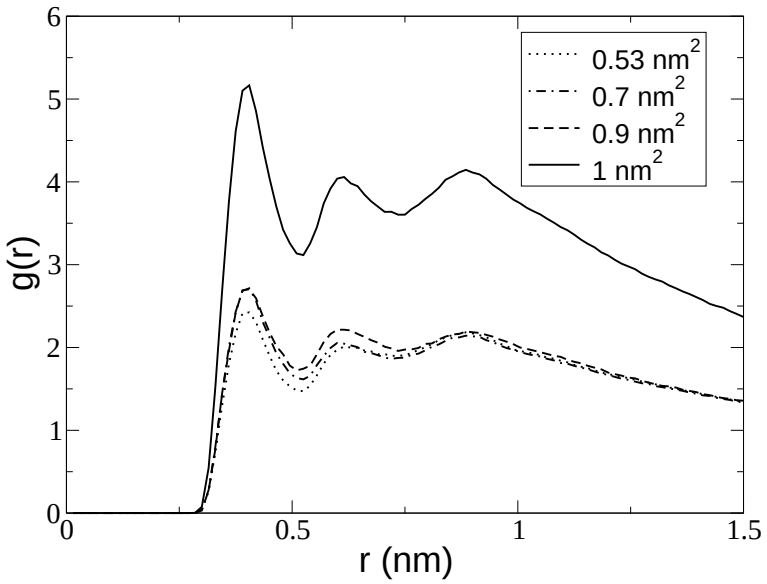

Figure 4.20: Radial distribution of phosphate oxygen (atom 4) around carbon of a tail carbonyl group (atom 27), for different values of lipid area.

lipids in the monolayer, Figure 4.21 shows two lipid molecules, at 1.00 nm^2 per molecule (left) and 0.40 nm^2 per molecule (right), pointing out the atomistic resolution imparted by our molecular dynamics simulation. As Figure 4.21 shows, in the gas phase the phosphate oxygen of one DMPA molecule is pointing towards the carbon of the tail carbonyl group of a neighboring lipid, as we mentioned above. However, in the solid phase, coordination between neighboring lipids results from the higher packing adopted by the lipid leaflet.

In addition, we examined the change in the hydration of the lipid heads with compression. The coordination number of water molecules was calculated from the radial distribution function as the sum of its individual contributions. Thus, we found that 4.81 and 4.05 water molecules coordinate phosphate oxygen from 1.00 nm^2 to 0.40 nm^2, respectively. For the carbonyl

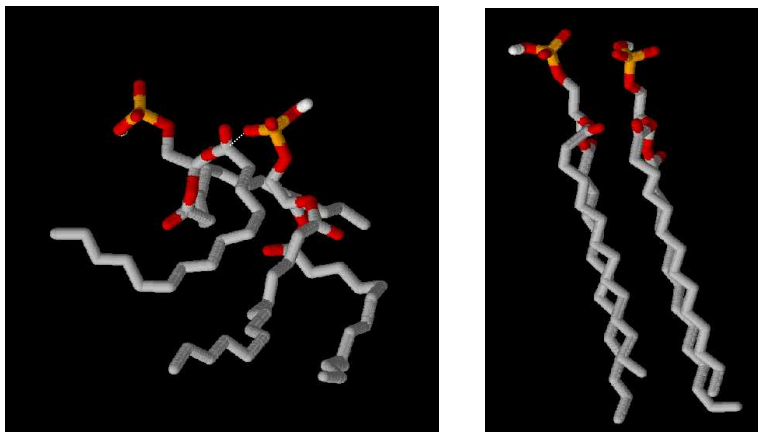

Figure 4.21: Snapshot of two lipid molecules for 1.00 nm2 (left) and 0.40 nm^2 (right). Gray: Hydrocarbon tails. Red: Oxygens. White: hydrogen. Orange: Phosphorous atom.

oxygen, the hydration numbers calculated from simulations were 1.43 and 0.85 water molecules from gas to solid phase. Thus from the values calculated above, the following values for total lipid hydration were the following: 7.68 and 5.75 for 1.00 and 0.40 nm^2 for the surface area per lipid molecule, respectively. The first consequence of lipid compression is the dehydration of the lipid head by roughly 2 water molecules from its gas to solid phase. This result agrees with the experimental data obtained by Schalke et al.,[38] where they measured that the lipid head hydration of $DMPA^-$ ranges from 6.5 to 4.8 water molecules from the gas to solid phase, giving a dehydration of 1.7 water molecules.

With this information, an atom-by-atom picture is drawn for the formation and subsequent compression of the monolayer. Here, the $DMPA^-$

Langmuir monolayer at high available areas has its phosphate group mostly lying underneath of water. In this setting, the interaction between carbonyl groups and the phosphate group are responsible of interactions that lead to lipid domain formations. While compressing, lipids get closer and phosphate groups become confined in their parallel crystallographic structure, while lipid head dehydration takes place.

With the goal of providing insight related to the roughness of the lipid/water interface, Figure 4.22 depicts the inner side of one lipid leaflet for the solid condensed and gas phases, corresponding to surface area per lipid of 0.4 and 1 nm^2/lipid, respectively. From this figure, it is clear that for most compressed situations (condensed phase), the lipid head surface is smoother than in the gas phase where a rougher surface is attained.

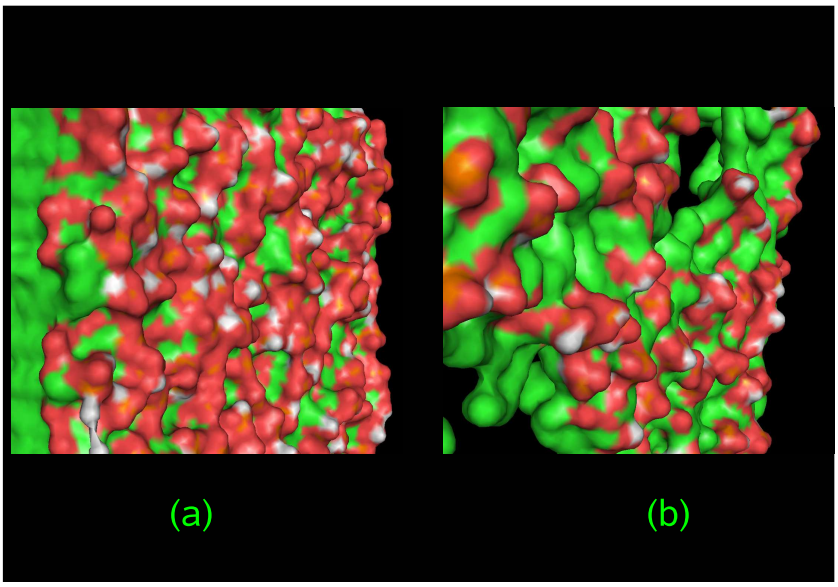

Figure 4.22: Roughness of the lipid/water interface: (a) solid condensed phase and (b) gas phase. Green: Hydrocarbon tails. Red: Phosphate oxygens. Orange: Phosphorous atom.

Lipid Tail and Head Structure

The lipid tail structures were examined from our simulated monolayers with atomic detail, and two snapshots of both lipid behaviors, corresponding to the gas and solid phases, are displayed in Figure 4.15. One of the main advantages of computer simulations is the possibility of adding information with atomic detail to experimental techniques such as BAM, X-ray synchrotron, and so forth. Thus, this study is twice as valuable for highly expanded monolayers in the gas phase, where our studies enhance the knowledge of this system with atomic detail.

The structure of the hydrocarbon tails can be studied by NMR experiments by measuring the deuterium order parameters along the lipid ethylene tails. Thus, the order parameter tensor is defined as

$$S_{ab} = \frac{\langle 3\cos(\theta_a)\cos(\theta_b) - \delta_{ab}\rangle}{2} \qquad a, b = x, y, z \tag{4.10}$$

where x, y and z are the local coordinates of the system, θ_a is the angle made by the molecular axis with the perpendicular axis to the lipid monolayer, and δ_{ab} is the Kronecker delta. From simulation, the order parameter, $-S_{CD}$ can be determined using the relation proposed by Egberts and Berendsen[39]

$$-S_{CD} = \frac{2S_{xx}}{3} + \frac{S_{yy}}{3} = \langle \frac{3\cos^2\theta_n - 1}{2} \rangle \tag{4.11}$$

where S_{xx} and S_{yy} are the terms of the order parameter tensor of the equation 4.10 and θ_n the angle made by the lipid hydrocarbon chain with respect to X axis. According to Pickholz et al.,[40] a value of $-S_{CD} = 0.5$ is interpreted as

an orientation fully perpendicular respect to the Z axis, and when the value of the order parameter reaches 0, a random orientation of the tail respect to the Z axis is assumed.

It is commonly accepted that lipid tails forming a Langmuir monolayer in the gas phase are randomly oriented. However, there is not much experimental evidence of this assumption because of inherent difficulties for performing experiments at this phase. Order parameters for each hydrocarbon tail atom of the simulated monolayers are shown in Figure 4.23. From this Figure, we see as the order parameters in the case of the monolayer in gas phase are null, which confirms the experimental assumption. With increasing the compression of the lipid monolayer, lipid tails get more ordered, as shown in Figure 4.23.

To attain better insight related to lipid tail orientation respect to the z axis, the angular distribution functions of the tail angles were calculated (Figure 4.24). In accordance with deuterium order parameters, in the gas phase, a broad Gaussian-like shape is obtained, pointing out the random distribution in the tail orientation. However, in the solid phase, a narrow distribution profile with a maximum value around 11°is obtained for monolayers in its solid phase. Although no experimental study was performed about this matter for DMPA, Schalke and Lösche[17] published analogous results for a DPPC monolayer on water by X-ray and neutron reflectivity measurements. When DDMPA were used instead of normal DMPA, we observe how the angular distribution function for the condensed phase (corresponding to a surface area of 0.4 nm^2) perfectly matches the shape of the angular distribution obtained for the DMPA. However, for the gas phase, a shift in the maximum of

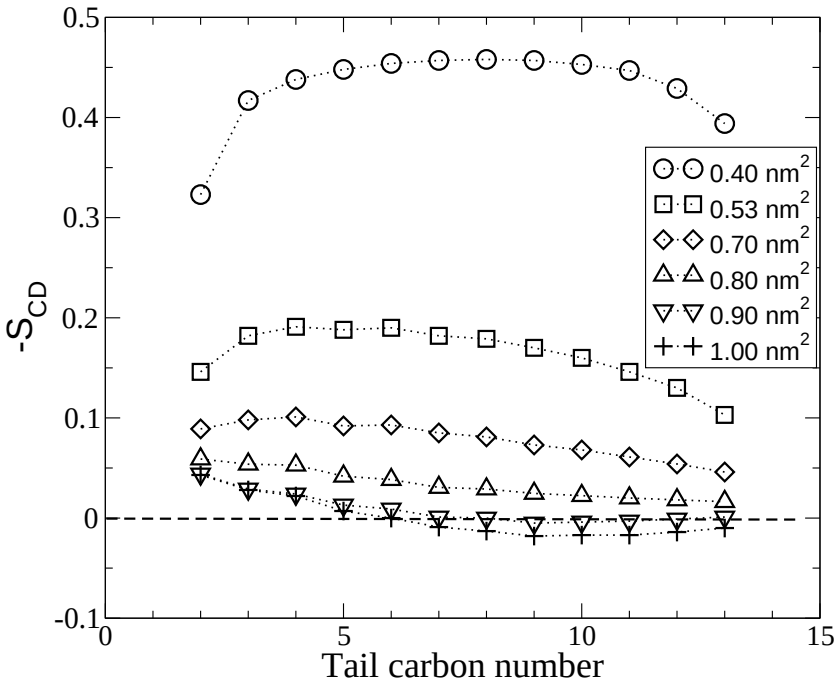

Figure 4.23: Order parameters of lipid hydrocarbon tails for different surface area per lipid.

the angular distribution is observed. Thus, from Figure 4.25 we observe how for the gas phase a mean tail orientation of 45°is measured as compared to 55°in the DMPA case. In other words, a diminishing of the dipole interactions of the DDMPAs generates a higher orientation of the lipids perpendicularly to the lipid/water interface compared with DMPA.

Lipid conformation is also described through lipid head orientation in terms of lipid head tilt, which is defined as the inclination of the vector formed by the hydrogen atom and the esther oxygen (atoms 1 and 6, respectively) with respect to z axis. Mean values for this angle are displayed in Figure 4.25 for different values of area per lipid, comparing our simulation results with experimental data.[38] Excellent agreement between experimen-

tal and simulation data is attained. When using modified DDMPA, almost no variation in the lipid head orientation is observed compared with using DMPA in both the solid and gas phases.

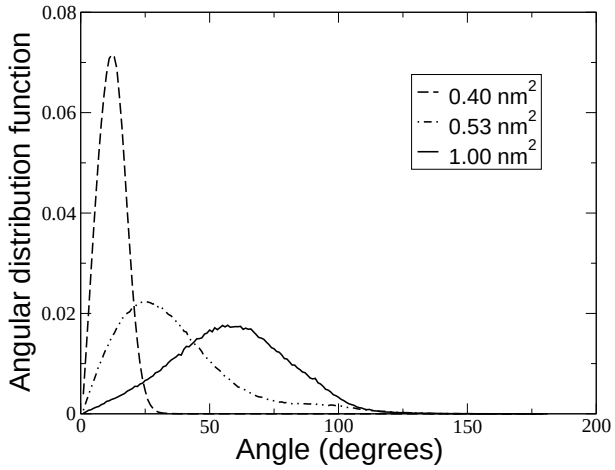

Figure 4.24: Angular distribution function of lipid tails respect to Z axis (normal to the lipid surface) at different values of area per lipid molecule.

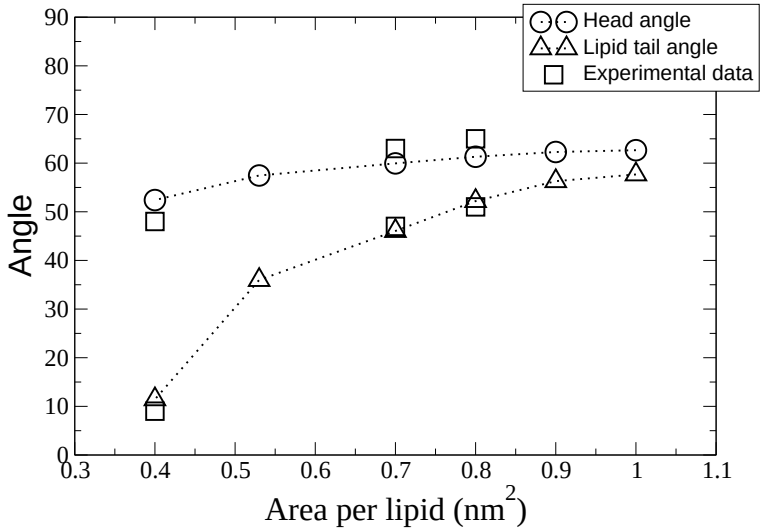

Figure 4.25: Tilt of lipid heads and lipid tails, respect to the perpendicular direction to the lipid surface. Experimental data were taken from.[38]

At the end of compression in its solid condensed phase, a hexagonal, highly ordered arrangement[15] is expected. Plotting the center of mass of the lipid tails in the xy plane, Figure 4.26 shows the mentioned hexagonal structure. From crystallographic measurements of the hexagonal structure, a crystallographic distance of 0.48±0.04 nm was estimated which agrees with experimental values of 0.472 nm measured by Winter[41] for the hexagonal packaging of a DPPC bilayer in its gel phase L'_β.

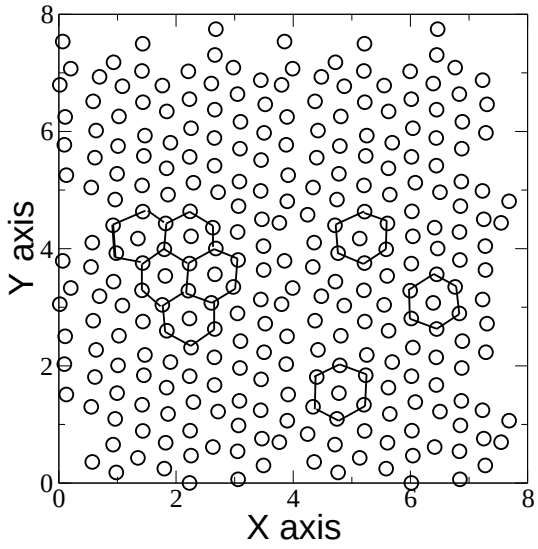

Figure 4.26: Center of mass of the lipid tails plotted over XY plane in their solid condensed state (0.4 nm^2 per lipid molecule).

4.2.4. Concluding remarks

A Langmuir monolayer at the air/water interface was studied by molecular dynamics simulation. In this setting, certain properties that traditionally have been poorly or not reproduced in computer simulations, such as lipid domain formations or surface pressure−area isotherm, have been properly

studied in our simulations, providing insight with atomic detail into these processes.

In this sense, these studies complete the experimental description of this system and provides access to information for the highly expanded isotherm regions, which is very difficult to measure using experimental techniques. Thus, lipid-lipid interactions that rule lipid domain formation in the gas phase were examined and commented on.

Finally, the structure and packaging of lipids was examined in order to get a reliable description of their behaviour at the air/water interface. What is more remarkable is that gas-phase data that are not accesible by experimentalist were estimed from molecular dynamics simulations.

Acknowledgements

JJLC wishes to thank Spanish Government (Ministerio de Educacion y Ciencia, MEC) and Fundacion Seneca for his financial support through the projects BQU-2001-04777 and 00483/PI/04, respectively. LC, MTMR and JJGC thank the Spanish CICYT for financial support of this research in the framework of Projects No. CTQ2004-03246/BQU and MAT2004-03849. Also, JJGC thanks Ministerio de Educacion y Ciencia for a Formacion Profesorado Universitario (FPU) predoctoral fellowship.

References

1. van Gunsteren, W. F.; Berendsen, H. J. C. *Angew. Chem Int. Ed.* **1990,** *29,* 992.

2. Lopez-Cascales, J. J.; Garcia de la Torre, J.; Marrink, S. J.; Berendsen, H. *J. Chem. Phys.* **1996,** *104,* 2713.

3. Tieleman, D.; Marrink, S.; Berendsen, H. *Biochimica et Biophysica Acta* **1997,** *1331,* 235.

4. Lopez-casacles, J. J.; Otero, T.; Smith, B.; Gonzalez, C.; Marquez, M. *J. Phys. Chem. B* **2006,** *110,* 2358.

5. Pandit, S.; Bostick, D.; Berkowitz, M. *Biophys. J.* **2003,** *84,* 3743.

6. Kox, A.; Michels, J.; Wiegel, F. *Nature* **1980,** *287,* 317.

7. Böcker, J.; Schlenkrich, M.; Brickmann, J. *J. Phys. Chem.* **1992,** *96,* 9915.

8. Tarek, M.; Tobias, D.; Klein, M. *J. Phys. Chem.* **1995,** *99,* 1393.

9. Dhathathreyan, A.; Collins, S. *Langmuir* **2002,** *18,* 928.

10. Cuny, V.; Antoni, M.; Arbelot, M.; Liggieri, L. *J. Phys. Chem. B* **2004,** *108,* 13353.

11. Kaznessis, Y.; Kim, S.; R.G., L. *Biophys. J.* **2002,** *82,* 1731.

12. Nielsen, S.; Lopez, C.; Moore, P.; Klein, M. *J. Phys. Chem. B* **2003,** *107,* 13911.

13. van Buuren, A.; Berendsen, H. *Langmuir* **1994,** *10,* 1703.

14. Dutta, P.; Peng, J.; Lin, B.; Prakash, M.; Georgopoulos, P.; Ehrlich, S. *Phys. Rev. Lett.* **1987,** *58,* 2228.

15. Möhwald, H. Phospholipid Monolayers. In *Handbook of biological physics*; Lipowsky, R.; Sackmann, E., Eds.; Elsevier Science B.V.: 1995.

16. Dluhy, R. *Appl. Spectrosc. Rev.* **2000,** *35,* 315.

17. Schalke, M.; Lösche, M. *Adv. in Colloid. and Int. Sci.* **2000,** *88,* 243.

18. Dynarowicz-Latka, P.; Dhanalaban, A.; Oliveira Jr., O. N.; *Adv. Coll. Surf. Sci.* **2001,** *91,* 221.

19. Hönig, D.; Möbius, D. *J. Phys. Chem.* **1991,** *95,* 4590.

20. Martin, M.; Prieto, I.; Camacho, L.; Möbius, D. *Langmuir* **1996,** *12,* 6554

21. Ahuja, R.; Caruso, P.; Möbius, D.; Wildburg, G.; Ringsdorf, H.; Philp, D.; Preece, J.; Stoddart, J. *Langmuir* **1993,** *9,* 1534.

22. Riegler, H. amd Essler, F. *Langmuir* **2002,** *18,* 6694.

23. Pavinatto, F.; Caseli, L.; Pavinatto, A.; dos Santos Jr., D.; Nobre, T. M.; Zaniquelly, M.; Silva, H.; Miranda, P.; Oliveira Jr., O. N.; *Langmuir* **2007,** *23,* 7666.

24. Berendsen, H.; Grigera, J.; Straatsma, T. *J. Phys. Chem.* **1987,** *91,* 6269.

25. Lindahl, E.; Hess, B.; van der Spoel, D. *J. Mol. Mod.* **2001,** *7,* 306.

26. Berendsen, H.; van der Spoel, D.; van Drunen, R. *Comp. Phys. Comm.* **1995,** *91,* 43.

27. Darden, T.; York, D.; Pedersen, L. *J. Chem. Phys.* **1993,** *98,* 10089.

28. Essmann, U.; Perea, L.; berkowitz, M.; Darden, T.; Lee, H.; Pedersen, L. *J. Chem. Phys.* **1995,** *103,* 8577.

29. van Gunsteren, W.; Berendsen, H. *Mol. Phys.* **1977,** *34,* 1311.

30. Berendsen, H. J. C.; Postma, J. P. M.; van Gunsteren, W. F.; DiNola, A.; Haak, J. R. *J. Chem. Phys.* **1984,** *8,* 3684.

31. Nandi, N.; Vollhardt, D. *Chem. Rev.* **2003,** *103,* 4033.

32. Thirumoorthy, K.; Nandi, N.; Vollhardt, D. *J. Phys. Chem. B* **2005,** *109,* 10820.

33. Nandi, N.; Vollhardt, D. *Acc. Chem. Res.* **2007,** *40,* 351.

34. Lide, D., Ed.; *Handbook of Chemistry and Physics;* CRC: 2002-2003.

35. Giner-Casares, J. J; Perez-Morales, M.; Bolink, H.; Muñoz, E.; de Miguel, G.; Martin-Romero, M.; Camacho, L. *J. Coll. Int. Sci.* **2007,** *315,* 278.

36. Cascales, J. L.; Giner-Casares, J. J. "Video movie: Gas and solid phase of a lipid Langmuir Monolayer by Molecular Dynamics", 2007 ISBN:978-84-95781-87-1.

37. Thirumoorthy, K.; Nandi, N.; Vollhardt, D. *Langmuir* **2007,** *23,* 6991.

38. Schalke, M.; Krüger, P.; Weygand, M.; Lösche, M. *Biochim. et Biophys. Acta (BBA)* **2000,** *1464,* 113.

39. Egberts, E.; Berendsen, H. *J. Chem. Phys.* **1988,** *89,* 3718.

40. Pickholz, M.; Oliveira, Jr. O. N.; Munir, M. S. *J. Phys. Chem. B* **2006,** *110,* 8804.

41. Winter, R. *Curr. Op. Coll. Int. Sci.* **2001,** *6,* 303.

4.3. Effect of Na^+ and Ca^{2+} ions on a $DMPA^-$ lipid Langmuir monolayer

Studying the effect of alkali and alkaline-earth metal cations on Langmuir monolayers is relevant from a biophysical and nanotechnological points of view. In this work, the effect of Na^+ and Ca^{2+} on a model of an anionic Langmuir lipid monolayer of dimyristoylphosphatidate ($DMPA^-$) is studied by molecular dynamics simulations. The influence of the type of cation on the lipid structure, lipid-lipid interactions, and lipid ordering is analyzed in terms of electrostatic interactions. It is found that for a lipid monolayer in its solid phase, the effect of the cations on the properties of the lipid monolayer can be neglected. The influence of the cation is enhanced for the lipid monolayer in its gas phase, where sodium ions show a high degree of dehydration compared with calcium ions. This loss of hydration shell is partly compensated by the formation of lipid-ion-lipid bridges. This difference is ascribed to the higher charge-to-radius, q/r for Ca^{2+}, which makes ion dehydration less favorable compared to Na^+. Owing to the different dehydration behavior of sodium and calcium ions, diminished lipid-lipid coordination, lipid-ion coordination and lipid ordering are observed for the Ca^{2+} compared to Na^+. Furthermore, for both gas and solid phases of the lipid Langmuir monolayers, lipid conformation and ion dehydration across the lipid/water are studied.

Paper published in *ChemPhysChem*, 2008, 9, 2538-2543

4.3.1. Introduction

The effect of alkali and alkaline-earth metal cations on Langmuir monolayers is relevant from a nanotechnological,[1–3] and biophysical point of view, as models of lipid bilayers,[4,5] since a lipid monolayer resembles half of a symmetric lipid bilayer. Thus, an understanding of the interactions that control cation-lipid interactions is highly desirable.

Since pioneering works,[6] this topic is still the target of intensive and recent research.[7–9] A broad spectrum of experimental techniques is available for *in situ* studies at the air/water interface, for example FTIR spectroscopy,[10,11] Vibrational Sum-Frequency Generation (VSFG)[7] or Brewster Angle Microscopy (BAM).[12,13]

In spite of the incessant improvements in the resolution of these experimental techniques, computer simulations have emerged as a valuable method for obtaining an atomistic description of this system. Thus, the main motivation of this work is to offer further insights into the experimental description of interactions between alkali and alkaline-earth cations and lipid Langmuir monolayers by means of molecular dynamics simulations. For this purpose, the anionic lipid dimyristoylphosphatidate ($DMPA^-$) was chosen as the component of the Langmuir monolayer. As representative and biological relevant cations, Na^+ and Ca^{2+} were chosen. Five simulations of DMPA Langmuir monolayers at different values of surface area for each cation, were performed and subsequently analyzed. To our knowledge, this is the first computational study on cationic effects on Langmuir monolayers performed at different values of lipid density, for which experimental information is usually difficult

to obtain, especially the highly expanded case. This work focused on the limiting phases of any Langmuir monolayer, that is, its gas and solid phases.

4.3.2. Method and Model

Periodical conditions were considered along the three-dimensional space. The absence of interactions between the two lipid leaflets along the z axis was achieved by introducing an empty gap of 2 nm above and below each lipid leaflet. The final dimensions of the computing box were 8.75, 8.67 and 12.05 nm, for the x, y and z axes, respectively. The system was set up by confining the water layer between two $DMPA^-$ leaflets to form a sandwich structure in which the lipid heads point toward the water layer. Figure 4.27 depicts two snapshots of the system in its solid phase in presence of NaCl and $CaCl_2$.

Gromacs 3.3. package[14,15] was used to run the MD simulations, and the analysis of the generated trajectories was performed with software code developed by us. Charge distribution on each lipid was published elsewhere.[16] The atom numberin scheme of the lipid is displayed in Figure 4.28. Long range interactions were modeled by a Lennard-Jones potential with a cutoff of 0.8 nm, and the electrostatic interactions by the Ewald algorithm.[17,18] All the bonds of the system were constrained by SHAKE.[19] The time step used in all the simulations was of 2 fs. After the system was set up, it was subjected to a steepest descent energy-minimization process to remove undesired overlaps between neighboring atoms. Once the system reached a relative energy minimum, five simulations were carried out for different values of lipid surface

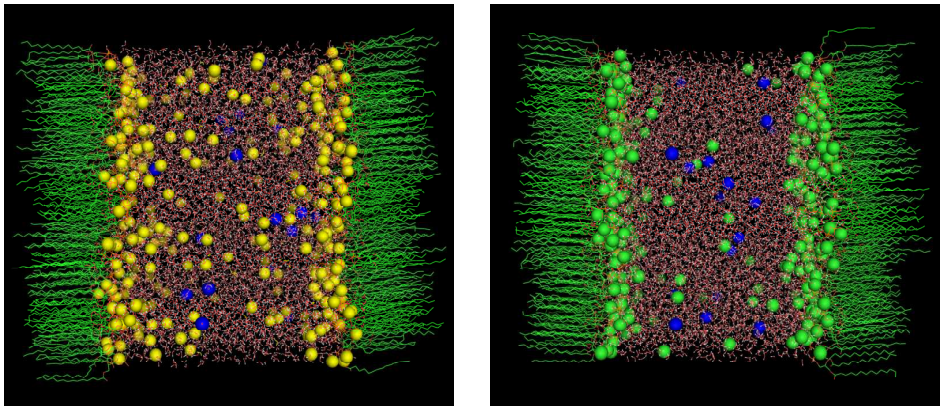

Figure 4.27: Snapshots of the whole system in its solid phase. Left: in presence of NaCl, (sodium : yellow, chloride : blue). Right: in presence of $CaCl_2$ (calcium : green, chloride: blue).

area and cation, that is, a total of ten simulations. In every case, a cation concentration of 0.1 N was used[**]. This ionic concentration was chosen to ensure that differences in lipid behavior arise only from the different type of cation. Thus, the desired value of surface area per lipid was fitted by removing a certain number of lipids in both leaflets until the right value was achieved. Because our system was simulated under NVT thermodynamic conditions, that is, the number of particles of the system N, box volume V and temperature T remained constant, the system was coupled to an external temperature bath by using the Berensend algorithm[20] with coupling temperature constants τ_T, of 0.1 ps. All the simulations were carried out for 20 ns. The simulations were carried out at 293 K, which is the usual temperature under laboratory conditions. In all the cases, the first 4 ns of trajectory

[**]Note that Normality=Molarity x Charge[23]

length were discarded for analysis associated with the time required to reach the equilibrium. SPCE water molecules[21] were used. The simulations were carried out on an HP160 parallel computer using 16 processors, with a performance of 1.5 ns of trajectory length per hour.

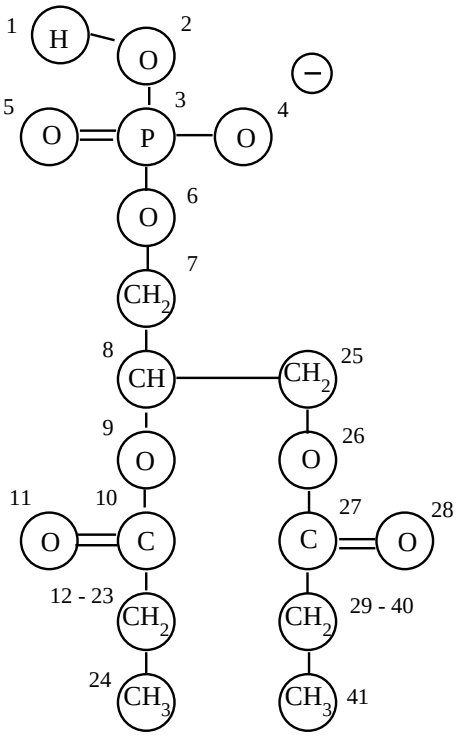

Figure 4.28: Atom numbering of a single $DMPA^-$.

4.3.3. Results and Discussion

Lipid-Lipid Interactions

The effect of ions on charged Langmuir monolayers has been thoroughly studied and described by a pile of experimental data (for a complete review,

see ref.[22]). In this context, the aim of this work is to obtain a deeper understanding of this phenomenon by means of the atomistic resolution given by the Molecular Dynamics Simulation technique. To this end, the radial distribution function $g(r)$ can be used to attain information on coordination between different atoms. This function is defined as

$$g(r) = \frac{N(r)}{4\pi r^2 \rho \delta r} \tag{4.12}$$

where $N(r)$ is the number of atoms in a spherical shell at distance r and thickness δr from a reference atom, and ρ is the number density in the computing box.

For example, the radial distribution function of atom 4 (a phosphate, O atom) around atom 3 (a P atom) of a neighbor lipid is displayed on Figure 4.29, from which two conclusions can be made:

1. Radial distribution function, and hence coordination between lipids, reaches higher values for lipid monolayer in its solid state (lower surface area per lipid). This result is clearly related to the increasing packing of lipids associated with lipid compression.

2. Due to its higher q/r ratio[***], Ca^{2+} ions lead to reduce formation of charge bridge between neighboring lipids compared to Na^{+} ions. This effect can be clearly associated with the lower degree of dehydration of calcium compared to sodium, as will be described in the next section.

[***]Given, $r_{Na^+} = 1.18$ Å and $r_{Ca^{2+}} = 1.12$ Å, q/r ratio of Ca^{2+} is almost twice than of Na^{+}[23]

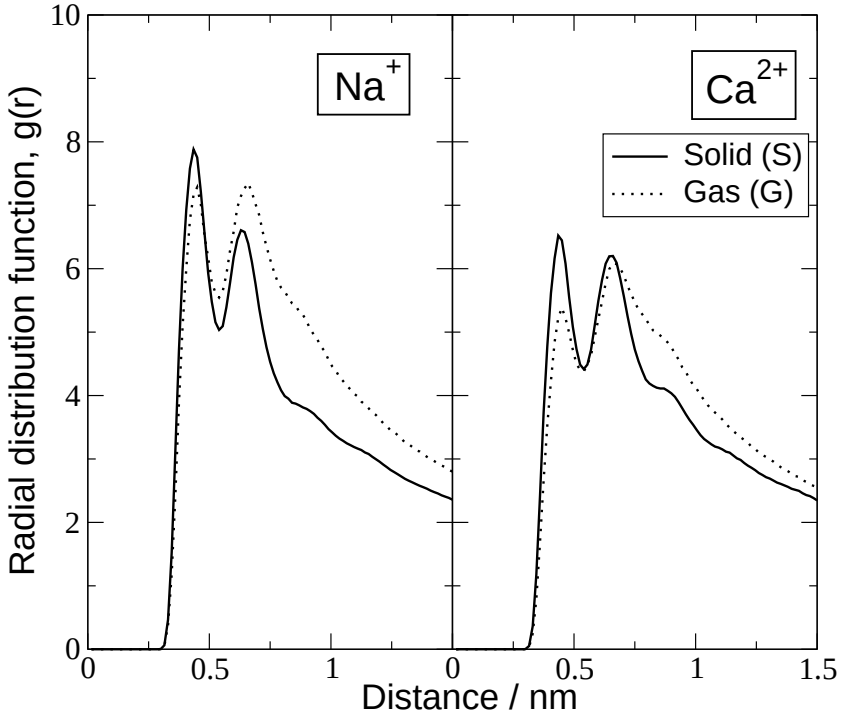

Figure 4.29: Radial distribution function $g(r)$ for atom 4 (phosphate O atom) of a given lipid around atom 3 (P atom) of a neighbor lipid. Left: DMPA monolayer with a subphase of 0.1 N Na^+. Right: DMPA monolayer with a subphase of 0.1 N Ca^{2+}. Solid line: area per lipid molecule of 0.4 nm^2 (solid phase). Dotted line: area per lipid molecule of 1.0 nm^2 (gas phase).

Ion Hydration Across Lipid/Water Interface

This section discusses the effect of the dehydration of ions from bulk solution to the deepest zones in the interior of the lipid leaflet, associated to the gas and solid phases of the lipid monolayer. By integration of the first peak of the radial distribution function $g(r)$ of water around the different ions, we are able to calculate the hydration number of sodium, calcium and chloride ions from bulk solution to the interior of the lipid leaflet (Tables 4.6 and 4.7), where the zones bulk solution, interface, and deep lipid are as defined in Figure 4.30.

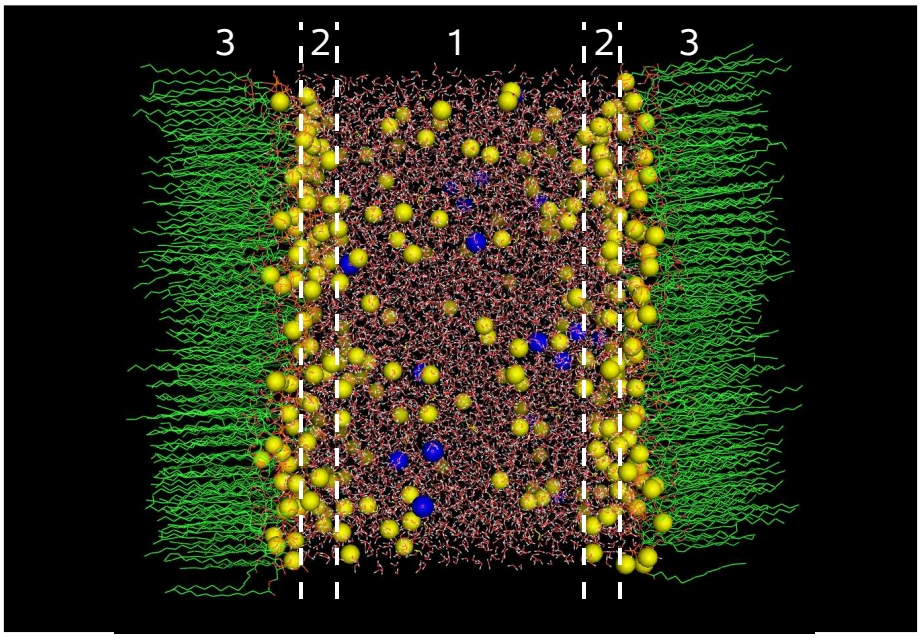

Figure 4.30: Snapshot of a DMPA monolayer in presence of NaCl 0.1 N (Na^+ : yellow, Cl^- : blue beads) in its solid phase, which the three zones considered in the text labeled: 1.- bulk solution, 2.- interface, and 3.- deep lipid.

Gas Phase(G)		
	Na^+	Ca^{2+}
deep lipid	2.7	5.5
interface	3.3	5.9
bulk	4.9	6.0

Table 4.6: Hydration numbers of sodium and calcium ions for different zones of the system, from bulk solution to the deepest zones in the lipid monolayer in its gas phase.

In the $NaCl$ subphase, Na^+ loses between two and three water molecules of its hydration shell in gas and solid phases, respectively, and thus becomes almost naked with only one water molecule in the gas phase, when sodium

Solid Phase(S)		
	Na^+	Ca^{2+}
deep lipid	1.4	4.5
interface	4.0	5.8
bulk	4.9	6.3

Table 4.7: Hydration numbers of sodium and calcium ions for different zones of the system from bulk solution to the deepest zones in the lipid monolayer in its solid phase.

penetrates into the lipid from bulk solution. In the case of using $CaCl_2$ as electrolyte, almost no dehydration occurs for calcium ions in the lipid monolayer in its gas phase, as opposed to a degree of dehydration of two water molecules in the solid phase, and thus bears at least four water molecules in its hydration shell in gas or solid phase.

From the above results we conclude that, due to the higher charge density of calcium versus sodium ions, calcium almost completely retains its hydration shell in both solid and gas phases in a DMPA Langmuir monolayer. However, in the case of sodium ions, noticeable dehydration is observed in both gas and solid phases.

Lipid-Ion Coordination

Coordination of ions to the polar head of a lipid monolayer is a widely studied and discussed topic at present.[24–29] With the aim of gaining insight into the process, the radial distribution function for both Na^+ and Ca^{2+} around a phosphate oxygen atom of the lipid polar head group (atom 4) was computed (Figure 4.31), this Figure shows that sodium/lipid coordination is more pronounced than calcium/lipid coordination. This behavior is expected from

the results obtained on ion hydration. Thus, dehydration of the sodium ion is clearly compensated by the sodium/lipid coordination, compensating in both solid and gas phase. In the case of calcium case, a first small coordination peak is observed in Figure 4.31 for gas and solid phase. This behavior is in accordance with the values listed in tables 4.6 and 4.7, which show negligible calcium dehydration in the gas phase and only a small degree of dehydration of two water molecules in the solid state, in good agreement with the coordination data shown in Figure 4.31, in which a higher peak is obtained in the solid phase than in the gas phase.

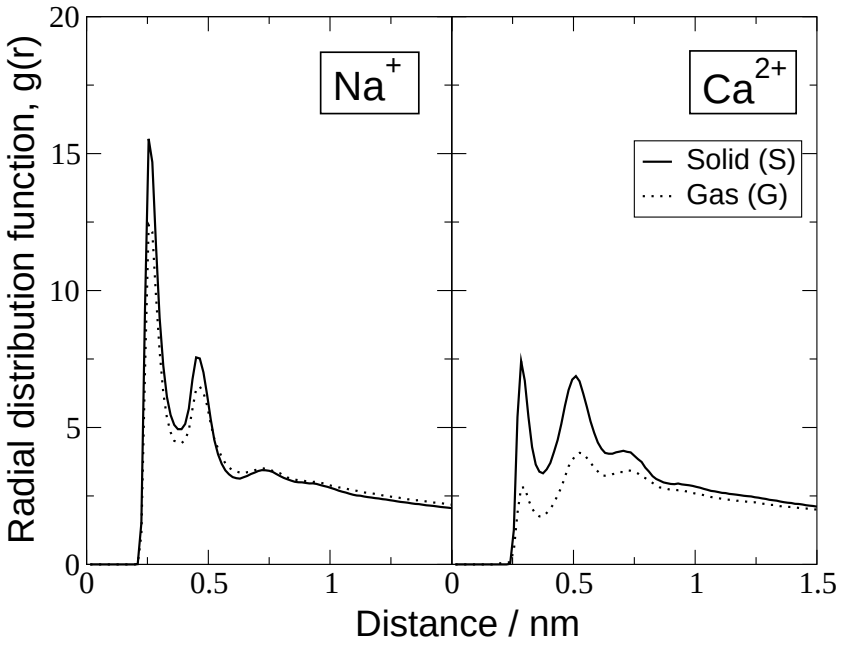

Figure 4.31: Radial distribution function for Na^+ and Ca^{2+} ions around a phosphate oxygen atom (atom 4) of a DMPA molecule. Left: DMPA monolayer with a subphase of 0.1 N Na^+. Right: DMPA monolayer with a subphase of 0.1 N Ca^{2+}. Solid line: area per lipid molecule of 0.4 nm^2 (solid phase). Dotted line: area per lipid molecule of 1.0 nm^2 (gas phase).

To visualize the cation arrangement at the vicinity of the lipid/water

interface, a snapshot showing the lipid head/cation coordination of the lipid monolayer at its solid phase is displayed in Figure 4.32. The cations are coordinated exclusively by the phosphate oxygen atoms of the lipid head groups.

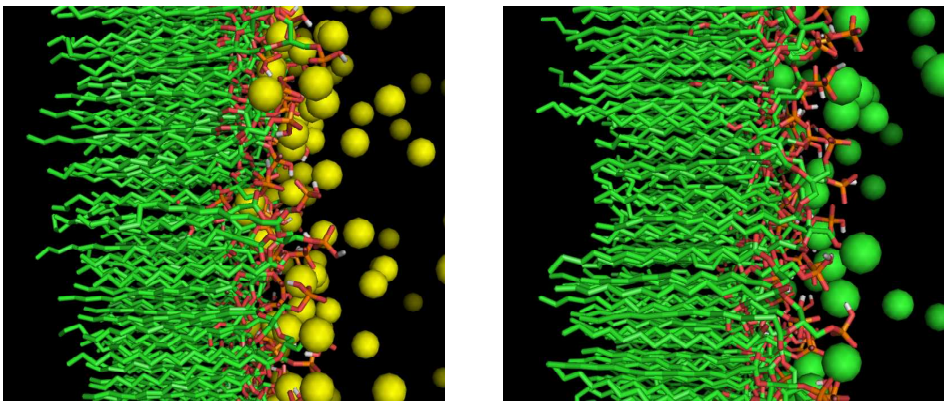

Figure 4.32: Lateral view of the lipid/water interface showing the arrangement of Na^+ and Ca^{2+} with respect to the lipid polar head group. O: red, P: orange, Na^+: yellow, Ca^{+2}: green.

Effect of Ions on Lipid Ordering

The effect of compression on the lipid molecules that form a Langmuir monolayer can be experimentally studied by *in situ* spectroscopy at the air/water interface. In most cases, these techniques allow two different zones of the lipid to be discriminated: tails and head[30] group. Given adequate signals, it is possible to infer changes in both orientation and order.[10,27]

With the aim to complement this experimental information, the order

of DMPA lipids in the Langmuir monolayer was analyzed for the different subphases. This information is obtained in terms of the order parameter for each ethylene group of the lipid tails, and also expressed by the tilt angles of the hydrophobic lipid tails and polar lipid head group.

Tilt angles for lipid head groups and tails are displayed in Table 4.8. The head tilt angle was defined as the angle formed by the P-N vector (formed by atoms 6 and 1) and the z axis. In the case of lipid monolayer in its solid phase, there are not any significant differences for both head and tail tilt angles. This is an intuitive result, since at a reduced value of area per lipid, DMPA molecules are arranged very close to each other with scarce degree of freedom.

Conditions	Head group		Tail	
	Solid phase	Gas phase	Solid phase	Gas phase
0.1 N Na^+	52.59	60.14	11.3	39.5
0.1 N Ca^{2+}	51.15	60.90	10.7	43.3
Pure water[16]	52.4	62.6	11.5	57.77
Experimental[31]	48	65	9	51

Table 4.8: Head and tail tilt angles of the DMPA in different phases. Experimental and simulation data are shown for comparison. Each value is expressed in degrees with respect to the z axis normal to the monolayer surface.

However, a different behavior is observed for the lipid monolayer in its gas phase. As discussed above, Na^+ ions promote stronger electrostatic bridging interactions between neighboring lipids than Ca^{2+} ions. Simulation data show significant differences between tail tilt angles for the different subphases induced by the two types of ion. Moreover, these differences are almost irrelevant in the case of head tilt angles compared with the tilt of the lipid

tails. These results may seem surprising, since small change in head tilt can result in bigger changes in the tail ordering.

The above-described behavior can be easily explained from Figures 4.34 and 4.33. Thus, we observe that neither sodium nor calcium penetrates into the monolayer beyond the carbonyl oxygen atom in either gas or solid phase. Calcium ions do not reach the lipid carbonyl oxygen atoms either in gas or solid phase. Hence, lipid head group orientation is expected to be similar in the presence of sodium and calcium ions because in both cases lipid head groups are coordinated to these ions. However lipid tail orientation is expected to be noticeably affected in presence of sodium compared to calcium ions, since sodium ions can coordinate to lipid carbonyl oxygen atoms to form charge bridges between neighboring lipids, and thus the lipid tails are tilted compared to the case of calcium ions, which are not able to reach this zone in the lipid monolayer.

To expand our description, we studied the order parameters of the hydrocarbon tails along the lipid. The parameter can be studied in lipid bilayers by NMR experiments, measuring the deuterium order parameters along the lipid ethylene tails. The order parameter tensor is defined as:

$$S_{ab} = \frac{\langle 3\cos(\theta_a)\cos(\theta_b) - \delta_{ab}\rangle}{2} \quad a, b = x, y, z \tag{4.13}$$

where x, y and z are the local coordinates of the system, θ_a is the angle made by the molecular axis with the perpendicular axis to the lipid monolayer, and δ_{ab} is the Kronecker delta. From simulation, the order parameter, $-S_{CD}$ can be determined by using the relation proposed by Egberts and Berendsen,[32]

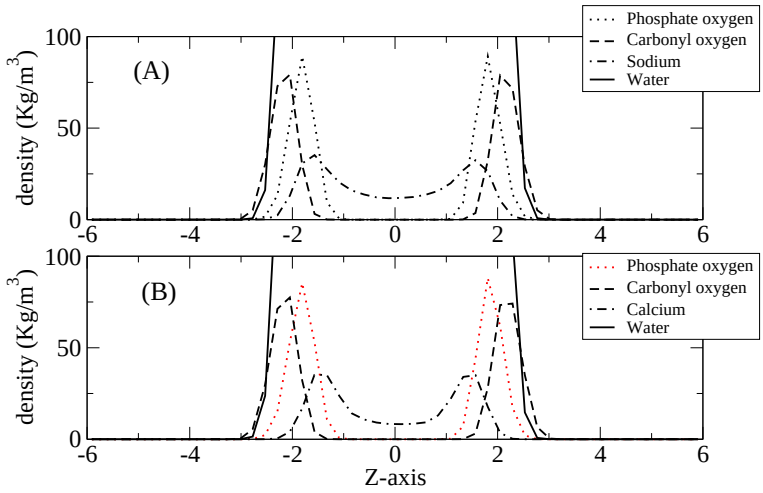

Figure 4.33: Distribution of phosphate and carbonyl oxygen atoms of DMPA in its gas phase, in presence of sodium (A) and calcium (B) ions along the axis perpendicular to the lipid monolayer. Zero was placed in the middle of the box.

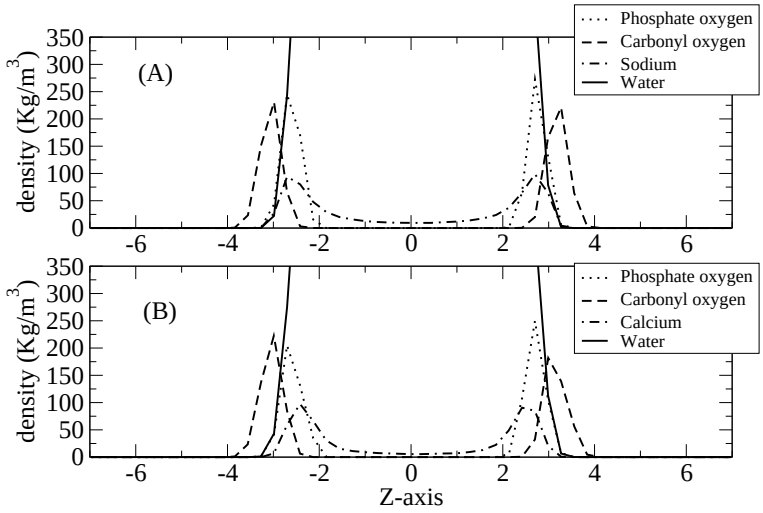

Figure 4.34: Distribution of phosphate and carbonyl oxygen atoms of DMPA in its solid phase, in presence of sodium and calcium ions along the axis perpendicular to the lipid monolayer. Zero was placed in the middle of the computing box.

$$-S_{CD} = \frac{2S_{xx}}{3} + \frac{S_{yy}}{3} = \langle \frac{3\cos^2\theta_n - 1}{2} \rangle \tag{4.14}$$

where S_{xx} and S_{yy} are the terms of the order parameter tensor of the equation 4.13 and θ_n the angle made by the lipid hydrocarbon chain with respect to x axis. According to ref.,[33] a value of $-S_{CD} = 0.5$ is interpreted as an orientation fully perpendicular to the z axis, and for an order parameter of zero, a random orientation of the tail respect to the z axis is assumed.

To the best of our knowledge, it is not possible to perform NMR measurements *in situ* at the air/water interface of Langmuir monolayers. By means of computer simulations, order parameters were obtained for each hydrocarbon tail (Figure 4.35). For the lipid monolayer in its solid phase, the deuterium order parameters are practically coincident due to the close packing of the lipids in this phase. However, for the lipid monolayer in its gas phase, there are significant differences between the order parameters obtained in the cases of Na^+ and Ca^{2+}. Sodium ions promote the lipid-ion-lipid interaction, and hence an increase in of the order parameter of the monolayer is expected.

4.3.4. Conclusions

A model of Langmuir monolayer of anionic lipid dimyristoylphosphatidate ($DMPA^-$) was analyzed in terms of its interactions with different subphases containing Na^+ or Ca^{2+} cations. These fundamental studies on cation-lipid interactions are particularly relevant from a biophysical and nanotechnological points of view. This work focused on offering a complementary atomistic point of view from molecular dynamics simulations in addition to the experimental descriptions.

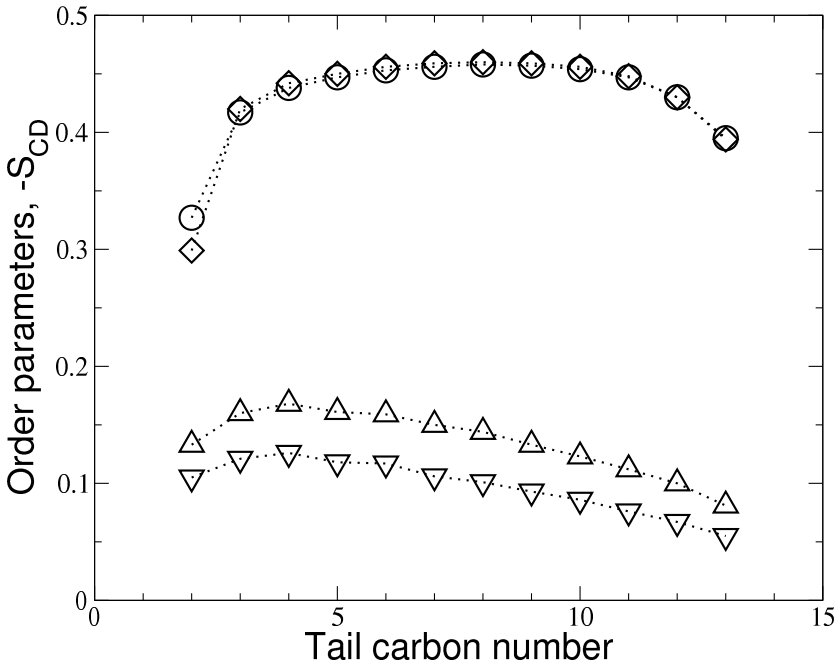

Figure 4.35: Order parameters of DMPA lipid hydrocarbon tails. ∘ and ⋄ denote a lipid monolayer with an area of 0.4 nm^2 per lipid molecule (solid phase) and 0.1 N Na^+ and 0.1 N Ca^{2+} as subphase, respectively. △ and ▽ denote a lipid monolayer with an area of 1.0 nm^2 per lipid molecule (gas phase) and 0.1 N Na^+ and 0.1 N Ca^{2+} as subphase, respectively. The dotted line is a guide for the eye.

This study has elucidated the effects of Na^+ and Ca^{2+} cations at a concentration of 0.1 N on the electrostatic interactions between lipids. Thus, lipid-ion interactions, lipid-lipid interactions, and the lipid order were analyzed for lipid monolayers in their gas and solid phases. At the same surface area per lipid, less coordination between neighboring lipids was observed in presence of calcium ions than in the presence if sodium ions. Ordering of the lipids was analyzed in terms of head group and tail tilt angles and by lipid-tail order parameters. In the solid phase, Na^+ and Ca^{2+} do not have any effect on the lipid conformation due to the low degree of freedoms of the lipids in this phase associated with the high applied surface pressure. Howe-

ver, in the gas phase, a more highly ordering on Na^+ subphase was found, associated with dehydration of sodium ions, which becomes almost naked in the deepest zones of the lipid monolayer, as opposed to calcium ions, which remained hydrated in any case. Thus, sodium ions can induce charge bridges between neighboring lipids to compensate their dehydration. In the Ca^{2+} subphase, the lipids were more disordered due to the poor dehydration of calcium, and hence charge-bridge formation between neighboring lipids was almost absent.

Acknowledgments

LC, MTMR and JJGC thank the Spanish CICYT for financial support of this research in the framework of Projects No. CTQ2007-64474/BQU and MAT2004-03849. Also, JJGC thanks Ministerio de Educacion y Ciencia for a Formacion Profesorado Universitario (FPU) predoctoral fellowship. The authors wish to acknowledge the staff of the Computing Center of the Polytechnic University of Cartagena (SAIT) for their support in carrying out this work.

References

1. Guo, S.; Popovitz-Biro, R.; Weissbuch, I.; Cohen, H.; Hodes, G.; Lahav, M. *Adv. Mater.* **1998,** *10,* 121.

2. Peng, J. B.; Barnes, G. T.; Gentle, I. R. *Adv. Coll. Int. Sci.* **2001,** *91,* 163.

3. Kalinina, M. A.; Golubev, N. V.; Raitman, O. A.; Selector, S. L.; Arslanov, V. V. *Sensors and Actuators B* **2006,** *114,* 19.

4. Brockman, H. *Curr. Opin. Struct. Biol.* **1999,** *9,* 438.

5. Kaganer, V. M.; Möhwald, H.; Dutta, P. *Rev. Mod. Phys.* **1999,** *71,* 779.

6. Shah, D. O.; Schulman, J. H. *J. Lip. Res.* **1965,** *6,* 341.

7. Sovago, M.; Wurpel, G. W. H.; Smits, M.; Müller, M.; Bonn, M. *J. Am. Chem. Soc.* **2007,** *129,* 11079.

8. Shapovalov, V. L.; Brezesinski, G. *J. Phys. Chem. B* **2006,** *110,* 10032.

9. Shapovalov, V. L.; Ryskin, M. E.; Konovalov, O. V.; Hermelink, A.; Brezesinski, G. *J. Phys. Chem. B* **2007,** *11,* 3927.

10. Flach, C. R.; Wrauner, B. J.; Mendelsohn, R.; *Biophys. J.* **1993,** *65,* 1994.

11. Dluhy, R. A. *Appl. Spectrosc. Rev.* **2000,** *35,* 315.

12. Grigoriev, D.; Krustev, R.; Miller, R.; Pison, U. *J. Phys. Chem. B* **1999,** *103,* 1013.

13. Hönig, D.; Möbius, D. *J. Phys. Chem.* **1991,** *95,* 4590.

14. Lindahl, E.; Hess, B.; van der Spoel, D. *J. Mol. Mod.* **2001,** *7,* 306.

15. Berendsen, H.; van der Spoel, D.; van Drunen, R. *Comp. Phys. Comm.* **1995,** *91,* 43.

16. Giner-Casares, J. J.; Camacho, L.; Martín-Romero, M. T.; López-Cascales, J. J. *Langmuir* **2008,** *24,* 1832.

17. Darden, T.; York, D.; Pedersen, L. *J. Chem. Phys.* **1993,** *98,* 10089.

18. Essmann, U.; Perea, L.; Berkowitz, M.; Darden, T.; Lee, H.; Pedersen, L. *J. Chem. Phys.* **1995,** *103,* 8577.

19. van Gunsteren, W. F.; Berendsen, H. *Mol. Phys.* **1977,** *34,* 1311.

20. Berendsen, H. J. C.; Postma, J. P. M.; van Gunsteren, W. F.; DiNola, A.; Haak, J. R. *J. Chem. Phys.* **1984,** *8,* 3684.

21. Berendsen, H.; Grigera, J.; Straatsma, T. *J. Phys. Chem.* **1987,** *91,* 6269.

22. Koelsch, P.; Viswanath, P.; Motschmann, H.; Shapovalov, V. L.; Brezesinski, G.; Möhwald, H.; Horinek, D.; Netz, R. R.; Giewekemeyer, K.; Salditt, T.; Schollmeyer, H.; von Klitzing, R.; Daillant, J.; Guenoun, P. *Coll. Surf. A* **2007,** *303,* 110.

23. Lide, D., Ed.; *Handbook of Chemistry and Physics;* CRC: 2002-2003.

24. Grigoriev, D.; Miller, R.; Wüstneck, R.; Wüstneck, N.; Pison, U.; Möhwald, H. *J. Phys. Chem. B* **2003,** *107,* 14283.

25. Watanabe, I.; Tanida, H.; Kawauchi, S. *J. Am. Chem. Soc.* **1997,** *119,* 12018.

26. Le Calvez, E.; Blaudez, D.; Buffeteau, T.; Desbat, B. *Langmuir* **2001,** *17,* 670.

27. Gericke, A.; Hühnerfuss, H. *Thin Solid Films* **1994,** *245,* 74.

28. Kmetko, J.; Datta, A.; Evmenenko, G.; Dutta, P. *J. Phys. Chem. B* **2001,** *105,* 10818.

29. Aroti, A.; Leontidis, E.; Maltseva, E.; Brezesinski, G. *J. Phys. Chem. B* **2004,** *108,* 15238.

30. Ma, G.; Allen, H. C. *Langmuir* **2006,** *22,* 5341.

31. Schalke, M.; Krüger, P.; Weygand, M.; Lösche, M. *Biochimica et Biophysica Acta* **2000,** *1464,* 113.

32. Egberts, E.; Berendsen, H. *J. Chem. Phys.* **1988,** *89,* 3718-3732.

33. Pickholz, M.; Oliveira Jr., O. N.; Skaf, M. S. *Biophys. Chem.* **2007,** *125,* 425-434.

Capítulo 5

Dispositivos Orgánicos Electroluminiscentes

5.1. Highly Pure and Stable White Light from an Externally Modified Organic Light-Emitting Device

In this work, a blue organic light-emitting device (OLED) is modified by addition of an external inorganic phosphor layer, CaS:Eu, resulting in a white organic light-emitting device (WOLED). To improve light extraction characteristics of the external phosphor layer, a pre treatment of the phosphor particles, prior to external phosphor layer deposition, was tested, reducing phosphor particle size by a high speed stirring of a phosphor dispersion. The effect of this pre treatment on the device electroluminescent characteristics of the device is discussed, showing that there is an improvement on light extraction at high values of current density. Using this design, a good quality white light emission is achieved, with Commission Internationale de l´Eclairage coordinates, CIE(x, y) = (0.32, 0.35), close to reference D65 white, with CIE coordinates (x,y) = (0.31, 0.33). This white light is specially suitable for solid state lightning applications, where a good white colour is required. In this regard, shortcomings derived from a multilayered WOLED structure, such as different emitted colour at different values of applied voltage, have been overcome by the use of a single emitting layer. In the present WOLED, there is no significant change in emitted light colour by the device, along the whole work range of current density, from 25 to 510 mA/cm^2.

Paper to be submitted

5.1.1. Introduction

White light organic light-emitting devices, WOLEDs, are a subject of intense research, as promising candidates for backlight emitters in devices, such as LCDs, and solid state lighting.[1] For these applications, some characteristics are highly desirable: a) simple design of the organic light-emitting device, OLED, making device performance reproducible, and minimizing problems associated with a multilayer structure, b) stability of the emitted light colour against changes in operating voltage/current range, as well as with the aging process of the device.

White light in OLEDs can be produced by combination of individual complementary colours. To achieve this task, it is possible to use either a doped emitting layer, or a combination of different emitting layers. A fundamental issue for WOLEDs, when considering them for solid state lighting applications, is both colour quality and stability of the emitted light. In this regard, doped emitting layers WOLEDs[2,3] under different values of voltage can lead to variations of intensity of dopant emission, which will result in the last term on colour variation. In the case of multilayer WOLEDs, three emitting layers are used in the same device, obtaining white light by combination of the three basic colours, red, green, and blue (RGB).[4,5] This combination can be produced by either vertical or horizontal stacking of the basic colours emitting layers. For the case of vertical stacking of the layers, the recombination zone of electrons and holes may vary with the voltage, making the emission colour dependent on the applied voltage.[6] In the case of a horizontal stacking of the layers, this problem is avoided since there is

not physical contact between emitting layers. However, for both vertical and horizontal stacking of the RGB emitting layers, different degradation rate of the constituent emitting layers may lead to colour change, resulting in a dependence of the emitted colour on the device age.

As an alternative way to overcome the above mentioned problems, in this work, a simple design for a WOLED is used. A blue OLED is modified by the addition of an external inorganic phosphor layer,resulting in a overall white light emission. This design was firstly successfully reported by Duggal et al.,[7] and subsequently applied by other groups.[8,9] In this setting, the phosphor layer does not form any interface with the emitting layer, as they are physically separated. Therefore, there is not a phosphor-emitting layer interface, which may result in a different current flow or form any charge carrier trapping site. Furthermore, given the fact that there is only one emitting layer, it is also expected that there are not any shortcomings derived from a multilayer OLED design. As commented above, in multilayer OLEDs, different degradation rates of the different emissive layers may lead to emission colour change with device aging. Moreover, variation on recombination zone with different applied voltage, may lead to different rate of emission from each layer, which may lead to different emitted colour.

The presented WOLED shows a high stability on the emitted colour for the complete operating voltage range. Furthermore, the white colour emitted by the WOLED, CIE(x, y) = (0.32, 0.35), is located close to reference D65 CIE white, with CIE(x,y) = (0.31, 0.33).

In the present study, all the organic layers were deposited using solution-processing methods, spin-coating and drop-casting. Solution processing met-

hods are expected to offer lower manufacturing cost,[10,11] therefore making this approach suitable for industrial applications.

5.1.2. Experimental

Materials

OXD-7 (1, 3, 4 - oxadiazole, 2,2'-(1,3 - phenylene)bis(5-(4-(1,1-dimethylethyl)phenyl)) and FIrpic were purchased from Luminescence Technology Corp. and supplied by Rubipy Scientific Inc. PEDOT:PSS (poly(3,4-ethylenedioxythiophene): poly(styrene-sulfonate)), PVK (polyvinilcarbazole) and PMMA (polymethyl methacrylate) were acquired from Sigma-Aldrich. The cathode metals, Al and CsF, were purchased from Lesker, Co. The used solvents, chlorobenzene and toluene, were Analar grade from BDH. All chemical compounds and solvents were used with no further purification. Transparent anodes, Indium-tin oxide (ITO) coated glass, with a sheet resistance of 20 Ω per square, was acquired from Merck. CaS:Eu and SrS:Eu, materials used as external phosphors, were kindly given by Phosphor Technologies, Ltd.

Phosphor pre-treatment and external phosphor layer building

The CaS:Eu was previously treated under a high speed stirring process. In this pre treatment, a dispersion of CaS:Eu in toluene was stirred at 10000 r.p.m. for ten cycles, and consisting on: 10 minutes under stirring, and 5 minutes for solution cooling, using an ULTRA TURRAX (IKA) high speed

stirrer. A blend of the phosphor (13 mg) and a PMMA solution in toluene (33 g L^{-1}) was used for the drop casting process. The planar density of the solution was 200 $\mu L \cdot cm^{-2}$, and gave a final thickness of the external phosphor layer of ca. 100 μm. To improve the quality of the drop casted film, the film was dried under a saturated atmosphere of toluene overnight. Then, the substrate was kept in an nitrogen atmosphere for 24 hours, to ensure that the solvent was completely removed. After the drying process, the substrates were ready for the deposition of the OLED onto the ITO side. Once the OLED was built, it was kept under vacuum until the characterization process, with a storage time between 24 and 48 hours. The characterization process was performed under a separate chamber, which was kept under vacuum.

OLED Fabrication

The deposition of the organic layers and the cathode metals was performed inside a glove box under an atmosphere of inert nitrogen. PEDOT:PSS was used as the hole injection layer. The PEDOT:PSS layer was deposited by spin-coating, from its aqueous solution, giving a final thickness of 40 nm. There were no storage time since PEDOT:PSS layer deposition and next layer deposition. The active, light-emitting layer, was formed by PVK, OXD-7, and an iridium phosphorescent dye, FIrpic. The proportion between these three materials, as expressed by weight, is 60 % PVK + 30 % OXD-7 + 10 % FIrpic. The emitting layer was deposited by spin coating, giving a final thickness of 60 nm. After the deposition of the organic layers, a thermal annealing at 80 °C during 30 minutes was performed, to remove any trace of solvent.

After the thermal annealing, the cathode metals, 2 nm of CsF, followed by 150 nm of Al, were deposited using thermal evaporation at high vacuum. The basic configuration[12] of the starting blue OLED was: Al (150nm)/CsF (2nm)/PVK-OXD-7-FIrpic (60 nm)/PEDOT:PSS (40 nm)/ITO/Glass. For the case of WOLEDs, the procedure was similar, with the only exception that a modified glass substrate was used. These modifications consisted in the drop casting deposition of the phosphor onto the external layer of the OLED, that is, on the glass side. Figure 5.1 shows the final structure of the WOLED.

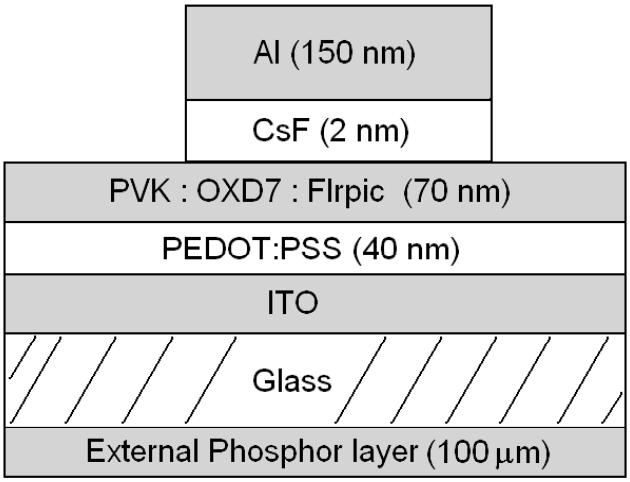

Figure 5.1: Structure of the WOLED. On parenthesis the thicknesses of each layer.

OLED Characterization

The DC bias was applied and the current was measured by a Keithley 485 digital picoammeter. For external quantum efficiency measurements, the

light power was calculated using the photocurrent and the conversion factor (wavelength dependent) of the photodiode (ampere/watt). Electroluminescence spectra were measured using an Ocean Optics USB 2000 Miniature Fibre Optic Spectrometer. AFM pictures were acquired using a Digital Instruments NanoManII from Veeco.

5.1.3. Results and discussion

Colour modification of a blue emitting OLED into white light has been carried out by means of and external inorganic phosphor layer. The advantages of this design are: 1) a simple design, 2) there is only one emitting layer, 3) all the organic materials are solution-processed.

The distinct effect of two different inorganic phosphors, CaS:Eu and SrS:Eu, as external phosphors, on the resultant emitted colour of the OLED was studied. The CIE(x,y) coordinates of the unmodified blue OLED, and the coordinates of those externally modified OLEDs as well, are shown in Figure 5.2 a). As a reference, D65 White is also shown. An excess of phosphor leads to the blue colour, emitted by the unmodified OLED, is turned into red and yellowish, with the use of an external layer of CaS:Eu phosphor and SrS:Eu phosphor, respectively.

Due to the yellowish conversion of blue light using SrS:Eu, a pure white light could not be achieved. For this reason, the rest of the study will be focused on the use of CaS:Eu as an external phosphor.

The electroluminescent spectra of the blue OLED, the WOLED, as well as the modified OLED with an excess of phosphor in the external phosphor

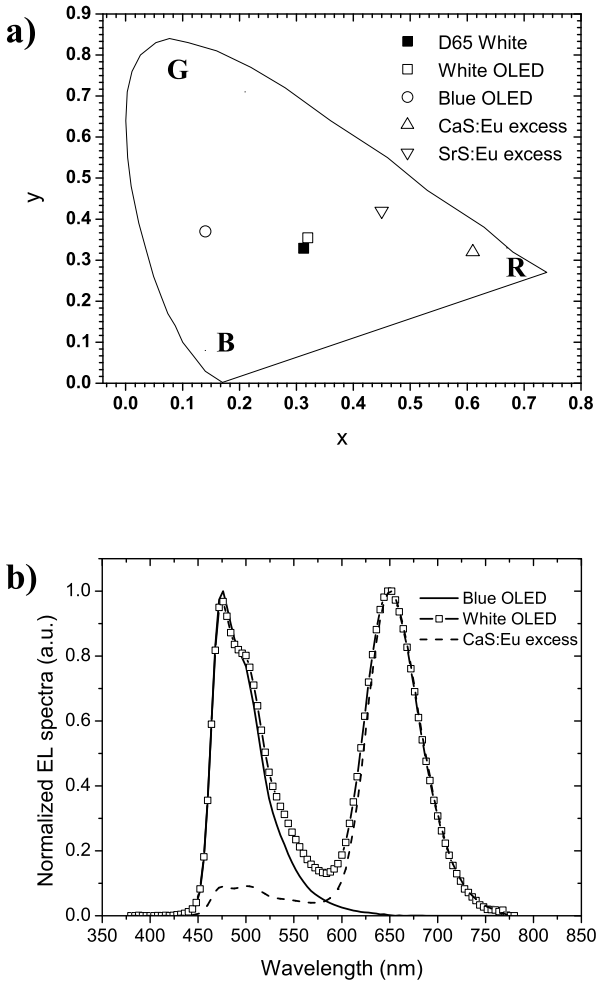

Figure 5.2: a) CIE (x,y) coordinates for OLEDs and D65 white. **b)** Electroluminescent spectra for blue OLED (straight line), white OLED (open squares) and OLED with an excess of phosphor in the external layer (dashed line).

layer, are shown in Figure 5.2b). With an adequate balance between the two emission peaks, one from the blue OLED (476 nm), and the other one from the phosphor (652 nm), a white colour can be achieved in the resultant light. Using the adequate amount of phosphor in the external phosphor layer, a

good quality of the white light of the WOLED can be achieved. This emitted white light presents a CIE coordinates of CIE (x,y) = (0.32, 0.35), when compared to D65 white, with CIE (x,y) = (0.31, 0.33). Conversion of emitted blue light into red light has been found to be proportional to the amount of inorganic phosphor in the external phosphor layer. However, variation of PMMA concentration up to 5 times, giving no variation on electroluminescent characteristics observed. Thus, PMMA concentration was adjusted to get a good quality of the external phosphor layer.

The stability of the white colour of the emitted light was checked. In Figure 5.3 a), the electroluminescent spectra emitted by the WOLED are displayed along the entire current density operation range, it was found not significant variation. As a result, the CIE (x,y) coordinates of the WOLED remain unchanged for the whole operating range of current, from 25 to 510 mA/cm^2. It is worthy to be highlighted that this colour stability is a highly desirable feature of a WOLED, since commercial applications require a stable colour.

Given the fact that the active layer of the OLED remains unchanged when the blue OLED is turned into a WOLED by the use of an external phosphor layer, current density-voltage (I-V) curves show no change, within experimental error, as expected. Figure 5.3 b) displays I-V curves for both blue OLED and WOLED.

Once reached the conversion of the emitted blue light into white light, a pre-treatment of the phosphor particles was performed, in order to improve the efficiency of the WOLED. With the aim of reducing the phosphor particle size, a dispersion of the CaS:Eu phosphor was processed under high speed

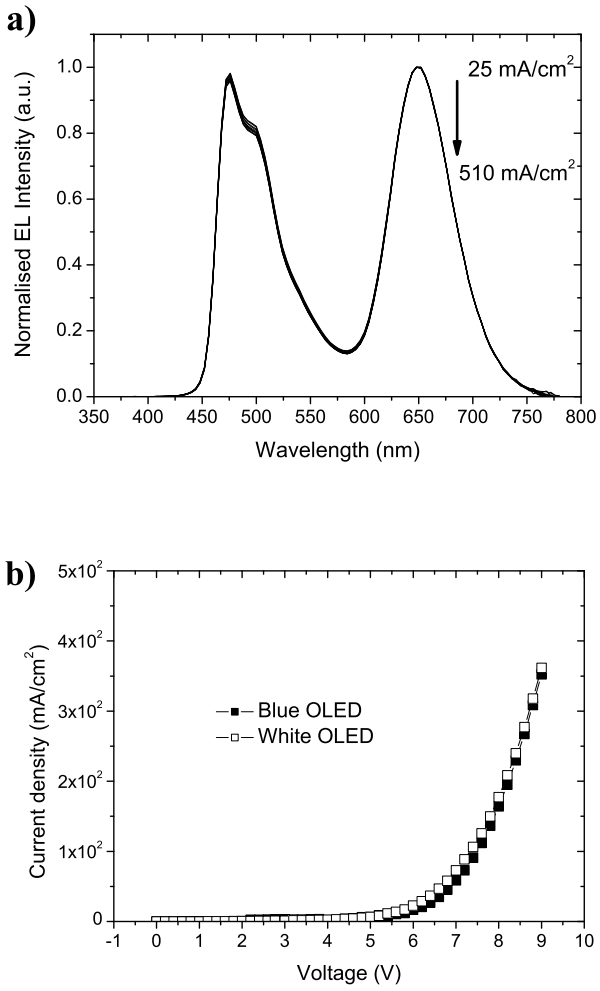

Figure 5.3: a) Evolution of the electroluminescent spectra for the WOLED along the entire current density operation range. **b)** I-V curves for a blue OLED (closed circles) and a white OLED (open circles).

stirring, leading to a decrease of the particle size. For this pre-treatment of the phosphor, a high speed stirrer was used, using a 10000 r.p.m. stirring of the CaS:Eu phosphor particles dispersed in toluene.

After pretreatment, a noticeable diminution of phosphor particle size can be observed by AFM (Figure 5.4). For comparison purposes, a pure PMMA film deposited under the same conditions as the external phosphor layer is shown (Fig. 5.4c).

The phosphor particle size goes down to 0.5-1 micron size, with the phosphor pre-treatment. The phosphor layer without pre-treatment appears with a higher polidispersity of the particle size, with respect to the phosphor layer with pre-treatment. In the latter case, the phosphor particles appear with a similar size. Figure 5.4b) shows a significant grade of aggregation between phosphor particles. This aggregation between particles may cause a negative effect on phosphorescence quantum yield.

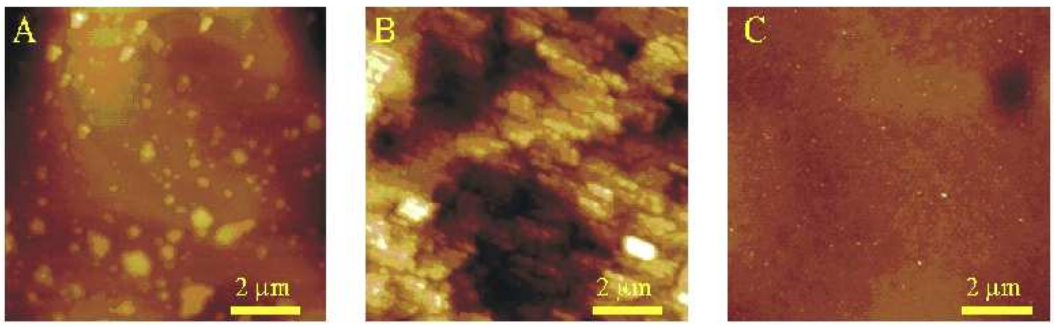

Figure 5.4: AFM pictures of: a) External phosphor layer without any pre treatment, b) External phosphor layer pre treated under high speed stirring, c) PMMA film with no phosphor, showed for comparison purposes. Square side corresponds to 10 μm.

Once the blue light is emitted by the active layer, it reaches the external phosphor layer. In the interaction with the external phosphor layer, the blue light may be either dispersed or absorbed by the phosphor, with subsequent phosphorescent emission in the last case. This phosphorescent emission is

produced in a ratio of absorbed/emitted photons determined by quantum yield of the phosphor.

The increase of efficiency with light dispersion have been described previously,[13,14] using particle size on the micron range, which coincides with the particle size used in this study. In this environment, the limiting process for an efficient extraction of the light is the absorption and emission of the phosphor, that is, the quantum yield of the phosphorescence process.

Electroluminescent characteristics of both blue and white OLEDs, using pre treatment of phosphor, are shown in Table 5.1, measured at a constant applied current of 50 mA/cm^2. Turn-on voltage value remains unchanged for both blue and white OLED. However, overall light emission, and then, efficiency, reaches higher values, for the blue OLED, when expressed as lm/W, that for the externally modified, WOLED. Though it may exists some dispersion of the emitted light, as described in previous papers, it seems that the existence of phosphor particles aggregation could result in: a) opaque regions, trapping emitted light and b) phosphorescence quenching, diminishing phosphorescence quantum yield. Thus, phosphor particles aggregation may be responsible for the lowered efficiency of the WOLED device.

However, this loss of efficiency is widely compensated by: 1) the combination of emissive peaks of the blue OLED and the phosphor, resulting in a pure, high quality white light, and 2) colour stability along the complete voltage operating range.

In Figure 5.5, efficiency of the WOLED is shown, using an external phosphor layer, either with or without, pre treatment, as well as for the unmodified blue OLED for comparison purposes. Regarding the pre treatment of

	Blue OLED	White OLED
$\eta_{ext}(\%)$	4.1	3.0
CIE x	0.14	0.32
CIE y	0.36	0.35
cd/A	14.7	5.0
lm/W	6.2	2.3
cd/m^2	748	254
Turn-on voltage (v)	4.0	4.0

Table 5.1: Compared electroluminescent and efficiency characteristics of the blue (top) and white (bottom) OLED measured, at a constant current density of 50 mA/cm^2

the CaS:Eu phosphor particles, the pre treatment leads to a more stable efficiency value along operating current range, softening the lowering of the efficiency with increasing current density.

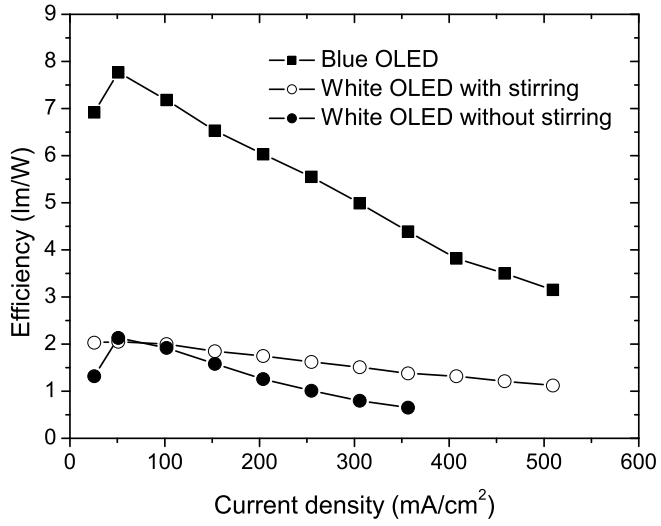

Figure 5.5: Efficiency of the WOLEDs vs current density

The pre treatment of the external phosphor layer has proven to improve

light extraction of the WOLED, when comparing to an external phosphor layer without pre treatment. This improvement is probably due to the avoid to some extent the opaque regions formation, allowing light to be extracted in an easier manner, as well as avoiding self quenching of the phosphorescence process by diminution of phosphor particle size.

5.1.4. Conclusions

A WOLED has been formed by the combination of a blue emitting OLED and an external phosphor layer. This design presents some advantages over the WOLEDs built by combination of separate red, green and blue emitting layers, e. g., stability of emitted colour at different values of current. Two inorganic phosphors, namely, CaS:Eu and SrS:Eu, were tested as phosphorescent materials for the external phosphor layer, proving that CaS:Eu was more suitable for obtaining white light, and was chosen as the phosphorescent material for the external phosphor layer. In this regard, the emitted white light from the WOLED could be considered as good quality, with CIE (x,y) = (0.32, 0.35), close to reference D65 CIE white, with CIE(x,y) = (0.31, 0.33). Furthermore, there is not significant change on colour coordinates of the emitted light along the whole operating current range. In order to improve light extraction from the WOLED, a pre-treatment consisting on high speed stirring of the phosphor particles, prior to external phosphor layer building, was used. This pre-treatment showed to improve light extraction at high values of current density. This improvement on light extraction have been adscribed to diminution on phosphor particle size, which may lead to a

higher phosphorescence quantum yield.

Acknowledgments

The authors thank the Spanish CICYT for financial support of this research in the framework of Project CTQ2007-64474 (FEDER-2)/BQU. J. J. G. C. thanks MICINN for a FPU predoctoral grant. Phosphor Technologies, Ltd. is gratefully acknowledged for kindly providing inorganic phosphor samples.

References

1. D'Andrade, B. W.; Forrest, S. R. *Adv. Mater.* **2004,** *16,* 1585.
2. Walzer, K.; Maennig, B.; Pfeiffer, M.; Leo, K. *Chem. Rev.* **2007,** *107,* 1233.
3. Baldo, M. A.; O'Brien, D. F.; You, Y.; Shoustikov, A.; Sibley, S.; Thompson, M. E.; Forrest, S. R. *Nature* **1998,** *395,* 151.
4. D'Andrade, B. W.; Thompson, M. E.; Forrest, S. R. *Adv. Mater.* **2002,** *14,* 147.
5. Kido, J.; Kimura, M.; Nagai, K. *Science* **1995,** *267,* 1332.
6. Colvin, V. L.; Schlamp, M. C.; Allvisatos, A. P. *Nature* **1994,** *370,* 354.
7. Duggal, R. A.; Shiang, J. J.; Heller, C. M.; Foust, D. F. *Appl. Phys. Lett.* **2002,** *80,* 3470.
8. Krummacher, B. C.; Mathai, M. K.; So, F.; Choulis, S. A.; Choong, V. *Journal of Display Technology* **2007,** *3,* 200.
9. Ahn, J. H.; Bertoni, C.; Dunn, S.; Wang, C.; Talapin, D. V.; Gaponik, N.; Eychmüller, A.; Hua, Y.; Bryce, M. R.; Petty, M. C. *Nanotechnology* **2007,** *18,* 335202.
10. Meerholz, K. *Nature* **2005,** *437,* 327.
11. Tullo, A. H. *Chem. Eng. News* **2008,** *86,* 20.
12. Krummacher, B. C.; Choong, V.; Mathai, M. K.; Choulis, S. A.; So, F.; Jermann, F.; Fiedler, T.; Zachau, M. *Appl. Phys. Lett.* **2006,** *88,* 113506.
13. Nakamura, T.; Tsutsumi, N.; Juni, N.; Fujii, H. *J. Appl. Phys.* **2004,** *96,* 6016.
14. Shiang, J. J.; Faircloth, T. J.; Duggal, R. A. *J. Appl. Phys.* **2004,** *95,* 2889.

Capítulo 6

Conclusiones

Al final de cada uno de los capítulos de esta Memoria, se incluye un conjunto de conclusiones particulares al estudio desarrollado. En este apartado se presentan las conclusiones mas generales, teniendo en cuenta tanto el grado de alcance anvanzado como sus implicaciones prácticas.

1. Las técnicas de Langmuir y Langmuir−Blodgett se han aplicado con éxito para preparar monocapas mixtas con un alto grado de ordenación a nivel molecular. Estas monocapas están formadas por una matriz de fosfolípido y un colorante orgánico o un complejo organometálico de Iridio (III). Las monocapas que contienen complejo organometálico de Iridio (III), que son particularmente interesantes debido a su uso potencial en OLEDs, se han transferido con éxito a un soporte sólido.

2. Se ha combinado el uso de medidas termodinámicas, ópticas, espectroscópicas, y en ocasiones computacionales, para la descripción y el análisis de monocapas de Langmuir, tanto de DMPA puro como en combinación con otro componente. La regla de aditividad se ha aplicado para la descripción de uno de los sistemas de interés, y se ha extendido su aplicación a medidas de tipo óptico, en concreto elipsometría.

3. Los resultados presentados en esta Memoria contribuyen a la comprensión de la formación y el comportamiento de monocapas con un alto grado de ordenación a nivel molecular, y abren nuevas perspectivas a aplicaciones potenciales que exploten la funcionalidad de dichas películas.

4. La simulación por ordenador de monocapas de Langmuir ha permitido obtener una descripción complementaria a la experimental. Lo que es más, se ha podido estudiar el efecto de distintas condiciones experimentales en los lípidos que conforman la monocapa, tales como variaciones en la presión lateral o en la fuerza iónica.

5. La construcción de dispositivos electroluminiscentes orgánicos emisores de luz blanca, mediante el uso de una capa externa de material fosforescente a un dispositivo emisor de luz azul, ha demostrado ser una estrategia de gran interés para la construcción de dispositivos destinados a ser usados en iluminación.

Each Chapter of this Report ends with the specific conclusions relevant to the work described in it. In this section, a summary of the more general conclusions according to both the degree of improvement achieved and its practical trascendence is presented.

1. Langmuir and Langmuir−Blodgett techniques have been successfully applied for the preparation of molecularly ordered mixed monolayers. These mixed monolayers are formed by DMPA lipid and either an organic dye or an Iridium (III) organometallic complex. The latter, of particular interest due to its potential application on OLEDs, has been successfully transferred to a solid substrate.

2. Monolayer, optical and spectroscopical techniques, as well as computational techniques in some cases, have been combined to arrive at a description and analysis of the molecular organization of Langmuir monolayers of DMPA and mixed monolayers. Additivity rule has been applied to one of the studied system, and its application has been extended to ellipsometry measurements.

3. The results presented contribute to the understanding of the formation and behaviour of organized monolayers and open new perspectives for potential application of such thin films.

4. A complementary description of Langmuir monolayers was obtained by means of computer simulations. Furthermore, the effect of different experimental conditions, such as surface pressure and ionic strenght, on lipid Langmuir monolayers has been studied.

5. White emitting OLEDs have been achieved by the use of an external phosphor layer, modificating a blue emitting OLED. This strategy has been shown to be a useful way of build devices for lightning purposes.

Capítulo 7

Trabajo Pendiente de Publicación

La presente Memoria discute distintos aspectos de la organización molecular en Películas de Langmuir, tanto desde su estudio básico, como de sus posibles aplicaciones. Las líneas de investigación presentadas han dado lugar a resultados que complementan y amplían a los presentados en los Capítulos previos de esta Memoria. Los temas generales tratados pueden englobarse en:

1. Estudio computacional de monocapas de Langmuir, tanto puras como mixtas. La información obtenida mediante técnicas computacionales se valida mediante los parámetros experimentales que sean accesibles. Así, se realizan estudios que combinan las técnicas computacionales con las experimentales.

2. Estudio de organización molecular en monocapas de Langmuir y Langmuir-Blodgett. Para ello, se usan las técnicas ópticas ya expuestas en esta Memoria. Adicionalmente, se pretende usar otras técnicas como PM-IRRAS, que ha sido adquirida recientemente por el grupo de investigación al que el doctorando pertenece.

3. Uso de sistemas ordenados molecularmente para construcción, diseño y mejora de dispositivos optoelectrónicos. Para ello se combina el uso de las técnicas Langmuir−Blodgett y Langmuir−Schaeffer.

4. Monocapas de Langmuir como modelos biofísicos. Además de moléculas anfifílicas de estructura molecular simple, como ácidos grasos o lípidos, se estudia el comportamiento interfacial de proteínas. Mediante las transferencias a sustratos sólidos de películas que contengan biomoléculas, se estudian las posibles aplicaciones de las mismas.

A continuación se presentarán algunos resultados obtenidos, con el objetivo de ilustrar con ejemplos las cuatro líneas nombradas.

Estudio termodinámico de la interacción entre moléculas sonda y monocapas de Langmuir

Los estudios termodinámicos en monocapas de Langmuir, tanto de aquellas formadas por lípidos puros como la interacción de las mismas con moléculas sonda, son de gran interés. Este interés puede ser nanotecnológico, en cuanto permite la construcción de estructuras de tamaño nanométrico con un alto grado de ordenación a nivel molecular.[1] Además, este interés puede provenir del campo de la Biofísica, donde las monocapas de Langmuir se usan como modelo de bicapas celulares.[2]

Aunque experimentalmente puede estimarse el efecto de la introducción de una determinada molécula en el diagrama de fases de una monocapa lipídica, no puede obtenerse el cambio neto de la energía libre asociada a la introducción de dicha molécula en la monocapa. Las simulaciones por ordenador mediante Dinámica Molecular pueden aportar información sobre esta magnitud termodinámica, complementando así a las técnicas experimentales.

Se ha determinado el potencial de fuerza media, PMF, para una molécula de colorante, en concreto azul de metileno, que se reparte entre el seno del agua y el interior de una monocapa de Langmuir lipídica, formada exclusivamente por DMPA. El perfil de Energía Libre para una molécula de azul de metileno que va desde el seno de agua al interior de una monocapa puede ser calculado mediante:

$$\Delta G_b(z) = -RT \ln \frac{C_{MB}^{eq}(z)}{C_{MB}^{*}} = -RT \ln(PMF) \tag{7.1}$$

donde R es la constante de los gases, T la temperatura, $C_{MB}^{eq}(z)$ el perfil de la concentración en equilibrio del azul de metileno a diferente profundidad en el interior de la monocapa lipídica, y C_{MB}^{*} la concentración en equilibrio de azul de metileno en el seno del agua.

En el caso de una simulación para la cual la molécula de azul de metileno se mueva libremente, ésta tenderá a difundir y permanecer en la posición con respecto a la monocapa de mayor estabilidad. Previsiblemente, dicha posición será cercana a la cabeza polar de los lípidos, donde dicha molécula quedará retenida por interacciones electrostáticas, dada la carga opuesta del DMPA y el azul de metileno. En este caso, se obtendrá un muestreo pobre de la concentración del azul de metileno para el tiempo de simulación usado, sobre todo en la zona más hidrofóbica de la monocapa. Con objeto de superar esta limitación, se usa el *Umbrella Sampling Method*[3] para calcular el potencial de fuerza media, PMF. En este método, se fuerza a la molécula de azul de metileno a permanecer en la región de interés con respecto al eje z mediante la aplicación de un potencial armónico.[4] De esta forma, y partiendo de las configuraciones iniciales de una monocapa lipídica de DMPA, para ambos estados, sólido y gas, se construyeron las siguientes simulaciones independientes, reflejadas en la Tabla 7;

En cada una de las simulaciones, se restringió el movimiento del azul de metileno a una posición dada del eje z mediante un potencial armónico, de forma que la molécula mantiene su coordenada z constante, pudiendo moverse libremente en el plano $x-y$. La constante de fuerza para este potencial

Estado	Área molecular	Simulaciones	Tiempo total (ns)
Gas	1.00	37	1480
Sólido	0.40	47	1880

Tabla 7.1: Detalles computacionales para el estudio termodinámico de azul de metileno en interacción con una monocapa lipídica. Estado: Estado de agregación de la monocapa. Área molecular: Área por molécula de lípido. Simulaciones: Número total de simulaciones independientes para cada estado. Tiempo total: Tiempo de simulación empleado para cada estado teniendo en cuenta el total de las simulaciones realizadas.

aplicado fue de 3000 kJ·mol^{-1}·nm^2. La molécula de azul de metileno se desplazó 0.1 nm para cada ventana consecutiva de simulación. Con el objeto de ahorrar tiempo de computación, se calculó el PMF para dos moléculas de azul de metileno por cada simulación. Las dos moléculas se separaron una distancia de $Z_{tot}/2$, a lo largo del eje z, donde Z_{tot} es la longitud total del eje z. Con esta distancia de separación, se asegura la interacción nula entre ambas moléculas, que podría dar lugar a artefactos de simulación. De esta forma, se generaron $37 + 47 = 84$ trayectorias distintas, que suman un total de 3360 ns. Una vez que todas las trayectorias están disponibles, se usó el método WHAM,[5] de sus siglas en inglés *Weighted Histogram Analysis Method* para obtener el PMF del azul de metileno a lo largo de las distintas posiciones que puede ocupar en la monocapa de Langmuir. De esta forma se obtuvo el perfil de incremento de energía libre (ΔG) para una molécula de azul de metileno que interacciona con una monocapa de DMPA. Dicho perfil, así como las densidades atómicas de las cadenas metálicas y los átomos de fósforo de las moléculas de DMPA, se calculó y se muestra en las Figuras 7.1 (para la monocapa de DMPA en fase Gas) y 7.2 (para la monocapa en fase sólido).

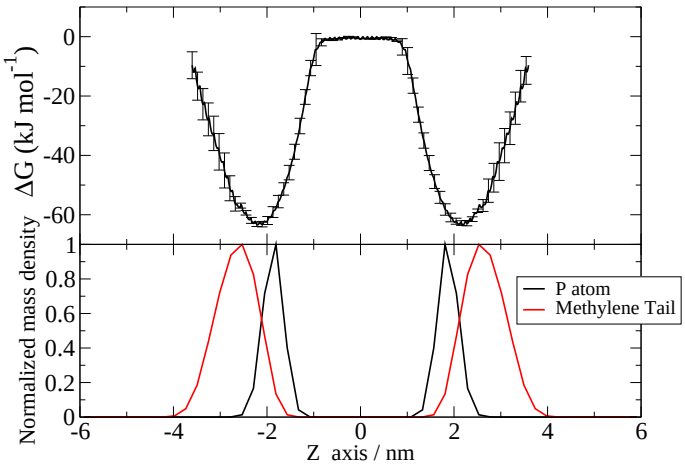

Figura 7.1: Arriba: Perfil de incremento de energía libre para una molécula de azul de metileno que interacciona con una monocapa de DMPA puro. Abajo: Densidades atómicas de grupos metileno y átomos de fósforo para una monocapa de fosfolípido en fase Gas.

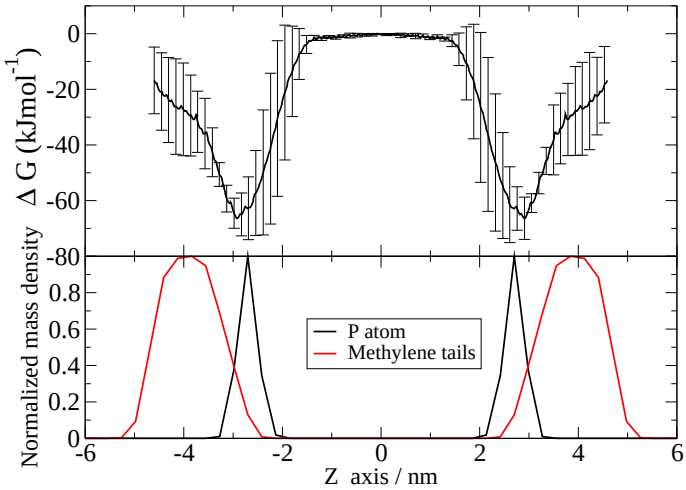

Figura 7.2: Arriba: Perfil de incremento de energía libre para una molécula de azul de metileno que interacciona con una monocapa de DMPA puro. Abajo: Densidades atómicas de grupos metileno y átomos de fósforo para una monocapa de fosfolípido en fase Sólido.

Del perfil de energía ΔG, se puede estimar computacionalmente el coeficiente de reparto del azul de metileno entre la monocapa y el seno del agua.

Con el valor del mínimo en el perfil de incremento de energía libre, el coeficiente de reparto K viene dado por:

$$K = exp\left[-\frac{\Delta G_{min}}{k_B T}\right] \tag{7.2}$$

Tomando el valor mínimo del perfil de energía libre, se estimó el coeficiente de reparto del azul de metileno, mostrado en la Tabla 7.2.

Estado	$\Delta G(kJ \cdot mol^{-1})$	**K**
Gas	-66.1	$4.18 \cdot 10^{11}$
Sólido	-63.3	$1.35 \cdot 10^{11}$

Tabla 7.2: Valores del coeficiente de reparto de azul de metileno entre el seno del agua y una monocapa lipídica de DMPA.

Dada la gran afinidad del azul de metileno por la monocapa de DMPA, como ya se discutió en uno de los Capítulos de esta Memoria, el coeficiente de reparto alcanza valores muy altos para ambas fases de la monocapa. Estos valores resultan difíciles de comprobar experimentalmente, ya que en ese orden de magnitud, la relación entre la concentración de azul de metileno entre la monocapa y el agua hace que sea necesario, o bien una monocapa más extensa de lo alcanzable en el laboratorio, o bien una concentración de azul de metileno tan baja que quede fuera de los límites de detección para las técnicas experimentales disponibles. No obstante, la ecuación de Nernst puede aportar una vía para estimar experimentalmente el incremento de energía libre del sistema aquí estudiado. La ecuación de Nernst se expresa como:

$$\Delta E \cdot n \cdot F = \Delta G^0 + k_B T \cdot \ln \frac{c_i^\alpha}{c_i^\beta} \tag{7.3}$$

donde ΔG^0 es el incremento de energía libre total, que proviene de la suma de dos términos: $k_B T \cdot \ln \frac{c_i^\alpha}{c_i^\beta}$, la aportación de la diferencia de potencial químico expresado en un gradiente de concentraciones, y de ΔE, el término que da cuenta de las interacciones electrostáticas entre ambas moléculas. De hecho, dado que se trata de dos moléculas cargadas, se espera que la contribución más importante provenga del término de interacción electrostática. Este término sí resulta evaluable a nivel experimental, mediante la medida del potencial superficial de una monocapa de DMPA con una pequeña cantidad de azul de metileno. El potencial superficial varía con el área molecular tal y como se muestra en la Figura 7.3.

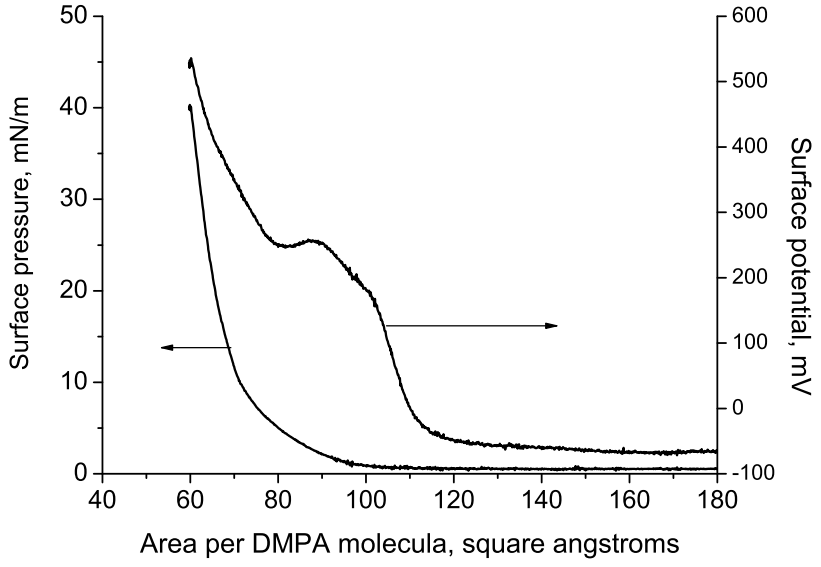

Figura 7.3: Variación del potencial superficial (ΔV) de una monocapa de DMPA con el área molecular.

Tomando un valor límite de 0.5 voltios, el valor de incremento de energía libre sería de $\Delta G = 51$ kJ·mol^{-1}. Este valor se acerca al obtenido compu-

tacionalmente. La diferencia, de aproximadamente un 20 %, entre el valor experimental y el calculado computacionalmente se atribuye al término relativo al potencial químico. Como ya se comentó, este término es de menor importancia, al compararse con el término que da cuenta de las interacciones electrostáticas.

Películas delgadas de nuevos materiales

A lo largo de esta Memoria se ha discutido la organización molecular en monocapas de distintos compuestos, estableciéndose modelos teóricos con objeto de explicar la estructura molecular en estas monocapas. Con objeto de generalizar y/o comprobar estos modelos, se han usado distintos compuestos. La organización molecular de las películas se estudia en función de los componentes de las mismas. Para ello se usa la técnica de Langmuir en conjunción con las técnicas de Langmuir−Blodgett y Langmuir−Schaeffer.

En primer lugar, y en referencia a los complejos organometálicos de Ir(III) usados en esta Memoria, se usan compuestos análogos, también suministrados por el grupo del Dr. Bolink (www.icmol.es). La estructura de dichos compuestos se muestra en la Figura 7.4A.

En ese sentido, es interesante estudiar los cambios en la organización molecular de una monocapa cuando se cambia la molécula que forma la matriz tensioctiva en sí misma. De esta forma, se intercambió la matriz fosfolipídica de DMPA por otra molécula anfitrión en combinación con el complejo organometálico de Iridio (III) descrito en un capítulo anterior de esta Memoria, en concreto por el calix[8]areno. Este calixareno se muestra en la Figura

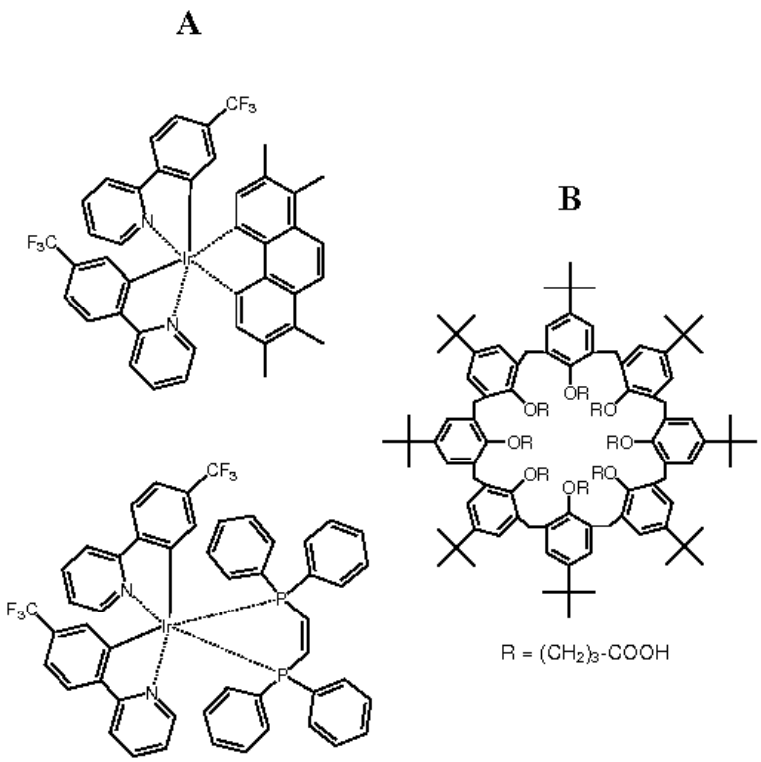

Figura 7.4: A Estructura molecular de los complejos organometálicos de iridio (III), análogos a los descritos en Capítulos anteriores. **B** Calixareno anfifílico usado para la preparación de monocapas mixtas.

7.4B. Para esta monocapa mixta preparada mediante coesparcimiento de una mezcla en proporción molar 1:1 se obtiene la $\pi - A$ mostrada en la Figura 7.5.

La presencia del complejo organometálico modifica la isoterma presión superficial-área molecular del calix[8]areno,[6] produciendo una expansión de la misma. Este efecto se atribuye a la presencia del complejo organometálico en la interfase aire−agua. Con objeto de confirmar dicha presencia del complejo organometálico en la monocapa, se obtuvieron espectros de reflexión UV-vis en la interfase aire−agua(ver Figura 7.6). Dado que sólo las molécu-

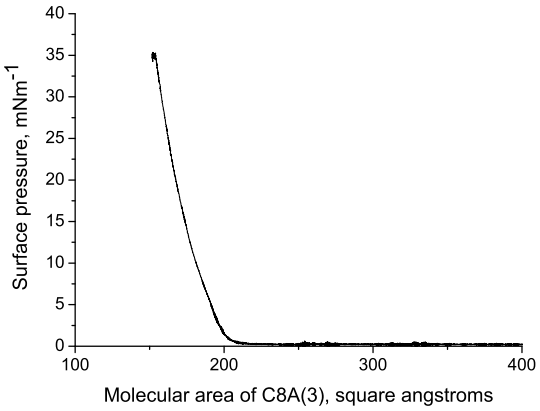

Figura 7.5: Isoterma presión superficial frente a área molecular para una mezcla Ir-dye/calix[8]areno en proporción molar 1:1.

las presentes en la interfase son detectadas por esta técnica, se confirmó la retención del complejo organometálico por la matriz de calixareno. La retención mediante interacciones electrostáticas de moléculas pequeñas a una monocapa de calixareno ya ha sido descrita en bibliografía, como por ejemplo para el caso de una porfirina tetracatiónica.[7] Se espera que esta monocapa mixta, así como otras derivadas, aporten nuevos datos sobre la organización molecular en la interfase aire−agua de sistemas con interés posterior en nanotecnología y en construcción de dispositivos optoelectrónicos.

Películas delgadas en dispositivos optoelectrónicos.

La aplicación de los conocimientos obtenidos durante el estudio de las monocapas a los dispositivos orgánicos optoelectrónicos es el siguiente paso en la línea de investigación centrada en la construcción y/o mejora de dispositivos tales como OLEDs, células fotovoltaicas orgánicas, etc. En ese

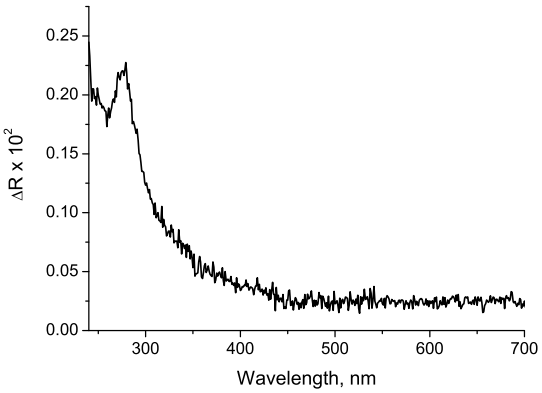

Figura 7.6: Espectro de reflexión UV-visible para una monocapa de calixareno:complejo organometálico de Iridio en proporción molar 1:1 a una presión superficial de 10 mN/m.

sentido, existen informes en la bibliografía que describen una mejora en el rendimiento de ciertos dispositivos mediante la modificación de una o más interfases, gracias a la técnica de Langmuir−Blodgett[8] y otras relacionadas.[9]

Usando monocapas descritas en los Capítulos anteriores de esta Memoria, se han construido OLEDs de una sola capa activa. La estructura de dichos dispositivos es: Ánodo (ITO)/capa activa/Cátodo (metal, p. ej., Aluminio). Para la fabricación de la capa activa, se depositaron monocapas mixtas de complejo organometálico de Iridio (III) y DMPA en proporción equimolar. Se usó la técnica de Langmuir−Schaeffer (LS) para su transferencia. En la Figura 7.7 se muestran los espectros UV-visible de un soporte ITO cubierto con distinto número de monocapas mixtas, transferidas mediante la técnica de Langmuir-Schaeffer. Puede observarse como el valor de absorbancia de los espectros aumenta linealmente con el número de monocapas transferidas, por lo que se asume que la transferencia de complejo organometálico de Iridio

(III) es proporcional al número de monocapas transferidas.

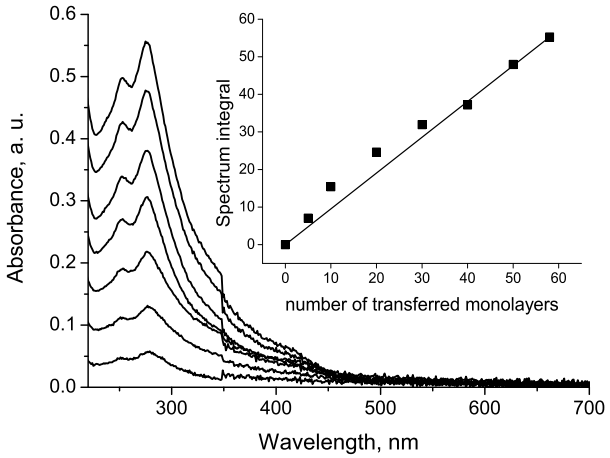

Figura 7.7: Espectros UV-visible de un soporte ITO cubierto con distinto número de monocapas mixtas Ir-dye/DMPA, transferidas mediante la técnica de Langmuir-Schaefer. Gráfica insertada: Valor del área integrada de los espeectros frente a número de monocapas transferidas.

Con estas transferencias LS se construyeron dispositivos orgánicos electroluminiscentes de una sola capa activa. Para ello, se depositaron un número variable de monocapas LS sobre soporte ITO. Posteriormente, se depositó una capa de cátodo metálico mediante evaporación térmica a alto vacío sobre las transferencias LS. De esta forma, los dispositivos tuvieron una estructura final: ITO/Ir-dye:DMPA (nº variable monocapas)/Al (150 nm). Estos dispositivos fueron caracterizados eléctricamente, Figura 7.8. Puede observarse como los valores de intensidad a una diferencia de potencial dada son inversamente proporcionales al número de monocapas Ir-dye:DMPA transferidas. Este efecto podría atribuirse, en principio, a un efecto aislante por parte de las cadenas metilénicas del fosfolípido.

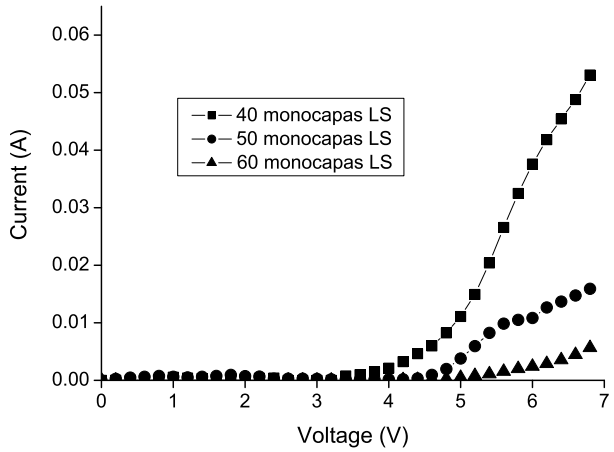

Figura 7.8: Curvas Intensidad-Voltaje para distintos dispositivos orgánicos electroluminiscentes, fabricados a partir de transferencias tipo Langmuir-Schaeffer de monocapas mixtas Ir-dye/DMPA.

Adsorción de proteínas en la interfase aire−agua: bacterioferritina

La química superficial de proteínas es de un gran interés tanto tecnológico como biofísico.[10–13] En colaboración con el grupo de investigación del Prof. Dr. J. M. Domínguez-Vera, en la Universidad de Granada, se ha estudiado el comportamiento de la proteína bacterioferritina[14] en la interfase aire−agua.

Se ha retenido dicha proteína, que no tiene actividad superficial por sí misma, con una matriz de eicosilamina ($C_{20}NH_2$) en la interfase aire−agua.[15] En este estudio se usó la técnica de adsorción para preparar la monocapa mixta. Para ello, se usó una disolución acuosa de la proteína como subfase, sobre la que se esparció una monocapa de eicosilamina, que posteriormente fué comprimida. La presencia de la bacterioferritina en la interfase aire−agua se confirmó por el cambio en las isotermas presión supericial-área molecular de

la eicosilamina.

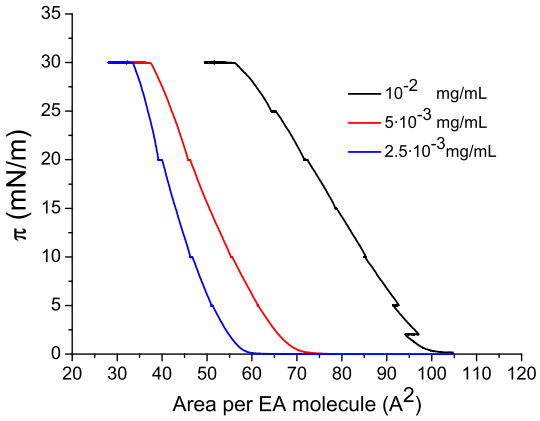

Figura 7.9: Isotermas presión superficial−área molecular para una monocapa de eicosilamina esparcida sobre una subfase de disolución acuosa de bacterioferritina a distintas concentraciones.

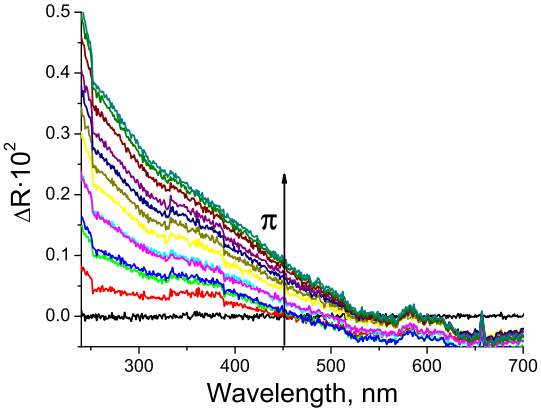

Figura 7.10: Espectros de reflexión UV-visible para una monocapa de eicosilamina esparcida sobre una subfase de bacterioferritina $5{\cdot}10^{-3}$ mg/mL.

Se registraron espectros de reflexión UV-vis en la interfase aire−agua, que confirman la presencia de la bacterioferritina en la monocapa. En la Figura

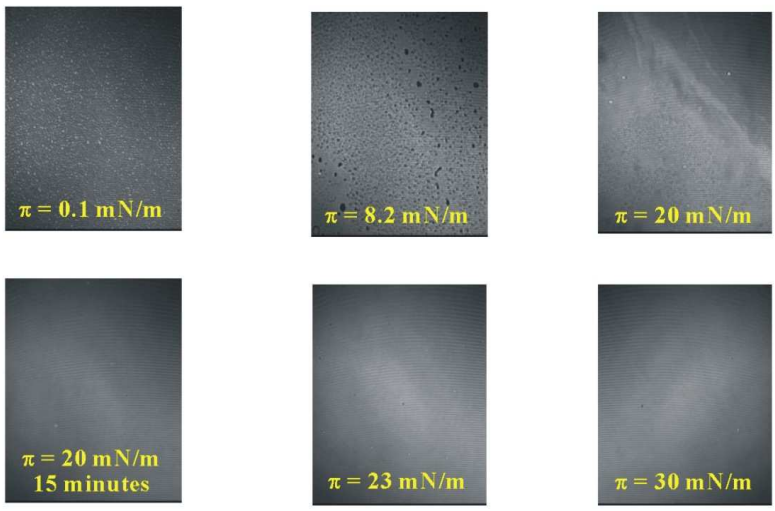

Figura 7.11: Imágenes BAM para una monocapa de eicosilamina esparcida sobre una subfase de bacterioferritina $5{\cdot}10^{-3}$ mg/mL a distintas presiones superficiales.

7.10 se muestran los espectros de reflexión para la monocapa de eicosilamina esparcida sobre una subfase con concentración de ferritina $5{\cdot}10^{-3}$ mg/mL. A medida que la monocapa se comprime, la concentración superficial de bacterioferritina aumenta, provocando un aumento de los picos en el espectro de reflexión.

La morfología de la monocapa se observó mediante microscopía de ángulo Brewster (BAM), obteniéndose las imágenes mostradas en la Figura 7.11. Para bajas presiones superficiales, se observan pequeños agregados, que posiblemente correspondan a agregados de proteína. A partir de una presión superficial de 20 mN/m, se observa una monocapa homogénea, incluso si se mantiene la presión superficial a un valor constante durante 15 minutos.

Referencias

1. Petty, M. C. *Langmuir-Blodgett Films: An Introduction;* Cambridge University Press: Cambridge, 1996.

2. Brockman, H. *Curr. Op. Struct. Biol.* **1999,** *9,* 438.

3. Torrie, G.; Valleau, J. *J. Comp. Phys.* **1977,** *23,* 187.

4. McCallum, J. L.; Tieleman, D. P. *J. Am. Chem. Soc.* **2006,** *128,* 125.

5. Kumar, S.; Bouzida, D.; Swensen, R.; Kollman, P.; Rosemberg, J. *J. Comp. Chem.* **1992,** *13,* 1011.

6. De Miguel, G.; Pedrosa, J. M.; Martín-Romero, M. T.; Muñoz, E.; Richardson, T. H.; Camacho, L. *J. Phys. Chem. B* **2005,** *109,* 3998.

7. De Miguel, G.; Pérez-Morales, M.; Martín-Romero, M. T.; Muñoz, E.; Richardson, T. H.; Camacho, L. *Langmuir* **2007,** *23,* 3794.

8. Bolink, H. J.; Baranoff, E.; Clemente-León, M.; Coronado, E.; López-Muñoz, A.; Repetto, D.; Sessolo, M.; Nazeeruddin, M. K. *Langmuir* **2009,** *25,* 79.

9. Koch, N. *ChemPhysChem* **2007,** *8,* 1438.

10. Kasemo, B. *Surf. Sci.* **2002,** *500,* 656.

11. Chapman, R. G.; Ostuni, E.; Takayama, S.; Homlin, R. E.; Yan, L.; Whitesides, G. M. *J. Am. Chem. Soc.* **2000,** *122,*.

12. Chen, C. S.; Mrksich, M.; Huang, S.; Whitesides, G. M.; Ingber, D. E. *Science* **1997,** *276,* 1425.

13. Elwing, H. *Biomaterials* **1998,** *19,* 397.

14. Fernández, B.; Gálvez, N.; Cuesta, R.; Hungría, A. B.; Calvino, J.; Domínguez-Vera, J. M. *Adv. Funct. Mater.* **2008,** *18,* 3931.

15. Britt, D. W.; Möbius, D.; Hlady, V. *Phys. Chem. Chem. Phys.* **2000,** *2,* 4594.